EXTRACELLULAR MATRIX (ECM)-BASED BIOMATERIAL STRATEGIES TO CONTROL DELIVERY OF GENE AND SMALL MOLECULE THERAPIES IN WOUND REPAIR

by

Jeongmin Hwang

A dissertation submitted to the Faculty of the University of Delaware in partial fulfillment of the requirements for the degree of Doctor of Philosophy in Biomedical Engineering

Fall 2022

EXTRACELLULAR MATRIX (ECM)-BASED BIOMATERIAL STRATEGIES TO CONTROL DELIVERY OF GENE AND SMALL MOLECULE THERAPIES IN WOUND REPAIR

by

Jeongmin Hwang

Approved: _____
Kristi L. Kiick, Ph.D.
Chair of the Department of Biomedical Engineering

Approved: _____
Levi T. Thompson, Ph.D.
Dean of the College of Engineering

Approved: _____
Louis F. Rossi, Ph.D.
Vice Provost for Graduate and Professional Education and
Dean of the Graduate College

I certify that I have read this dissertation and that in my opinion it meets the academic and professional standard required by the University as a dissertation for the degree of Doctor of Philosophy.

Signed: _____

Millicent O. Sullivan, Ph.D.
Professor in charge of dissertation

I certify that I have read this dissertation and that in my opinion it meets the academic and professional standard required by the University as a dissertation for the degree of Doctor of Philosophy.

Signed: _____

Kristi L. Kiick, Ph.D.
Member of dissertation committee

I certify that I have read this dissertation and that in my opinion it meets the academic and professional standard required by the University as a dissertation for the degree of Doctor of Philosophy.

Signed: _____

Xinqiao Jia, Ph.D.
Member of dissertation committee

I certify that I have read this dissertation and that in my opinion it meets the academic and professional standard required by the University as a dissertation for the degree of Doctor of Philosophy.

Signed: _____

April M. Kloxin, Ph.D.
Member of dissertation committee

ACKNOWLEDGMENTS

I would like to first express my deepest appreciation to my advisers Professor Millicent O. Sullivan and Professor Kristi L. Kiick, for all their support, patient, and encouragement that led to complete this work. I cannot imagine how I could complete this such a long and challenging adventure without them. They were not only the Ph.D. dissertation advisers but also mentors and role models for me to guide on my next career. Their enthusiasm toward to science kept me motivated, and their patient and encouragement also kept me brave enough to try. I also have learned the developing critical thinking and hypothesis driven solving science questions, which shape me into who I am now. I am deeply grateful to Professors Sullivan and Kiick for all their efforts to guide me as an independent researcher.

I also would like to thank my committee members, Professor Xinqiao Jia, and Professor April M. Kloxin for their profound scientific advice and informative discussions to complete this work. Their comments and suggestions aided me to understand and move forward the projects. I also really would like to thank their flexibility on scheduling on committee meetings, proposal, and defense.

I sincerely thank all my past and current Sullivan and Kiick groups members (Dr. Tianzhi Luo, Dr. Hang Kuen Lau, Dr. Michael Haider, Dr. Jingya Qin, Dr. Lucas Dunshee, Dr. Rachel Lieser, Dr. Rebecca Scott, Dr. Anuraag Boddupallie, Dr. Raj

Thapa, Colleen Fridley, Dr. Ramadan Abouomar, Cristobal Garcia Garcia, Luisa Palmese, Haofu Huang, Sai Patkar, Bin Wang, James Mullin, Daniel Yur, Esther Roh, Katie Nelson, Antonio Goncalves, Mruthula Rammohan, Chris Domalewski, Hugo Hu, Daniel Liu, and Blake Richards) for their support and help. I especially want to thank Dr. Rebecca Scott, Dr. Raj Thapa, and Colleen Fridley for their help on initiating and learning all the technical skills. I also want to thank Dr. Jingya Qin, Cristo, Luisa Palmese, Sai Patkar, Haofu Huang, Daniel Yur and Esther Roh for not only supporting me about my research work as co-workers but also sharing the moments of joy and sadness as friends. I also want to thank Dr. Jingya Qin and Haofu Huang for their help and great discussion for our collaborating works.

I would like to thank Christina Stinger, Jean Ross, Dr. Sylvain Le Marchand, and Dr. Chandran Sabanayagam for training me on technical skills necessary for my thesis work. Especially, Christine helped me on reducing my fear of mice. I could not complete my *in vivo* studies without Christine's aid. And, Chandran and I worked together to conquer the most difficult project that I have worked. I really thank Chandran for his patients and all great advice to work on that project.

I would like to thank all my friends, especially, Minjung, Hyeyoung, Kyunghee, Jiyeon, Daseul, Jiwon, and Sungcheol for their support. They help me make my work-life balance. The time that I spent with them was a driving force to continue my works.

Lastly, I would like to express my sincere gratitude to my family and my boyfriend's family for their constant support and love. Although we were far away from each other and we have not seen for long years, I could still feel the love and warm-

hearted to make me motivated. I really miss and love my parents and my precious little brother, Kyunghwan, so much. And, I want to thank my boyfriend's brother, Minkyu, for helping me on work and life balance. Finally, I want to thank my love, Siyoung, for always being there for me. There are no words in the world that I can show my appreciation to you. I really could not complete this work without your support. The past nine years with you has been amazing moments in my life. And, I cannot wait to see our future. Thank you and love you so much.

TABLE OF CONTENTS

LIST OF TABLES

LIST OF FIGURES

ABSTRACT

Despite the great potential of topically administered therapeutics in wound repair, due to the harsh wound environment, topically administered therapeutics are cleared out from the wound quickly, resulting in the reduced local concentration and their effectiveness of therapeutics. To overcome this limitation, the overall goal of my dissertation work is to improve the efficacy of topically administered therapeutics through the control over the therapeutic delivery kinetics using the interactions between therapeutic carriers and matrices. I specifically leverage the hybridization of collagen mimetic/like peptides (CMP or CLP) with a native collagen through the strand invasion process to tether CMP/CLP modified nanostructure carriers onto collagen-containing matrices. I hypothesize that CMP/CLP modified carrier and collagen tether approach would result in the extended the duration of therapeutic effects and control over the delivery of the cargo in response to cell-mediated collagen degradation.

The first/second objectives of this thesis were to control growth factor gene transfer kinetics while regulating cell behaviors via manipulating both the number of CMP-collagen tethers and the ECM composition for the improved wound repair. Disruption in vascularization during wound healing can severely impair healing. Pro-angiogenic growth factor therapies have shown great healing potential; however, controlling growth factor activity and cellular behavior over desired healing time scales remains a critical challenging. I developed gene-activating hyaluronic acid-collagen matrix (GAHCM) comprising DNA/polyethylenimine (PEI) polyplexes retained on hyaluronic acid (HA)-collagen (HCM) hydrogels using CMPs. First, I observed that

polyplexes with 50% CMP-modified PEI (50 CP) showed enhanced retention of polyplexes in HCM hydrogels by 2.7-fold as compared to non-CMP modified polyplexes. Moreover, the enhanced the retention of polyplex through CMP modification, as well as HA-CD44 interaction via the incorporation of HA in the collagen hydrogel increased the gene transfection efficiency to fibroblast. Furthermore, when fibroblasts were exposed to pro-angiogenic and pro-healing vascular endothelial growth factor-A (VEGF-A)-GAHCM, the 50 CP matrix facilitated sustained VEGF-A production for up to 7 days, with maximal expression at day 5. This sustained VEGF-A production using VEGF-GAHCM with 50 CP stimulated prolonged pro-healing responses, including the TGF-β1-induced myofibroblast transformation. In addition, application of fibroblasts containing VEGF-GAHCM with 50 CP stimulated the increased growth and persistent migration of endothelial cells (ECs) for at least 7 days, as compared to non-CMP modified GAHCM. Moreover, this resulted in the high CD31 expression on ECs and formation of an interconnected EC network with a significantly higher network volume and a larger diameter network structure. Lastly, application of VEGF-GAHCM with 50 CP in murine splinted excisional wounds facilitated prolonged pro-healing and pro-angiogenic responses resulting in the overall enhanced wound closure via increased myofibroblasts differentiation and blood vessel formation, improved granulation tissue formation, and faster re-epithelialization. Overall, these findings demonstrate the use of ECM-based materials to stimulate efficient gene transfer and regulate cellular phenotype, resulting in improved control of growth factor activity for wound repair.

The third objective of this thesis was to design new antibiotic delivery systems that maximize pharmacological effects and minimize side effects. Despite the great

promise for antibiotic therapy in wound infections, antibiotic resistance stemming from frequent dosing diminishes drug efficacy and contributes to recurrent infection. To overcome the limitations of current antibiotic therapies, I developed elastin-like peptide and collagen-like peptide (ELP-CLP) nanovesicles tethered to collagen-containing matrices to control vancomycin delivery and provide extended antibacterial effects against methicillin-resistant Staphylococcus aureus (MRSA). I observed that as compared to liposome formulations, ELP-CLP nanovesicles showed enhanced entrapment efficacy of vancomycin by 3-fold and enabled the controlled release of vancomycin at a constant rate with zero-order kinetics. Moreover, ELP-CLP nanovesicles could be retained on both collagen-fibrin (co-gel) matrices and collagen-only matrices, with differential retention and release on/from the two biomaterials resulting in different release profiles of vancomycin. Overall, the biphasic release profiles of vancomycin from ELP-CLP tethered collagen/co-gel more effectively inhibited and delayed the growth of MRSA even after repeated bacterial inoculation as compared to matrices containing free vancomycin. Thus, this newly developed antibiotic delivery system exhibited distinct advantages for controlled vancomycin delivery and prolonged antibacterial activity relevant to the treatment of wound infections.

In summary, this dissertation describes CMP modification of nanocarriers enables not only the extended delivery of therapeutics from collagen-containing matrices through CMP and collagen tethers, but also the maximized therapeutic effects *in vitro*. Thus, this work suggest that CMP-collagen tether approach has significant potential to overcome key challenges in the topically administrated therapeutics for wound healing and regenerative medicine.

Chapter 1

TARGETED DRUG DELIVERY VIA THE USE OF ECM-MIMETIC MATERIALS

The use of drug delivery vehicles to improve the efficacy of drugs and to target their action at effective concentrations over desired periods of time has been an active topic of research and clinical investigation for decades. Both synthetic and natural drug delivery materials have facilitated locally-controlled as well as targeted drug delivery. Extracellular matrix (ECM) molecules have generated widespread interest as drug delivery materials owing to the various biological functions of ECM. Hydrogels created using ECM molecules can provide not only biochemical and structural support to cells, but also spatial and temporal control over the release of therapeutic agents, including small molecules, biomacromolecules, and cells. In addition, the modification of drug delivery carriers with ECM fragments used as cell-binding ligands has facilitated cell-targeted delivery and improved the therapeutic efficiency of drugs through interaction with highly-expressed cellular receptors for ECM. The combination of ECM-derived hydrogels and ECM-derived ligand approaches shows synergistic effects, leading to a great promise for the delivery of intracellular drugs, which require specific endocytic pathways for maximal effectiveness. In this chapter, I provide an overview of cellular receptors that interact with ECM molecules and discuss examples of selected ECM components that have been applied for drug delivery in both local and systemic platforms. Finally, I highlight the potential impacts of utilizing the interaction between

ECM components and cellular receptors for intracellular delivery, particularly in tissue regeneration applications.

1.1 Introduction

Conventional drugs have been critical to the effective management of disease. Despite the benefits of free drugs, 118 drugs approved from 1980 to 2009 in the United States were withdrawn from the market, 22% of them due to safety reasons including hepatic toxicity, severe cardiovascular effects, gastrointestinal issues, and allergic reactions (1, 2). In addition, safety concerns and inadequate efficacy (78%) were the main reasons for the failure of 54% of the 640 therapeutics that entered phase 3 trials between 1998 and 2008, with follow-up through 2015 (3). The pharmacokinetics of any drug compound, including its efficacy and safety, is critically affected by the route of drug entry (4). For example, systemically administrated drugs are exposed to the entire circulatory system, and may access multiple tissues/organs within the body in the absence of direct targeting (5); for drugs with intracellular targets, additional challenges are posed by the need to navigate the intracellular landscape. The challenges are compounded for drugs that are highly toxic to healthy cells, such as cytostatic drugs for chemotherapeutics or immunosuppressants, adding an extra set of barriers during pre-clinical and clinical evaluation.

To overcome the pharmacokinetic limitations of free drugs, drug delivery systems (DDS) have been designed based on nanomaterials, polymers, and lipids, which can be attached to drugs or used to encapsulate drugs in order to better localize their delivery or control drug release over extended periods (6-9). Nanometer-scale therapeutics can extravasate from circulation and accumulate in some tissues via passive targeting effects (10). Such advances were the basis of the improvements in chemotherapy efficacy using liposomal formulations of doxorubicin (Doxil), which was introduced for the treatment of Kaposi's sarcoma in 1995. In addition, over 340 DDS have been approved by the FDA and employed clinically to date (Table 3 from (11)), and it is clear that

nanomaterial DDS have great potential for the targeted delivery of drugs. However, passive targeting is only useful for targeting very specific organs such as tumors (12), and even in those cases, some regions of tumors exhibit variations in microvascular permeability that diminish the efficacy of passive targeting.

Local administration provides a simple strategy to enhance active targeting to specific sites, taking advantage of physical localization (13). Employing DDS for localized therapy can improve drug efficacy by preventing the loss of therapeutic agent from the administration site, which minimizes necessary doses and maximizes potency. In addition, polymeric or liposomal carriers can be tailored to achieve sustained release of drugs at optimal therapeutic concentrations in a particular tissue(14-16). As DDS for localized therapy, hydrophilic polymeric hydrogels (for hydrophilic drugs) or nanoparticles (for encapsulation of hydrophobic drugs) can be directly injected or applied to the tissue of interest to achieve sustained and controlled drug release to a particular site through diffusion (4, 17). The tailoring of hydrogel and nanoparticle composition, structure, and porosity has been possible owing to the enormous range of polymers and crosslinking chemistries developed for these applications.

Hydrogels have been designed to exploit the mechanical and biochemical activities of the native extracellular matrix (ECM) to influence cells through cell-matrix interactions (18-22). These cell-matrix interactions are pivotal to enhance cell infiltration into the hydrogel and promote cell responses in hydrogels that are appropriate for tissue regeneration and drug delivery applications. To create hydrogels that support cell-matrix interactions, ECM molecules are often utilized in hydrogel formulations. For example, decellularized ECM (dECM) matrices derived from tissues and organs are composed of native ECM molecules, and dECM therefore mimics the structural properties of the native matrix (23, 24). Owing to the preservation of biochemical cues from the native tissue microenvironment, dECM matrices trigger cellular response that have been exploited clinically in tissue engineering and regenerative medicine (Tissue Mend® (Stryker Orthopaedics, USA), AlloDerm®

(LifeCell Corp. USA), CutffPatchTM (Organogenesis, USA)). In addition, the delivery of growth factors (25) and microRNA (26) using dECM has recently been explored.

Owing to the myriad cellular interactions with ECM-based materials, the surfaces of drug-loaded nanoparticles also have been modified with ECM-based materials to increase the extent of ligand-mediated, site-specific DDS. The incorporation of bio-specific ligands such as proteins, polysaccharides, peptides, aptamers, and small molecules, facilitates interaction with specific receptors that are either over-expressed or expressed only in specific tissues or cells to achieve active targeting. For example, it has been reported that $\alpha_v\beta_3$ integrin and CD44 receptors are upregulated in various tumor tissues (27). The RGD sequence derived from multiple ECM proteins to target integrin receptors, and hyaluronic acid to target CD44 receptor on cancerous cells, have been widely employed to transport anti-tumor agents (28-31). Furthermore, target receptor-mediated siRNA delivery has been developed utilizing ligands such as peptides, GalNAc, and aptamers (32). Alnylam Pharmaceuticals launched the first RNA interference (RNAi) drug, ONPATTRO®, which uses lipid nanoparticles to deliver RNAi intravenously and treat polyneuropathy caused by hereditary ATTR amyloidosis (33). As next-generation alternatives of ONPATTRO®, the GalNac ligand has been employed to target asialoglycoprotein receptor (ASGP-R) on the hepatocytes. ASGP-R has been shown to mediate endocytosis and degradation of wide variety of desialylated glycoproteins and neoglycoproteins which contain GalNAc residues on the their N-linked carbohydrate chains, and it recognizes specific markers of autoimmune hepatitis (34). The GalNAc conjugated RNAi systems for treatment of liver diseases are currently in phase III (Table 1 from (35)). Thus, active targeting strategies have great potential to optimize the delivery of intracellularly active drugs such as many small molecules, as well as biomacromolecules including nucleic acids, peptides, or proteins, which require specific endocytic pathways for action.

Here, I focus on recent developments in the use of ECM components for actively targeted DDS. In particular, I briefly review ligand-receptor mediated endocytosis and cellular interactions with various ECM components as targeting strategies, and I

consider the advantages afforded by each approach. I then provide examples of the use of key ECM components in DDS, either as hydrogels or as ligands applied for targeted intracellular DDS.

1.2 ECM-cell interaction mediated drug delivery applications

Researchers have exploited an expanded understanding of the interactions between cells and the extracellular matrix (ECM), as well as increased knowledge about signaling pathways and molecules relevant to the treatment of disease, in designing new, more cell-specific therapeutics and drug delivery systems (DDS). Cell surface receptors are attractive pharmacological targets since they transduce signals from the extracellular environment to modulate cell responses. Integrins, a major class of transmembrane receptors whose primary role is to recognize and bind ECM, have been a target of therapeutic development for nearly 30 years in the pharmaceutical industry (36, 37). However, despite some promising therapeutic advances, the complex biology of integrins has often confounded drug development. Integrins are involved in canonical processes ranging from embryonic development to mature tissue function through binding to their ligands. Therefore, it is critical to understand the mechanisms by which cell-ECM interactions enable cells to sense and respond to extracellular signals encoded in the matrix.

Each ECM molecule has an affinity to a cell surface receptor or receptors, including integrins (Figure 1.1); moreover, the specific integrins expressed by a given cell depend both on the cell type as well as on the cell's physiological state. Accordingly, DDS can be modified with ECM molecules to serve as ligands that will facilitate drug

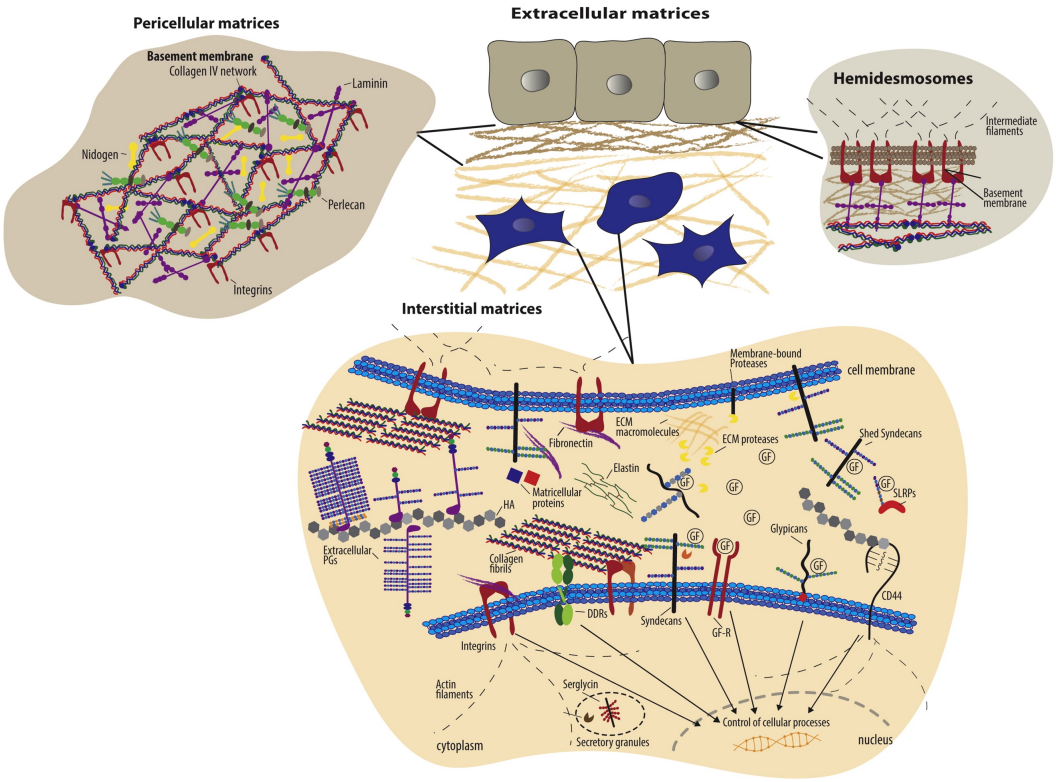

Figure 1.1. Schematic overview of extracellular matrix components and their cell surface receptors (196)). Copyright 2016. Reproduced with permission from Elsevier Inc. Cells have specific surface receptors, such as integrins, cell surface proteoglycans (ex. syndecans and glypicans), the HA receptor CD44, and DDRs, to bind ECM components for regulation of various cellular functions.

targeting. These approaches are described below for various classes of ECM that have been particularly fruitful in targeted delivery. Types of ECM molecules

1.2.1.1 Proteins

ECM proteins include fibrous proteins such as collagen and elastin, and glycoproteins such as fibronectin, laminins, vitronectin, thrombospondin, chondronectin, osteonectin, and fibrin. Collagen is a major extracellular matrix component that provides mechanical support, regulates cellular behaviour, and directs tissue development. Collagen fibrils, which are formed by self-assembly of triple helical

collagen molecules, are cross-linked to provide mechanical strength and integrity to the extracellular matrix, and collagens strongly influence the tensile strength and elasticity of tissue. In addition, collagens interact with integrins to regulate cell adhesion, proliferation, and migration, and collagens also interact with other ECM components to direct matrix remodelling (38). Fibronectin also regulates a wide variety of cellular functions including cell adhesion, migration, growth and proliferation, embryonic morphogenesis, and wound healing (39, 40). Fibronectin usually exists as a dimer composed two nearly identical subunits (type I, type II, and type III) linked together through disulfide bond formation at their C-termini. The type III subunit contains about 100 amino acids in two anti-parallel β-sheets, which are also present in collagens, and the type III subunit also encodes integrin binding (via the RGD motif) and heparin-binding domains. Laminins promote cell adhesion and migration, neurite outgrowth, angiogenesis. Laminins are a major component of basement membrane along with collagen type IV, with a structure that is comprised of heterotrimeric glycoproteins; three subunits, α, β, and γ, come together to form at least 19 laminin isoforms (41, 42). These laminin isoforms are specifically expressed in tissues to promote biological activities, including cell differentiation, cell shape and movement, and managing tissue phenotypes and survival. The isoforms can bind to other laminins, proteoglycans, and other ECM proteins via various integrins receptors. Due to the ability of ECM proteins to influence cell fate via interactions with integrins, the biocompatible and biodegradable ECM proteins are widely used natural materials for biomedical application (43-45).

1.2.1.2 Polysaccharides

ECM polysaccharides including heparin sulfate, chondroitin sulfate, dermatan sulfate, keratin sulfate and hyaluronic acid provide largely a structural network, as most ECM polysaccharides are not directly involved in cellular interactions, but indirectly through interaction with other proteins. Heparan sulfate/heparin is a linear

polysaccharide of repeating N-acetyl glucosamine (GlcNAc)-D-glucuronic acid (GlcA) disaccharide units (46), and is often covalently attached to cell-associated proteins such as the syndecans (SDCs) and glypicans (GPCs) to form heparan sulfate proteoglycans (HSPGs) (47). HSPGs such as syndecans and glypicans are able to modulate the cellular uptake of bound ligands; in addition, heparin interacts with various proteins to regulate biological process including growth factor or cytokine signalling, coagulation factor activity, microbe-host interactions, and lipoprotein metabolism (48). The interaction is highly specific, involving electrostatic forces between the negatively charged heparin and positively charged amino acid residues (e.g., lysine and arginine), and both protects the stability of proteins and increases their affinity for cell receptors (49). Due to the ability of heparin to interact with proteins, particularly growth factors, heparin has been utilized widely in DDS, with a focus on binding of growth factors (rather than to cell-surface receptors). Heparin-based hydrogels have been widely employed as growth factor carriers for tissue regeneration (50-55).

On the other hand, chondroitin sulfate and hyaluronic acid have an affinity to non-integrin cell receptors such as CD44. Chondroitin sulfate is also composed of a sulfated β-1,3-linked N-acetyl galactosamine (GalNAc) and β-1,4-linked D-glucuronic acid (GlcA) disaccharide repeating units. The sulfation pattern defines the different roles of chondroitin sulfate and its selective interaction with molecules mediating such functions as regulation of signal transduction, cell division and morphogenesis, and development of the central nervous system (56). Hyaluronic acid is a non-sulfated polysaccharide composed of disaccharide repeating units of glucuronic acid and N-acetylglucosamine. Hyaluronic acid as a major role in tissue architecture, tissue regeneration, ingrowth of blood vessels, and cellular functions such as motility, adhesion, and proliferation (57) has been utilized in DDS to improve long-acting and target-specific delivery (58-60). In particular, due to the highly specific cellular receptor interaction and cellular uptake of hyaluronic acid in kidney, liver, lymphatic vessels, and tumor sites, hyaluronic acid often has been employed as carriers for intracellular drugs such as anti-tumor agents, and nucleic acids (31, 61-64).

1.2.2 Interactions of ECM with cell receptors

	Integrin	Non-integrin receptors
Collagen	$\alpha_1\beta_1$, $\alpha_2\beta_1$, $\alpha_{10}\beta_1$, $\alpha_{11}\beta_1$	Discoidin domain receptors (DDR1 and DDR2), GPVI (platelets), LAIR (immune cell), OSCAR (osteoblast), and mannose receptors (Endo180 or uPARAP), Syndecan, CD44
Fibronectin	$\alpha_5\beta_1$, $\alpha_3\beta_1$, $\alpha_8\beta_1$, and $\alpha_v\beta_3$, $\alpha_4\beta_1$, $\alpha_4\beta_7$, $\alpha_9\beta_1$,	Syndecan
Laminin	$\alpha_1\beta_1$, $\alpha_2\beta_1$, $\alpha_3\beta_1$, $\alpha_6\beta_1$, $\alpha_7\beta_1$, $\alpha_{10}\beta_1$, $\alpha_6\beta_4$, $\alpha_v\beta_8$	Syndecan, α-Dystroglycan CD44
Heparan sulfate		Syndecan, Glypicans
Chondroitin sulfate		CD44, NG2, RPTP-σ, GPI-brevican
Hyaluronic acid		CD44, RHAMM, Toll-like receptors

Table 1.1 The extracellular matrix components and their cell surface receptors.

ECM molecules typically interact with cells through both integrin and non-integrin cell surface receptors (Table 1.1). The integrin receptors primarily bind the extracellular matrix proteins to connect with the cytoskeleton and to cooperate with growth factor receptors for cell survival, cell cycle progression, and cell migration (65-67). As introduced above, integrins consist of heterodimeric non-covalent association of α and β subunits which comprise a specific receptor. In particular, α subunits have a highly specific role in ligand binding for signal transduction (68), with α2β1, for example, binding to the collagen family, α5β1 binding to fibronectin, and αvβ3 binding to fibronectin, vitronectin and fibrinogen as summarized in Table 1.1 (from (69)). Integrin-mediated binding has been leveraged for an enormous range of applications, as multiple integrin receptors, including $\alpha_v\beta_3$, $\alpha_v\beta_5$, $\alpha_v\beta_6$, $\alpha_v\beta_8$, $\alpha_{IIb}\beta_3$, $\alpha_5\beta_1$, and $\alpha_8\beta_1$

recognize and bind to the Arg-Gly-Asp (RGD) motif which is found in multiple ECM proteins including collagens, fibronectin, laminin, tenascin, vitronectin, and thrombospondin (70, 71). The RGD sequence as a 'minimal' ligand for multiple integrins has been widely used over numerous decades in the development of targeted polymeric and nanoparticle-based therapies. The selectivity of RGD peptide for a specific integrin can be modulated by conformation of the RGD sequence and its flanking residues (72). Cyclic peptides, cRGDfK, cRGDyK, and RGDC4 are selective for the integrins αvβ3 and αvβ5, which are overexpressed in vasculature of tumor tissue. Likewise, the GFOGER sequence of collagen binds to four different integrin cell receptors ($\alpha_1\beta_1$, $\alpha_2\beta_1$, $\alpha_{10}\beta_1$, and $\alpha_{11}\beta_1$) (73); since the $\alpha_2\beta_1$ integrin receptor is involved in osteogenesis, the GFOGER sequence has been utilized to assist in bone repair (74).

The REDV sequence from fibronectin is a cell adhesion motif to integrin $\alpha_4\beta_1$, selective for the endothelial cells (75, 76). Owing to the specificity toward endothelial cells, the REDV sequence has been modified on the system to transport gene to vascular endothelial cells (77, 78). In addition, the active peptide sequences from laminin are able to interact with integrins, syndecans, α-dystroglycan, and CD44, to perform various biological activities, cell adhesion and neurite outgrowth and proliferation, and angiogenesis, such as those mediated by laminin (79). The YIGSR sequence and IKVAV sequence from laminin are also cell adhesion domains (80, 81), and the RKRLQVQLSIRT (AG73) sequence derived from the mouse laminin α1 chain interacts with syndecans to promote cell adhesion, neurite outgrowth, and angiogenesis (82). In contrast, DFKLFAVYIKYR-GGC (C16Y), derived from the mouse laminin γ1 chain, binds to integrin $\alpha_v\beta_3$ and $\alpha_5\beta_1$ receptors (83). Laminin-derived peptides have been incorporated into the delivery systems of anti-tumor agents to enhance their specificity to highly expressed laminin receptors on cancer cells, including YIGSR for the 32/67 kD receptor, IKVAV for the $\alpha_3\beta_1$ and $\alpha_6\beta_1$ integrin receptors, AG73 for syndecan-2 receptor and C16Y for the $\alpha_v\beta_3$ integrin receptors (83-87).

Short synthetic peptides derived from ECM proteins retain the integrin-binding function, thus are attractive in the design of materials. For example, the Stupp group has developed bioactive peptide amphiphiles (PA) for regenerative medicine applications (88-90). The RGDS sequence has been attached to PA to induce integrin-mediated adhesion, spreading or migration of fibroblasts, breast cancer cells, and bone marrow mononuclear cells in vitro (91-93). In addition, the IKVAV sequence has been added to PA to induce differentiation of progenitor cells into neurons (94). In addition, these ECM proteins have binding sites for both integrin and growth factors. Once ECM proteins engage integrins for adhesion, the proximity of the cell to the ECM localizes the growth factors to their cell surface receptors to induce and/or amplify the signaling for development or repair. Capitalizing on this biological cooperativity offers an enormous advantage in ECM protein-based systems for delivery of growth factors, particularly, in inflammatory diseases where the growth factors are easily degraded (95). ECM protein-based DDS are able to protect growth factors while delivering them to their receptor sites to regulate cellular responses.

Non-integrin cell receptors for extracellular matrix molecules include CD36, certain laminin-binding proteins, and proteoglycans (68) comprising glycosaminoglycan (GAG) chains such as heparan sulfate, chondroitin sulfate, dermatan sulfate and keratin sulfate (96). Proteoglycan co-receptors (CD44, glypicans, neuropilins, syndecans, and TβRIII/betaglycan) mediate interactions with ligands, ECM proteins or other cell surface receptors to promote the formation of cell surface receptor-signaling complexes, and also to regulate cell adhesion, migration, morphogenesis, and differentiation. Among the proteoglycan co-receptors, syndecan and CD44 receptors also bind ECM molecules. Syndecan receptors bind collagens, fibronectin, and laminin and growth factors (e.g., fibroblast growth factor) to assemble signaling complexes with other receptors to control cellular differentiation and development (97), and CD44 receptors bind to type I and IV collagens and hyaluronan to regulate cell adhesion and movement (98). These ECM molecules have been exploited in the DDS not only to

target cells that highly expressed those receptors in certain pathological conditions, but also to control the regulation of cellular responses.

Collagen directly interacts with four different integrin cell receptors, α1β1, α2β1, α10β1, and α11β1, depending on the type and form of collagen (73). α2β1 and α11β1 integrins primarily interact with the fibrillar collagen type I (e.g., α2β1 integrin mediates collagen type I binding for phagocytosis in fibroblasts (99), while α1β1 and α10β1 interact with the non-fibrillar collagens IV and VI. Collagen also binds to non-integrin receptors such as discoidin domain receptors (DDR1 and DDR2), the GPVI receptor on platelets, the LAIR receptor of immune cells, the OSCAR receptor of osteoblasts, and mannose receptors (Endo180 or uPARAP) (100). Under particular pathological conditions, these collagen receptors are highly expressed. Endo180/uPARAP receptor is overexpressed by malignant cells in sarcomas, glioblastomas, subsets of acute myeloid leukemia (101). For integrins, expression of α1β1 and α2β1 was localized to scleral fibroblast focal adhesions and expression of integrin α11β1 is restricted to tumor stroma or other fibrotic disease (102, 103). Collagen as a ligand to target these pathological conditions thus represents a powerful therapeutic strategy.

Fibronectin binds both integrin receptors and other ECM molecules. Fibronectin type III10 domain which includes the RGD sequence, is the binding sites for integrins, α5β1, α3β1, α8β1, and αvβ3 in a broad range of cell types and tissues (39). In particular, α5β1 integrin is required for internalization of fibronectin through caveolin-1 dependent endocytosis in myofibroblasts (99). And, α4β1 and α4β7 integrins recognize the LDV and REDV motifs in the alternatively spliced V region, IDAPS in the III14 domain, and KLDAPT in the III5 domain. In addition, α4β1 and α9β1 binds the EDGIHEL sequence in the alternatively spliced EDA segment. Fibronectin also contains two heparin-binding domains within its V domain to interact with heparin and chondroitin sulfate for cell adhesion, and the fibronectin I6-9 and II1,2 domains recognize denatured collagens to clear them from blood and tissue. The expression of the various fibronectin integrin

receptors depends on the pathological conditions, providing targets for DDS. The integrins α5β1 and αvβ3 are upregulated in angiogenic vessels during angiogenesis (104); in particular, the integrin αvβ3 is not expressed in healthy adult animal tissue but overexpressed during angiogenesis in tumor tissues, allowing for the targeting of integrin αvβ3 with fibronectin-based, chemotherapeutic DDS.

Moreover, laminin binds various integrins receptors (α1β1, α2β1, α3β1, α6β1, α7β1, α10β1, α6β4, and αvβ8) (69). Laminin-1, 2, 5, 8, 10, 11 isoforms interact with integrins α3β1 and α6β1 which regulate embryonic development, epithelial regeneration, and wound healing processes, and which also internalize to endosome as well (105). Laminin binding cell receptors are highly expressed in various cancer cells types. For example, integrins α3β1 and α6β1 are overexpressed in various epithelial cancers. Amongst non-integrin receptors, laminin receptor (LAM 67R) is overexpressed on human prostate cancer cells and syndecan-2 is overexpressed in various cancer cell lines and during angiogenesis (106). Based on expression of laminin receptors in certain pathological condition, laminin or synthetic laminin mimetic peptides as ligand are utilized as ligands to target and deliver therapeutic agents.

Chondroitin sulfate interacts with cell-surface CD44 receptors. CD44 receptors are an attractive target as they are a cancer stem cell marker which is overexpressed about 4- to 5-fold in metastasis and cancer progression (107). Owing to the interaction between chondroitin sulfate and CD44 receptor, chondroitin sulfate has been utilized in DDS to target CD44 overexpressing cancer cells and promote receptor-mediated endocytosis. The polysaccharide hyaluronic acid binds toll-like receptors, CD44, and RHAMM on cell membrane. Interactions with toll-like receptors regulate signalling in inflammatory cells and other cell types, and those with CD44 control leukocyte homing and recruitment. In addition, hyaluronic acid interactions with CD44 and RHAMM regulates tumour growth and metastasis. CD44 expression is characteristic in cells under certain pathological conditions such as infarcted myocardium, infiltrating leukocytes, wound myofibroblasts, vascular cells, and many tumor cells.

1.2.3 Receptor-mediated endocytosis

The efficacy, biomedical function, biodistribution, and toxicity of drugs with intracellular targets of action are dictated by their internalization into the cells through interaction with the exterior of the plasma membrane and their endocytic pathway (108, 109). Endocytosis occurs via two primary routes - phagocytosis and pinocytosis (110), with phagocytosis characteristic of dendritic cells, neutrophils, monocytes and macrophages (111) and pinocytosis, which occurs via clathrin-mediated endocytosis, caveolae-mediated endocytosis, clathrin/caveolae-independent endocytosis, and micropinocytosis (108, 110), possible for all cell types. Micropinocytosis is an actin-driven endocytic process that initiates the activation of receptor tyrosine kinases (e.g., via growth factors) to polymerize actin and form macropinosomes for cell entry. Unlike micropinocytosis, receptor-mediated endocytosis (e.g., clathrin-mediated endocytosis, caveolae-mediated endocytosis, and clathrin/caveolase-independent endocytosis) is regulated by specific interactions between a receptor and an extracellular ligand or particle (110). Physical properties of the extracellular cargo, including particle size, shape, and surface charge, all influence the cellular uptake pathway. In addition to these physical properties, very specific ligand-receptor interactions dictate the receptor-mediated endocytosis pathways of ligand-decorated cargo.

The majority of DDS are internalized into cells through the clathrin-mediated endocytosis pathway using interactions with numerous receptors on cell membrane including transferrin, asialoglycoprotein receptor, epidermal growth factor receptor, chemokine receptors, and cell adhesion receptors (112-117). In this process, particular ligands in the extracellular fluid bind to the receptors on the surface of the cell membrane, which is rich in clathrin, to form a ligand-receptor complex (118) that forms a clathrin-coated pit and results in the formation of clathrin-coated vesicles approximately 10 to 200 nm in diameter for internalization. After internalization, the clathrin coat on the vesicles is expelled and recycled to the plasma membrane and the vesicle fuses with the early endosomes. The cargo within early endosomes will reach lysosomes and eventually be degraded by the acidic pH and digestive enzyme of the

lysosome. Given the relatively large number of binding molecules, clathrin-mediated endocytosis is a primary uptake pathway for most polymeric DDS.

Polymer-mediated nucleic acid delivery systems have been reported with both clathrin-mediated endocytosis and caveolae-mediated endocytosis as their uptake pathways, depending on the size, types, and surface charge of their cargos, and cellular microenvironment (2D vs 3D) (119, 120). However, trafficking of cargo through caveolae-mediated endocytosis routes enhances gene expression owing to the low or non-acidifying pathway (121, 122). Caveolae-mediated endocytosis occurs via association of the delivery vehicle with cholesterol-rich lipid rafts in the plasma membrane for cellular entry (108). Once cargo molecules bind to the caveolae surface rich in glycosphingolpids including GM-1 and Gb3, the caveolae engulf the cargo to form vesicles approximately 50 nm in diameter. The detached caveolar vesicles can fuse with early endosomes, but because the caveolar vesicles have neutral pH, they generally avoid fusion with lysosomes thus preventing lyososomal degradation of drug cargo.

Clathrin-and caveolae-independent endocytosis occurs without binding of the cargo to clathrin or caveolae (110); the pathway depends instead on cell-surface molecules such as Arf-6, flotillin, Cdc42, and RhoA, involving different subtypes of internalization routes depending on the specific cell-surface molecule. Once cargo is internalized, it is usually delivered to the early endosome and trafficked though lysosomal pathways.

The ECM is constantly remodeled, via balancing of synthesis, deposition, and degradation to control tissue homeostasis, and during this process ECM molecules themselves are internalized through receptor-mediated endocytic pathways. Degradation of the ECM occurs largely through two pathways; extracellular degradation mediated by matrix metalloproteases (MMPs) and lysosomal degradation after receptor-mediated internalization (99). The internalization of the most abundant component of ECM, collagen, is controlled by integrin-mediated phagocytic uptake and Endo-180 dependent clathrin mediated pathway. Fibrillar collagen type I binds to $\alpha 2\beta 1$ integrin receptor, promoting internalization of collagen to early endosomes (123). On

the other hand, soluble collagen type I, IV and V fragments bind Endo180 or uPARAP to internalize to endosome via the clathrin-dependent endocytic pathway (124).

Similar to collagens, fibronectin is degraded by lysosomal degradation after endocytosis. Endocytosis of both soluble and matrix fibronectin is mediated by α5β1 integrin receptor via caveolin-1 dependent uptake (125). Fibronectin binding to α2β1 integrin receptor, ultimately leading to endosomal sorting and transport to the lysosome (126). The internalization of the major component of basement membrane, laminin, is controlled by α3β1 integrin receptor and dystroglycan for protein turnover. Interestingly, the activation of the α3β1 integrin receptor by laminin binding results in phagocytosis of other ECM molecules as well (127). The internalization of laminin requires dystroglycan for receptor-mediated and dynamin-dependent pathways, leading to lysosomal degradation (128). Meanwhile, degradation of hyaluronic acid is controlled by multiple events. High molecular weight hyaluronic acid is degraded to smaller fragments by the extracellular hyaluronic acid-digesting enzyme, hyaluronidase 2 (Hyal 2) (129). These fragments can be endocytosed by either receptor-mediated endocytosis (104 Da) or micropinocytosis (106 Da), depending on the molecular weight of the fragment. Hyaluronic acid fragments binding to CD44 and lymphatic vessel endothelial-1 (LYVE-1) receptors promote the endocytosis of hyaluronic acid via the clathrin-mediated pathway. The wide range of different internalization mechanisms for ECM molecules can be exploited in DDS for the selective uptake of intracellularly active drugs.

1.3 ECM-targeted delivery of particle-based DDS

ECM molecules	Peptides	Cell receptor	Application	Reference
Collagen	GGYGGGP$(GPP)_5$G FOGER$(GPP)_5$GPC	$\alpha_2\beta_1$	Local protein delivery	Shekaran et al. 2014

	$(GPO)_4$GVKGDKGNPGWPGAP$(GPO)_4$	Chondroitin sulfate modified CD44	Anti-cancer drug delivery	Ndinguri et al. 2012
	VCLCL-DDRT (Recombinant protein)	DDRs	Block the activity of cancer cell	An and Brodsky 2016
ECM proteins	cRGD4C	$\alpha_v\beta_3$ and $\alpha_v\beta_5$	Anti-cancer drug delivery	Arap, Pasqualini, and Ruoslahti 1998
	cRGDfC	$\alpha_v\beta_3$ and $\alpha_v\beta_5$	Anti-cancer drug delivery	Bibby et al. 2005
	cACRGDMFGCA	$\alpha_v\beta_3$ and $\alpha_v\beta_5$	VEGFR2-SiRNA delivery	Schiffelers et al. 2004
Laminin	RKRLQVQLSIRT	Syndecan	Anti-cancer drug delivery	Negishi and Nomizu 2019
	DFKLFAVYIKYR-GGC (C16Y)	Integrin $\alpha_v\beta3$	Anti-cancer drug delivery	Hamano et al. 2012

Table 1.2. Extracellular matrix protein-derived peptides as ligands to bind to cell surface receptors in drug delivery system.

ECM molecules have been successfully formulated into particles for drug delivery applications. The chondroitin-sulfate modified CD44 receptor is able to bind to triple helical sequence from collagen Type IV (130); Fields and co-workers thus developed CD44-binding, collagen-mimetic peptides ((GPO)4GVKGDKGNPGWPGAP(GPO)4) and used them to modify liposomes as a DDS to cancer cells with highly expressed CD44 cell receptor (Table 1.2). They demonstrated that doxorubicin delivered via this DDS reduced the tumor size up to 60%, compared to untreated control in a CD44+ mouse melanoma model (131). Moreover, others have taken advantage of another collagen receptors, DDR2, which is highly

expressed in fast-growing invasive tumors (132). The Brodsky group reported a recombinant collagen protein (VCLCL-DDRT) that binds DDR2 and could thus serve as a potential tumor treatment (100). They showed the delay of megakaryocyte migration as a result of the competition between the recombinant VCLCL-DDRT and animal collagen for binding to DDR2. In addition, our group recently has developed conjugates of the collagen-like peptide ((GPO)4GFOGER(GPO)4GG, CLP) and elastin-like peptide ((VPGFG)6, ELP) to serve as thermoresponsive vesicles as a drug carrier (Figure 1.2(A)) (133). This CLP-decorated vesicle has both thermally responsive assembly behavior owing to the temperature-responsiveness of the CLP domain's triple helix formation, and a strong affinity to native collagen through collagen triple helix hybridization, and is therefore able to sequester, for at least 21 days, a hydrophobic model compound (fluorescein) in collagen type II films, with subsequent thermally triggered release. The vesicles also show high cytocompatibility with both fibroblasts and chondrocytes and essentially no activation of a macrophage cell line. The ELP-CLP conjugates have the potential to deliver intracellularly active drugs through receptor-mediated endocytosis using interactions between the GFOGER sequence on CLP and integrin receptors ($\alpha_1\beta_1$, $\alpha_2\beta_1$, $\alpha_{10}\beta_1$, and $\alpha_{11}\beta_1$) (73).

The use of fibronectin-based molecules has also been employed for successful targeting and increased intracellular uptake of local DDS. The Akaike group incorporated fibronectin in a calcium phosphate co-precipitated, non-viral gene delivery system (134); the fibronectin coating in calcium phosphate and pDNA precipitate allowed cell-surface

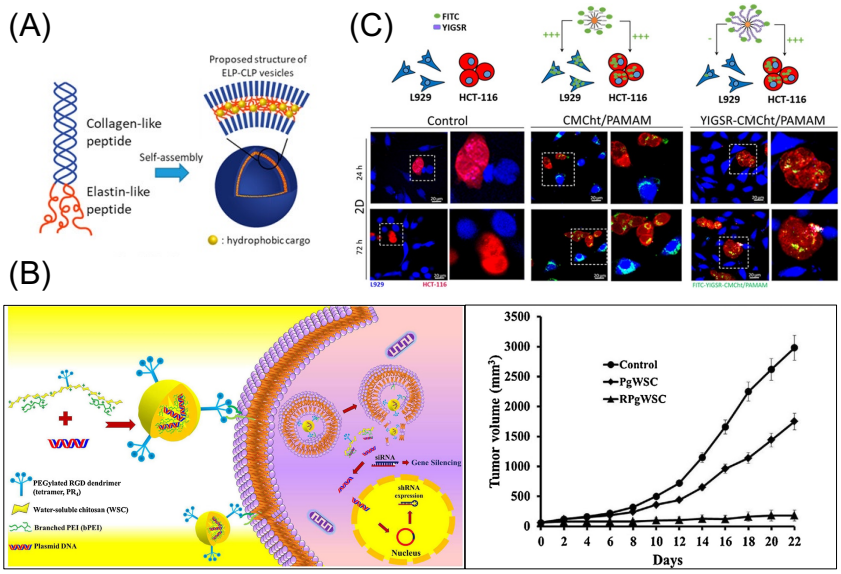

Figure 1.2. ECM-based targeted delivery of particle-based DDS. (A) Schematic of ELP-CLP conjugate-based thermoresponsive nanovesicles (133). Copyright 2017. Reproduced with permission from American chemical society. (B) RGD dendrimer peptide modified polyethyleneimine-grafted chitosan for siRNA delivery. In vivo tumor growth of treatment with non-RGD-modified system (PgWSC) and RGD-modified system (RpgWSC), and non-treatment (136). Copyright 2017. Reproduced with permission from Elsevier Inc. (C) Confocal images of internalization of dendrimer particles (CMCht/PAMAM and YIGSR-CMCht/PAMAM) on HCT-116 cancer cells (red) and L929 fibroblasts (blue) (138). Copyright Wiley-VCH Verlag GmbH. & Co. KGaA. Reproduced with permission.

integrin receptor binding for internalization into cells and supported 100-fold higher levels of gene expression than without the fibronectin coating. In the past, direct conjugation of the cyclic RGD peptide, RGD4C, on the anticancer agent, doxorubicin,

demonstrated better efficacy in suppressing tumor progression than doxorubicin alone, in mouse models bearing human breast carcinoma cells (135). The RGD peptide-modified DDS showed improved localization and intracellular uptake into cancer cells. The Jang group investigated the dendrimeric RGD peptides modified on co-polymer, which consists of polyethyleneimine and water soluble chitosan (RpgWSC), for an siRNA delivery system to target $\alpha_v\beta_3$ integrin-overexpressing tumor cells for cancer therapy (Figure 1.2(B)) (136). The delivery systems allow the cellular uptake of siRNA to PC3 cancer cells through microtubule-dependent micropinocytosis and clathrin-mediated endocytosis. The delivery of siRNA, via the use of their DDS with RGD (RpgWSC), for silencing the mRNA encoding the hBCL2 protein in a PC3 tumor xenograft mouse model, presented greater inhibition of tumor growth through the blocking of BCL2 protein expression, compared to a non-RGD modified delivery system (PgWSC) (Figure 1.2(B)). These results are a recent illustration of the power of employing RGD in DDS for improving delivery of intracellularly active cancer therapeutics into $\alpha_v\beta_3$ integrin overexpressing tumor cells.

The active sequence peptides from laminin are able to interact with cell surface receptors, integrins, syndecans, α-dystroglycan, and CD44, to perform various biological activities like those mediated by full-length laminin. The laminin-derived RKRLQVQLSIRT (AG73) peptide was modified with PEGylated liposomes to deliver plasmid DNA in human embryonic kidney carcinoma cells, which overexpress syndecan-2 (84, 137). On the other hand, cancer cells, including bile duct carcinoma, colorectal carcinoma, cervical cancer, and breast carcinoma, highly express the 67 KDa laminin receptor (67LR), for which the laminin-derived YIGSR sequence has high affinity. YIGSR-modified carboxylmethychitosan/poly(amidoamine)

(CMCht/PAMAM) dendrimer nanoparticles were developed to drive targeted internalization into colorectal cancer cells (HCT-116 CRC cells) (138) via this interaction. The YIGSR-modified CMCht/PAMAM nanoparticles were more selectively internalized by HCT-116 colorectal cancer cells than by L929 fibroblasts and non-YIGSR-modified CMCht/PAMAM nanoparticles were non-selectively internalized by both types of cells (Figure 1.2(C)). Laminin-based material modification are a promising strategy to improve the specificity of the delivery system on the laminin receptor expressed cells such as tumor.

Heparin is incorporated in DDS to target overexpressed angiogenic growth factors in tumor tissues (139). Tae groups demonstrated heparin-coated PLGA nanoparticle to accumulate in the tumor in SCC7 tumor-bearing athymic mice (140). In addition, dendronized heparin-doxorubicin conjugate-based nanoparticle developed by Gu group represented the improvement of antitumor efficacy and anti-angiogenic effects in a mouse 4T1 breast cancer tumor model, compared to free doxorubicin (141). On the other hand, many studies have investigated the DDS incorporating hyaluronic acid or chondroitin sulfate as a ligand to target CD44-overexpressing cancer cells. Gupta and co-workers formulated polyehtylenimine (PEI) conjugated chondroitin sulfate to form complexes with plasmid DNA (142). Their system, administrated by intravenous injection in Ehrlich ascites tumor (EAT)-bearing mice, accumulated in tumor mass to a significantly greater extent as compared to non-chondroitin sulfate-modified PEI/pDNA complex. The attachment of hyaluronic acid on liposomes loaded with doxorubicin resulted in the selective binding of the DDS on CD44-expressing murine melanoma cells, resulting in a substantial reduction in the IC50 (143). In addition, Zhang group developed ternary complex based on hyaluronic acid, dexamethasone conjugated

polyethyleneimine (PEI) and plasmid DNA to enhance CD44 receptor-mediated endocytosis (144). This ternary complex improved cellular uptake and nuclear transport of DNA in melanoma tumor cells, leading to the highest transfection efficiency and suppressed the growth of tumor in mice. Hyaluronic acid has also been utilized to target CD44 receptors overexpressed in macrophages as a strategy for the treatment of inflammatory disease. Pilehvar-Soltanahmadi and co-workers reported hyaluronic acid-conjugated polylactide nanoparticles encapsulated curcumin delivered to macrophage to achieve the modulation of macrophage polarity from the pro-inflammatory M1 phenotype to the anti-inflammatory M2 phenotype (145). The modification of ECM polysaccharides accomplishes the delivery of drugs at the target sites where their receptors are highly expressed.

1.4 ECM-based hydrogel matrices for drug delivery

Drug transport within a hydrogel can be controlled by manipulating its mesh size and/or its interaction with drugs using chemical strategies (146-150). Hydrogels comprise crosslinked polymer networks, and drugs smaller than the network mesh size can simply diffuse through the hydrogel, whereas drugs larger than the mesh size are entrapped in the hydrogel and released upon degradation of the network. The polymer backbone and crosslinks can be degraded by either slow hydrolysis of ester bonds or peptide bonds, by the scission of thiol-based crosslinks, or by bio-responsive mechanisms such as enzyme activity (151-153). The degradation of hydrogels in biomedical applications can be tuned based on the local cellular environment by incorporating crosslinks comprising peptides that are degradable by different types of matrix metalloproteinases (154). Moreover, drug release from the hydrogel can be modulated by incorporating non-covalent or covalent drug-matrix interactions (146,

155-157). Non-covalent interactions include electrostatic interactions such as heparin and heparin binding proteins (50, 51), or hydrophobic associations such as cyclodextrin and hydrophobic drugs (158). Otherwise, covalent interactions can be designed using non-cleavable and cleavable linkages between drugs and hydrogels that are incorporated via reactions such as click chemistries (e.g. copper-free click, thiol-ene, Diels-Alder reactions, and oxime and hydrazine ligation) and photochemistries (e.g. nitrobenzyl and coumarin photocleavage reactions); these reactions also are employed for hydrogel crosslinking (157, 159-164). Thus, the chemical tunability of hydrogels, particularly their mesh size, crosslinking chemistry, and drug interactions, enables fine-tuned control over drug transport through the hydrogel.

1.4.1 Simple Diffusion

ECM-based hydrogels for local drug delivery not only support cells biochemically and mechanically through cell-matrix interactions, but also release the drugs into infiltrated cells. Since the hydrogel is formed by the crosslinked polymer network, the mesh space between polymer chains allows the diffusion of liquid and small molecules (146). Depending on the mesh size of a hydrogel, small molecule drugs can diffuse through the hydrogel and be released from the hydrogel for delivery to the surrounding cells.

Due to its structural properties, collagen is often utilized as the matrix for local drug delivery. A type I collagen matrix on the surface of polyurethane films enhanced fibroblast attachment, proliferation, and growth (165). While collagen matrices provide a physiologically-inspired microenvironment to cells, collagen also can control the delivery of drugs such as small molecules, proteins, and genes via simple diffusion and/or biodegradation. Collagen matrices have been loaded with a variety of small molecules such as antibiotics for wound care, cisplatin for local cancer therapy, and anti-inflammatory reagents for tissue regeneration in ophthalmology (166-168). Small molecule gentamicin-eluting collagen matrix (Collatamp® (Schering-Plough, Stockholm, Sweden), Sulmycin®-Implant (Schering-Plough, USA), and Septocoll®(Biomet Merck, Germany)) have been used in the clinic as wound care

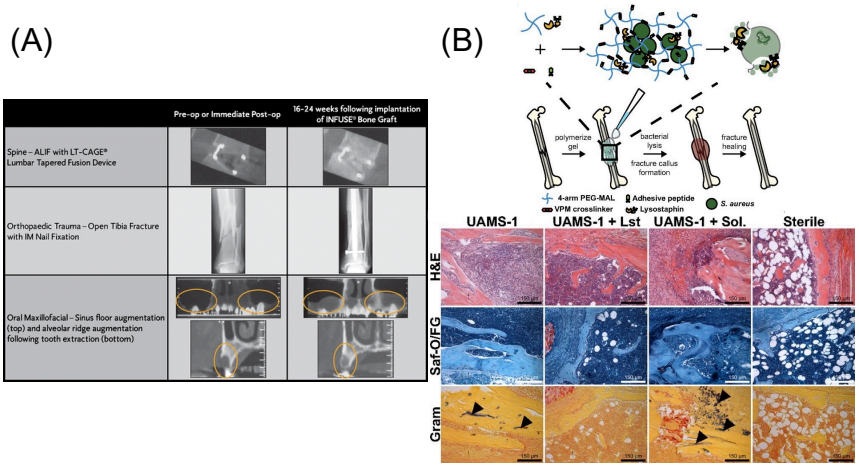

Figure 1.3. Simple diffusion of drugs from ECM based matrices. (A) Computed tomography (CT) images for the efficacy of INFUSE® Bone Graft in clinical applications (172). Copyright 2007. Reproduced with permission from Springer Nature. (B) The scheme of overall study design. Histologic analysis using H&E, Saf-O/FG, and Gram staining of femurs after treating with hydrogel (UAMS-1), Lysostaphin-delivering hydrogel (UAMS-1+Lst), and Lysostaphin, and sterilization (174). Copyright 2018. Reproduced with permission from the National Academy of Sciences.

products to promote both granulation tissue formation and epithelialization, and to protect tissues from potential infection(169-171).

In addition to small molecule delivery, proteins such as growth factors can be loaded into the collagen matrix; for example the delivery of bone morphogenetic protein (BMP) from a collagen matrix has been shown to promote bone formation. Recombinant human BMP-2 (rhBMP-2)-loaded collagen matrices (INFUSE® bone graft and MASTERGRAFT ®) are available in the clinic to treat bone fracture and spinal fusion (146). Clinical trials using INFUSE® in spinal orthopedic trauma, and oral maxillofacial applications have demonstrated the efficacy of INFUSE® to form de novo bone (Figure 1.3(A)) (172). The Garcia group created a collagen mimetic peptide (GFOGER)-modified PEG synthetic hydrogel to deliver BMP-2 to murine radial critical-sized defects (173). The GFOGER-modified hydrogel increased osteoprogenitor localization in the defect site and sustained release of BMP-2 to enhance bone formation and healing. In addition, the Garcia group investigated RGD and GFOGER-modified PEG synthetic hydrogels for the delivery of lysostaphin to treat staphylococcus aureus infections in bone fractures (Figure 1.3(B)) (174). Based on histological analysis, lysostaphin delivery using the RGD/GFOGER-based PEG hydrogel system (UAMS-1 + Lst) demonstrated the ability of the system to reduce bacterial infection compared to the non-treatment control (UAMS-1), and these materials were shown to promote fracture repair of femoral bone in mouse such that the resulting healed tissue was similar to sterile positive control groups. A lysostaphin solution without hydrogel (UAMS-1 + Sol.) failed both in reducing bacterial infection and in improving bone repair. ECM-based hydrogel matrices create a microenvironment

conductive to supporting growth of recruited cells while also controlling drug release to enhance tissue regeneration.

1.4.2 ECM-based matrix and drug/carrier interactions

Drug release from ECM-based matrix is also dependent upon drug-ECM interactions. Electrostatic and hydrophobic attractive forces between drug molecules and ECM molecules can reduce and/or prohibit drug diffusion through the network, leading to prolonged drug retention and alternate controlling parameters for release from the matrix. The electrostatic interactions between highly negative polysaccharides and drugs are employed in the sustained delivery/retention of many drugs. For example, Cool and colleagues validated the delivery efficacy of BMP-2 using thiol-modified hyaluronan (GlycosilTM), and these materials were compared to collagen sponges (e.g. as a mimic of INFUSE® bone grafts) in terms of their influence on ectopic bone formation (175). The electrostatic interaction between BMP-2 and negatively charged hyaluronic acid hydrogels resulted in a low burst followed by sustained release of BMP-2, whereas collagen hydrogels showed high burst and sustained release of BMP-2. The low burst and sustained release of BMP-2 from hyaluronic acid hydrogels improved the bone formation to the greatest extent in a rat intramuscular ectopic model.

Moreover, due to the ability of ECM molecules to interact with growth factors, ECM molecules are utilized in DDS for the sustained release of growth factors from hydrogel matrices. In particular, heparin-based hydrogels have been widely employed as growth factor carriers for tissue regeneration (50, 51, 176-178). Netti and co-workers developed porous PEG-heparin hydrogels encapsulating the angiogenic growth factor

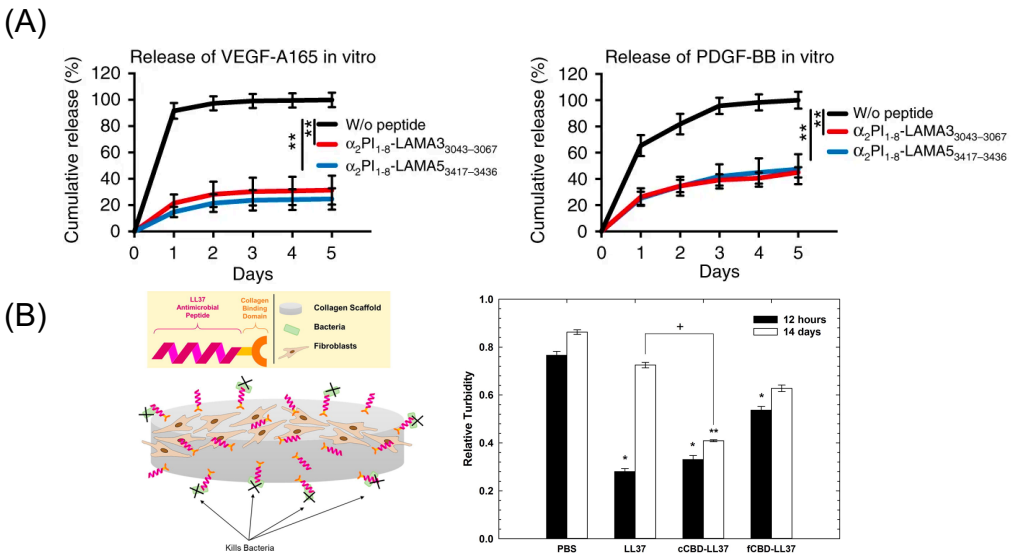

Figure 1.4. ECM-based matrices and drug interaction-based delivery systems. (A) Growth factor retention in fibrin matrices with laminin-mimetic peptides (α2PI1–8-LAMA33043–3067 or α2PI1–8-LAMA53417–3436) or without peptide. (182). Copyright 2018. Reproduced with permission from Springer Nature. (B) The scheme of study design. Antimicrobial activity of LL37 and with collagen-binding domains (cCBD-LL37 or fCBD-LL37) on collagen scaffold after 12 h and 14 days (183). Copyright 2017. Reproduced with permission from Elsevier Inc

VEGF. Because of the interaction between heparin and VEGF, VEGF was released in a controlled manner and the released VEGF promoted angiogenesis in vivo (179). Also, the Werner group investigated RGD-functionalized star PEG-heparin hydrogels with a variable degree of heparin sulfation for controlled release of angiogenic growth factors from the hydrogel and capture of inflammatory chemokines in the hydrogel for the chronic wound healing applications (180, 181). In addition, the Hubbell group developed laminin-mimetic peptides, which include heparin-binding domains, and employed them to decorate a fibrin matrix for the delivery of VEGF-A165 and platelet derived growth factor PDGF-BB in a chronic wound treatment application (182). Since

the heparin-binding domain in laminin-mimetic peptides has a strong affinity to syndecan cell surface receptors, as well as to VEGF-A165 and PDGF-BB, the system enhanced cell adhesion through interaction with syndecan, and also enabled the sustained release of growth factors from the matrix (Figure 1.4(A)). This resulted in promotion of wound healing in a type-2 diabetic mouse. With a similar approach, the Christman group applied decellularized ECM-derived hydrogels in heparin-binding growth factor delivery systems for tissue regeneration in the post-myocardial infarction (25). Porcine pericardia were decellularized using 1% SDS and digested with pepsin to prepare decellularized ECM-derived hydrogel with intact native sulfated glycosaminoglycans (PPM). Plasmid DNA encoding fibroblast growth factors (pFGF) in PPM injected into rats with post myocardial infarction was still retained in the tissue after 5 days of administration, and the amount of pFGF retained was greater than the amount of bFGF retained in collagen hydrogels or in saline (Figure 1.4(B)).

While controlled drug release via drug-ECM interactions is a powerful strategy to improve retention and sustained delivery, existing examples are mostly limited to the use of heparin-binding growth factors and charged molecules. To address this limitation, as described above, active peptide sequences from various ECM proteins have been identified and exploited in controlling the drug release from ECM-based matrices. Chemical modifications of the active sequences and their attachment to drugs or polymeric carriers enable immobilization in ECM-based hydrogel matrices for sustained drug release. Rolle and co-workers utilized a collagen-binding domain (cCBD derived from collagenase or fCBD derived from fibronectin) to tether synthetic human antimicrobial peptides, catelicidin LL37, on collagen scaffolds for treatment of wound infection (Figure 1.4(C)) (183). Even after 14 days, LL37 with collagen domains

(cCBD-LL37 and fCBD-LL37) was still retained on the collagen scaffold and showed similar levels of antimicrobial activity after 12 h. However, due to the burst release of LL37 from collagen scaffold, the antimicrobial activity of LL37-loaded collagen scaffolds was reduced at 14 days compared to 12 h. In another example, the Hubbell group developed strategies for the delivery and release of both immune checkpoint inhibitor antibodies (αCTLA4 + αPD-L1) and interleukin-2 (IL-2) using collagen-binding domains (CBDs) derived from the von Willebrand factor (vWF) A3 domain to immobilize drugs on collagen in the tumor stroma for cancer immunotherapy (184). Systemically-administered CBD-tumor drug conjugates mainly accumulated in the tumor sites in murine cancer models, whereas non-CBD modified drugs did not. Drug delivery and release from the tumor collagen matrix-DDS interaction improved safety by eliminating antibody hepatotoxicity and by ameliorating pulmonary edema by IL-2, and it also improved efficacy through reducing the size of tumor. Overall, these examples demonstrate that the immobilization of therapeutic agents on the matrix using peptides prolongs the effectiveness of the therapeutic agents via controlled release from the scaffold.

1.4.3 ECM-based matrix and carrier interaction for intracellular delivery

DDS that combine these two approaches, e.g. immobilizing a drug in an ECM-based hydrogel and exploiting ECM-mediated cell uptake, have demonstrated enhanced therapeutic efficacy. In particular, this hybrid strategy will have enormous benefit on the delivery of intracellular therapeutic agents such as nucleic acids, which require DDS to facilitate cellular internalization and prevent the degradation of nucleic acids in the extra- and intracellular environments before they transfer to the appropriate cellular compartment. BMP-delivery systems using ECM-based hydrogels (INFUSE,

MASTERGRAFT, OP-1) are clinically available. However, gene delivery systems often fail to meet their clinical potential due to their relative low transfection efficiency and off-target expression (146, 185). The ideal gene delivery system in tissue regeneration applications should be able to sustain the delivery of active genes throughout the tissue formation process. Thus, immobilization of gene carriers in ECM-based hydrogels has the potential to achieve sustained delivery in response to cell-secreted proteases that are present during tissue repair and regeneration process, and the subsequent targeted cell uptake mediated by cell-receptor/ECM interactions.

Polymer and DNA complexes (polyplexes) have been encapsulated into scaffolds through non-specific and specific interactions between the complex and scaffold, leading to sustained DNA release from the matrix (186, 187). Collagen-based matrix has been widely utilized to incorporate DNA complexes via non-specific interactions with the matrix to promote skin tissue repair and bone regeneration applications (188, 189). For example, Gao and co-workers demonstrated the incorporation of cationic trimethylchitosan chloride (TMC) and DNA encoding VEGF-165 complex into the collagen-chitosan/silicone membrane bilayer dermal scaffold (TMC/pDNA-VEGF complexes loaded scaffold) to enhance angiogenesis for wound repair applications (190). Immunohistological analysis, RT-qPCR, and Western blotting analysis showed that the TMC/pDNA-VEGF complex-loaded scaffold was able to promote wound healing in incisional porcine wounds via VEGF-driven angiogenesis. The Salem group explored the delivery of polyethylenimine (PEI) and DNA encoding PDGF-B complex (Polyplex-PDGF-B) using collagen scaffolds for bone regeneration (188). In vivo studies using a calvarial defect rat model revealed

that after 4 weeks of sample implantation, polyplex-PDGF-B in collagen promoted significantly higher new bone formation as compared to collagen-only scaffold, suggesting the effective approach and potential clinical translation for bone regeneration.

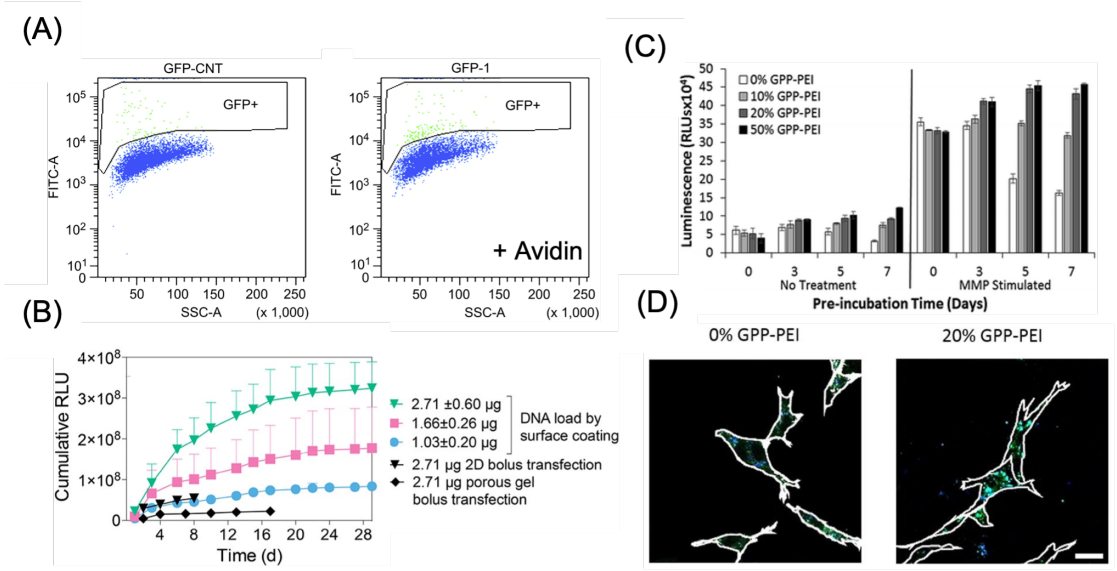

Figure 1.5. Polyplex immobilized in an ECM-based matrix for gene delivery. (A) Flow-activated cell sorting (FACS) analysis of biotin-functionalized pGFP polyplex immobilized in avidin-modified collagen hydrogel through avidin-biotin interaction (right graph) and avidin-free collagen hydrogel (left) (Orsi et al. 2010). Copyright 2010. Reproduced with permission from Elsevier Inc. (B) pGluc expression for 30 days of cell culture in the presence of immobilized pGluc polyplex on the surface of hyaluronic acid hydrogel through electrostatic interaction, and bolus transfection controls (Truong and Segura 2018). Copyright 2018. Reproduced with permission from the American Chemical Society. (C) pGluc expression of immobilized GPP-PEI in the collagen hydrogel and free GPP polyplex in hydrogel after a week of pre-incubation in media with and without the presence of metalloproteinase (Urello, Kiick, and Sullivan 2014). Copyright 2014. Reproduced with permission from The Royal Society of Chemistry. (D) Colocalization study of FITC labeled collagen (Green) with Alexa Fluor 350 labeled GPP-PEI (Blue) in NIH3T3 cells after 5 days of pre-incubation in the media (Urello, Kiick, and Sullivan 2017). The scale bar is 25 µm. Copyright 2017. Reproduced with permission from Elsevier Inc.

Polyplexes also have been incorporated into the matrix via specific interactions between polyplex and matrix. Netti et al. developed gene-activated matrices through immobilization of biotin-polyethylenimine (PEI) and DNA complexes (polyplexes) in avidin-functionalized collagen matrix (191). The immobilized polyplexes provided higher bioavailability to NIH3T3 cells recruited into the collagen matrix. The use of avidin-biotin interactions increased the transfection efficiency by approximately two-fold as compared polyplexes in collagen matrix lacking avidin-biotin linkages (Figure 1.5(A)). Moreover, Segura and co-workers recently investigated electrostatically-immobilized PEI/DNA complexes (polyplexes) in porous hyaluronic acid hydrogels (192). The hydrogel formulation approach reduced the cytotoxicity of the polyplexes in murine mesenchymal stem cells as compared to 2D bolus transfections with multiple doses. These observations suggested that the immobilized polyplex on the hydrogel enhanced and sustained the transgene expression over 30 days of cell culture, compared to a non-coated bolus transfection (Figure 1.5(B)). In addition to these two strategies for noncovalent immobilization of poyplex to ECM hydrogels, our group has developed approaches to immobilize polyplexes in collagen hydrogels through interactions with collagen-mimetic peptides (e.g. GPP: (GPP)3GPRGEKGERGPR(GPP)3GPCCG) that have affinity for native collagen through strand invasion and triple-helical binding (193-195). With higher amounts of GPP incorporated in the polyplex, the polyplex was retained in the hydrogel longer, with retention up to 35 days (193). In addition, GPP-modified PEI polyplexes, after a week of pre-incubation within collagen hydrogels in media, still showed greater gene expression by murine fibroblasts compared to GPP-free polyplexes. In particular, gene transfer in MMP-stimulated cells was highly robust, suggesting potential treatment options for chronic inflammatory diseases such as

chronic wounds (Figure 1.5(C)). A collagen-polyplex colocalization study revealed that the GPP-PEI, along with collagen fragments, were internalized in cells largely via caveolar endocytosis, suggesting integrin interaction with the integrin-binding sites of collagen fragments are involved in cellular internalization (Figure 1.5(D)) (195). GPP-PEI and collagen hydrogel interactions allowed both the controlled release and ligand-mediated efficient endocytosis into cells.

1.5 Summary and future prospects

For the past several decades, significant progress has been made in the development of targeted DDS using both local administration and ligand-based active targeting strategies. Hydrogel-based local delivery and ligand-cell interaction-mediated delivery enable drugs such as biomacromolecules (e.g., growth factors or genes) and small molecules to better localize at the target sites. Owing to the biological versatility of ECM molecules, ECM-based DDS have been applied not only to provide structural and biochemical signals to cells, but also to serve as ligands for cell receptors in specific pathological conditions to improve therapeutic efficacy of growth factor, gene, and small molecule treatments. However, despite progressive improvements, many challenges and unmet clinical needs still remain, particularly for intracellularly active drugs such as genes, which require control over cellular uptake mechanisms for optimized delivery and activity.

The innovative combination of these two targeting approaches using immobilizing drug carriers in ECM-based hydrogels has generated promising cell-responsive gene-activated matrices for regenerative medicine and functional tissue repair. ECM scaffolds not only function as substrates for cell infiltration, organization, and differentiation, but also enable resident cells to efficiently uptake genes on demand

to supply essential tissue inductive factors. However, many challenges remain in further developing this type of DDS to, for example, enable the delivery of multiple drugs from a single system, or provide mechanisms for on-demand drug release with a high level of control to a specific cell type. The sequential signaling of multiple growth factors typically regulates tissue repair and regeneration. Although researchers have demonstrated the release of multiple drugs, obtaining release of a specific molecule with optimal timing remains a challenge. Further, despite the advances in targeting, materials that localize only at or in their target cells are still difficult to design due to the lack of cell-specific gene expression relevant to a given disease physiology. Use of multiple ECM-inspired peptides in conjunction may offer a promising strategy to increase affinity to a particular cell type, using information about the cell's natural ECM receptor expression patterns, or to promote the sequential delivery of a series of drugs in a desired profile. In the future, ECM molecule-based DDS are likely to have an increasingly significant impact on disease treatment and tissue regeneration.

1.6 Overview of dissertation

The overall aim of this dissertation is to improve the efficacy of topically administered therapeutics through the control over the therapeutics delivery using the ability of CMP modified therapeutic carrier tethering on collagen-containing matrices via CMP strand invasion to the native collagen. Owing to the advantage of CMP-collagen tethers, I hypothesize that CMP/CLP modified carrier and collagen tether approach would demonstrate the extended the duration of therapeutic effects and control over the delivery of the cargo in response to cell-mediated collagen degradation. Chapter 3 and 4 will discuss the control over the growth factor gene transfer kinetics while regulating cell phenotypes both in vitro and in vivo for the enhanced wound repair

through the manipulating the numbers of CMP-collagen tethers and ECM compositions in gene-activating hyaluronic acid-collagen matrix (GAHCM) comprising CMP modified DNA/polyethylenimine (PEI) polyplexes and hyaluronic acid (HA)-collagen (HCM). Chapter 5 will include the utilizing the different degree of retention and release profiles of elastin-like peptide and collagen-like peptide (ELP-CLP) nanovesicles with collagen containing matrices to control antibiotic delivery and support the extended antibacterial effects. Lastly, Chapter 6 will discuss the potential future studies to develop from this dissertation.

REFERENCES

1. Prasad V. The withdrawal of drugs for commercial reasons: the incomplete story of tositumomab. JAMA Intern Med. 2014;174(12):1887-8. Epub 2014/11/11. doi: 10.1001/jamainternmed.2014.5756. PubMed PMID: 25383420.

2. Qureshi ZP, Seoane-Vazquez E, Rodriguez-Monguio R, Stevenson KB, Szeinbach SL. Market withdrawal of new molecular entities approved in the United States from 1980 to 2009. Pharmacoepidemiol Drug Saf. 2011;20(7):772-7. Epub 2011/05/17. doi: 10.1002/pds.2155. PubMed PMID: 21574210.

3. Hwang TJ, Carpenter D, Lauffenburger JC, Wang B, Franklin JM, Kesselheim AS. Failure of Investigational Drugs in Late-Stage Clinical Development and Publication of Trial Results. JAMA Intern Med. 2016;176(12):1826-33. Epub 2016/10/11. doi: 10.1001/jamainternmed.2016.6008. PubMed PMID: 27723879.

4. Tibbitt MW, Dahlman JE, Langer R. Emerging Frontiers in Drug Delivery. J Am Chem Soc. 2016;138(3):704-17. Epub 2016/01/08. doi: 10.1021/jacs.5b09974. PubMed PMID: 26741786.

5. Blanco E, Shen H, Ferrari M. Principles of nanoparticle design for overcoming biological barriers to drug delivery. Nat Biotechnol. 2015;33(9):941-51. Epub 2015/09/09. doi: 10.1038/nbt.3330. PubMed PMID: 26348965; PMCID: PMC4978509.

6. Langer R. Drug delivery and targeting. Nature. 1998;392(6679 Suppl):5-10. Epub 1998/05/14. PubMed PMID: 9579855.

7. Liu D, Yang F, Xiong F, Gu N. The Smart Drug Delivery System and Its Clinical Potential. Theranostics. 2016;6(9):1306-23. Epub 2016/07/05. doi: 10.7150/thno.14858. PubMed PMID: 27375781; PMCID: PMC4924501.

8. Hu Q, Sun W, Wang C, Gu Z. Recent advances of cocktail chemotherapy by combination drug delivery systems. Adv Drug Deliv Rev. 2016;98:19-34. Epub 2015/11/08. doi: 10.1016/j.addr.2015.10.022. PubMed PMID: 26546751; PMCID: PMC4998845.

9. Kanamala M, Wilson WR, Yang M, Palmer BD, Wu Z. Mechanisms and biomaterials in pH-responsive tumour targeted drug delivery: A review. Biomaterials. 2016;85:152-67. Epub 2016/02/13. doi: 10.1016/j.biomaterials.2016.01.061. PubMed PMID: 26871891.

10. Allen TM, Cullis PR. Drug delivery systems: entering the mainstream. Science. 2004;303(5665):1818-22. Epub 2004/03/20. doi: 10.1126/science.1095833. PubMed PMID: 15031496.

11. Zhong H, Chan G, Hu Y, Hu H, Ouyang D. A Comprehensive Map of FDA-Approved Pharmaceutical Products. Pharmaceutics. 2018;10(4). Epub 2018/12/20. doi: 10.3390/pharmaceutics10040263. PubMed PMID: 30563197; PMCID: PMC6321070.

12. Torchilin VP. Multifunctional, stimuli-sensitive nanoparticulate systems for drug delivery. Nat Rev Drug Discov. 2014;13(11):813-27. Epub 2014/10/08. doi: 10.1038/nrd4333. PubMed PMID: 25287120; PMCID: PMC4489143.

13. Panyam J, Labhasetwar V. Biodegradable nanoparticles for drug and gene delivery to cells and tissue. Adv Drug Deliv Rev. 2003;55(3):329-47. Epub 2003/03/12. PubMed PMID: 12628320.

14. Sheikhpour M, Barani L, Kasaeian A. Biomimetics in drug delivery systems: A critical review. J Control Release. 2017;253:97-109. Epub 2017/03/23. doi: 10.1016/j.jconrel.2017.03.026. PubMed PMID: 28322976.

15. Raave R, van Kuppevelt TH, Daamen WF. Chemotherapeutic drug delivery by tumoral extracellular matrix targeting. J Control Release. 2018;274:1-8. Epub 2018/02/01. doi: 10.1016/j.jconrel.2018.01.029. PubMed PMID: 29382546.

16. Cervadoro A, Palomba R, Vergaro G, Cecchi R, Menichetti L, Decuzzi P, Emdin M, Luin S. Targeting Inflammation With Nanosized Drug Delivery Platforms in Cardiovascular Diseases: Immune Cell Modulation in Atherosclerosis. Front Bioeng Biotechnol. 2018;6:177. Epub 2018/12/14. doi: 10.3389/fbioe.2018.00177. PubMed PMID: 30542650; PMCID: PMC6277804.

17. Kohane. TRHDS. Hydrogels in drug delivery: Progress and challenges. polymer. 2008;49:1993-2007.

18. Kharkar PM, Kiick KL, Kloxin AM. Designing degradable hydrogels for orthogonal control of cell microenvironments. Chem Soc Rev. 2013;42(17):7335-72. Epub 2013/04/24. doi: 10.1039/c3cs60040h. PubMed PMID: 23609001; PMCID: PMC3762890.

19. Cai L, Heilshorn SC. Designing ECM-mimetic materials using protein engineering. Acta Biomater. 2014;10(4):1751-60. Epub 2013/12/25. doi: 10.1016/j.actbio.2013.12.028. PubMed PMID: 24365704; PMCID: PMC3973542.

20. Caliari SR, Burdick JA. A practical guide to hydrogels for cell culture. Nat Methods. 2016;13(5):405-14. Epub 2016/04/29. doi: 10.1038/nmeth.3839. PubMed PMID: 27123816; PMCID: PMC5800304.

21. Ooi HW, Hafeez S, van Blitterswijk CA, Moroni L, Baker MB. Hydrogels that listen to cells: a review of cell-responsive strategies in biomaterial design for tissue regeneration. Materials Horizons. 2017;4:1020-40. doi: 10.1039/c7mh00373k.

22. Zhang YS, Khademhosseini A. Advances in engineering hydrogels. Science. 2017;356(6337). Epub 2017/05/06. doi: 10.1126/science.aaf3627. PubMed PMID: 28473537; PMCID: PMC5841082.

23. Crapo PM, Gilbert TW, Badylak SF. An overview of tissue and whole organ decellularization processes. Biomaterials. 2011;32(12):3233-43. Epub 2011/02/08. doi: 10.1016/j.biomaterials.2011.01.057. PubMed PMID: 21296410; PMCID: PMC3084613.

24. Saldin LT, Cramer MC, Velankar SS, White LJ, Badylak SF. Extracellular matrix hydrogels from decellularized tissues: Structure and function. Acta Biomater. 2017;49:1-15. Epub 2016/12/05. doi: 10.1016/j.actbio.2016.11.068. PubMed PMID: 27915024; PMCID: PMC5253110.

25. Seif-Naraghi SB, Horn D, Schup-Magoffin PJ, Christman KL. Injectable extracellular matrix derived hydrogel provides a platform for enhanced retention and delivery of a heparin-binding growth factor. Acta Biomater. 2012;8(10):3695-703. Epub 2012/07/04. doi: 10.1016/j.actbio.2012.06.030. PubMed PMID: 22750737; PMCID: PMC3429632.

26. Hernandez JM, Gaetani R, Pieters MV, Ng WN, Chang EA, Martin TR, van Ingen E, Mol AE, Dzeciatkowsk M, Hansen CK, Sluijter GP, Christman KL. Decellularized Extracellular Matrix Hydrogels as a Delivery Platform for MicroRNA and Extracellular Vesicle Therapeutics. Advanced Therapeutics. 2018;1(3).

27. Danhier F, Feron O, Preat V. To exploit the tumor microenvironment: Passive and active tumor targeting of nanocarriers for anti-cancer drug delivery. J Control Release. 2010;148(2):135-46. Epub 2010/08/28. doi: 10.1016/j.jconrel.2010.08.027. PubMed PMID: 20797419.

28. Murphy EA, Majeti BK, Barnes LA, Makale M, Weis SM, Lutu-Fuga K, Wrasidlo W, Cheresh DA. Nanoparticle-mediated drug delivery to tumor vasculature suppresses metastasis. Proc Natl Acad Sci U S A. 2008;105(27):9343-8. Epub 2008/07/09. doi: 10.1073/pnas.0803728105. PubMed PMID: 18607000; PMCID: PMC2453735.

29. Fu S, Xu X, Ma Y, Zhang S, Zhang S. RGD peptide-based non-viral gene delivery vectors targeting integrin alphavbeta3 for cancer therapy. J Drug Target. 2019;27(1):1-11. Epub 2018/03/23. doi: 10.1080/1061186X.2018.1455841. PubMed PMID: 29564914.

30. Danhier F, Le Breton A, Preat V. RGD-based strategies to target alpha(v) beta(3) integrin in cancer therapy and diagnosis. Mol Pharm. 2012;9(11):2961-73. Epub 2012/09/13. doi: 10.1021/mp3002733. PubMed PMID: 22967287.

31. Huang G, Huang H. Hyaluronic acid-based biopharmaceutical delivery and tumor-targeted drug delivery system. J Control Release. 2018;278:122-6. Epub 2018/04/13. doi: 10.1016/j.jconrel.2018.04.015. PubMed PMID: 29649528.

32. Nikam RR, Gore KR. Journey of siRNA: Clinical Developments and Targeted Delivery. Nucleic Acid Ther. 2018;28(4):209-24. Epub 2018/03/28. doi: 10.1089/nat.2017.0715. PubMed PMID: 29584585.

33. Garber K. Alnylam launches era of RNAi drugs. Nat Biotechnol. 2018;36(9):777-8. Epub 2018/09/07. doi: 10.1038/nbt0918-777. PubMed PMID: 30188543.

34. Roggenbuck D, Mytilinaiou MG, Lapin SV, Reinhold D, Conrad K. Asialoglycoprotein receptor (ASGPR): a peculiar target of liver-specific autoimmunity.

Auto Immun Highlights. 2012;3(3):119-25. Epub 2012/12/01. doi: 10.1007/s13317-012-0041-4. PubMed PMID: 26000135; PMCID: PMC4389076.

35. Morrison C. Alnylam prepares to land first RNAi drug approval. Nat Rev Drug Discov. 2018;17(3):156-7. Epub 2018/03/01. doi: 10.1038/nrd.2018.20. PubMed PMID: 29487392.

36. Goodman SL, Picard M. Integrins as therapeutic targets. Trends Pharmacol Sci. 2012;33(7):405-12. Epub 2012/05/29. doi: 10.1016/j.tips.2012.04.002. PubMed PMID: 22633092.

37. Raab-Westphal S, Marshall JF, Goodman SL. Integrins as Therapeutic Targets: Successes and Cancers. Cancers (Basel). 2017;9(9). Epub 2017/08/24. doi: 10.3390/cancers9090110. PubMed PMID: 28832494; PMCID: PMC5615325.

38. Leitinger B, Hohenester E. Mammalian collagen receptors. Matrix Biol. 2007;26(3):146-55. Epub 2006/12/05. doi: 10.1016/j.matbio.2006.10.007. PubMed PMID: 17141492.

39. Pankov R, Yamada KM. Fibronectin at a glance. J Cell Sci. 2002;115(Pt 20):3861-3. Epub 2002/09/24. doi: 10.1242/jcs.00059. PubMed PMID: 12244123.

40. Zollinger AJ, Smith ML. Fibronectin, the extracellular glue. Matrix Biol. 2017;60-61:27-37. Epub 2016/08/09. doi: 10.1016/j.matbio.2016.07.011. PubMed PMID: 27496349.

41. Colognato H, Yurchenco PD. Form and function: the laminin family of heterotrimers. Dev Dyn. 2000;218(2):213-34. Epub 2000/06/08. doi: 10.1002/(SICI)1097-0177(200006)218:2<213::AID-DVDY1>3.0.CO;2-R. PubMed PMID: 10842354.

42. Yao Y. Laminin: loss-of-function studies. Cell Mol Life Sci. 2017;74(6):1095-115. Epub 2016/10/04. doi: 10.1007/s00018-016-2381-0. PubMed PMID: 27696112.

43. Ramshaw JA, Peng YY, Glattauer V, Werkmeister JA. Collagens as biomaterials. J Mater Sci Mater Med. 2009;20 Suppl 1:S3-8. Epub 2008/04/02. doi: 10.1007/s10856-008-3415-4. PubMed PMID: 18379858.

44. Hinderer S, Layland SL, Schenke-Layland K. ECM and ECM-like materials - Biomaterials for applications in regenerative medicine and cancer therapy. Adv Drug Deliv Rev. 2016;97:260-9. Epub 2015/12/15. doi: 10.1016/j.addr.2015.11.019. PubMed PMID: 26658243.

45. Benton G, Arnaoutova I, George J, Kleinman HK, Koblinski J. Matrigel: from discovery and ECM mimicry to assays and models for cancer research. Adv Drug Deliv Rev. 2014;79-80:3-18. Epub 2014/07/06. doi: 10.1016/j.addr.2014.06.005. PubMed PMID: 24997339.

46. Meneghetti MC, Hughes AJ, Rudd TR, Nader HB, Powell AK, Yates EA, Lima MA. Heparan sulfate and heparin interactions with proteins. J R Soc Interface. 2015;12(110):0589. Epub 2015/08/21. doi: 10.1098/rsif.2015.0589. PubMed PMID: 26289657; PMCID: PMC4614469.

47. Christianson HC, Belting M. Heparan sulfate proteoglycan as a cell-surface endocytosis receptor. Matrix Biol. 2014;35:51-5. Epub 2013/10/23. doi: 10.1016/j.matbio.2013.10.004. PubMed PMID: 24145152.

48. Belting M. Heparan sulfate proteoglycan as a plasma membrane carrier. Trends Biochem Sci. 2003;28(3):145-51. Epub 2003/03/14. doi: 10.1016/S0968-0004(03)00031-8. PubMed PMID: 12633994.

49. Gospodarowicz D, Cheng J. Heparin protects basic and acidic FGF from inactivation. J Cell Physiol. 1986;128(3):475-84. Epub 1986/09/01. doi: 10.1002/jcp.1041280317. PubMed PMID: 3528177.

50. Liang Y, Kiick KL. Heparin-functionalized polymeric biomaterials in tissue engineering and drug delivery applications. Acta Biomater. 2014;10(4):1588-600. Epub 2013/08/06. doi: 10.1016/j.actbio.2013.07.031. PubMed PMID: 23911941; PMCID: PMC3937301.

51. Freudenberg U, Liang Y, Kiick KL, Werner C. Glycosaminoglycan-Based Biohybrid Hydrogels: A Sweet and Smart Choice for Multifunctional Biomaterials. Adv Mater. 2016;28(40):8861-91. Epub 2016/10/21. doi: 10.1002/adma.201601908. PubMed PMID: 27461855; PMCID: PMC5152626.

52. Zieris A, Prokoph S, Levental KR, Welzel PB, Grimmer M, Freudenberg U, Werner C. FGF-2 and VEGF functionalization of starPEG-heparin hydrogels to modulate biomolecular and physical cues of angiogenesis. Biomaterials. 2010;31(31):7985-94. Epub 2010/08/03. doi: 10.1016/j.biomaterials.2010.07.021. PubMed PMID: 20674970.

53. Zieris A, Chwalek K, Prokoph S, Levental KR, Welzel PB, Freudenberg U, Werner C. Dual independent delivery of pro-angiogenic growth factors from starPEG-heparin hydrogels. J Control Release. 2011;156(1):28-36. Epub 2011/07/19. doi: 10.1016/j.jconrel.2011.06.042. PubMed PMID: 21763368.

54. Prokoph S, Chavakis E, Levental KR, Zieris A, Freudenberg U, Dimmeler S, Werner C. Sustained delivery of SDF-1alpha from heparin-based hydrogels to attract circulating pro-angiogenic cells. Biomaterials. 2012;33(19):4792-

800. Epub 2012/04/10. doi: 10.1016/j.biomaterials.2012.03.039. PubMed PMID: 22483246.

55. Tsurkan MV, Hauser PV, Zieris A, Carvalhosa R, Bussolati B, Freudenberg U, Camussi G, Werner C. Growth factor delivery from hydrogel particle aggregates to promote tubular regeneration after acute kidney injury. J Control Release. 2013;167(3):248-55. Epub 2013/02/12. doi: 10.1016/j.jconrel.2013.01.030. PubMed PMID: 23395667.

56. Zhao L, Liu M, Wang J, Zhai G. Chondroitin sulfate-based nanocarriers for drug/gene delivery. Carbohydr Polym. 2015;133:391-9. Epub 2015/09/08. doi: 10.1016/j.carbpol.2015.07.063. PubMed PMID: 26344295.

57. Jiang D, Liang J, Noble PW. Hyaluronan as an immune regulator in human diseases. Physiol Rev. 2011;91(1):221-64. Epub 2011/01/21. doi: 10.1152/physrev.00052.2009. PubMed PMID: 21248167; PMCID: PMC3051404.

58. Highley CB, Prestwich GD, Burdick JA. Recent advances in hyaluronic acid hydrogels for biomedical applications. Curr Opin Biotechnol. 2016;40:35-40. Epub 2016/03/02. doi: 10.1016/j.copbio.2016.02.008. PubMed PMID: 26930175.

59. Tripodo G, Trapani A, Torre ML, Giammona G, Trapani G, Mandracchia D. Hyaluronic acid and its derivatives in drug delivery and imaging: Recent advances and challenges. Eur J Pharm Biopharm. 2015;97(Pt B):400-16. Epub 2015/11/29. doi: 10.1016/j.ejpb.2015.03.032. PubMed PMID: 26614559.

60. Jiao Y, Pang X, Zhai G. Advances in Hyaluronic Acid-Based Drug Delivery Systems. Curr Drug Targets. 2016;17(6):720-30. Epub 2015/06/02. doi: 10.2174/1389450116666150531155200. PubMed PMID: 26028046.

61. Oh EJ, Park K, Kim KS, Kim J, Yang JA, Kong JH, Lee MY, Hoffman AS, Hahn SK. Target specific and long-acting delivery of protein, peptide, and nucleotide therapeutics using hyaluronic acid derivatives. J Control Release. 2010;141(1):2-12. Epub 2009/09/18. doi: 10.1016/j.jconrel.2009.09.010. PubMed PMID: 19758573.

62. Dosio F, Arpicco S, Stella B, Fattal E. Hyaluronic acid for anticancer drug and nucleic acid delivery. Adv Drug Deliv Rev. 2016;97:204-36. Epub 2015/11/26. doi: 10.1016/j.addr.2015.11.011. PubMed PMID: 26592477.

63. Miyazaki M, Yuba E, Hayashi H, Harada A, Kono K. Hyaluronic Acid-Based pH-Sensitive Polymer-Modified Liposomes for Cell-Specific Intracellular Drug Delivery Systems. Bioconjug Chem. 2018;29(1):44-55. Epub 2017/12/01. doi: 10.1021/acs.bioconjchem.7b00551. PubMed PMID: 29183110.

64. Lallana E, Rios de la Rosa JM, Tirella A, Pelliccia M, Gennari A, Stratford IJ, Puri S, Ashford M, Tirelli N. Chitosan/Hyaluronic Acid Nanoparticles: Rational Design Revisited for RNA Delivery. Mol Pharm. 2017;14(7):2422-36. Epub 2017/06/10. doi: 10.1021/acs.molpharmaceut.7b00320. PubMed PMID: 28597662.

65. Giancotti FG. A structural view of integrin activation and signaling. Dev Cell. 2003;4(2):149-51. Epub 2003/02/15. PubMed PMID: 12586058.

66. Giancotti FG, Ruoslahti E. Integrin signaling. Science. 1999;285(5430):1028-32. Epub 1999/08/14. doi: 10.1126/science.285.5430.1028. PubMed PMID: 10446041.

67. Harburger DS, Calderwood DA. Integrin signalling at a glance. J Cell Sci. 2009;122(Pt 2):159-63. Epub 2009/01/02. doi: 10.1242/jcs.018093. PubMed PMID: 19118207; PMCID: PMC2714413.

68. Rosso F, Giordano A, Barbarisi M, Barbarisi A. From cell-ECM interactions to tissue engineering. J Cell Physiol. 2004;199(2):174-80. Epub 2004/03/25. doi: 10.1002/jcp.10471. PubMed PMID: 15039999.

69. Alam N, Goel HL, Zarif MJ, Butterfield JE, Perkins HM, Sansoucy BG, Sawyer TK, Languino LR. The integrin-growth factor receptor duet. J Cell Physiol. 2007;213(3):649-53. Epub 2007/09/22. doi: 10.1002/jcp.21278. PubMed PMID: 17886260.

70. Ruoslahti E, Pierschbacher MD. Arg-Gly-Asp: a versatile cell recognition signal. Cell. 1986;44(4):517-8. Epub 1986/02/28. doi: 10.1016/0092-8674(86)90259-x. PubMed PMID: 2418980.

71. Kim SH, Turnbull J, Guimond S. Extracellular matrix and cell signalling: the dynamic cooperation of integrin, proteoglycan and growth factor receptor. J Endocrinol. 2011;209(2):139-51. Epub 2011/02/11. doi: 10.1530/JOE-10-0377. PubMed PMID: 21307119.

72. Dunehoo AL, Anderson M, Majumdar S, Kobayashi N, Berkland C, Siahaan TJ. Cell adhesion molecules for targeted drug delivery. J Pharm Sci. 2006;95(9):1856-72. Epub 2006/07/20. doi: 10.1002/jps.20676. PubMed PMID: 16850395.

73. Zeltz C, Orgel J, Gullberg D. Molecular composition and function of integrin-based collagen glues-introducing COLINBRIs. Biochim Biophys Acta. 2014;1840(8):2533-48. Epub 2013/12/24. doi: 10.1016/j.bbagen.2013.12.022. PubMed PMID: 24361615.

74. Wojtowicz AM, Shekaran A, Oest ME, Dupont KM, Templeman KL, Hutmacher DW, Guldberg RE, Garcia AJ. Coating of biomaterial scaffolds with the

collagen-mimetic peptide GFOGER for bone defect repair. Biomaterials. 2010;31(9):2574-82. Epub 2010/01/09. doi: 10.1016/j.biomaterials.2009.12.008. PubMed PMID: 20056517; PMCID: PMC2813962.

75. Mould AP, Komoriya A, Yamada KM, Humphries MJ. The CS5 peptide is a second site in the IIICS region of fibronectin recognized by the integrin alpha 4 beta 1. Inhibition of alpha 4 beta 1 function by RGD peptide homologues. J Biol Chem. 1991;266(6):3579-85. Epub 1991/02/25. PubMed PMID: 1750929.

76. Massia SP, Hubbell JA. Vascular endothelial cell adhesion and spreading promoted by the peptide REDV of the IIICS region of plasma fibronectin is mediated by integrin alpha 4 beta 1. J Biol Chem. 1992;267(20):14019-26. Epub 1992/07/15. PubMed PMID: 1629200.

77. Zhou F, Jia X, Yang Q, Yang Y, Zhao Y, Fan Y, Yuan X. Targeted delivery of microRNA-126 to vascular endothelial cells via REDV peptide modified PEG-trimethyl chitosan. Biomater Sci. 2016;4(5):849-56. Epub 2016/04/09. doi: 10.1039/c5bm00629e. PubMed PMID: 27055482.

78. Wang H, Feng Y, Yang J, Guo J, Zhang W. Targeting REDV peptide functionalized polycationic gene carrier for enhancing the transfection and migration capability of human endothelial cells. Journal of Materials Chemistry B. 2015;3(16):3379-91. doi: 10.1039/C4TB02019G.

79. Farrukh A, Ortega F, Fan W, Marichal N, Paez JI, Berninger B, Campo AD, Salierno MJ. Bifunctional Hydrogels Containing the Laminin Motif IKVAV Promote Neurogenesis. Stem Cell Reports. 2017;9(5):1432-40. Epub 2017/10/11. doi: 10.1016/j.stemcr.2017.09.002. PubMed PMID: 28988991; PMCID: PMC5829305.

80. Graf J, Iwamoto Y, Sasaki M, Martin GR, Kleinman HK, Robey FA, Yamada Y. Identification of an amino acid sequence in laminin mediating cell attachment, chemotaxis, and receptor binding. Cell. 1987;48(6):989-96. Epub 1987/03/27. doi: 10.1016/0092-8674(87)90707-0. PubMed PMID: 2951015.

81. Tashiro K, Sephel GC, Weeks B, Sasaki M, Martin GR, Kleinman HK, Yamada Y. A synthetic peptide containing the IKVAV sequence from the A chain of laminin mediates cell attachment, migration, and neurite outgrowth. J Biol Chem. 1989;264(27):16174-82. Epub 1989/09/25. PubMed PMID: 2777785.

82. Hoffman MP, Engbring JA, Nielsen PK, Vargas J, Steinberg Z, Karmand AJ, Nomizu M, Yamada Y, Kleinman HK. Cell type-specific differences in glycosaminoglycans modulate the biological activity of a heparin-binding peptide (RKRLQVQLSIRT) from the G domain of the laminin alpha1 chain. J Biol Chem. 2001;276(25):22077-85. Epub 2001/04/17. doi: 10.1074/jbc.M100774200. PubMed PMID: 11304538.

83. Hamano N, Negishi Y, Fujisawa A, Manandhar M, Sato H, Katagiri F, Nomizu M, Aramaki Y. Modification of the C16Y peptide on nanoparticles is an effective approach to target endothelial and cancer cells via the integrin receptor. Int J Pharm. 2012;428(1-2):114-7. Epub 2012/03/17. doi: 10.1016/j.ijpharm.2012.02.006. PubMed PMID: 22421321.

84. Negishi Y, Nomizu M. Laminin-derived peptides: Applications in drug delivery systems for targeting. Pharmacol Ther. 2019. Epub 2019/06/04. doi: 10.1016/j.pharmthera.2019.05.017. PubMed PMID: 31158392.

85. Dubey PK, Singodia D, Vyas SP. Polymeric nanospheres modified with YIGSR peptide for tumor targeting. Drug Deliv. 2010;17(7):541-51. Epub 2010/06/22. doi: 10.3109/10717544.2010.490249. PubMed PMID: 20560774.

86. Okur AC, Erkoc P, Kizilel S. Targeting cancer cells via tumor-homing peptide CREKA functional PEG nanoparticles. Colloids Surf B Biointerfaces. 2016;147:191-200. Epub 2016/08/12. doi: 10.1016/j.colsurfb.2016.08.005. PubMed PMID: 27513587.

87. Negishi Y, Hamano N, Omata D, Fujisawa A, Manandhar M, Nomizu M, Aramaki Y. Effects of doxorubicin-encapsulating AG73 peptide-modified liposomes on tumor selectivity and cytotoxicity. Results Pharma Sci. 2011;1(1):68-75. Epub 2011/05/01. doi: 10.1016/j.rinphs.2011.10.001. PubMed PMID: 25755984; PMCID: PMC4210273.

88. Boekhoven J, Stupp SI. 25th anniversary article: supramolecular materials for regenerative medicine. Adv Mater. 2014;26(11):1642-59. Epub 2014/02/06. doi: 10.1002/adma.201304606. PubMed PMID: 24496667; PMCID: PMC4015801.

89. Hendricks MP, Sato K, Palmer LC, Stupp SI. Supramolecular Assembly of Peptide Amphiphiles. Acc Chem Res. 2017;50(10):2440-8. Epub 2017/09/07. doi: 10.1021/acs.accounts.7b00297. PubMed PMID: 28876055; PMCID: PMC5647873.

90. Sato K, Hendricks MP, Palmer LC, Stupp SI. Peptide supramolecular materials for therapeutics. Chem Soc Rev. 2018;47(20):7539-51. Epub 2018/09/07. doi: 10.1039/c7cs00735c. PubMed PMID: 30187042; PMCID: PMC6188840.

91. Zhou S, Hokugo A, McClendon M, Zhang Z, Bakshi R, Wang L, Segovia LA, Rezzadeh K, Stupp SI, Jarrahy R. Bioactive peptide amphiphile nanofiber

gels enhance burn wound healing. Burns. 2019;45(5):1112-21. Epub 2019/05/03. doi: 10.1016/j.burns.2018.06.008. PubMed PMID: 31043333.

92. Storrie H, Guler MO, Abu-Amara SN, Volberg T, Rao M, Geiger B, Stupp SI. Supramolecular crafting of cell adhesion. Biomaterials. 2007;28(31):4608-18. Epub 2007/07/31. doi: 10.1016/j.biomaterials.2007.06.026. PubMed PMID: 17662383.

93. Webber MJ, Tongers J, Renault MA, Roncalli JG, Losordo DW, Stupp SI. Development of bioactive peptide amphiphiles for therapeutic cell delivery. Acta Biomater. 2010;6(1):3-11. Epub 2009/07/29. doi: 10.1016/j.actbio.2009.07.031. PubMed PMID: 19635599; PMCID: PMC2787676.

94. Silva GA, Czeisler C, Niece KL, Beniash E, Harrington DA, Kessler JA, Stupp SI. Selective differentiation of neural progenitor cells by high-epitope density nanofibers. Science. 2004;303(5662):1352-5. Epub 2004/01/24. doi: 10.1126/science.1093783. PubMed PMID: 14739465.

95. Park JW, Hwang SR, Yoon IS. Advanced Growth Factor Delivery Systems in Wound Management and Skin Regeneration. Molecules. 2017;22(8). Epub 2017/07/28. doi: 10.3390/molecules22081259. PubMed PMID: 28749427; PMCID: PMC6152378.

96. Mythreye K, Blobe GC. Proteoglycan signaling co-receptors: roles in cell adhesion, migration and invasion. Cell Signal. 2009;21(11):1548-58. Epub 2009/05/12. doi: 10.1016/j.cellsig.2009.05.001. PubMed PMID: 19427900; PMCID: PMC2735586.

97. Yoneda A, Couchman JR. Regulation of cytoskeletal organization by syndecan transmembrane proteoglycans. Matrix Biol. 2003;22(1):25-33. Epub 2003/04/26. PubMed PMID: 12714039.

98. Cichy J, Pure E. The liberation of CD44. J Cell Biol. 2003;161(5):839-43. Epub 2003/06/11. doi: 10.1083/jcb.200302098. PubMed PMID: 12796473; PMCID: PMC2172964.

99. Rainero E. Extracellular matrix endocytosis in controlling matrix turnover and beyond: emerging roles in cancer. Biochem Soc Trans. 2016;44(5):1347-54. Epub 2016/12/03. doi: 10.1042/BST20160159. PubMed PMID: 27911717.

100. An B, Brodsky B. Collagen binding to OSCAR: the odd couple. Blood. 2016;127(5):521-2. Epub 2016/02/06. doi: 10.1182/blood-2015-12-682476. PubMed PMID: 26847065; PMCID: PMC4742544.

101. Nielsen CF, van Putten SM, Lund IK, Melander MC, Norregaard KS, Jurgensen HJ, Reckzeh K, Christensen KR, Ingvarsen SZ, Gardsvoll H, Jensen KE, Hamerlik P, Engelholm LH, Behrendt N. The collagen receptor uPARAP/Endo180 as a novel target for antibody-drug conjugate mediated treatment of mesenchymal and leukemic cancers. Oncotarget. 2017;8(27):44605-24. Epub 2017/06/03. doi: 10.18632/oncotarget.17883. PubMed PMID: 28574834; PMCID: PMC5546505.

102. McBrien NA, Metlapally R, Jobling AI, Gentle A. Expression of collagen-binding integrin receptors in the mammalian sclera and their regulation during the development of myopia. Invest Ophthalmol Vis Sci. 2006;47(11):4674-82. Epub 2006/10/27. doi: 10.1167/iovs.05-1150. PubMed PMID: 17065473.

103. Schnittert J, Bansal R, Storm G, Prakash J. Integrins in wound healing, fibrosis and tumor stroma: High potential targets for therapeutics and drug delivery. Adv Drug Deliv Rev. 2018;129:37-53. Epub 2018/02/08. doi: 10.1016/j.addr.2018.01.020. PubMed PMID: 29414674.

104. Ruoslahti E. Drug targeting to specific vascular sites. Drug Discov Today. 2002;7(22):1138-43. Epub 2003/01/28. PubMed PMID: 12546857.

105. Das L, Anderson TA, Gard JM, Sroka IC, Strautman SR, Nagle RB, Morrissey C, Knudsen BS, Cress AE. Characterization of Laminin Binding Integrin Internalization in Prostate Cancer Cells. J Cell Biochem. 2017;118(5):1038-49. Epub 2016/08/11. doi: 10.1002/jcb.25673. PubMed PMID: 27509031; PMCID: PMC5553695.

106. Shukla R, Chanda N, Zambre A, Upendran A, Katti K, Kulkarni RR, Nune SK, Casteel SW, Smith CJ, Vimal J, Boote E, Robertson JD, Kan P, Engelbrecht H, Watkinson LD, Carmack TL, Lever JR, Cutler CS, Caldwell C, Kannan R, Katti KV. Laminin receptor specific therapeutic gold nanoparticles (198AuNP-EGCg) show efficacy in treating prostate cancer. Proc Natl Acad Sci U S A. 2012;109(31):12426-31. Epub 2012/07/18. doi: 10.1073/pnas.1121174109. PubMed PMID: 22802668; PMCID: PMC3411993.

107. Goebeler M, Kaufmann D, Brocker EB, Klein CE. Migration of highly aggressive melanoma cells on hyaluronic acid is associated with functional changes, increased turnover and shedding of CD44 receptors. J Cell Sci. 1996;109 (Pt 7):1957-64. Epub 1996/07/01. PubMed PMID: 8832418.

108. Sahay G, Alakhova DY, Kabanov AV. Endocytosis of nanomedicines. J Control Release. 2010;145(3):182-95. Epub 2010/03/17. doi: 10.1016/j.jconrel.2010.01.036. PubMed PMID: 20226220; PMCID: PMC2902597.

109. Foroozandeh P, Aziz AA. Insight into Cellular Uptake and Intracellular Trafficking of Nanoparticles. Nanoscale Res Lett. 2018;13(1):339. Epub 2018/10/27. doi: 10.1186/s11671-018-2728-6. PubMed PMID: 30361809; PMCID: PMC6202307.

110. Yameen B, Choi WI, Vilos C, Swami A, Shi J, Farokhzad OC. Insight into nanoparticle cellular uptake and intracellular targeting. J Control Release. 2014;190:485-99. Epub 2014/07/02. doi: 10.1016/j.jconrel.2014.06.038. PubMed PMID: 24984011; PMCID: PMC4153400.

111. Aderem A, Underhill DM. Mechanisms of phagocytosis in macrophages. Annu Rev Immunol. 1999;17:593-623. Epub 1999/06/08. doi: 10.1146/annurev.immunol.17.1.593. PubMed PMID: 10358769.

112. Tsuji T, Yoshitomi H, Usukura J. Endocytic mechanism of transferrin-conjugated nanoparticles and the effects of their size and ligand number on the efficiency of drug delivery. Microscopy (Oxf). 2013;62(3):341-52. Epub 2012/12/04. doi: 10.1093/jmicro/dfs080. PubMed PMID: 23204307.

113. D'Souza AA, Devarajan PV. Asialoglycoprotein receptor mediated hepatocyte targeting - strategies and applications. J Control Release. 2015;203:126-39. Epub 2015/02/24. doi: 10.1016/j.jconrel.2015.02.022. PubMed PMID: 25701309.

114. Phuc LTM, Taniguchi A. Epidermal Growth Factor Enhances Cellular Uptake of Polystyrene Nanoparticles by Clathrin-Mediated Endocytosis. Int J Mol Sci. 2017;18(6). Epub 2017/06/21. doi: 10.3390/ijms18061301. PubMed PMID: 28629179; PMCID: PMC5486122.

115. Nieto Gutierrez A, McDonald PH. GPCRs: Emerging anti-cancer drug targets. Cell Signal. 2018;41:65-74. Epub 2017/09/22. doi: 10.1016/j.cellsig.2017.09.005. PubMed PMID: 28931490.

116. Hu H, Wan J, Huang X, Tang Y, Xiao C, Xu H, Yang X, Li Z. iRGD-decorated reduction-responsive nanoclusters for targeted drug delivery. Nanoscale.

2018;10(22):10514-27. Epub 2018/05/26. doi: 10.1039/c8nr02534g. PubMed PMID: 29799599.

117. Xu S, Olenyuk BZ, Okamoto CT, Hamm-Alvarez SF. Targeting receptor-mediated endocytotic pathways with nanoparticles: rationale and advances. Adv Drug Deliv Rev. 2013;65(1):121-38. Epub 2012/10/03. doi: 10.1016/j.addr.2012.09.041. PubMed PMID: 23026636; PMCID: PMC3565049.

118. Munsell EV, Ross NL, Sullivan MO. Journey to the Center of the Cell: Current Nanocarrier Design Strategies Targeting Biopharmaceuticals to the Cytoplasm and Nucleus. Curr Pharm Des. 2016;22(9):1227-44. Epub 2015/12/18. doi: 10.2174/1381612822666151216151420. PubMed PMID: 26675220; PMCID: PMC4792758.

119. El-Sayed A, Harashima H. Endocytosis of gene delivery vectors: from clathrin-dependent to lipid raft-mediated endocytosis. Mol Ther. 2013;21(6):1118-30. Epub 2013/04/17. doi: 10.1038/mt.2013.54. PubMed PMID: 23587924; PMCID: PMC3677298.

120. Truong NF, Lesher-Perez SC, Kurt E, Segura T. Pathways Governing Polyethylenimine Polyplex Transfection in Microporous Annealed Particle Scaffolds. Bioconjug Chem. 2019;30(2):476-86. Epub 2018/12/05. doi: 10.1021/acs.bioconjchem.8b00696. PubMed PMID: 30513197.

121. Reilly MJ, Larsen JD, Sullivan MO. Polyplexes traffic through caveolae to the Golgi and endoplasmic reticulum en route to the nucleus. Mol Pharm. 2012;9(5):1280-90. Epub 2012/03/17. doi: 10.1021/mp200583d. PubMed PMID: 22420286.

122. Rejman J, Bragonzi A, Conese M. Role of clathrin- and caveolae-mediated endocytosis in gene transfer mediated by lipo- and polyplexes. Mol Ther. 2005;12(3):468-74. Epub 2005/06/21. doi: 10.1016/j.ymthe.2005.03.038. PubMed PMID: 15963763.

123. Arora PD, Wang Y, Bresnick A, Dawson J, Janmey PA, McCulloch CA. Collagen remodeling by phagocytosis is determined by collagen substrate topology and calcium-dependent interactions of gelsolin with nonmuscle myosin IIA in cell adhesions. Mol Biol Cell. 2013;24(6):734-47. Epub 2013/01/18. doi: 10.1091/mbc.E12-10-0754. PubMed PMID: 23325791; PMCID: PMC3596245.

124. Madsen DH, Ingvarsen S, Jurgensen HJ, Melander MC, Kjoller L, Moyer A, Honore C, Madsen CA, Garred P, Burgdorf S, Bugge TH, Behrendt N, Engelholm LH. The non-phagocytic route of collagen uptake: a distinct degradation pathway. J Biol Chem. 2011;286(30):26996-7010. Epub 2011/06/10. doi: 10.1074/jbc.M110.208033. PubMed PMID: 21652704; PMCID: PMC3143658.

125. Shi F, Sottile J. Caveolin-1-dependent beta1 integrin endocytosis is a critical regulator of fibronectin turnover. J Cell Sci. 2008;121(Pt 14):2360-71. Epub 2008/06/26. doi: 10.1242/jcs.014977. PubMed PMID: 18577581; PMCID: PMC2587120.

126. Lobert VH, Brech A, Pedersen NM, Wesche J, Oppelt A, Malerod L, Stenmark H. Ubiquitination of alpha 5 beta 1 integrin controls fibroblast migration through lysosomal degradation of fibronectin-integrin complexes. Dev Cell. 2010;19(1):148-59. Epub 2010/07/21. doi: 10.1016/j.devcel.2010.06.010. PubMed PMID: 20643357.

127. Coopman PJ, Thomas DM, Gehlsen KR, Mueller SC. Integrin alpha 3 beta 1 participates in the phagocytosis of extracellular matrix molecules by human breast cancer cells. Mol Biol Cell. 1996;7(11):1789-804. Epub 1996/11/01. doi: 10.1091/mbc.7.11.1789. PubMed PMID: 8930900; PMCID: PMC276026.

128. Leonoudakis D, Huang G, Akhavan A, Fata JE, Singh M, Gray JW, Muschler JL. Endocytic trafficking of laminin is controlled by dystroglycan and is disrupted in cancers. J Cell Sci. 2014;127(Pt 22):4894-903. Epub 2014/09/14. doi: 10.1242/jcs.152728. PubMed PMID: 25217627; PMCID: PMC4231305.

129. Racine R, Mummert EM. Hyaluronan Endocytosis: Mechanisms of Uptake and Biological Functions. In: Ceresa B, editor. Molecular Regulation of Endocytosis. United Kingdom: IntechOpen; 2012. p. 377-90.

130. Rezler EM, Khan DR, Lauer-Fields J, Cudic M, Baronas-Lowell D, Fields GB. Targeted drug delivery utilizing protein-like molecular architecture. J Am Chem Soc. 2007;129(16):4961-72. Epub 2007/04/03. doi: 10.1021/ja066929m. PubMed PMID: 17397150; PMCID: PMC2519954.

131. Ndinguri MW, Zheleznyak A, Lauer JL, Anderson CJ, Fields GB. Application of Collagen-Model Triple-Helical Peptide-Amphiphiles for CD44-Targeted Drug Delivery Systems. J Drug Deliv. 2012;2012:592602. Epub 2012/12/06. doi: 10.1155/2012/592602. PubMed PMID: 23213537; PMCID: PMC3505660.

132. Leitinger B. Discoidin domain receptor functions in physiological and pathological conditions. Int Rev Cell Mol Biol. 2014;310:39-87. Epub 2014/04/15. doi: 10.1016/B978-0-12-800180-6.00002-5. PubMed PMID: 24725424; PMCID: PMC4021107.

133. Luo T, David MA, Dunshee LC, Scott RA, Urello MA, Price C, Kiick KL. Thermoresponsive Elastin-b-Collagen-Like Peptide Bioconjugate Nanovesicles for Targeted Drug Delivery to Collagen-Containing Matrices. Biomacromolecules. 2017;18(8):2539-51. Epub 2017/07/19. doi: 10.1021/acs.biomac.7b00686. PubMed PMID: 28719196; PMCID: PMC5815509.

134. Chowdhury EH, Akaike T. Fibronectin-coated nano-precipitates of calcium-magnesium phosphate for integrin-targeted gene delivery. J Control Release. 2006;116(2):e68-9. Epub 2007/08/28. doi: 10.1016/j.jconrel.2006.09.054. PubMed PMID: 17718977.

135. Arap W, Pasqualini R, Ruoslahti E. Cancer treatment by targeted drug delivery to tumor vasculature in a mouse model. Science. 1998;279(5349):377-80. Epub 1998/02/07. doi: 10.1126/science.279.5349.377. PubMed PMID: 9430587.

136. Kim YM, Park SC, Jang MK. Targeted gene delivery of polyethyleneimine-grafted chitosan with RGD dendrimer peptide in alphavbeta3 integrin-overexpressing tumor cells. Carbohydr Polym. 2017;174:1059-68. Epub 2017/08/20. doi: 10.1016/j.carbpol.2017.07.035. PubMed PMID: 28821028.

137. Negishi Y, Omata D, Iijima H, Hamano N, Endo-Takahashi Y, Nomizu M, Aramaki Y. Preparation and characterization of laminin-derived peptide AG73-coated liposomes as a selective gene delivery tool. Biol Pharm Bull. 2010;33(10):1766-9. Epub 2010/10/12. doi: 10.1248/bpb.33.1766. PubMed PMID: 20930391.

138. Carvalho RM, Carvalho RC, Maia RF, Caballero D, Kundu CS, Reis LR, Oliverira MJ. Peptide-Modified Dendrimer Nanoparticles for Targeted Therapy of Colorectal Cancer. Advanced Therapeutics. 2019. doi: 10.1002/adtp.201900132.

139. Shing Y, Folkman J, Sullivan R, Butterfield C, Murray J, Klagsbrun M. Heparin affinity: purification of a tumor-derived capillary endothelial cell growth factor. Science. 1984;223(4642):1296-9. Epub 1984/03/23. doi: 10.1126/science.6199844. PubMed PMID: 6199844.

140. Chung YI, Kim JC, Kim YH, Tae G, Lee SY, Kim K, Kwon IC. The effect of surface functionalization of PLGA nanoparticles by heparin- or chitosan-conjugated Pluronic on tumor targeting. J Control Release. 2010;143(3):374-82. Epub 2010/01/30. doi: 10.1016/j.jconrel.2010.01.017. PubMed PMID: 20109508.

141. She W, Li N, Luo K, Guo C, Wang G, Geng Y, Gu Z. Dendronized heparin-doxorubicin conjugate based nanoparticle as pH-responsive drug delivery system for cancer therapy. Biomaterials. 2013;34(9):2252-64. Epub 2013/01/10. doi: 10.1016/j.biomaterials.2012.12.017. PubMed PMID: 23298778.

142. Pathak A, Kumar P, Chuttani K, Jain S, Mishra AK, Vyas SP, Gupta KC. Gene expression, biodistribution, and pharmacoscintigraphic evaluation of chondroitin sulfate-PEI nanoconstructs mediated tumor gene therapy. ACS Nano. 2009;3(6):1493-505. Epub 2009/05/20. doi: 10.1021/nn900044f. PubMed PMID: 19449835.

143. Eliaz RE, Szoka FC, Jr. Liposome-encapsulated doxorubicin targeted to CD44: a strategy to kill CD44-overexpressing tumor cells. Cancer Res. 2001;61(6):2592-601. Epub 2001/04/06. PubMed PMID: 11289136.

144. Fan Y, Yao J, Du R, Hou L, Zhou J, Lu Y, Meng Q, Zhang Q. Ternary complexes with core-shell bilayer for double level targeted gene delivery: in vitro and in vivo evaluation. Pharm Res. 2013;30(5):1215-27. Epub 2012/12/28. doi: 10.1007/s11095-012-0960-9. PubMed PMID: 23269504.

145. Farajzadeh R, Zarghami N, Serati-Nouri H, Momeni-Javid Z, Farajzadeh T, Jalilzadeh-Tabrizi S, Sadeghi-Soureh S, Naseri N, Pilehvar-Soltanahmadi Y. Macrophage repolarization using CD44-targeting hyaluronic acid-polylactide nanoparticles containing curcumin. Artif Cells Nanomed Biotechnol. 2018;46(8):2013-21. Epub 2017/12/01. doi: 10.1080/21691401.2017.1408116. PubMed PMID: 29183161.

146. Li J, Mooney DJ. Designing hydrogels for controlled drug delivery. Nat Rev Mater. 2016;1(12). Epub 2016/12/01. doi: 10.1038/natrevmats.2016.71. PubMed PMID: 29657852; PMCID: PMC5898614.

147. Merino S, Martin C, Kostarelos K, Prato M, Vazquez E. Nanocomposite Hydrogels: 3D Polymer-Nanoparticle Synergies for On-Demand Drug Delivery. ACS Nano. 2015;9(5):4686-97. Epub 2015/05/06. doi: 10.1021/acsnano.5b01433. PubMed PMID: 25938172.

148. Sood N, Bhardwaj A, Mehta S, Mehta A. Stimuli-responsive hydrogels in drug delivery and tissue engineering. Drug Deliv. 2016;23(3):758-80. Epub 2014/07/22. doi: 10.3109/10717544.2014.940091. PubMed PMID: 25045782.

149. Dimatteo R, Darling NJ, Segura T. In situ forming injectable hydrogels for drug delivery and wound repair. Adv Drug Deliv Rev. 2018;127:167-84. Epub 2018/03/24. doi: 10.1016/j.addr.2018.03.007. PubMed PMID: 29567395; PMCID: PMC6003852.

150. Oliva N, Conde J, Wang K, Artzi N. Designing Hydrogels for On-Demand Therapy. Acc Chem Res. 2017;50(4):669-79. Epub 2017/03/17. doi: 10.1021/acs.accounts.6b00536. PubMed PMID: 28301139; PMCID: PMC6527116.

151. Zustiak SP, Leach JB. Hydrolytically degradable poly(ethylene glycol) hydrogel scaffolds with tunable degradation and mechanical properties. Biomacromolecules. 2010;11(5):1348-57. Epub 2010/04/02. doi: 10.1021/bm100137q. PubMed PMID: 20355705; PMCID: PMC3050024.

152. Lutolf MP, Lauer-Fields JL, Schmoekel HG, Metters AT, Weber FE, Fields GB, Hubbell JA. Synthetic matrix metalloproteinase-sensitive hydrogels for the conduction of tissue regeneration: engineering cell-invasion characteristics. Proc Natl Acad Sci U S A. 2003;100(9):5413-8. Epub 2003/04/11. doi: 10.1073/pnas.0737381100. PubMed PMID: 12686696; PMCID: PMC154359.

153. Wang Y. Programmable hydrogels. Biomaterials. 2018;178:663-80. Epub 2018/03/20. doi: 10.1016/j.biomaterials.2018.03.008. PubMed PMID: 29549970; PMCID: PMC6054804.

154. Patterson J, Hubbell JA. Enhanced proteolytic degradation of molecularly engineered PEG hydrogels in response to MMP-1 and MMP-2. Biomaterials. 2010;31(30):7836-45. Epub 2010/07/30. doi: 10.1016/j.biomaterials.2010.06.061. PubMed PMID: 20667588.

155. Narayanaswamy R, Torchilin VP. Hydrogels and Their Applications in Targeted Drug Delivery. Molecules. 2019;24(3). Epub 2019/02/13. doi: 10.3390/molecules24030603. PubMed PMID: 30744011; PMCID: PMC6384686.

156. Appel EA, Tibbitt MW, Webber MJ, Mattix BA, Veiseh O, Langer R. Self-assembled hydrogels utilizing polymer-nanoparticle interactions. Nat Commun. 2015;6:6295. Epub 2015/02/20. doi: 10.1038/ncomms7295. PubMed PMID: 25695516; PMCID: PMC4651845.

157. Ruskowitz RE, DeForest AC. Photoresponsive biomaterials for targeted drug delivery and 4D cell culture. Nature Reviews Materials. 2018;3:1-17. doi: 10.1038/natrevmats2017.87.

158. Mateen R, Hoare T. Injectable, in situ gelling, cyclodextrin-dextran hydrogels for the partitioning-driven release of hydrophobic drugs. J Mater Chem B. 2014;2:5157-67. doi: 10.1039/C4TB00631C.

159. Yigit S, Sanyal R, Sanyal A. Fabrication and functionalization of hydrogels through "click" chemistry. Chem Asian J. 2011;6(10):2648-59. Epub 2011/09/29. doi: 10.1002/asia.201100440. PubMed PMID: 21954074.

160. Phelps EA, Enemchukwu NO, Fiore VF, Sy JC, Murthy N, Sulchek TA, Barker TH, Garcia AJ. Maleimide cross-linked bioactive PEG hydrogel exhibits improved reaction kinetics and cross-linking for cell encapsulation and in situ delivery. Adv Mater. 2012;24(1):64-70, 2. Epub 2011/12/17. doi: 10.1002/adma.201103574. PubMed PMID: 22174081; PMCID: PMC3517145.

161. Ulrich S, Boturyn D, Marra A, Renaudet O, Dumy P. Oxime ligation: a chemoselective click-type reaction for accessing multifunctional biomolecular constructs. Chemistry. 2014;20(1):34-41. Epub 2013/12/05. doi: 10.1002/chem.201302426. PubMed PMID: 24302514.

162. Kolmel DK, Kool ET. Oximes and Hydrazones in Bioconjugation: Mechanism and Catalysis. Chem Rev. 2017;117(15):10358-76. Epub 2017/06/24. doi: 10.1021/acs.chemrev.7b00090. PubMed PMID: 28640998; PMCID: PMC5580355.

163. Christman KL, Broyer RM, Schopf E, Kolodziej CM, Chen Y, Maynard HD. Protein nanopatterns by oxime bond formation. Langmuir. 2011;27(4):1415-8.

Epub 2011/01/05. doi: 10.1021/la103978x. PubMed PMID: 21192671; PMCID: PMC3050016.

164. Palmese LL, Thapa R, Sullivan MO, Kiick KL. Hybrid hydrogels for biomedical applications. Current Opinion in Chemical Engineering. 2019;24:143-57. doi: https://doi.org/10.1016/j.coche.2019.02.010.

165. Park JC, Hwang YS, Lee JE, Park KD, Matsumura K, Hyon SH, Suh H. Type I atelocollagen grafting onto ozone-treated polyurethane films: cell attachment, proliferation, and collagen synthesis. J Biomed Mater Res. 2000;52(4):669-77. Epub 2000/10/18. PubMed PMID: 11033549.

166. Zilberman M, Elsner JJ. Antibiotic-eluting medical devices for various applications. J Control Release. 2008;130(3):202-15. Epub 2008/08/09. doi: 10.1016/j.jconrel.2008.05.020. PubMed PMID: 18687500.

167. De Souza R, Zahedi P, Allen CJ, Piquette-Miller M. Polymeric drug delivery systems for localized cancer chemotherapy. Drug Deliv. 2010;17(6):365-75. Epub 2010/05/01. doi: 10.3109/10717541003762854. PubMed PMID: 20429844.

168. Duxfield L, Sultana R, Wang R, Englebretsen V, Deo S, Rupenthal ID, Al-Kassas R. Ocular delivery systems for topical application of anti-infective agents. Drug Dev Ind Pharm. 2016;42(1):1-11. Epub 2015/09/02. doi: 10.3109/03639045.2015.1070171. PubMed PMID: 26325119.

169. Chia CL, Shelat VG, Low W, George S, Rao J. The use of Collatamp G, local gentamicin-collagen sponge, in reducing wound infection. Int Surg. 2014;99(5):565-70. Epub 2014/09/13. doi: 10.9738/INTSURG-D-13-00171.1. PubMed PMID: 25216422; PMCID: PMC4253925.

170. Raja SG. Local application of gentamicin-containing collagen implant in the prophylaxis and treatment of surgical site infection following cardiac surgery. Int J Surg. 2012;10 Suppl 1:S10-4. Epub 2012/06/05. doi: 10.1016/j.ijsu.2012.05.018. PubMed PMID: 22659309.

171. de Bruin AF, Gosselink MP, van der Harst E, Rutten HJ. Local application of gentamicin collagen implants in the prophylaxis of surgical site infections following gastrointestinal surgery: a review of clinical experience. Tech Coloproctol. 2010;14(4):301-10. Epub 2010/06/30. doi: 10.1007/s10151-010-0593-0. PubMed PMID: 20585822; PMCID: PMC2988990.

172. McKay WF, Peckham SM, Badura JM. A comprehensive clinical review of recombinant human bone morphogenetic protein-2 (INFUSE Bone Graft). Int Orthop. 2007;31(6):729-34. Epub 2007/07/20. doi: 10.1007/s00264-007-0418-6. PubMed PMID: 17639384; PMCID: PMC2266665.

173. Shekaran A, Garcia JR, Clark AY, Kavanaugh TE, Lin AS, Guldberg RE, Garcia AJ. Bone regeneration using an alpha 2 beta 1 integrin-specific hydrogel as a BMP-2 delivery vehicle. Biomaterials. 2014;35(21):5453-61. Epub 2014/04/15. doi: 10.1016/j.biomaterials.2014.03.055. PubMed PMID: 24726536; PMCID: PMC4033404.

174. Johnson CT, Wroe JA, Agarwal R, Martin KE, Guldberg RE, Donlan RM, Westblade LF, Garcia AJ. Hydrogel delivery of lysostaphin eliminates orthopedic implant infection by Staphylococcus aureus and supports fracture healing. Proc Natl Acad Sci U S A. 2018;115(22):E4960-E9. Epub 2018/05/16. doi: 10.1073/pnas.1801013115. PubMed PMID: 29760099; PMCID: PMC5984524.

175. Bhakta G, Lim ZX, Rai B, Lin T, Hui JH, Prestwich GD, van Wijnen AJ, Nurcombe V, Cool SM. The influence of collagen and hyaluronan matrices on the delivery and bioactivity of bone morphogenetic protein-2 and ectopic bone formation. Acta Biomater. 2013;9(11):9098-106. Epub 2013/07/23. doi: 10.1016/j.actbio.2013.07.008. PubMed PMID: 23871940.

176. Sakiyama-Elbert SE, Hubbell JA. Development of fibrin derivatives for controlled release of heparin-binding growth factors. J Control Release. 2000;65(3):389-402. Epub 2000/03/04. doi: 10.1016/s0168-3659(99)00221-7. PubMed PMID: 10699297.

177. Tanihara M, Suzuki Y, Yamamoto E, Noguchi A, Mizushima Y. Sustained release of basic fibroblast growth factor and angiogenesis in a novel covalently crosslinked gel of heparin and alginate. J Biomed Mater Res. 2001;56(2):216-21. Epub 2001/05/08. doi: 10.1002/1097-4636(200108)56:2<216::aid-jbm1086>3.0.co;2-n. PubMed PMID: 11340591.

178. Jeong KJ, Panitch A. Interplay between covalent and physical interactions within environment sensitive hydrogels. Biomacromolecules. 2009;10(5):1090-9. Epub 2009/03/24. doi: 10.1021/bm801270k. PubMed PMID: 19301930.

179. Oliviero O, Ventre M, Netti PA. Functional porous hydrogels to study angiogenesis under the effect of controlled release of vascular endothelial growth factor. Acta Biomater. 2012;8(9):3294-301. Epub 2012/05/30. doi: 10.1016/j.actbio.2012.05.019. PubMed PMID: 22641106.

180. Freudenberg U, Zieris A, Chwalek K, Tsurkan MV, Maitz MF, Atallah P, Levental KR, Eming SA, Werner C. Heparin desulfation modulates VEGF release

and angiogenesis in diabetic wounds. J Control Release. 2015;220(Pt A):79-88. Epub 2015/10/20. doi: 10.1016/j.jconrel.2015.10.028. PubMed PMID: 26478015.

181. Lohmann N, Schirmer L, Atallah P, Wandel E, Ferrer RA, Werner C, Simon JC, Franz S, Freudenberg U. Glycosaminoglycan-based hydrogels capture inflammatory chemokines and rescue defective wound healing in mice. Sci Transl Med. 2017;9(386). Epub 2017/04/21. doi: 10.1126/scitranslmed.aai9044. PubMed PMID: 28424334.

182. Ishihara J, Ishihara A, Fukunaga K, Sasaki K, White MJV, Briquez PS, Hubbell JA. Laminin heparin-binding peptides bind to several growth factors and enhance diabetic wound healing. Nat Commun. 2018;9(1):2163. Epub 2018/06/06. doi: 10.1038/s41467-018-04525-w. PubMed PMID: 29867149; PMCID: PMC5986797.

183. Lozeau LD, Grosha J, Kole D, Prifti F, Dominko T, Camesano TA, Rolle MW. Collagen tethering of synthetic human antimicrobial peptides cathelicidin LL37 and its effects on antimicrobial activity and cytotoxicity. Acta Biomater. 2017;52:9-20. Epub 2016/12/27. doi: 10.1016/j.actbio.2016.12.047. PubMed PMID: 28017866.

184. Ishihara J, Ishihara A, Sasaki K, Lee SS, Williford JM, Yasui M, Abe H, Potin L, Hosseinchi P, Fukunaga K, Raczy MM, Gray LT, Mansurov A, Katsumata K, Fukayama M, Kron SJ, Swartz MA, Hubbell JA. Targeted antibody and cytokine cancer immunotherapies through collagen affinity. Sci Transl Med. 2019;11(487). Epub 2019/04/12. doi: 10.1126/scitranslmed.aau3259. PubMed PMID: 30971453; PMCID: PMC6541444.

185. Al-Dosari MS, Gao X. Nonviral gene delivery: principle, limitations, and recent progress. AAPS J. 2009;11(4):671-81. Epub 2009/10/17. doi: 10.1208/s12248-009-9143-y. PubMed PMID: 19834816; PMCID: PMC2782077.

186. Wang C, Gao C. Design of gene-activated matrix for the repair skin and cartilage. Polymer Journal. 2014(46):476-82. doi: 10.1038/pj.2014.50.

187. De Laporte L, Shea LD. Matrices and scaffolds for DNA delivery in tissue engineering. Adv Drug Deliv Rev. 2007;59(4-5):292-307. Epub 2007/05/22. doi: 10.1016/j.addr.2007.03.017. PubMed PMID: 17512630; PMCID: PMC1949490.

188. Elangovan S, D'Mello SR, Hong L, Ross RD, Allamargot C, Dawson DV, Stanford CM, Johnson GK, Sumner DR, Salem AK. The enhancement of bone regeneration by gene activated matrix encoding for platelet derived growth factor. Biomaterials. 2014;35(2):737-47. Epub 2013/10/29. doi: 10.1016/j.biomaterials.2013.10.021. PubMed PMID: 24161167; PMCID: PMC3855224.

189. Mao Z, Shi H, Guo R, Ma L, Gao C, Han C, Shen J. Enhanced angiogenesis of porous collagen scaffolds by incorporation of TMC/DNA complexes encoding vascular endothelial growth factor. Acta Biomater. 2009;5(8):2983-94. Epub 2009/05/02. doi: 10.1016/j.actbio.2009.04.004. PubMed PMID: 19406694.

190. Guo R, Xu S, Ma L, Huang A, Gao C. Enhanced angiogenesis of gene-activated dermal equivalent for treatment of full thickness incisional wounds in a porcine model. Biomaterials. 2010;31(28):7308-20. Epub 2010/07/06. doi: 10.1016/j.biomaterials.2010.06.013. PubMed PMID: 20598366.

191. Orsi S, De Capua A, Guarnieri D, Marasco D, Netti PA. Cell recruitment and transfection in gene activated collagen matrix. Biomaterials. 2010;31(3):570-6. Epub 2009/10/10. doi: 10.1016/j.biomaterials.2009.09.054. PubMed PMID: 19815270.

192. Truong NF, Segura T. Sustained Transgene Expression via Hydrogel-Mediated Gene Transfer Results from Multiple Transfection Events. ACS Biomater Sci

Eng. 2018;4(3):981-7. doi: https://doi-org.udel.idm.oclc.org/10.1021/acsbiomaterials.7b00957.

193. Urello MA, Kiick KL, Sullivan MO. A CMP-based method for tunable, cell-mediated gene delivery from collagen scaffolds. J Mater Chem B. 2014(2):8174-85. doi: 10.1039/c4tb01435a.

194. Urello MA, Kiick KL, Sullivan MO. Integration of growth factor gene delivery with collagen-triggered wound repair cascades using collagen-mimetic peptides. Bioeng Transl Med. 2016;1(2):207-19. Epub 2016/12/17. doi: 10.1002/btm2.10037. PubMed PMID: 27981245; PMCID: PMC5125401.

195. Urello MA, Kiick KL, Sullivan MO. ECM turnover-stimulated gene delivery through collagen-mimetic peptide-plasmid integration in collagen. Acta Biomater. 2017;62:167-78. Epub 2017/09/04. doi: 10.1016/j.actbio.2017.08.038. PubMed PMID: 28865990; PMCID: PMC5654588.

196. Theocharis AD, Skandalis SS, Gialeli C, Karamanos NK. Extracellular matrix structure. Adv Drug Deliv Rev. 2016;97:4-27. Epub 2015/11/13. doi: 10.1016/j.addr.2015.11.001. PubMed PMID: 26562801.

Chapter 2

MATERIALS AND METHODS FOR GENE ACTIVATED HYALURONIC ACID AND COLLAGEN MATRIX (GAHCM)

This chapter explains the materials and methods for preparation of gene activated hyaluronic acid and collagen matrix (GAHCM) with collagen mimetic peptide (CMP) modification, which is a combination of CMP-modified pDNA/Polyethyleneimine (PEI) polyplex and HCM matrix. GAHCM would be the major samples to be evaluated in chapter 3 and chapter 4. Thus, the most of content in this chapter are derived and reused from chapter 3 and chapter 4. In particular, this chapter describes the details about the synthesis and purification of CMP and CMP-PEI conjugate, polyplex formation, HCM formulation, and finally, GAHCM preparation.

2.1 Materials

TentaGel R RAM Resin (90 μm), O-benzotriazole-N,N,N′,N′-tetramethyl-uronium-hexafluoro-phosphate (HBTU), and Fmoc-protected amino acids were procured from Peptides International (Louisville, KY), Aapptec (Louisville, KY), and ChemPep, Inc. (Wellington, FL), respectively. Trifluoroacetic acid (TFA), N,N-dimethyl formamide (DMF), acetonitrile, methanol, and anhydrous ethyl ether were acquired from Fisher Scientific (Fairlawn, NJ). Piperidine, diisopropylethylamine (DIEA), Triisopropylsilane, 1,2-Ethaneithiol, and branched PEI (25 kDa) were procured from SigmaAldrich (St. Louis, MO). The gWIZ-GFP plasmid was procured from Genlantis (San Diego, CA). pCMV-GLuc plasmids were acquired from New England

Biolabs (Ipswich, MA). Following the manufacturer's protocols, the pCMV-GLuc plasmids were amplified in NEB 5-α electrocompetent Escherichia coli (New England Biolabs, Ipswich, MA) purified using a Qiagen Maxiprep Kit (Germantown, MD).

2.2 Synthesis and purification of collagen mimetic peptide (CMP)

The CMP [$(GPP)_3$GPRGEKGERGPR$(GPP)_3$GPCCG] and scrambled CMP (sCMP) [EGKPPCGRGPRGGPPPCRPGPGEGPGGPPPPPPGG] were synthesized via standard Fmoc and HBTU chemistry based solid phase peptide synthesis (SPPS) using a Focus XC automatic peptide synthesizer (AAPPTec Inc., Louisville, KY). In details, TentaGel R RAM Resin with a loading capacity of 0.18 mmol/g (0.2 mmol scale) was used for the synthesis. The resin was mixed with each Fmoc-amino acid in DMF (5 molar equivalence), HBTU in DMF (5 molar equivalence), and DIEA in NMP (7.5 molar equivalence) and incubated for 60 min with shaking and under nitrogen gas mixing for coupling reaction. And amino acid residues from 11^{th} were run twice of coupling reaction. Three times of incubation with piperidine for 10 min was used to deprotect the Fmoc group from amino acid to be prepared for coupling the next amino acid residue. Next, for carboxyfluorescein (CF) labeled CMP, CF (6 molar equivalence) was coupled to CMP on resin in a 24 hr reaction with PyAOP (6 molar equivalence) and DIPEA (12 molar equivalence). As described in our previous papers (1-4), the peptides were cleaved from resin with 2 h incubation in 94:2.5:2.5:1 TFA:TIS:water:EDT (v:v:v:v). After the cleavage reaction, the crude peptides in the cleavage cocktail solution were filtered out from the resin and precipitated out by rinsing with a cold anhydrous ethyl ether. After centrifugation, the ether was mostly removed from the crude peptide precipitate. The crude peptides were further incubated in chemical hood overnight to get rid of any residual ether and dry them, prior to HPLC purification. After

the crude peptides were dissolved in water and filtered through 0.25 µm syringe filter, the crude peptides were purified via reverse-phase HPLC (Waters Inc., Milford, MA) on a Waters XBridge BEH130 Prep C-18 column using a linear gradient mixture of water (0.1% TFA) and acetonitrile (0.1% TFA) (1% of acetonitrile increase per each min) at a temperature of 70 °C (Figure 2.1). Then, the molecular weights and purities of each of the purified peptides were confirmed with either MALDI-TOF MS (Bruker MicroFlex MALDI-TOF) or an ultra-performance liquid chromatographic unit

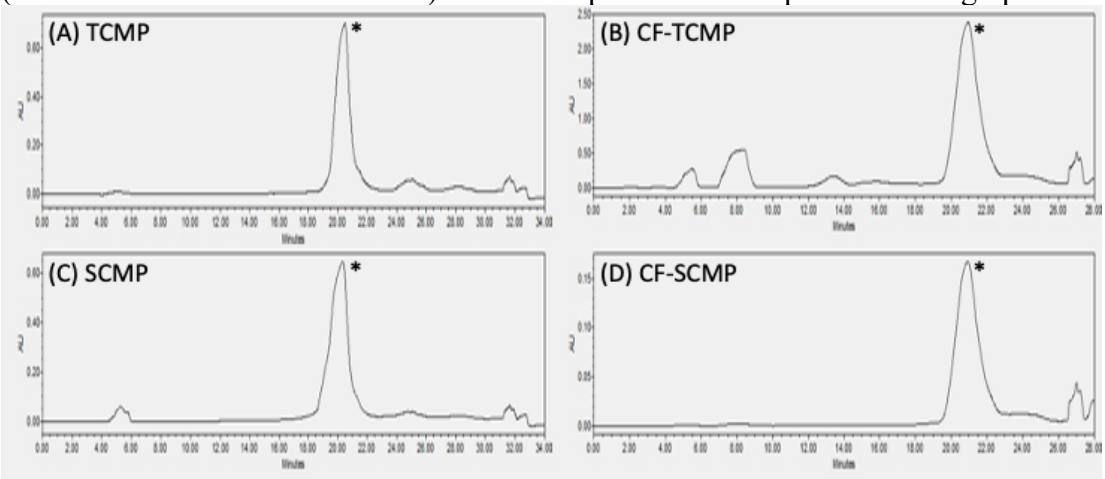

Figure 2.1. HPLC trace at 220 nm for crude peptides; (A) TCMP or CMP ($(GPP)_3$GPRGEKGERGPR$(GPP)_3$GPCCG) (B) CF-TCMP or CF-CMP (CF-$(GPP)_3$GPRGEKGERGPR$(GPP)_3$GPCCG) (C) SCMP (EGKPPCGRGPRGGPPPCRPGPGEGPGGPPPPPPGG) (D) CF-SCMP (EGKPPCGRGPRGGPPPCRPGPGEGPGGPPPPPPGG). * indicates the peak for the target peptide.

in line with an electrospray ionization (UPLC-ESI) Xevo G2-S QTof mass spectrometer (Waters Corporation, Milford, MA). SCMP, CF-CMP, and CF-SCMP were analysed by MALDI-TOF MS; m/z calculated 3219.092 [M + H^+] for SCMP, m/z calculated 3577 [M + H^+] for CF-CMP and m/z calculated 3577 [M + H^+] for CF-SCMP. In addition, CMP was analysed by UPLC-ESI (Figure. 2.2).

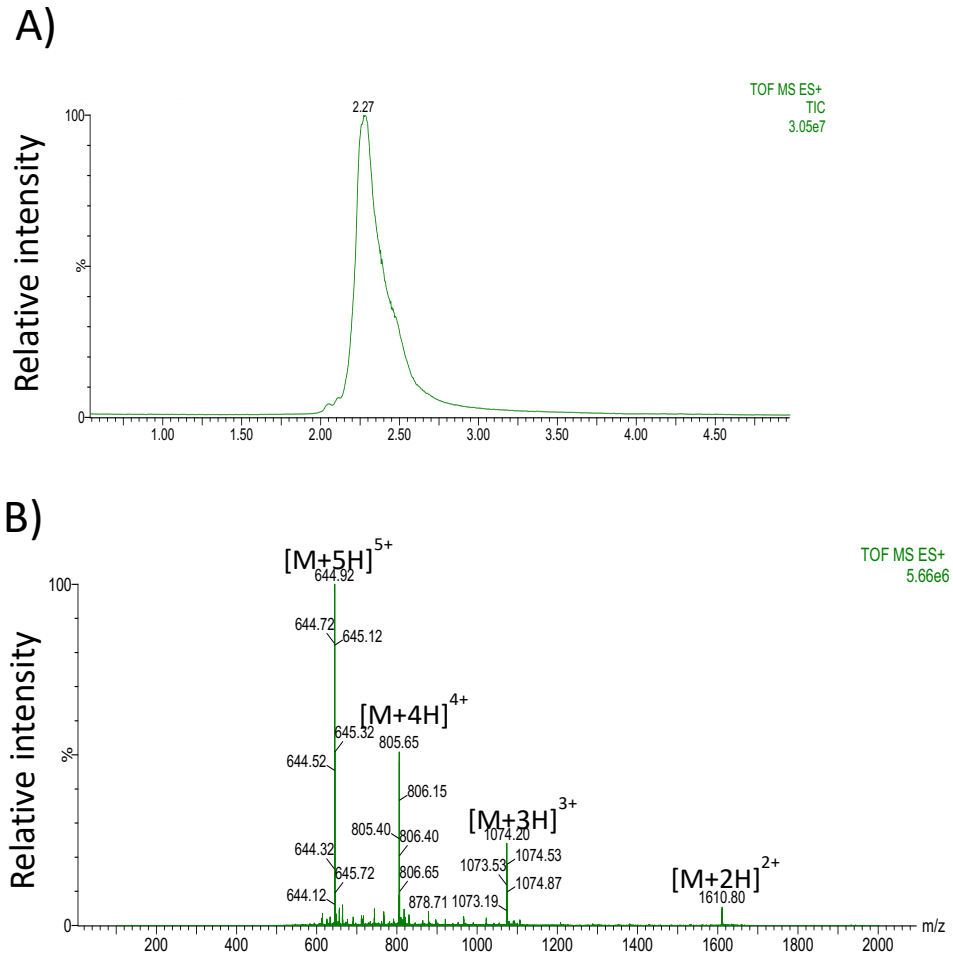

Figure 2.2. A) Ultra-performance liquid chromatography total ion chromatograms of the purified CMP. Integrations of the chromatograms displayed a greater than 95% of the total chromatogram for CMP, indicating high purity of CMP. B) Electrospray ionization mass spectrometry of the purified CMP; m/z=1610.6 $[(M + 2H)^{2+} = 1610.8]$, m/z= 1073.4 $[(M + 3H)^{3+} = 1074.2]$, m/z= 804.8 $[(M + 4H)^{4+} = 805.6]$, m/z= 643.6 $[(M + 5H)^{5+} = 644.9]$, m/z= 188.6.

2.3 CMP-PEI conjugation and purification

The purified peptides were conjugated to PEI using heterobifunctional sulfo-SMCC crosslinker (Thermo Fisher, Waltham, MA). A solution containing branched PEI

and sulfo-SMCC at a molar ratio of 1:2.5 was incubated with magnetic stirring at room temperature for 1 h. After removing the excess Sulfo-SMCC using a Sartorius Vivaspin 6 centrifugal concentrator with a 5 kDa molecular weight cut-off (MWCO), CMP (3 molar equivalence to PEI) was added to SMCC-PEI and incubated with magnetic stirring for 24 h at 37 ºC to facilitate the Michael-type reaction between the thiol of the cysteine in the CMP and the maleimide in SMCC-PEI. The products were purified via dialysis (using SnakeSkin dialysis tubing with a 10 kDa MWCO) (Thermo Fisher, Waltham, MA) against deionized water at 37 ºC for 3 days and lyophilized to a powder.

2.4 CMP-PEI conjugate characterization

Successful production of CMP-PEI conjugates was confirmed via gel permeation chromatography (GPC) on Waters Ultrahydrogel linear and 250 columns (Waters Inc., Milford, MA), using a 0.5 M acetate buffer at pH 4.7 (Figure. 2.3). GPC of CMP-PEI showed a peak shift to an earlier time point (~14.5 min) as compared to the peaks for PEI (~16 min) or SMCC-PEI (~15.5 min), which indicated an increased molecular weight and confirmed the successful CMP conjugation to PEI. In addition, the triple helical assembly of the CMP-PEI conjugate was confirmed via circular dichroism spectrometry (Jasco 810 spectrometer, Jasco Inc., Easton, MD), using a spectral scan measurement from 215 to 235 nm. Measurements were performed at both 4 °C, to examine the characteristic peaks for the CMP triple helical secondary s tructure of CMP-PEI (Figure. 2.4(A)), and 65 ºC, to examine the CMP-PEI above the T_m of the CMP

(43 °C) (3) (Figure. 2.4(B)), using a scanning speed of 20 nm/min, a data integration time of 16 s, and a data pitch of 1 nm.

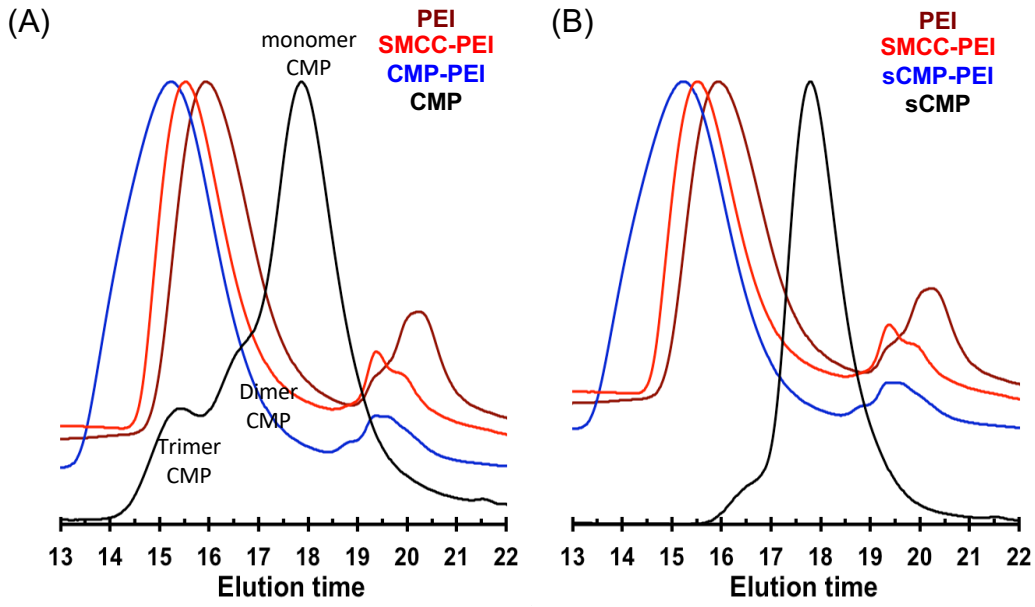

Figure 2.3. Gel permeation chromatography for (A) CMP-PEI (B) Scrambled CMP-PEI conjugates

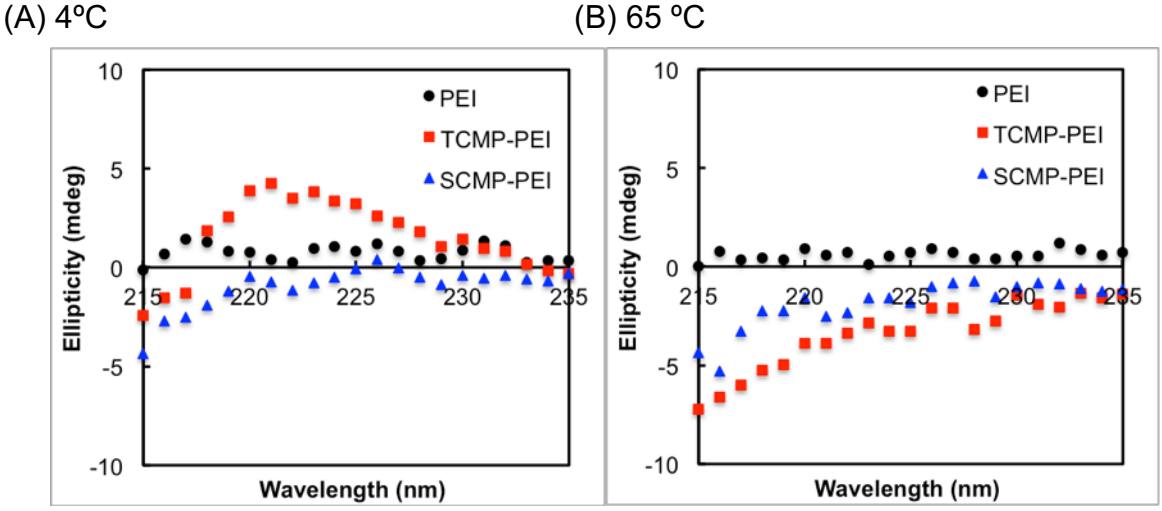

Figure 2.4. CD spectra measurement for PEI, CMP-PEI, Scrambled CMP-PEI conjugates at (A) 4 ºC and (B) 65 ºC

2.5 Polyplex formulation and characterization

CMP-modified polyplexes were formed by self-assembly driven by electrostatic interactions between negatively-charged plasmid DNA and positively charged PEI/CMP-PEI, as described in our previous reports (1-4). Briefly, after heating CMP-PEI solution for 30 min at 65 °C to disassemble the triple helix of the CMP, equal volumes of plasmid and PEI/CMP-PEI solutions in 20 mM HEPES (pH 6.0) were mixed to prepare a solution containing 20 μg/mL plasmid. While vortexing the plasmid solution with speed at 6, PEI/CMP-PEI solutions were added in dropwise. This mixture was incubated for 10 min at room temperature (or 65 °C for CMP-polyplex) to facilitate polyplex formation. The N:P ratio (number of amines (N) in PEI: the number of phosphates (P) in the plasmid) was adjusted by varying the concentration of PEI. CMP modification was varied by altering the ratio of CMP-PEI to total PEI (20% CMP-PEI to total PEI as 20 CP and 50% CMP-PEI to total PEI with as 50 CP). The polyplex were further mixed with 20 mM Sucrose and lyophilized at least overnight to prepare the lyophilized polyplex for incorporating HCM hydrogel.

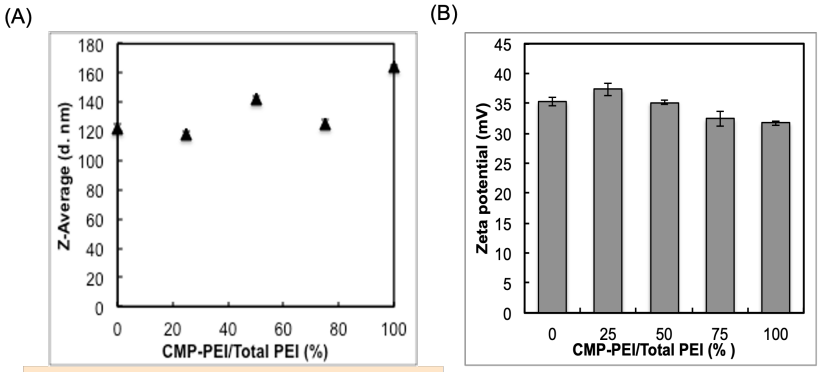

PDI	0	25	50	75	100
Ave.	0.173	0.215	0.194	0.212	0.221
Std.	0.012	0.019	0.008	0.012	0.027

Figure 2.5. Dynamic light scattering measurement for (A) hydrodynamic diameter (D_h) and (B) zeta potential of CMP-PEI/pGFP complex (N/P=8) with a varying CMP-PEI percentage.

Polyplex formation was characterized via dynamic light scattering (DLS) and agarose gel electrophoresis. The hydrodynamic radii of the polyplexes were measured using a ZetaSizer Nano Series (Nano ZS, Malvern Instruments, UK), using a scattering angle of 173° (Figure. 2.5(A)). The data fitting was performed by using the cumulant method. In addition, the polydispersity index (PDI) and ζ-potential of the polyplexes were calculated using the Nano DTS software (version 6.34) (Figure. 2.5(B)). All measurements were performed in triplicate for each sample at 25 °C with a sub-run count of at least 11 correlations. I acquired the size (<180 nm with PDI<0.3) and zeta potentials (+30 mV to +40 mV) of polyplexes (N/P=8) with varying CMP amounts, within the range for an efficient endocytosis by fibroblasts. To evaluate the efficiency

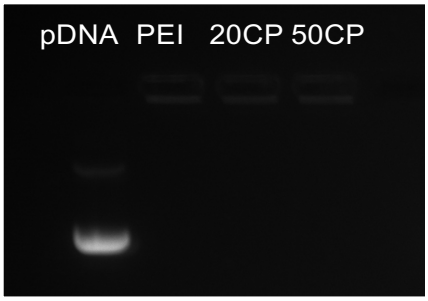

Figure 2.6. Representative gel electrophoresis image for ethidium bromide stained polyplex. White band indicates the destabilized and released GLuc from polyplex

of plasmid condensation in polyplexes, the polyplexes with analyzed by gel electrophoresis in 1% agarose gels containing ethidium bromide [0.5 μg per mL of tris/borate/ethylenediaminetetraacetic acid (TBE) buffer] and 1× gel loading dye blue. Gels were run for 1 h at 100 V and 400 mA and imaged with a BioRad Gel Doc XR (Hercules, CA) (Figure 2.6).

2.6 *In vitro* 2D transfection of fibroblasts

Fibroblasts (NIH/3T3 cells; ATCC, Manassas, VA) were cultured in complete DMEM containing 10% heat-inactivated fetal bovine serum and 1% penicillin-streptomycin at 37 °C with 5% CO2. Cells were passaged with 0.25% Trypsin containing 2.21 mM EDTA every 2-3 days. To optimize the N:P ratio (amine groups in the polymer to phosphate groups in the nucleic acid) of the polyplexes, bolus transfection of fibroblasts was studied using various N:P ratios in the polyplexes. Cells were plated at a density of 10,000 cells per cm2 for 24 h. GFP-encoding polyplexes with 4 μg of GFP plasmid in 20 mM HEPES at pH 6 were added dropwise into the cells growing in Opti-MEM, and the cells were incubated in the transfection solution for 90 min at 37 °C with 5% CO2. The Opti-MEM was replaced with complete DMEM and

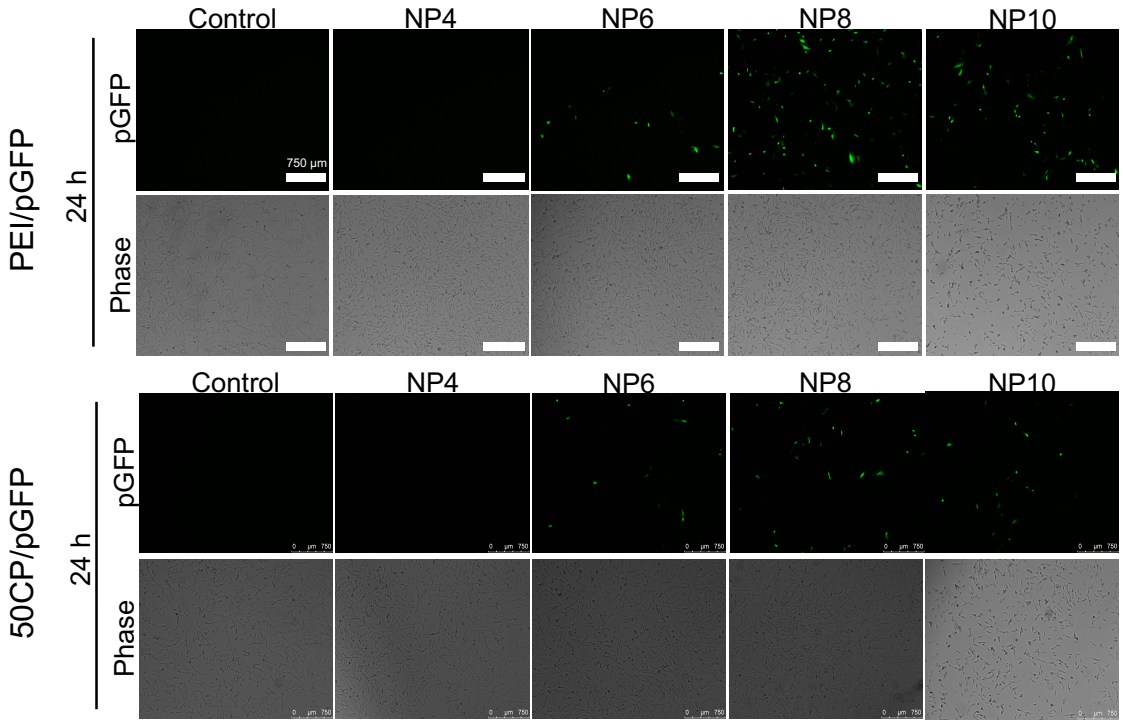

Figure 2.7. 24 h post-bolus transfection of NIH3T3 using PEI/pGFP complex and 50% CMP-PEI/pGFP complex with varying N/P ratio.

cells were incubated at 37 °C with 5% CO2 for an additional 24 h. GFP transfection was examined using microscopic imaging of GFP expression in the cells (Figure. 2.7). The optimal N:P ratio of polyplexes was identified as 8 using a visual evaluation of gene expression and an analysis of cell viability in the fibroblasts after 24 h of bolus transfection with GFP encoding polyplex. As used by previous our studies (1-4), PEI, 20 CP and 50 CP were formulated for this study.

2.7 Polyplex stability in the presence of HA

To evaluate the stability of polyplexes in the presence of negatively charged HA, fluorescence recovery assays and agarose gel electrophoresis experiments were conducted. For the YoYo-3 recovery assay, the GLuc plasmid was pre-stained with YoYo™-3 Iodide (0.02 µL per µg DNA, Thermo Fisher) for 10 min at room temperature before forming the polyplexes at an N:P ratio of 8. The polyplexes were incubated with heparin sodium salt from porcine intestinal mucosa (2 mg/mL, Sigma-Aldrich) or hyaluronic acid (430 K Da, 2 mg/mL) at room temperature for 45 min. After incubation with heparin or hyaluronic acid, the fluorescence intensity of YoYo-3 in the polyplexes was measured at λ_{ex} = 612 nm and λ_{em} = 638 nm using a SpectraMax i3 plate reader (Molecular Devices, San Jose, CA). As described in section 2.2, polyplexes were assessed by agarose gel electrophoresis following polyplex (N:P = 8) incubation with heparin (2 mg/mL) or hyaluronic acid (430 K Da, 2 mg/mL) at room temperature for 45 min.

To investigate whether anionic HA destabilized the polyplexes resulting in disassembly, fluorescence quenching assays and gel electrophoresis experiments were performed to detect plasmid DNA after polyplex incubation with HA. YoYo-3 fluorescence was used as a probe to monitor polyplex disassembly, as the fluorescence

of the YoYo-3 dye is quenched when plasmid DNA is condensed with a carrier in polyplex form (5). Polyplexes resisted disassembly in the presence of HA, whereas more than 60% of both CMP and non-CMP-modified polyplexes were significantly disassembled in the presence of high concentrations of heparin (Figure 2.8(A)). Moreover, agarose gel electrophoresis confirmed the stability of the polyplexes after incubation with anionic HA, as no free plasmid bands were observed for the polyplex samples after incubation was complete (Figure 2.8(B)), indicating that the presence of HA did not disrupt polyplex assembly.

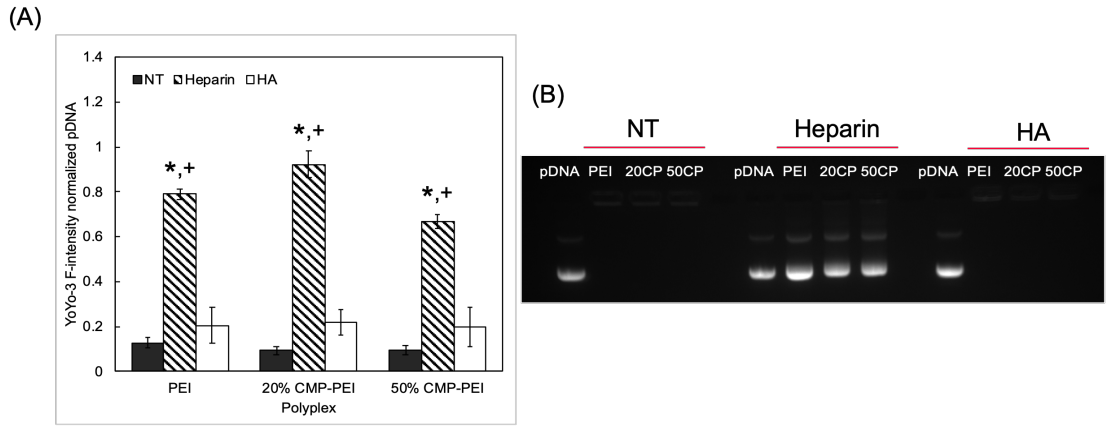

Figure 2.8. The stability of polyplex in the presence of hyaluronic acid. (A) The fluorescent measurement of pre-stained GLuc with YoYo-3 complexing with PEI, 20% CMP-PEI, and 50% CMP-PEI after treatments with no (Black), Heparin (1 mg/mL, Stripe) as a negative control, and Hyaluronic acid (~450K Da, 2 mg/mL, Blank) for 2 hr. The F-intensity is normalized to the initial F- intensity of YoYo-3 pre-stained pGLuc before complexing with PEI, 20% CMP-PEI and 50% CMP-PEI. Each data point represents the mean ± standard deviation for n=3. The statistically significant differences state +$P<0.05$ compared to HA, and *$P<0.05$ compared to NT. (B) Representative gel electrophoresis image for ethidium bromide stained polyplex after treatment with no, heparin, and HA for 2 h. White band indicates the destabilized and released GLuc from polyplex.

2.8 HCM hydrogel formulation and 3D culture of fibroblast

The HCM hydrogels were composed of self-assembly of bovine collagen type I, (Fibricol (4 mg/mL)) driven by pH, temperature and ionic strength, and disulfide bond formation in thiolated-HA (Glycosil®, HA-SH). The HCM hydrogels with various concentrations (0, 1, 2, and 4 mg/mL) of Glycosil® were evaluated for the optimum condition for fibroblast culture. The neutralized collagen (8 mg/mL) was prepared through mixing with acidic solubilized collagen (Fibricol,10 mg/mL), 10% total volume of 10× DPBS and 10% total volume of 0.1 N NaOH. Fibroblasts suspended in 1× DPBS (100,000 cells/mL) were added to the neutralized collagen and incubated at room temperature for 10 min. After Glycosil® (20 mg/mL) was dissolved in degassed water for 30 min incubation at 37 °C with regularly vortexing every 10 min for the complete dissolution, the various volumes of Glycosil®, depending on the concentration, were mixed with the fibroblasts suspended in the neutralized collagen. The pre-gel solution with fibroblasts were incubated for 45 min at 37 °C to form the gel and encapsulate the fibroblasts within HCM hydrogel. Then, the complete DMEM media were added on the top of fibroblasts containing HCM hydrogel and incubated at 37 °C with 5% CO2 for 2 days. After 2 days or 7 days of culture, the viability of the fibroblasts in the HCM hydrogels was examined using live/dead cell staining. After removing the culture medium, cells in hydrogels were washed with 1× DPBS three times and incubated with the mixture of Calcein-AM (2 μM) to detect live cells and EtDH-1 (4 μM) to detect dead cells in HEPES-based live cell imaging solution (Thermo Fisher, Waltham, MA) for 40 min. Cells were imaged with z-stack imaging to detect Calcein-AM stained live cells (ex. 495 nm) and EtDH-1 stained dead cells (ex. 535 nm) using a Zeiss LSM 880 confocal microscope with a EC Plan-Neofluar 10× objective (Carl Zeiss Microscopy, LLC, White Plains, NY). The images were analyzed to evaluate fibroblasts viability via

cell counting using Fiji, ImageJ software and were plotted as 3D view to evaluate the fibroblasts behavior within Hydrogel using Volocity software.

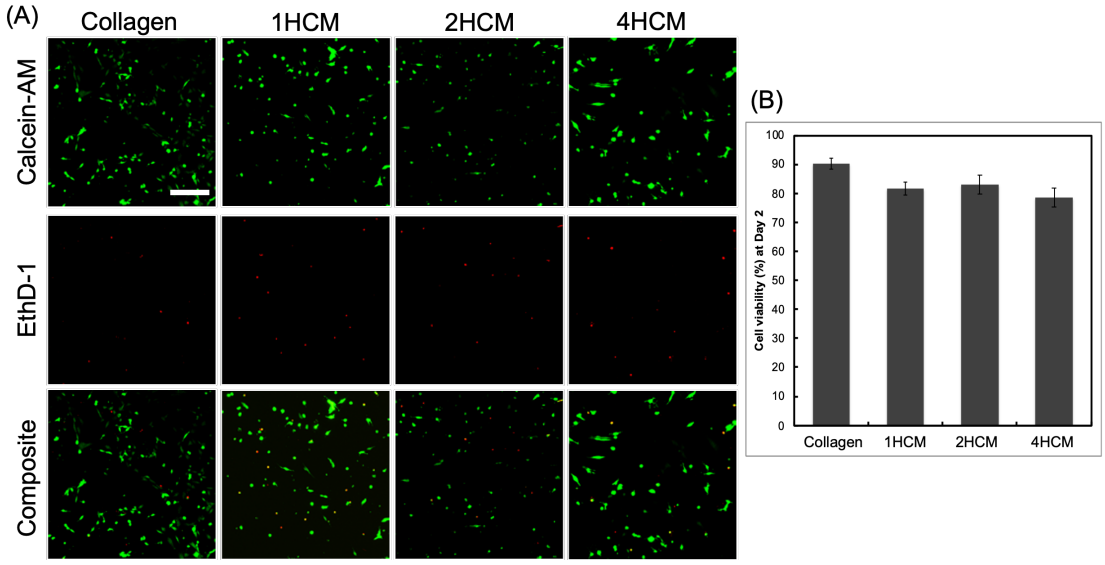

Figure 2.9. Live and dead staining of NIH3T3 3D-cultured in collagen hydrogel with a varying hyaluronic acid amounts. (A) Representative confocal image of live (Green) and dead (Red) stained fibroblasts cultured in the hydrogel for 2 days. Scale bar is 200 µm (B) Confocal Image quantitative analysis using cell count for live and dead cells to determine cell viability for 2 days culture. Collagen = HA (0 mg/mL) + Collagen (4 mg/mL), 1HCM = HA (1 mg/mL) + Collagen (4 mg/mL), 2HCM = HA (2 mg/mL) + Collagen (4 mg/mL), 4HCM = HA (1 mg/mL) + Collagen (4 mg/mL).

In order to identify appropriate formulation conditions for HA-collagen matrices (HCM), the HA-SH (Glycosil®) concentration in HCM was varied in order to maximize the viability of murine NIH3T3 fibroblasts cultured in HCM. After 2 days of culture, the calcein-AM stained live cells (green) and ethidium homodimer stained dead cells (red) were analyzed to quantify cell viability (Figure 2.9). Incorporation of various concentrations of HA-SH (1, 2, and 4 mg/mL) in the collagen hydrogel (4 mg/mL) did not cause significant changes to fibroblast viability, with fibroblast populations

exhibiting similar percentages of live cells in HA-collagen (1HCM = 81.7%, 2HCM = 82.9%, and 4HCM = 78.6%) as compared to collagen-only hydrogels (90.2%). Based on these results, I defined the mixture of HA-SH (2 mg/mL) and collagen (4 mg/mL) as the final HCM formulation.

Furthermore, after 7 days of 3D culture, fibroblasts cultured in HCM hydrogels

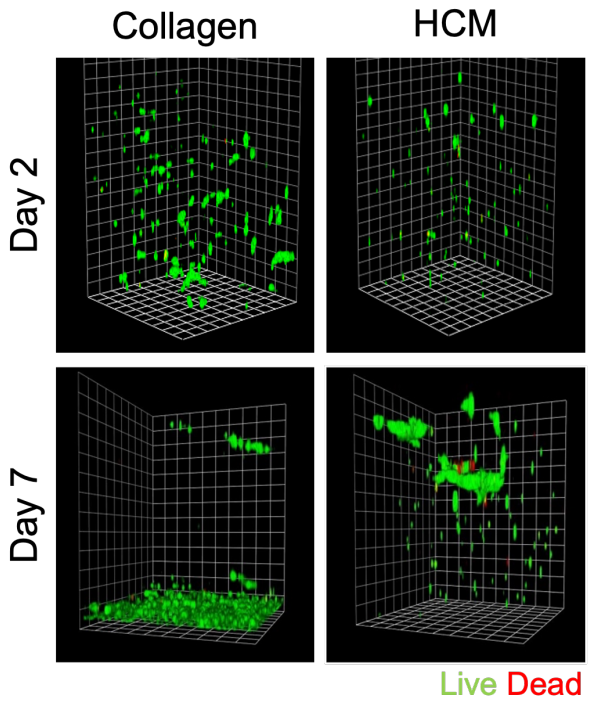

Figure 2.10. 3D plot of the z-stacked confocal microscopic images for Calcein-AM (Live) and Ethidium homodimer (dead) stained fibroblasts cultured in collagen hydrogel or HCM hydrogel for 2 days or 7 days. Each unit is 85.35 μm.

remained dispersed throughout the hydrogels, whereas cells in the collagen-only hydrogel had relocated entirely to the bottom side (Figure 2.10). This behavior demonstrated that the local microenvironment caused a significant difference in cellular migratory behavior.

2.9 GAHCM formulation

Based on the studies in sections 2.5-2.8, GAHCM formulation was finalized as the combination of polyplex with N:P = 8 (20 μg/mL of pDNA) and HCM (Collagen = 4 mg/mL and Glycosil® = 2 mg/mL). As described in section 2.5, equal volumes of plasmid DNA and PEI/heated CF-CMP-PEI solutions in 20 mM HEPES (pH 6.0) were mixed to prepare polyplexes (N:P = 8, 20 μg/mL of pDNA), and the polyplexes were lyophilized with 20 mM sucrose. The lyophilized polyplexes were mixed into neutralized collagen (8 mg/mL) which was prepared by mixing with acidic solubilized collagen (10 mg/mL), 10% total volume of 10× DPBS and 10% total volume of 0.1 N NaOH. Then, the polyplex and collagen mixture was incubated at 4 °C for 2 h for CMP hybridization with collagen. Fibroblasts (100,000 cells/mL) suspended in 1× DPBS were added into the polyplex/neutralized collagen mixture, and this solution was incubated at room temperature for 10 min. Next, Glycosil® or 1× DPBS were added into the fibroblast containing polyplex and collagen mixture to allow polyplex loaded HCM formation (GAHCM). After gelation for 45 min incubation at 37 °C, GAHCM was incubated in complete DMEM at 37 °C with 5% CO2 for 7 days. The culture medium was collected and replaced with the fresh culture medium every two days to detect the gene expression.

REFERENCES

1. Urello MA, Kiick KL, Sullivan MO. ECM turnover-stimulated gene delivery through collagen-mimetic peptide-plasmid integration in collagen. Acta Biomater. 2017;62:167-78. Epub 2017/09/04. doi: 10.1016/j.actbio.2017.08.038. PubMed PMID: 28865990; PMCID: PMC5654588.

2. Urello MA, Kiick KL, Sullivan MO. Integration of growth factor gene delivery with collagen-triggered wound repair cascades using collagen-mimetic peptides. Bioeng Transl Med. 2016;1(2):207-19. Epub 2016/12/17. doi: 10.1002/btm2.10037. PubMed PMID: 27981245; PMCID: PMC5125401.

3. Urello MA, Kiick KL, Sullivan MO. A CMP-based method for tunable, cell-mediated gene delivery from collagen scaffolds. J Mater Chem B. 2014;2(46):8174-85. Epub 2014/12/14. doi: 10.1039/c4tb01435a. PubMed PMID: 32262095.

4. Thapa RK, Margolis DJ, Kiick KL, Sullivan MO. Enhanced wound healing via collagen-turnover-driven transfer of PDGF-BB gene in a murine wound model. ACS Appl Bio Mater. 2020;3(6):3500-17. Epub 2020/07/14. doi: 10.1021/acsabm.9b01147. PubMed PMID: 32656505; PMCID: PMC7351314.

5. Choi JL, Tan JK, Sellers DL, Wei H, Horner PJ, Pun SH. Guanidinylated block copolymers for gene transfer: A comparison with amine-based materials for in vitro and in vivo gene transfer efficiency. Biomaterials. 2015;54:87-96. Epub 2015/04/25. doi: 10.1016/j.biomaterials.2015.03.008. PubMed PMID: 25907042; PMCID: PMC4409668.

Chapter 3

MODIFIED HYALURONIC ACID-COLLAGEN MATRICES TRIGGER EFFICIENT GENE TRANSFER AND PROHEALING BEHAVIOR IN FIBROBLASTS FOR IMPROVED WOUND REPAIR

Growth factor therapy has demonstrated great promise for chronic wound repair, but controlling growth factor activity and cell phenotype over desired time frames remains a critical challenge. In this study, I developed a gene-activated hyaluronic acid-collagen matrix (GAHCM) comprising DNA/polyethylenimine (PEI) polyplexes retained on hyaluronic acid (HA)-collagen hydrogels using collagen mimetic peptides (CMPs). I hypothesized that manipulating both the number of CMP-collagen tethers and the ECM composition would provide a powerful strategy to control growth factor gene transfer kinetics while regulating cell behavior, resulting in enhanced growth factor activity for wound repair. I observed that polyplexes with 50% CMP-modified PEI (50 CP) showed enhanced retention of polyplexes in HCM hydrogels by 2.7-fold as compared to non-CMP modified polyplexes. Moreover, the incorporation of HA in the hydrogel promoted a significant increase in gene transfection efficiency based upon analysis of Gaussia luciferase (GLuc) reporter gene expression, and gene expression could be attenuated by blocking HA-CD44 signaling. Furthermore, when fibroblasts were exposed to vascular endothelial growth factor-A (VEGF-A)-GAHCM, the 50 CP matrix facilitated sustained VEGF-A production for up to 7 days, with maximal expression at day 5. Application of these VEGF-A-50 CP samples stimulated prolonged pro-healing responses, including the TGF-β1-induced myofibroblast-like phenotypes and enhanced closure of murine splinted wounds. Overall, these findings demonstrate the use of ECM-based materials to stimulate efficient gene transfer and regulate cellular phenotype, resulting in improved control of growth factor activity for wound repair.

GAHCM have significant potential to overcome key challenges in growth factor therapy for regenerative medicine.

3.1 Introduction

The management of wounds is a prolonged challenge to the global healthcare system that is associated with annual healthcare costs of $50 billion for nonhealing wounds, $12 billion for scars from surgical incisions and trauma, and $7.5 billion for burns (1-3). While treatment options including traditional wound dressings are available (4), these methods often do not provide adequate healing, and more effective ways to manage wounds over reasonable time frames are necessary to overcome the societal and economic burdens of inadequate wound repair.

Growth factor application in the wound milieu has emerged as a promising strategy to mediate the healing response. The wound healing process is a complex orchestrated effort of multiple types of cells including fibroblasts, endothelial cells, keratinocytes, and leukocytes that utilize extracellular matrix (ECM) components and soluble mediators such as growth factors to regulate migration, proliferation, and differentiation in a timely and sequential manner (5). For example, the vascular endothelial growth factor (VEGF) protein family not only induces endothelial cell proliferation and migration leading to blood vessel formation in later-stage wound repair, but also promotes fibroblast proliferation, migration, and myofibroblast differentiation over the proliferative phase of wound healing (6-10). Topical treatments to extend growth factor activity over appropriate time frames offer advantages for improving wound repair, but clinical studies to date have demonstrated that the short half-life and instability of recombinant growth factors in the wound environment has limited the success of existing formulations owing to the need for high doses, corresponding off-target side effects, and modest clinical benefits (11, 12).

Two key challenges in growth factor therapy are the need for better control of growth factor delivery kinetics, in alignment with the wound healing process, and the need to provide an appropriate microenvironment for cells to maximize growth factor

signaling. Over the past ten years, biomaterials have emerged as both a delivery vehicle and a cell adhesion scaffold able to enhance growth factor stability and activity while promoting cell recruitment and differentiation (13-17). Due to their biochemical and physical similarity to tissues, ECM-mimicking materials including collagen, gelatin, and fibrin have exhibited especially promising potential to serve as a reservoir for growth factors and enable sustained growth factor delivery, activity, and cellular responses throughout the healing process (18-24). Meanwhile, gene activated matrix (GAM) approaches enable entrapment of genes for protection from protein-rich conditions like those in the wound bed. GAMs deliver the entrapped genes to infiltrating cells through diffusion and/or matrix degradation, resulting in localized and sustained transgene expression (25, 26). In fact, the use of GAM approaches has enabled growth factor gene expression to be sustained for 2 weeks in experimental wound models, with growth factor healing benefits occurring at orders-of-magnitude dose reductions as compared to topically administered growth factors (27-29).

Our groups previously developed biomaterials that further leveraged the ECM for gene delivery by harnessing the affinity of collagen mimetic peptides (CMPs) for collagen. CMPs were used as tethers to retain gene nanocarriers in collagen-based hydrogels. CMP-triggered gene delivery sustained gene expression by improving the availability of the DNA complex and controlling the expression of the gene on cellular demand (30-33). Collagen degradation is natively controlled by matrix metalloproteinases (MMPs), which are expressed during tissue remodeling processes including those involved in wound healing and various disease states (34, 35). Degraded collagen is internalized into cells through α2β1 integrin-mediated phagocytosis or clathrin-dependent endocytosis driven by Endo-180 or uPARAP (36-39). I proved that when CMP-polyplex-modified collagen hydrogels were degraded by cell-secreted MMPs, the polyplexes remained bound to the released collagen fragments, facilitating polyplex internalization and gene transfection (30-32). In order to promote cellular recruitment for wound healing, I also have incorporated fibrin into CMP-modified collagen hydrogels for PDGF-BB gene delivery, showing that these materials increased

PDGF gene expression by 30% in vitro, and improved wound closure by 19% after 9 days in vivo in comparison to wounds treated with non CMP-modified polyplex containing materials (33). These studies suggested that growth factor gene delivery and ECM signaling together may provide synergistic benefits that enhance the wound healing process.

Hyaluronic acid (HA) has been extensively utilized in wound healing to accelerate wound repair, decrease fibrosis, and improve the quality of healing by modulating inflammation, cellular recruitment, and angiogenesis (40, 41). The application of commercially available HA (IALUSET®) in clinical studies resulted in promising wound healing effects in patients with acute wounds (42), pressure ulcers (43), and venous leg ulcers (44). HA activates a variety of cells involved in wound healing, including fibroblasts, endothelial cells, and macrophages via interaction with the HA-specific receptors CD44, RHAMM, TLR-4, and LYVE-1 (45, 46). For example, HA fragments are internalized via interactions with CD44 receptors, enabling regulation of inflammation (as well as fibroblast proliferation and migration) during the wound healing process. In addition, HA-CD44 interactions stimulate transforming growth factor-β (TGF-β)-mediated differentiation of fibroblasts to myofibroblasts, critical for wound healing because of myofibroblast-mediated deposition of ECM components (47, 48). However, despite all of their promising wound healing benefits, commercially available HA-based wound dressings still present some limitations in cell adhesion, cell proliferation, and mechanical properties, necessitating further manipulation of HA-based materials to enable better healing outcomes (49, 50).

In this study, I developed multi-functional biomaterials combining HA matrix with CMP polyplex-modified collagen. Our new gene activated HCM (GAHCM) matrices are designed to overcome the limitations of HA matrix and improve growth factor delivery by leveraging collagen to enhance cell adhesion and proliferation while also stimulating growth factor gene transfer. The overall goal of this study was to demonstrate the advantages of the GAHCM on both the efficiency of gene transfer for growth factor production and its capacity to drive pro-healing behavior in fibroblasts

for wound repair. Due to the versatile roles of VEGF-A during the wound healing process, and in particular, its effect on fibroblasts for inducing collagen deposition and epithelialization via myofibroblast differentiation, plasmid DNA encoding for VEGF-A was used in this study. Herein, I demonstrate that GAHCM increased the efficiency and duration of VEGF-A production via CMP linkage to the collagen-HA matrix, while engineering the cellular microenvironment to mediate pro-healing myofibroblast-like phenotypic change and trigger complete wound closure. Our findings suggest the great potential for GAHCM as a treatment option to overcome the current challenges in growth factor therapy for wound healing, via control over the duration of growth factor expression and maximization of growth factor stimulated pro-healing cellular responses.

3.2 Materials and Methods

3.2.1 Materials

Type I bovine collagen (10 mg/mL) and Glycosil® were obtained from Advanced BioMatrix (San Diego, CA). pCMV3-VEGF-A plasmids were acquired from Sino Biological. Following the manufacturer's protocols, pCMV3-VEGF-A plasmids were amplified in MAX Efficiency™ DH5α competent Escherichia coli (Thermo Fisher, Waltham, MA) and purified using a Qiagen Maxiprep Kit (Germantown, MD). The Mouse VEGF-A Quantikine enzyme-linked immunosorbent assay (ELISA) kit and Mouse TGF-ß1 DuoSet ELISA kit were obtained from R&D Systems (Minneapolis, MN). Murine recombinant VEGF-A was acquired from Pepro Tech. (Cranbury, NJ). Rat IgG2b-CD44 monoclonal antibody (IM7) was purchased from Thermo Fisher (Waltham, MA). Mouse IgG2a monoclonal α-SMA-FITC antibody and mouse IgG2a-FITC antibody were obtained from Sigma-Aldrich (St. Louis, MO).

3.2.2 Animals

BALB/cJ mice (8-week-old, male) were procured from Jackson Laboratory (Bar Harbor, ME, USA). All experiments were performed in accordance with protocols and guidelines approved and established by the University of Delaware's Institutional Animal Care and Use Committee (IACUC).

3.2.3 In vitro 3D cell culture of fibroblasts in HCM hydrogel

The HCM hydrogels were formed by self-assembly of bovine collagen type I (Fibricol (4 mg/mL)), driven by pH, temperature, and ionic strength; and disulfide bond formation in thiolated-HA (Glycosil®) at various concentrations (0, 1, 2, and 4 mg/mL). The collagen was neutralized with 10× DPBS and 0.1 N NaOH. Fibroblasts suspended in 1× DPBS (100,000 cells/mL) were added to the neutralized collagen and incubated at room temperature for 10 min. After dissolving Glycosil® in degassed water at 37 °C, Glycosil® was mixed with the fibroblasts suspended in the neutralized collagen. The hydrogels were allowed to form and encapsulate the fibroblasts for 45 min at 37 °C. The hydrogels were incubated in complete DMEM at 37 °C with 5% CO_2 for 2 days. After 2 days of culture, the viability of the fibroblasts in the HCM hydrogels was assessed using live/dead cell staining. Cells in hydrogels were incubated with Calcein-AM (2 μM) and EtDH-1 (4 μM) in HEPES-based live cell imaging solution (Thermo Fisher, Waltham, MA) for 40 min. Cells were imaged with z-stack imaging to detect Calcein-AM stained live cells (ex. 495 nm) and EtDH-1 stained dead cells (ex. 535 nm) using a Zeiss LSM 880 confocal microscope with a EC Plan-Neofluar 10× objective (Carl Zeiss Microscopy, LLC, White Plains, NY). The images were analyzed to evaluate cell viability via cell counting using Fiji, ImageJ software.

3.2.4 Polyplex distribution and stability in HCM hydrogel

As described in chapter 2.2-2.4, CMP-PEI was prepared via covalent linkage between CMP and PEI using a sulfo-SMCC bifunctional linker. CMP-PEI was further analyzed for its propensity to undergo triple helical assembly at 4 ºC and disassembly at 65 ºC via circular dichroism spectra measurements from 215 to 235 nm. The CMP-PEI was mixed with PEI at various percentages, and the CMP-PEI/PEI solution was mixed with GLuc plasmid in 20 mM HEPES, pH 6 to prepare GLuc/PEI (Dh = 118 nm), GLuc/20% CMP modified PEI (20 CP) (Dh = 115 nm), or GLuc/50% CMP modified PEI (50 CP) (Dh = 140 nm) complexes, defined as PEI, 20 CP, or 50 CP polyplexes (N:P = 8, 20 μg/mL of GLuc). After the polyplexes were lyophilized with 20 mM sucrose, the lyophilized polyplexes were mixed into neutralized collagen and incubated at 4 °C for 2 h before adding Glycosil® to allow gelation to occur via a 45 min incubation at 37 °C. To visualize the plasmid within the gel, the gel was incubated with YoYo-3 (1:100) overnight at 37 °C and then rinsed with 1× DPBS overnight at 37 °C. YoYo-3 stained GLuc plasmid (λex 612 nm), carboxyfluorescein-labeled CMP-PEI (CF-CMP-PEI, λex 489 nm), and the autofluorescence of collagen fibers (reflected light at 405 nm) in HCM hydrogels were visualized using a Zeiss LSM 880 confocal microscope with a C-Apochromat 40× water objective. Volocity Imaging Software (Quorum Tech. Inc., Canada) was utilized to create a 3D image plot, and to perform image analysis and quantification of colocalization. The locations of YoYo-3 stained DNA and CFCMP-PEI were determined from measurement statistics associated with individual voxel intensities. The fraction of CFCMP-PEI (Magenta) that colocalized with the YoYo-3 stained GLuc (Cyan) was analyzed by calculation of the Mander's coefficient (M2), which represents the sum of the colocalized magenta intensity divided by the sum of the total cyan intensity. To distinguish signal from background, minimum

values for magenta and cyan intensities were automatically determined using Costes' auto-threshold method. Then, the sum of fluorescence intensity of CFCMP-PEI and YoYo-3 per volume (μm3) were calculated with the threshold.

3.2.5 GAHCM 3D-transfection studies

Fibroblast transfection in 3D culture was evaluated using GLuc encoding GAHCM. The lyophilized GLuc encoding polyplexes (20 μg/mL of pGLuc) with PEI, 20% CMP modified PEI (20 CP), or 50% CMP modified PEI (50 CP) were mixed into neutralized collagen and incubated at 4 °C for 2 h. Fibroblasts (100,000 cells/mL) suspended in 1× DPBS were added into the polyplex/neutralized collagen mixture, and this solution was incubated at room temperature for 10 min. Next, Glycosil® was mixed into the fibroblast/neutralized collagen. After gelation at 37 °C for 45 min, GAHCM was incubated in complete DMEM at 37 °C with 5% CO2 for 7 days. The culture medium was collected and replaced with the fresh culture medium every two days. Gene expression in the collected medium was evaluated by quantifying the luminescence using a Gaussia Luciferase Assay (Targeting Systems; El Cajon, CA), according to the manufacturer's protocol. To understand the influence of HA and cell interaction on gene transfection, the gene expression of fibroblasts cultured in GAHCM was evaluated after blocking the CD44 receptor for hyaluronic acid. First, the expression of CD44 receptors on fibroblasts cultured in collagen or HCM was evaluated using immunostaining for CD44. After 2 days of culture in collagen or HCM, fibroblasts were fixed with 4% paraformaldehyde for 30 minutes, permeabilized with 0.2% Triton X-100 for 45 min, and blocked with 3% BSA in PBS at room temperature overnight. Samples were incubated for 1 day at room temperature with rat CD44 monoclonal antibody (IM7) (1:50) in 1% BSA in PBS at room temperature with shaking. After incubation, the gel

samples were rinsed, and incubated with goat anti-rat AlexaFluor 488 (1:250, Life Technologies), Phalloidin-568 (1:100; Life Technologies), and the nuclear stain Hoechst 33258 (1:500; Life Technologies) for 2 days at room temperature with shaking. After rinsing by incubation in 3% BSA in 0.05% Tween-20 in PBS for 1 day, cells were visualized by z-stack imaging using a Zeiss LSM 880 confocal microscope with a 10× objective. Fibroblasts were incubated with rat CD44 monoclonal antibody (IM7) or rat IgG control antibody (10 μg/mL) at 37 °C with 5% CO2 for 12 hr. Then, fibroblasts treated with either IM7 antibody or IgG control antibody were encapsulated and cultured in GAHCM as described above.

3.2.6 VEGF-GAHCM 3D-transfection studies

Fibroblast transfection was examined using a GAHCM encoding for VEGF-A (VEGF-GAHCM) with PEI, 20 CP, or 50 CP. HCM without polyplexes as well as recombinant VEGF containing HCM (rVEGF) were used as controls. Fibroblasts cultured in VEGF-GAHCM were prepared separately for each time interval (1, 3, 5, and 7 days), and were incubated in complete DMEM at 37 °C with 5% CO2 for 7 days. The culture medium was collected and replaced with fresh medium every two days. VEGF expression by the fibroblasts were evaluated using ELISA assays (described below). Separately, the fibroblast viability in VEGF-GAHCM was determined at 2, 4, and 6 days using an MTS assay, following the manufacturer's procedure.

To evaluate fibroblast distribution in VEGF-GAHCM after culture in the hydrogels for various time periods, fibroblasts were fixed, permeabilized, and blocked as described in section 3.2.5. Samples were subsequently incubated for 2 days with the nuclear stain Hoechst 33258 (1:500) at room temperature with shaking. After rinsing, cells were visualized as a z-stack using a Zeiss LSM 880 confocal microscope with 10×

objective. Using a z-stack of full height in VEGF-GAHCM, 30 μm 'sections' of the z-stack from the top, center, and bottom were analyzed for cell counts using Fiji ImageJ Software.

3.2.7 Quantification of expressed growth factors via ELISA

VEGF-A expression in fibroblasts cultured in VEGF-GAHCM was examined by ELISA. Briefly, the culture medium was collected, and fibroblasts within the VEGF-GAHCM were washed three times with 1× DPBS after 1, 3, 5, and 7 days of culture. Then, fibroblasts within the VEGF-GAHCM were homogenized in lysis buffer (0.1 M Tris-HCl, 2mM EDTA, 0.1% Triton X-100) using disposable pellet pestles with a motor mixer. The lysate was centrifuged at 12,000 rpm at 4 °C for 5 min to collect the supernatant. The amount of VEGF-A in the homogenized supernatant and the collected medium were quantified via Mouse VEGF-A Quantikine ELISA kits following the procedure described in the manual. In addition, after acid activation of latent TGF-β1 in the collected medium to the immunoreactive form, the amount of TGF-β1 was quantified via mouse TGF-ß1 DuoSet ELISA following the manufacturer's manual. The amounts of VEGF-A/TGF-β1 were normalized to the total fibroblast number per sample, which was measured using tryptophan blue cell counting after the collagenase digestion of each sample.

3.2.8 α-SMA immunostaining and image analysis

After 3 or 7 days of culture in VEGF-GAHCM, fibroblasts were fixed, permeabilized, and blocked as described in section 3.2.5. Samples were incubated for 1 day with mouse anti-goat IgG (0.01 mg/mL, Sigma-Aldrich) at room temperature with shaking, rinsed in 3% BSA in 0.05% Tween-20 in PBS, and incubated with α-SMA-

FITC antibody or mouse IgG2a-FITC control antibody (1:100), Phalloidin-568 (1:100), and the nuclear stain Hoechst 33258 (1:500) for 2 days at room temperature with shaking. After rinsing, cells were visualized as a z-stack using a Zeiss LSM 880 confocal microscope with 20× objective as decribed in previous literature for α-SMA detection of cells cultured in hydrogel (51-55). Fiji ImageJ Software was utilized for image plots of the maximum intensity of z-projections, image analysis, and quantification of colocalization. To distinguish signal from background, minimum values for α-SMA (green) and F-actin (red) intensities were manually determined as a threshold by Fiji ImageJ software using JACoP plugins for each image. In addition, α-SMA expression was quantified using the sum of fluorescent intensity of α-SMA normalized to the in sum of fluorescent intensity of F-actin with the same threshold setting for each channel to avoid background signal.

3.2.9 Murine splinted excisional wound healing studies and α-SMA immunostaining

The murine splinted excisional wound healing studies were performed in 8-week-old BALB/cJ mice. The splint was used to prohibit murine physical wound contraction via the panniculus carnosus and loose attachment of the murine dermis, the primarily wound healing process used by mice, and to thereby employ a model better able to mimic the human wound healing processes that depend on granulation tissue formation and myofibroblast wound contraction via reorganization of granulation tissue, epithelialization, cellular proliferation, and angiogenesis (56-58). The splint was prepared using a silicone sheet, which was cut into disks (O.D. = 14 mm and I.D. = 6.35 mm) and sterilized by rinsing in 70% ethanol. OpSite wound dressing was cut into a similarly sized circle with a 14 mm diameter. Mice were anesthetized using isoflurane

and the fur on the back of mouse was removed using an electric razor. The area was sterilized with 4% chlorhexidine and isopropanol using a cotton tipped applicator. One wound per mouse was created at the mouse's midline at the level of the shoulders using a biopsy punch (D = 5 mm), as in prior published studies (56, 58). Then, the wound was treated with by application of 35 μL of saline, HCM gel with/without rVEGF (1 μg per wound), or VEGF-GAHCM with/without CMP tethering (200 μg/mL of pVEGF per wound, PEI or 50 CP polyplexes). To secure the splint, Krazy Glue was added dropwise on the outside edge of the silicone ring, and the splint was attached onto the top of the wound such that the inside orifice of the silicon ring encircled the wound. OpSite wound dressing was subsequently applied on the top side of the attached silicone ring. 6 to 8 interrupted sutures (5-0 Vicryl Suture with Cutting Needle, Ethicon Inc.) were placed around the outer edge of the O-ring to further secure the splint. Splints were maintained on the mice until Day 7, and then the splints were removed, as mice typically self-remove the splints between day 6 and 7, resulting in the secondary damage and misleading results (58). Body weights of the mice and photographs of the wound bed were recorded at days 0, 1, 3, 7, 10, and 14. Wound closure was calculated from photos obtained from 6 or 12 mice per group at each time point. As in prior sutdies (57, 59), the area of the remaining open wound was measured manually by the author using Fiji ImageJ software, and the area of the wound at various time points was compared to the wound area at day 0 and expressed as a percentage of its original size for wound closure analysis. After euthanizing mice at days 7 or 14, the wound skin tissue was collected using surgical scissors and fixed in 2% paraformaldehyde. For immunohistology analysis, the tissues were embedded in OCT for freezing and cut into 10 μm sections. Tissue sections were stained for α-SMA and nuclei as described in section 2.8. Tissue

section slides were incubated for 2 h with mouse anti-goat IgG (0.01 mg/mL, Sigma-Aldrich) at room temperature. After rinsing with PBS, tissue section slides were incubated with α-SMA-FITC antibody or mouse IgG2a-FITC control antibody (1:100), and the nuclear stain Hoechst 33258 (1:500) was applied overnight at 4 ºC. After rinsing with PBS, the tissue sections were mounted with a ProLongTM Gold Antifade mountant. The stained entire tissue sections were visualized using a tile function via Zeiss Axio Observer 7 inverted microscope with 10× objective. An average of α-SMA expression was quantified using Fiji ImageJ analyses performed on 5 random non-overlapping images within the wound or within the normal skin of each tissue section sample, marked as white/pink boxes in Figure 3.17, with six samples per group. While the dimensions of the pink boxes delineating the expanded regions of the image appear different in the non-expanded (tiled) view, the sizes of the expanded areas assessed were identical. As a result of the difference in size of skin tissue sections, the tiled images have the widths of the macroscopic skin sections, which varied slightly between samples. Thus, to standardize these images to the same figure width in Figure 3.17, some of the tiled images had to be expanded. The average of the α-SMA expression measured within the wound was further normalized to the average of α-SMA expression within the normal skin, which has minimum level of α-SMA expression, for measuring relative expression between the groups.

The skin wound tissue sections after 14 days of treatment were additionally analyzed for collagen deposition in the healed wounds using a Leica SP8-MP confocal/multiphoton microscope to detect forward and reverse second harmonic generation (SHG) signals with a 20× water immersion HCX APO L (1.00 NA) objective. The SHG signals generated from the collagen fibers in the skin wound tissue sections

were detected using a HyD-RLD2 with an emission filter in the range of 435-485 nm for detection of the backward SHG and a photomultiplier tube (PMT) with an emission filter in the range of 417-477 nm for detection of the forward SHG at 910 nm with the maximum laser output. The ratio of forward/backward signal was determined using integrated density measurements within select regions of interest, applying the same threshold range for 3 images in each mouse skin wound tissue section, as described in (33, 60).

3.2.10 Statistical Analysis

Unless indicated, all experimental data were expressed as the mean ± standard deviation of the mean. The statistical significance was analyzed using Kaleidagraph 4.0 (Synergy software) and Origin (OriginLab Corporation). Sample groups were compared using either one-way or two-way analysis of variance (ANOVA) with a Tuckey's post-hoc test for multiple comparison with a significance of 0.05.

3.3 Results

3.3.1 Polyplex stability and distribution in GAHCM

To investigate whether the CMP-modified polyplexes were stably distributed and retained in the GAHCM, confocal microscopy imaging was used to analyze the location of CFCMP-PEI and YoYo-3 plasmid within GAHCM (Figure 3.1.(A)). The hydrogel matrix was visualized by the reflected or back-scattered light from collagen

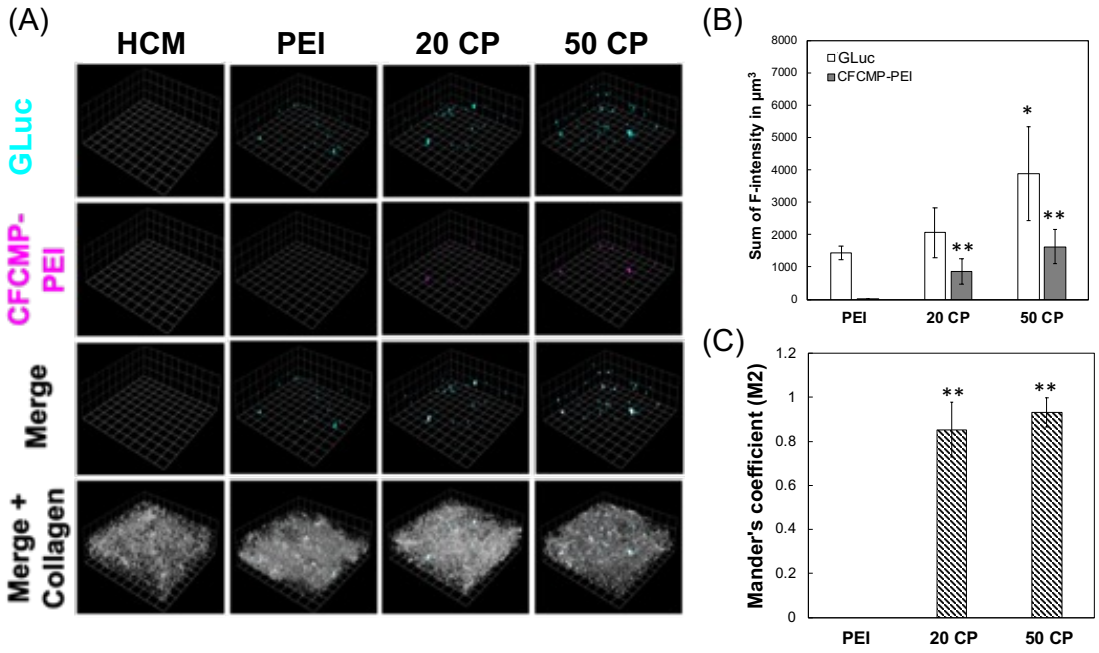

Figure 3.1. Polyplex distribution and stability in HCM hydrogel. (A) Representative confocal microscope images of fluorescently labeled polyplex (GLuc for Cyan and CFCMP-PEI for Margenta) and autofluorescence of collagen (Grey). 1 unit = 21.34 µm. (B) Image quantification for sum of fluorescent intensity of polyplex (GLuc for Blank and CFCMP-PEI for Grey) in HCM hydrogel. (C) Co-localization image analysis for stability of polyplex in ECM hydrogel. Mander's coefficient (M2) indicates CFCMP-PEI voxels overlap GLuc voxels, range from 0 (no co-localization) to 1 (complete co-localization). PEI: DNA/PEI complex, 20CP: 20% CMP modified DNA/PEI complex, 50CP: 50% CMP modified DNA/PEI complex. Each data point represents the mean ± standard deviation for total of 5 images. The statistically significant differences to PEI state *P<0.01 and **P<0.001.

fibers (61), and the colocalized signals of YoYo-3-plasmid and CFCMP-PEI were distributed throughout the GAHCM. Analyses comparing the sum of fluorescence intensity (F-intensity) per volume of YoYo-3 plasmid and CFCMP-PEI revealed that polyplexes with greater CMP modification (50% CMP modified polyplex, or 50 CP) presented 2.7-fold greater retention of polyplexes in GAHCM as compared to non-CMP modified polyplexes (Figure 3.1(B)). The sum of F-intensity per volume for 50

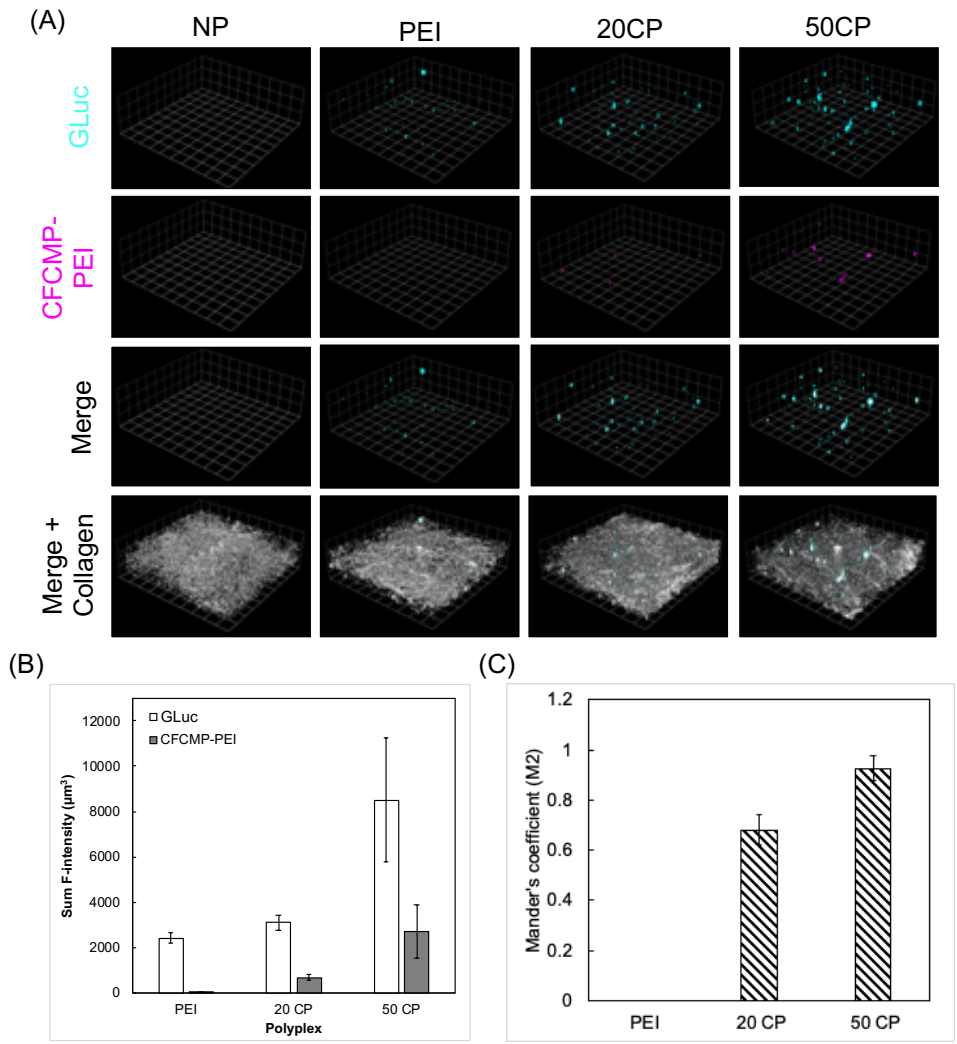

Figure 3.2. Polyplex distribution and stability in collagen hydrogel. (A) Representative confocal microscope images of fluorescently labeled polyplex (GLuc for Cyan and CFCMP-PEI for Margenta) and autofluorescence of collagen (Grey). 1 unit = 21.34 μm. (B) Image quantification for sum of fluorescent intensity of polyplex (GLuc for Blank and CFCMP-PEI for Grey) in collagen hydrogel. (C) Co-localization image analysis for stability of polyplex in collagen hydrogel. Mander's coefficient (M2) indicates CFCMP-PEI voxels overlap GLuc voxels, range from 0 (no co-localization) to 1 (complete co-localization). PEI: DNA/PEI complex, 20CP: 20% CMP modified DNA/PEI complex, 50CP: 50% CMP modified DNA/PEI complex. Each data point represents the mean ± standard deviation for total of 5 images.

CP was 2.5 times higher than the sum of F-intensity for 20% CMP modified polyplex

(20 CP). Moreover, the 50 CP polyplexes were retained to a greater extent in collagen-only hydrogels than the 20 CP or PEI polyplexes (Figure 3.2(B)). Thus, the greater retention of CMP-modified polyplexes in GAHCM was attributed to the ability of CMPs to strand invade with native collagen, which is in agreement with our previous studies showing the prolonged retention of CMP-modified polyplexes in both collagen and collagen-fibrin gel formulations (30, 33). In addition, analysis of the colocalization of CFCMP-PEI voxels overlapping the YoYo-3-plasmid voxels demonstrated an almost complete colocalization for 50 CP samples (0.93 ± 0.07) and less colocalization for 20 CP samples (0.68 ± 0.06) (Figure 3.2(C)) in collagen-only hydrogels. Meanwhile, GAHCM showed an almost complete colocalization of YoYo-3 plasmid and CFCMP-PEI for 50 CP samples (0.93 ± 0.07), but only slightly lower colocalization for 20 CP samples (0.85 ± 0.06) (Figure 3.1(C)), indicating that polyplexes with CMP modification were more intact within the GAHCM, as compared to collagen-only hydrogel.

3.3.2 Model gene transfer from GAHCM

The ability of the GAHCM to sustain and control transient gene expression over prolonged time periods was evaluated with NIH/3T3 fibroblasts due to the minimal variability of the response with these cell types. Gene expression by NIH/3T3 fibroblasts cultured in GAHCM or polyplexes in collagen hydrogel was monitored daily to determine the effects of CMPs on gene expression in the various samples (Figure 3.3(A)). Statistically significant increases in gene expression were observed for 50 CP polyplexes in collagen at day 5, 20 CP GAHCM at days 3, 5, and 7, and 50 CP GAHCM at days 3 and 5, as compared to the PEI polyplexes in collagen hydrogel (at a given

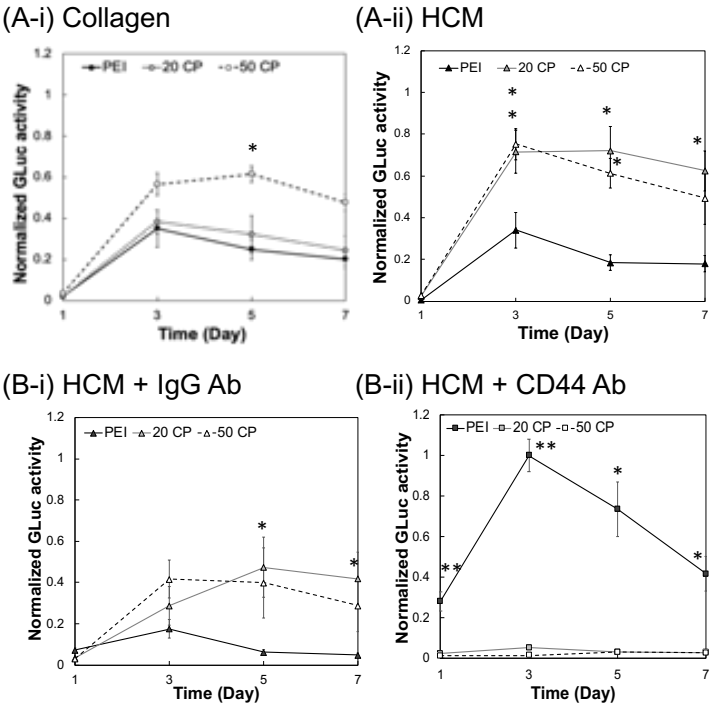

Figure 3.3. GLuc transfection of fibroblast 3D cultured in GAHCM. (A) Gaussia Luciferase expression of fibroblast cultured in GLuc encoding polyplex modified i) collagen (Circle) and ii) HCM (Triangle) hydrogel for 7 days. GLuc expression is normalized to the highest GLuc expression point, (A-ii) 50 CP at day 3. (B) Gaussia Luciferase expression of fibroblast cultured in GLuc encoding polyplex modified HCM hydrogel for 7 days with pre-treatment with i) IgG Rat antibody (Triangle) and ii) Anti-CD44 (IM7) Rat antibody (Square). GLuc expression is normalized to the highest GLuc expression point, (B-ii) PEI at day 3. PEI for Dark grey, 20CP for Grey, and 50CP for Blank. Each data point represents the mean ± standard error for n=5. The statistically significant differences to (A-i) PEI for A or (B-i) PEI for B at each time point state *P<0.05 and **P<0.0001

timepoint). Overall, CMP modification of the polyplexes enhanced gene expression in both polyplexes in collagen hydrogel and GAHCM, although CMP modification of polyplexes in the GAHCM further amplified this enhancement.

Based on our observation of enhanced gene transfer in the presence of HA, I hypothesized that HA-CD44 interactions might be stimulating gene transfer by CMP-

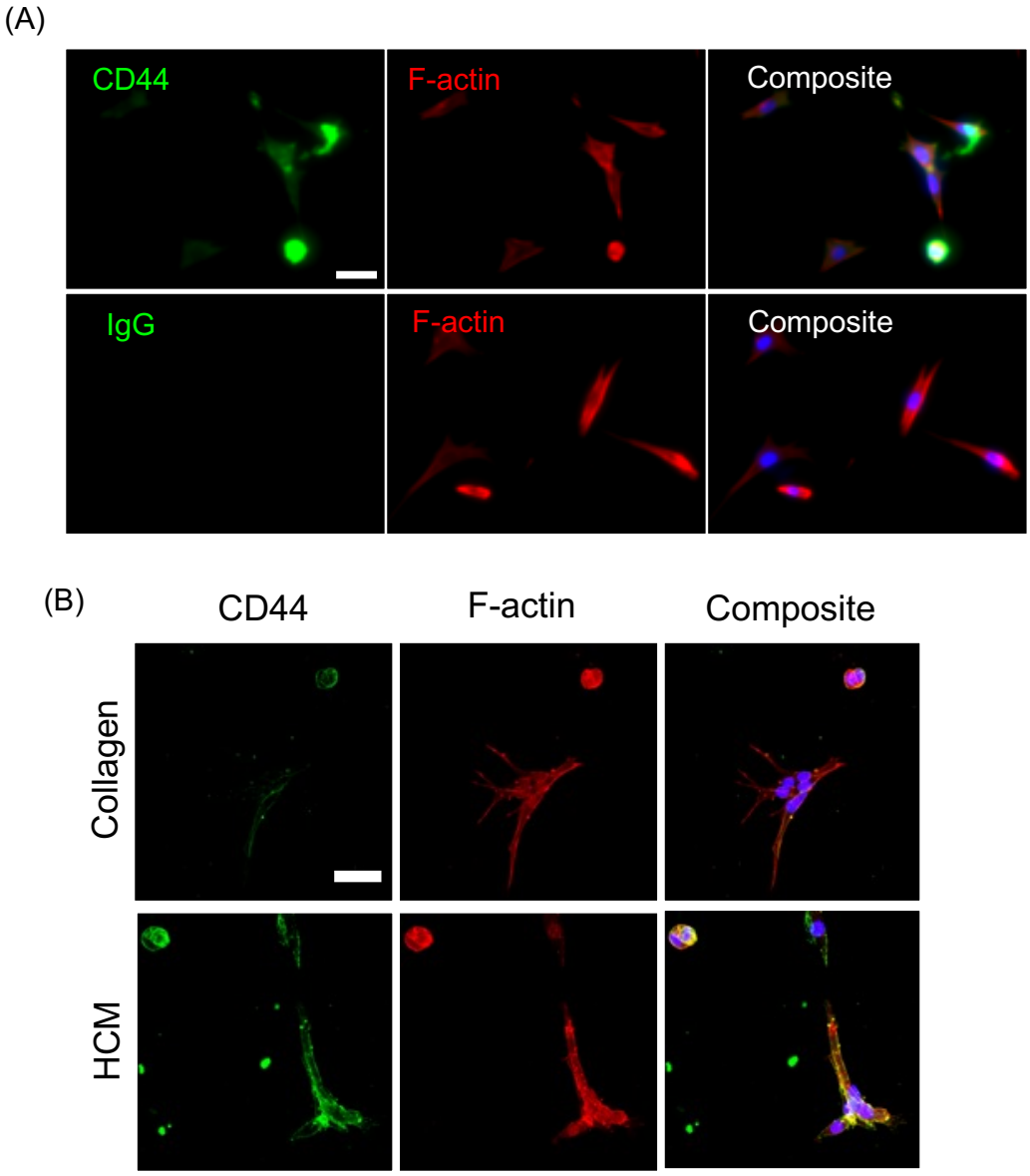

Figure 3.4. CD44 (IM7) immunostained NIH3T3 cells. (A) Representative fluorescent microscopic images of CD44 immunostained fibroblasts seeded on the tissue culture plate. (B) Representative confocal image of CD44 immunostained fibroblasts 3D cultured in collagen or HCM for 2 days. The scale bars are 40 μm. (Green - CD44/IgG control and Red - F-actin)

modified polyplexes in GAHCM. In order to evaluate HA-CD44 interactions in the HCM hydrogel, immunostaining of fibroblasts cultured in either collagen or HCM

hydrogel was conducted; these studies showed an enhancement of the CD44 signal on fibroblasts cultured in the HCM hydrogel (Figure 3.4). To investigate how HA-CD44 affected fibroblast transfection efficiency, fibroblasts were pre-treated with a CD44-blocking antibody to prevent the interaction between the CD44 receptor and the HCM hydrogel, prior to culture in the GAHCM. The trends for gene expression of the various GAHCM samples were similar with and without the addition of the IgG control antibody. In contrast, blocking the CD44 receptor in the fibroblasts resulted in highly significant reductions in gene expression of up to 10-fold for the 20 CP and 50 CP samples in GAHCM, as compared to the gene expression levels for 20 CP and 50 CP in IgG control GAHCM. However, the CD44-blocking antibody treatment induced a surprising increase in gene expression at all timepoints for fibroblasts growing in the PEI-containing GAHCM, with a 10-fold increase in gene expression at day 3 as compared to in the PEI-containing GAHCM treated with the IgG control antibody (Figure 3.3(B)).

3.3.3 VEGF gene transfer from GAHCM

Due to the crucial roles of VEGF in regulating angiogenesis, epithelization, and collagen deposition, sustained VEGF activity during wound healing is key for complete healing (62). Thus, I next sought to test the capacity of VEGF-A encoding GAHCM to induce VEGF production and signaling. VEGF expression by fibroblasts cultured in VEGF-A encoding GAHCM was measured using VEGF-A ELISA to evaluate the efficiency of GAHCM gene transfer. To accurately quantify and compare differences in VEGF expression within proliferating cells, VEGF levels were normalized by the total cell number at each time point. Both the total fibroblast count and the fibroblast viability at each timepoint showed that there were greater numbers of viable fibroblasts in the

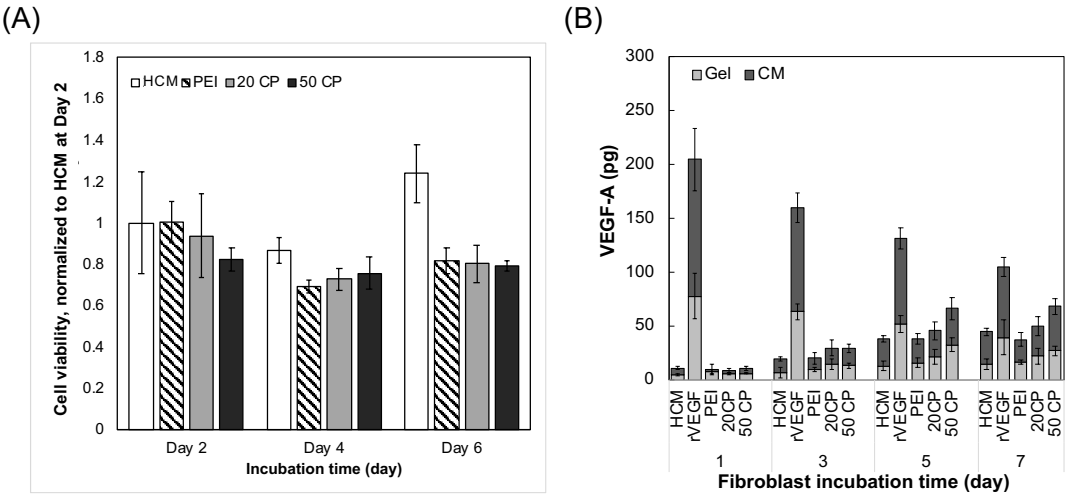

Figure 3.5. The bioactivity of expressed VEGF by NIH3T3 cultured in VEGF encoding GAHCM for 7 days. (A) The fibroblast viability after 2, 4, and 6 days of cultured in VEGF-GAECM is normalized to fibroblast cultured in HCM (HCM for Blank, PEI for Stripe, 20CP for Grey, and 50 CP for Dark Grey). Each data point represents the mean ± standard deviation for n=3. (B) VEGF-A expression (pg) of fibroblast using VEGF-A ELISA for 7 days. VEGF-A expression is measured from condition culture media (Dark Grey) and homogenized gel (Grey) Each data point represents the mean ± standard deviation for n=4.

HCM hydrogel and in the rVEGF-HCM hydrogel than in the VEGF-GAHCM hydrogel (Figure 3.5(A) & Figure 3.6(A)). VEGF levels detected in both the culture-conditioned media and in the hydrogel, however, indicated an overall increase in VEGF expression by fibroblasts cultured for 7 days in the VEGF-GAHCM, especially with CMP-modification, and statistically significant increases were detected at days 5 and 7 in the 50 CP VEGF-GAHCM sample, as compared to fibroblasts cultured in HCM hydrogel (Figure 3.5(B) & Figure 3.7). In contrast, the amount of VEGF detected in the HCM hydrogels loaded with recombinant VEGF-A protein decreased over time in culture; only 11% of initial amount (1800 pg) remained

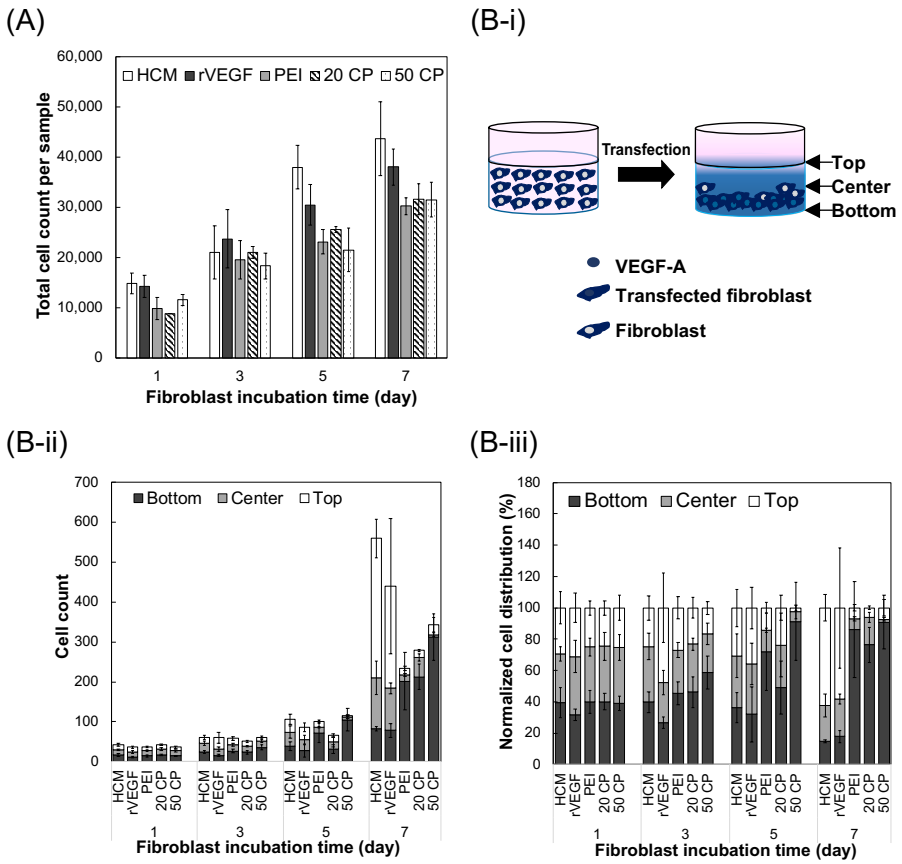

Figure 3.6. NIH3T3 cells distribution in VEGF encoding GAHCM for 7 days culture. (A) Fibroblast count per hydrogel using collagenase digestion of fibroblast cultured VEGF-GAHCM after 1, 3, 5, or 7 days of incubation (B-i) Schematic for fibroblast distribution and VEGF-A gradients within the hydrogel before and after transfection. (B-ii) Fibroblast count using confocal images of DAPI stained fibroblast cultured VEGF-GAHCM for 1, 3, 5, or 7 days at three different z-stack (30 μm) location (Top (Blank), Center (Grey), Bottom (Dark Grey)). (B-iii) Fibroblast distribution using (B-ii) normalized to total fibroblast count. Each data point represents the mean ± standard deviation for n=4.

after day 1, with further reductions to 5.5% at day 7. This result was attributed to the known instability and short half-life (30 min) of recombinant VEGF protein under physiological conditions (63, 64). The VEGF levels for cells growing in CMP-modified

VEGF-GAHCM, however, increased over the 7-day culture period, with statistically significant increases in VEGF levels in the 50 CP samples at days 5 and 7, when compared to PEI at the same timepoints. Taken together, similar to our observations of GLuc activity from GLuc-encoding GAHCM (Figure 3.3(A-ii)), the increased availability of CMP-modified polyplex and its strengthened interaction with the HCM

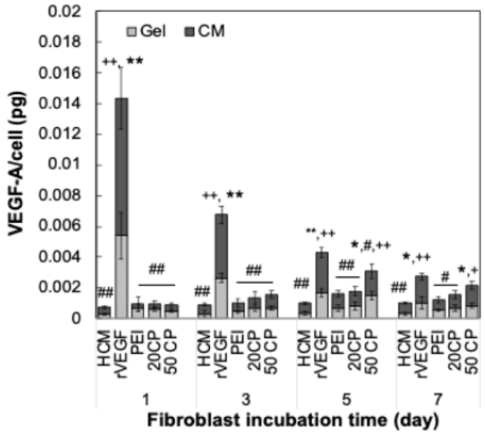

Figure 3.7. VEGF-A expression of NIH3T3 cultured in VEGF encoding GAHCM for 7 days. VEGF-A measurements from condition media (Dark grey) and homogenized gel (Grey) were normalized to total cell counts. Each data point represents the mean ± standard deviation for n=4. The statistically significant differences of total VEGF-A amounts per cell state +P<0.05 and ++P<0.001 compared to HCM, #P<0.05 and ##P<0.001 compared to rVEGF, and *P<0.05 and **P<0.001 compared to PEI.

hydrogel together stimulated sustained production of VEGF by the cells at least for 7 days, with maximized production at day 5.

I next sought to evaluate the distribution of fibroblasts within the VEGF-encoding GAHCM hydrogel; the distribution of non-transfected versus transfected fibroblasts was assessed by tracking the location of fibroblasts whose nuclei were labelled with Hoechst 33258. The schematic in Figure 3.6(B-i) illustrates the distribution of fibroblasts, transfected fibroblasts, and expressed VEGF-A in VEGF-

GAHCM. I expected the expressed VEGF-A to be concentrated away from the top of the VEGF-GAHCM where the culture media was replaced with fresh media every other day, and thus, that fibroblasts would migrate towards the bottom of the hydrogel, following the VEGF-A gradient. The locations of the cells over time were defined in 30 μm 'slices' based on z-stack imaging, with three 30 μm slices comprising the top, center, and bottom of the VEGF-GAHCM gel. Non-transfected fibroblasts in the HCM hydrogel or in the rVEGF-HCM hydrogel were dispersed uniformly in the z-direction of the gels over 5 days of culture, although fibroblasts migrated to the top of the HCM hydrogel by day 7 (Figure 3.6(B)). In contrast, the fibroblast distribution in VEGF-GAHCM showed a trend aligned with our expectations, with fibroblasts migrating toward the bottom of the hydrogel starting from day 3. Specifically, 60% of the fibroblasts were located at the bottom of the 50 CP VEGF-GAHCM at day 3, and 90% were located at the bottom at day 7.

3.3.4 VEGF-GAHCM-mediated myofibroblast-like phenotype

To evaluate the biological activities of both VEGF-A and CD44, myofibroblast-like phenotype was observed via immunocytochemical staining to detect α-smooth muscle actin (α-SMA). The expression of α-SMA also was quantified in fibroblasts cultured in the VEGF-GAHCM at day 3 and day 7 (Figure 3.8). At day 3, more intense α-SMA signals were observed for fibroblasts cultured in VEGF-GAHCM, in agreement with the α-SMA expression quantification analysis. Statistically significant differences in α-SMA expression were observed between fibroblasts cultured in PEI, 20 CP, and 50 CP VEGF-GAHCM versus the expression from fibroblasts cultured in the HCM hydrogel (Figure 3.8(A)&(B)). At day 7, α-SMA expression by fibroblasts cultured in 50 CP was still present at significantly higher levels than the levels detected in

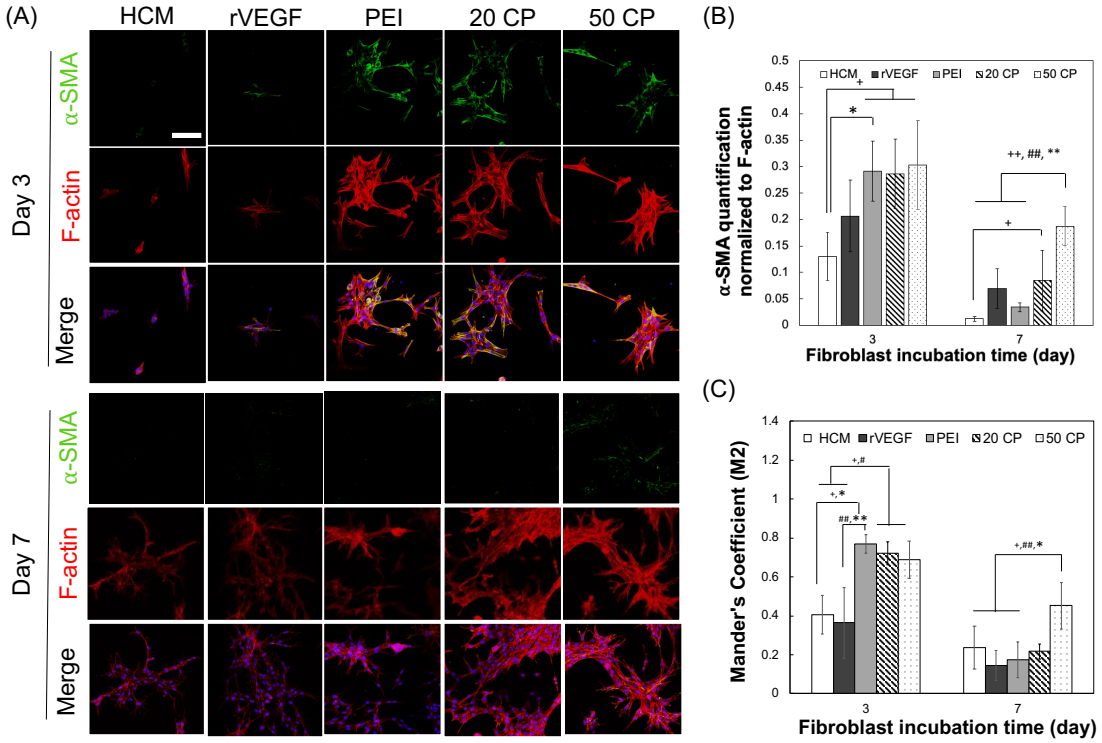

Figure 3.8. VEGF-GAHCM mediated myofibroblast transformation. (A) Representative confocal microscope images of α-SMA expressed fibroblasts cultured in VEGF-GAHCM for 3 or 7 days (α-SMA for green, F-actin for red, and nuclei for blue). Scale bar is 100 μm. (B) α-SMA quantification using confocal images (HCM for Blank, rVEGF for Dark grey, PEI for Grey, 20CP for Stripe, and 50CP for Dot). Sum of F-intensity for α-SMA is normalized to sum of F-intensity for F-actin. (C) Co-localization image analysis to define stress fibers in expressed a-SMA. Mander's coefficient (M2) indicates α-SMA voxels overlap F-actin voxels, range from 0 (no co-localization) to 1 (complete co-localization).. Each data point represents the mean ± standard deviation for total of 4 images. The statistically significant differences state +P<0.05 and ++P<0.001 compared to HCM, #P<0.05 and ##P<0.001 compared to rVEGF, and *P<0.05 and **P<0.001 compared to PEI.

fibroblasts cultured in the PEI, rVEGF, and HCM hydrogels. In addition, to identify myofibroblast-like phenotype characterized by the contractile element of the expressed α-SMA, the polymerized form of cytoplasmic actin microfilaments (stress fibers) containing α-SMA was further identified via colocalization analysis of α-SMA staining

overlapping with F-actin staining as described in previous studies (65, 66). The fraction of α-SMA (green) that colocalized with the F-actin (red) was analyzed by calculation of the Mander's coefficient (M2). α-SMA overlapped with the F-actin signal at significantly higher (ca. 2-fold) levels for the VEGF-GAHCM (0.8) relative to the rVEGF and HCM hydrogels (0.4) at day 3 (Figure 3.8(C)). At day 7, the overlap of the

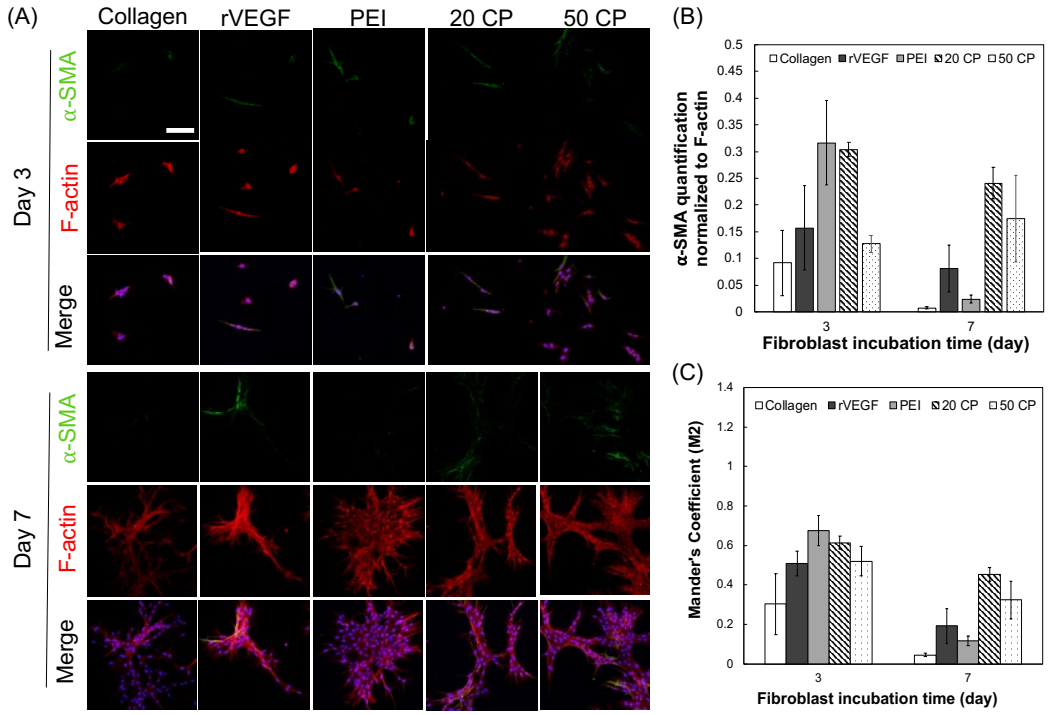

Figure 3.9. VEGF encoding polyplex integrated collagen hydrogel mediated myofibroblast transformation. (A) Representative confocal microscope images of α-SMA expressed fibroblasts cultured in VEGF-GAHCM for 3 or 7 days (α-SMA for green, F-actin for red, and nuclei for blue). Scale bar is 100 μm. (B) α-SMA quantification using confocal images (HCM for Blank, rVEGF for Dark grey, PEI for Grey, 20CP for Stripe, and 50CP for Dot). Sum of F-intensity for α-SMA is normalized to sum of F-intensity for F-actin. (C) Co-localization image analysis to define stress fibers in expressed a-SMA. Mander's coefficient (M2) indicates α-SMA voxels overlap F-actin voxels, range from 0 (no co-localization) to 1 (complete co-localization).

α-SMA and F-actin signals for the 50 CP VEGF-GAHCM was still significantly higher than the overlap observed for PEI, rVEGF, and HCM hydrogels. Moreover, the

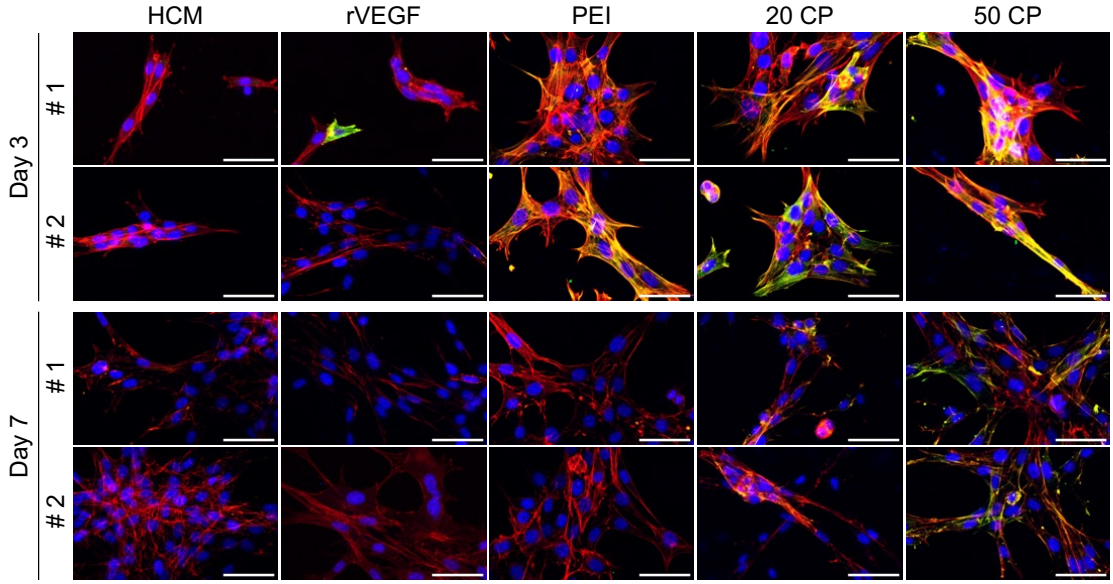

Figure 3.10. VEGF-encoding GAHCM mediated myofibroblast-like differentiation. Representative confocal microscope images of α-SMA expressed fibroblasts cultured in VEGF-GAHCM for 3 or 7 days. (α-SMA for green, F-actin for red, and nuclei for blue) to demonstrate localization of α-SMA signals on the F-actin fibers. Scale bar is 50 μm.

expanded versions of images were used to analyze Figure 3.9 (Figure 3.10) confirmed more clear colocalization between α-SMA and F-actin signals with at least three continuous straight overlapping lines in VEGF-GAHCM samples at day 3 and 50 CP VEGF-GAHCM at day 7, indicating the differentiated myofibroblast-like phenotypic appearance [66]. Thus, CMP modification of VEGF-GAHCM sustained α-SMA expression, consistent with myofibroblast differentiation, for at least 7 days.

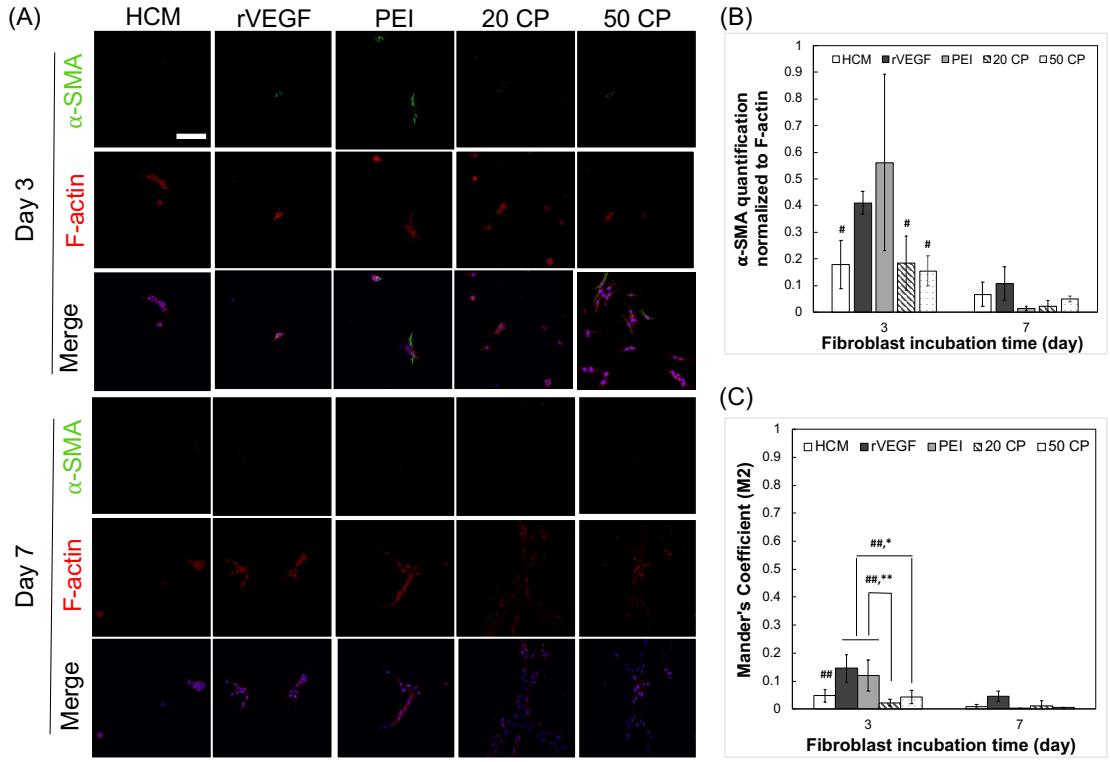

Figure 3.11. VEGF-encoding HCM hydrogels mediated α-SMA expression in fibroblasts pre-treated with CD44 antibody. (A) Representative confocal microscope images of α-SMA expressed fibroblasts cultured in VEGF-polyplex incorporated collagen hydrogel for 3 or 7 days (α-SMA for Green, F-actin for Red, and nuclei for blue). Scale bar is 100 μm. (B) α-SMA quantification using confocal images (HCM for Blank, rVEGF for Dark grey, PEI for Grey, 20CP for Stripe, and 50CP for Dot). Sum of F-intensity for α-SMA is normalized to sum of F-intensity for F-actin. (C) Co-localization image analysis to define stress fibers in expressed a-SMA. Mander's coefficient (M2) indicates the extent to which α-SMA voxels overlap F-actin voxels (with a range from 0 (no co-localization) to 1 (complete co-localization)). The statistically significant differences are indicated as $^{\#}P<0.05$ and $^{\#\#}P<0.001$ compared to rVEGF, and *P<0.05 and **P<0.001 compared to PEI.

To determine the impact of HA-CD44 signaling on α-SMA expression, I performed the same α-SMA expression analysis using VEGF-polyplex incorporated in a collagen

hydrogel lacking HA (Figure 3.9). The α-SMA expression quant ification and colocalization analysis revealed a similar trend as for the HCM hydrogel (Figure 3.8). However, due to low mechanical stiffness and limited long-term stability of the collagen hydrogel (67), an unequal cell distribution was observed within the hydrogel with increasing culture time (Figure 3.11), thus preventing a direct comparison of microscopy images of cells from the different z-locations in the collagen hydrogel (toward the bottom) vs. the HCM hydrogel. On the other hand, the α-SMA expression quantification and colocalization analysis revealed a greater reduction in α-SMA and less stress fiber formation in the 20 CP and 50 CP (Figure 3.10) HCM hydrogels for the CD44 receptor pre-blocked fibroblasts, indicating that HA-CD44 signaling was involved in the myofibroblast differentiation.

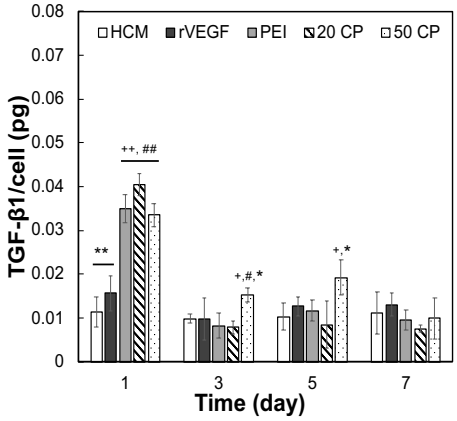

Figure 3.12. TGF-β1 expression of NIH3T3 cultured in VEGF encoding GAHCM for 7 days. TGF-β1 measurements from condition culture media for each sample (HCM for Blank, rVEGF for Dark grey, PEI for Grey, 20CP for Stripe, and 50 CP for Dot) were normalized to total cell counts. Each data point represents the mean ± standard deviation for n=4. The statistically significant differences of total VEGF-A amounts per cell state +P<0.05 and ++P<0.001 compared to HCM, #P<0.05 and ##P<0.001 compared to rVEGF, and *P<0.05 and **P<0.001 compared to PEI.

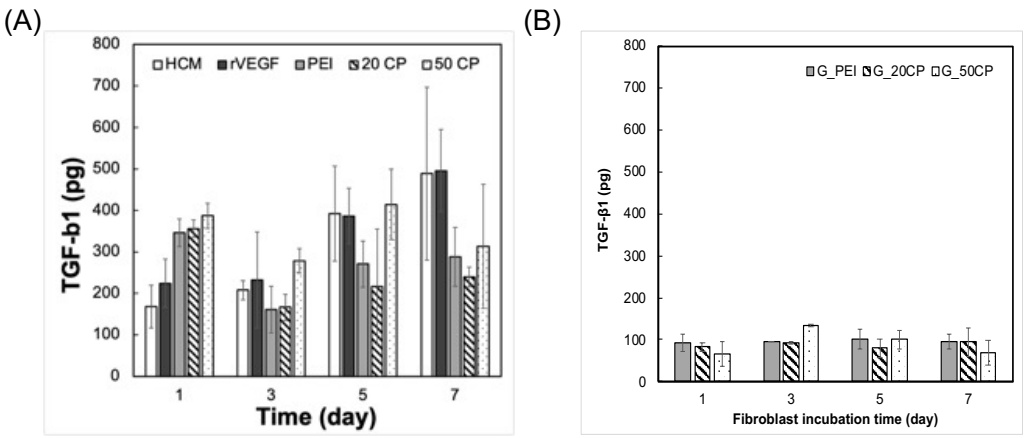

Figure 3.13. TGF-β1 expression (pg) of NIH3T3 cultured in (A) VEGF encoding GAHCM and (B) GLuc encoding GAHCM for 7 days. (A) TGF-β1 from condition culture media for each sample (HCM for Blank, rVEGF for Dark grey, PEI for Grey, 20 CP for Stripe, and 50 CP for Dot) were measured using TGF-β1 ELISA. Each data point represents the mean ± standard deviation for n=4. (B) TGF-β1 from condition culture media for each sample (GLuc-PEI for Grey, GLuc-20CP for Stripe, and GLuc-50 CP for Dot) were measured using TGF-β1 ELISA. Each data point represents the mean ± standard deviation for n=3.

To understand whether TGF-β1 induced by VEGF triggered myofibroblast-like phenotypic feature, I further evaluated TGF-β1 expression by fibroblasts cultured in VEGF-GAHCM for 7 days. In order to minimize effects arising from different cell numbers (Figure 3.6(A)), TGF-β1 amounts were normalized to the total cell number at each time point. TGF-β1 quantification of the collected culture media showed 4-fold higher expression levels for 20 CP and 3-fold higher levels for PEI and 50 CP than HCM at day 1, and significantly higher levels for 50 CP than any other samples at days 3 and 5 (Figure 3.12 & Figure 3.13(A)). These TGF-β1 levels of fold increase by VEGF-GAHCM were similarry observed in the previous studies, with approximately 2.8-fold increase TGF-β1 levels in rabbit fibrotic trabeculectormy eye tissue sample with a high myofibroblasts activity, as compared with normal rabbit eye samples [8]. Surprisingly,

TGF-β1 expression for the rVEGF positive control was slightly higher than that of the HCM samples at day 1, and this sample maintained similar levels of TGF-β1 as the HCM samples at days 3, 5, and 7.

Thus, the VEGF-GAHCM was more effective for stimulating TGF-β1 production than the rVEGF, even though the VEGF-GAHCM presented VEGF-A at concentrations that were nearly 15-fold lower than those of the rVEGF at day 1. Negative control experiments revealed that fibroblasts transfected by GLuc-GAHCM did not show increased TGF-β1 expression (Figure 3.13(B)), confirming that it was the VEGF-GAHCM that enhanced TGF-β1 production during culture. In particular, fibroblasts cultured in 50 CP sustained high TGF-β1 expression up to day 5. Taken together, these results suggest that TGF-β1 induced by the expressed VEGF triggered myofibroblast-like phenotypic transformation, with the enhanced TGF-β1 production directly correlated with the increased α-SMA expression and myofibroblast-like phenotypic feature. Moreover, the 50 CP hydrogels sustained the highest levels of TGF-β1 production, which supported myofibroblast-like phenotypic features over at least 7 days.

3.3.5 *In vivo* wound healing and α-SMA expression

To evaluate the efficacy of VEGF-GAHCM for stimulating wound repair, I investigated in vivo wound healing using a mouse splinted excisional wound model. Based upon in vitro analyses, I predicted that the topical application of CMP-modified VEGF-GAHCM (50 CP) on the wound would engage and extend the myofibroblast transformation response, resulting in robust wound healing and accelerated wound closure. Wounds were treated with saline, HCM hydrogel, recombinant VEGF in HCM

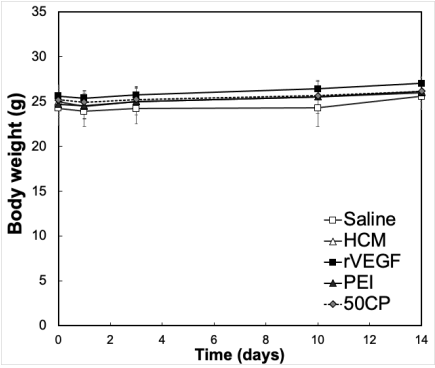

Figure 3. 14. Body weight of mouse during the wound healing studies. Each data point represents the mean ± standard deviation for n=12 for Day 0,1, and 3, and n=6 for Day 10 and 14.

hydrogel, or VEGF-GAHCM (PEI and 50 CP) and evaluated for 14 days. No significant changes were observed in the mouse body weights across all sample groups, indicating no adverse effects from the surgical process and materials (Figure 3.14). The wound closure process was recorded for 14 days, and wound size was quantified at various time points relative to the initial wound size (Figure 3.15 and Figure 3.16). At day 3, the wound size in PEI- (80.4%) and 50 CP- (77.1%) treated wounds was significantly reduced as compared to rVEGF- (87.7%), HCM- (89.7%), or saline- (91.7%) treated wounds. Furthermore, at day 7 (immediately prior to splint removal), wounds treated with PEI (63.5%) or 50 CP (62.0%) were significantly more closed than those treated with saline (78.6%) or HCM (75.2%), indicating that the bioactive VEGF produced by transfected cells using VEGF-GAHCM effectively stimulated healing responses leading to wound closure. After removing the splint to prevent secondary damage (58), the healing effect of 50 CP (19.3%) continued to reduce the wound size, with approximately 15% more closure in 50 CP treated wounds than in saline treated wounds (35.8%) at day 10. By day 14, wounds treated with 50 CP (10.2%) exhibited significantly increase wound closure compared to wounds treated with saline (21.0%) or HCM (16.7%),

showing that the extended VEGF bioactivity induced by 50 CP treatment triggered accelerated closure. However, no statistically significant differences were observed between PEI and 50 CP treated wounds.

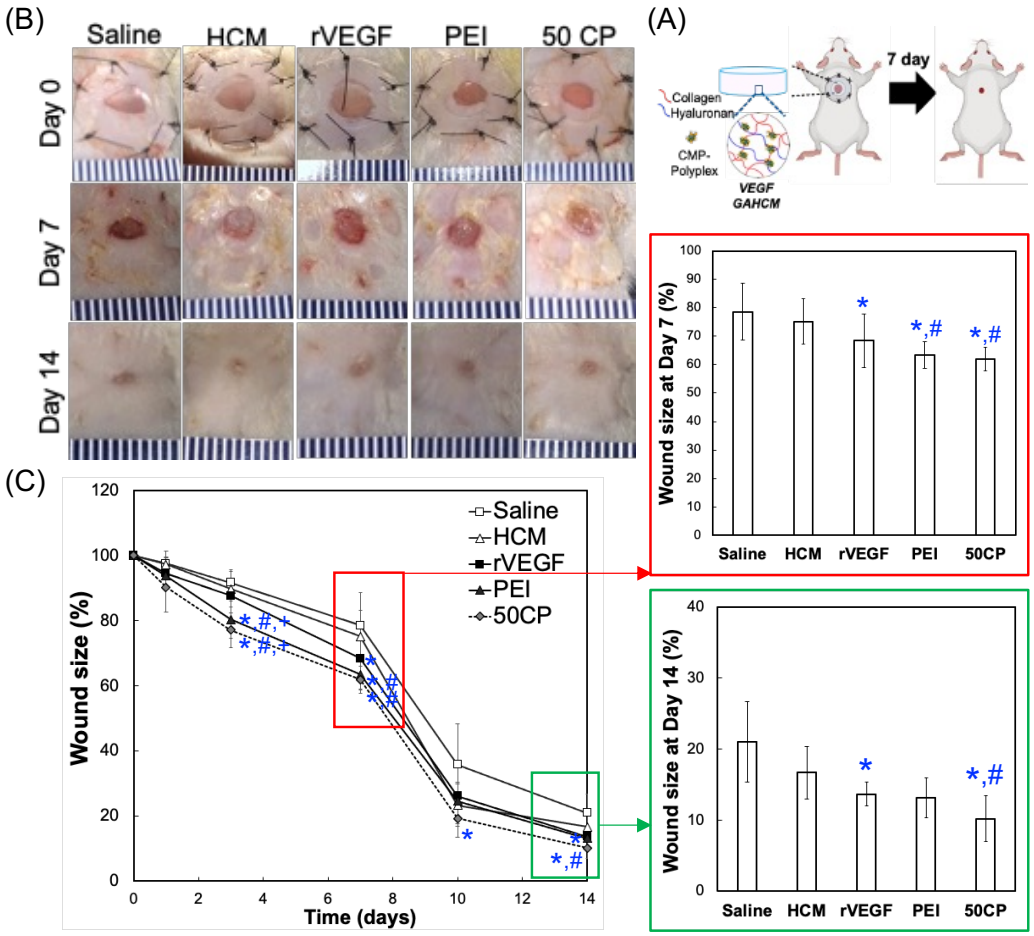

Figure 3.15. In vivo wound healing evaluation. (A) The schematic of the mouse splinted excisional wound model. After application of treatment, mouse was sutured with a silicone O-ring and covered with a Opsite dressing. The silicone O-ring was removed at day 7. (Created with Biorender.com) (B) Photograph of skin wounds. (C) The wound closure evaluation for 14 days. Each data point represents the mean ± standard deviation for n=12 for Day 0,1,3, and 7 and n=6 for Day 10 and 14. [*P < 0.05 for samples relative to Saline, #p < 0.05 for samples relative to HCM, and +P < 0.05 for samples relative to rVEGF].

Figure 3.16. Representative IVIS image of mouse with splinted excisional wounds at day 0.

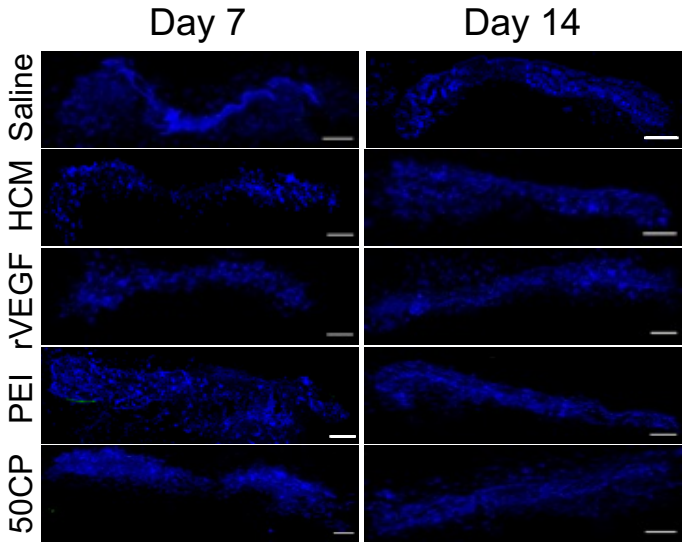

Figure 3.17. The tiled images of mouse IgG2a-FITC control antibody-stained mouse skin wound after 7 or 14 days of treatment with VEGF-GAHCM (α-SMA for green and nuclei for blue). Scale bar is 800 μm

To investigate whether the observed wound healing behavior was correlated with myofibroblast activity, myofibroblasts in the wound bed were detected using an immunostaining analysis for α-SMA at days 7 and 14. The specificity of α-SMA antibody was confirmed with the minimal signal on mouse skin tissue sections using IgG control antibody (Figure 3.17). Due to the variation of α-SMA expression in the

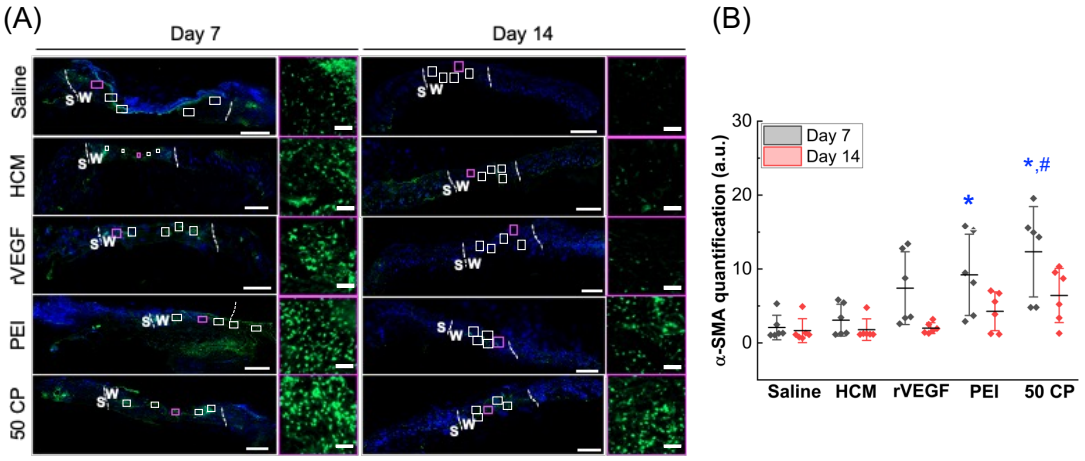

Figure 3. 18. α-SMA expression in mouse skin wound after treatment with VEGF-GAHCM (A) The tiled images of α-SMA expression in mouse skin wound tissue section after 7 or 14 days of treatment with VEGF-GAHCM (α-SMA for green and nuclei for blue) and the zoom-in image of pink-colored box in the tiled images (α-SMA for green). s = native skin and w = wound. Scale bar is 800 µm and scale bar for zoom-in image is 60 µm. (B) α-SMA quantification using images for five different areas (white/pink-colored boxes) in the wound or native skin of each tiled image. Each data represents the average of fluorescent intensity of α-SMA in the wound is normalized to average of fluorescent intensity of α-SMA in the native skin for each tiled image. The lines represent the mean ± standard deviation for total 6 mouse. The statistically significant differences state *P<0.05 for samples relative to Saline and #P<0.05 for samples relative to HCM.

native mouse skin tissues, α-SMA expression in the wound bed was determined relative to α-SMA expression in the native mouse skin (Figure 3.18). The lower magnification images on figure 3.18 were used to capture the overall distribution of α-SMA in the healed wound, as compared to the distribution in native skin. And, the higher mamigification images with similar power level with previously reported literature (68-71) were used to illustrate α-SMA expression levels and cellular morphology in order to enable comparison between groups and time points. Overall, α-SMA expression levels at day 7 were higher than α-SMA expression levels at day 14 in HCM, rVEGF,

PEI, and 50 CP-treated wounds, whereas similar α-SMA expression levels were observed at days 7 and 14 in saline-treated wounds. At day 7, α-SMA expression in 50 CP-treated samples (12 a.u.) was enhanced approximately 6-fold and 4-fold as compared to expression in saline- (2 a.u.) or HCM- (3 a.u.) treated wounds, respectively, and α-SMA expression in PEI-treated wounds (9 a.u.) was increased 4.5-fold higher than in saline-treated wounds. By day 14, α-SMA expression in 50 CP-treated wounds (6 a.u.) was still higher than expression in other groups (PEI (4 a.u.), and rVEGF, HCM and saline (2 a.u.)), but the differences were not statistically significant. This observation suggests that VEGF produced by 50 CP effectively engaged α-SMA expression in the wound bed.

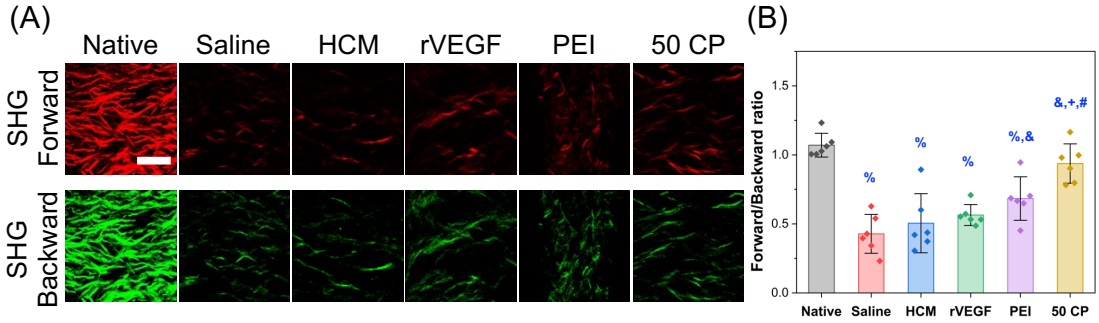

Figure 3.19. Collagen analysis in wound tissue sections after 14 days of treatment. (A) The representative SHG images of forward and backward scattering in the wound tissue sections. Scale bar is 40 μm. (B) Forward/Backward SHG ratio. Each data represents the mean ± standard deviation for total 6 mouse. The statistically significant differences state %P<0.05 for samples relative to Native, &P<0.05 for samples relative to Saline, +P<0.05 for samples relative to HCM, and #P<0.05 for samples relative to rVEGF.

In addition, I further evaluated collagen deposition, typically stimulated by myofibroblasts, in the healed skin wound tissue sections. Specifically, SHG imaging was used to detect the non-centrosymmetric structure of collagen fibers. Mature fibrils, which normally represent type I collagen, generate more SHG signal in the forward

direction, whereas immature fibrils, which normally represent type III collagen, produce more SHG signal in the backward direction (72). With an agreement of our previous observation (33), the intensity of the SHG signals in both the forward and backward directions for all treated wound tissue sections were visibly lower than the SHG signals for the native skin tissue sections, most likely because of the difference in the orientation of the collagen found in native skin (dense reticular pattern) vs. healed wounds (loose parallel bundles) (73) (Figure 3.19). The image quantification for the ratio of forward-emitted to backward-emitted SHG revealed a ratio of ~1 in the 50 CP treated wounds after 14 d, however, which was close to the ratio of ~1 that was detected in the native skin tissue section; moreover, the ratio in the 50 CP treated wounds exhibited a statistically different value than the ratios detected in all other treated samples (saline, HCM, and rVEGF). This result indicates that myofibroblast behavior stimulated by 50 CP VEGF-GAHCM application resulted in collagen deposition with a similar mature to immature collagen ratio as healthy skin tissue.

3.4 Discussion

Despite the great promise for growth factor therapy in wound and tissue repair, controlling growth factor acitivty and cell phenotype over desired time frames presents a significant roadblock to clinical translation. To overcome this challenge, I have developed an advanced therapeutic biomaterial, GAHCM, that offers key advantages in wound repair based on its capacity for triggering both efficient growth factor gene transfer and pro-healing behavior in fibroblasts.

Anionically charged HA improved the stability and retention of CMP modified polyplexes in the GAHCM (Figure 3.1). The negatively charged HA may serve to neutralize positive charges within the collagen, thereby preventing charge-repulsions

between collagen and polyplexes and thus further stabilizing 20 CP hybridization in GAHCM vs. collagen-only (74, 75). In addition, the negatively charged HA might interact with the positively charged polyplexes bound on the collagen, and further prevent disassembly of the DNA/PEI polyplex (76-78). Overall, greater amounts of CMP on the polyplexes were able to improve not only the polyplex stability but also the retention in the GAHCM.

Incorporation of HA also affected the gene transfection efficiency of fibroblasts cultured in GAHCM, with evidence indicating that the alterations in gene transfer were driven by the HA-CD44 interaction. I demonstrated that blocking HA-CD44 interactions led to decreased gene expression in the CMP-modified polyplexes within the GAHCM (Figure 3.3). HA interacts predominantly with the CD44 receptor to regulate various physiological events such as cell-cell and cell-substrate adhesion, cell migration, proliferation, intracellular GTPase activation, and HA uptake and degradation (46, 79). Specifically, CD44-HA binding promotes cell motility by both anchoring to filamentous actin and activating RhoGTPases via recruitment of guanine nucleotide exchange factors (GEFs) to the cell membrane (80). The Segura group has revealed the crucial roles of the RhoGTPases in regulating the internalization and effective intracellular processing of polyplexes for efficient gene transfer (81). An HA-RGD hydrogel-mediated 3D gene transfer system was employed for inhibition of ROCK to block the actin-myosin interaction in mouse mesenchymal stem cells (mMSCs), which significantly reduced the overall transgene expression by 81%, suggesting that cell motility is important for efficient gene transfer in 3D (82-85). Moreover, HA-mediated CD44 signaling in human fibroblasts has also been shown to increase production of proinflammatory cytokines such as TNF-α, which

correspondingly induces MMP secretion for ECM degradation, increased cell migration, and improved gene transfer (86). Given that our previous studies demonstrated that transfection from CMP polyplex-modified hydrogels was driven by MMP production (33), it is likely that the reduction in MMP secretion as a result of CD44 blocking diminished CMP-mediated transfection via an MMP-dependent mechanism (Figure 3.3(B)). Thus, the reduction of gene expression observed for the CMP-modified polyplex upon CD44 blocking is more likely due to the interruption of CD44-HA signaling, which impacts fibroblast motility and MMP secretion.

On the other hand, I have observed that blocking the CD44 receptor led to increased gene expression in the DNA/PEI polyplex-containing GAHCM (Figure 3.3(B)). Cellular uptake of DNA/PEI polyplexes occurs through both caveolar and clathrin-mediated pathways (87). Clathrin-mediated pathways regulate surface expression of receptors for internalization (88); for example, blocking the N-glycan usually present on the CD44 receptor has been shown to reduce the interaction with clathrin to prevent clathrin-mediated internalization (89). Although important for internalization, the clathrin-mediated pathway is not efficient for localization to the nucleus to stimulate gene transfection (81). Previous studies, including those from our group, have demonstrated that inhibiting the clathrin-mediated pathway resulted in an enhancement of gene expression (90, 91). These previous reports and observations are consistent with those of the current study. In the current study, blocking the CD44 receptor caused the inhibition of the clathrin-mediated endocytic pathway for DNA/PEI polyplexes. Thus, DNA/PEI polyplexes likely internalized into cells using mainly the more efficient caveolar pathway, resulting in increased gene expression in DNA/PEI polyplex-containing GAHCM. However, there was no enhancement of gene expression

by CD44 blocking in the CMP-modified polyplex GAHCM, in agreement with the observation that CMP-modified polyplexes are mainly internalized via caveolar-mediated pathways (32).

Next, I observed that fibroblast migratory behaviors were altered in VEGF-encoding GAHCM. The difference in the migration of the fibroblasts in the VEGF-encoding GAHCM vs. HCM and rVEGF-HCM hydrogels (Figure 3.6(B)) likely resulted from differences in VEGF-A expression levels (Figure 3.7). Specifically, the initial increased level of VEGF-A expression by fibroblasts within the 50 CP VEGF-GAHCM between day 1 and 3 in culture would be expected to increase the steepness of the VEGF-A gradient away from the culture media, which was freshly replaced every two days. Correspondingly, the altered VEGF-A profiles in the 50 CP VEGF-GAHCM likely increased MMP secretion by the fibroblasts, resulting in the observed further accelerated migration at days 5 and 7 following the VEGF-A gradient towards the bottom of the 50 CP VEGF-GAHCM (9, 92, 93). In addition, consistent with this interpretation, the persistent fibroblast migration in 50 CP VEGF-GAHCM starting from day 3 would contribute to enhanced VEGF-A expression at days 5 and 7 (Figure 3.7). The Shea group also has demonstrated a direct relationship between increasing cell migration and increasing gene delivery within hydrogels (94). Cells with persistent migration have increased contact with polyplexes retained within hydrogels, leading to sustained and elevated gene expression levels. The Shea group results are consistent with our observations of the sustained and increased VEGF-A production for 50 CP VEGF-GAHCM at day 5 and 7, based on the persistent fibroblast migratory behaviors in the 50 CP VEGF-GAHCM.

The signals from both VEGF-A and HA-CD44 from the VEGF-GAHCM hydrogels stimulated fibroblasts to differentiate into pro-healing myofibroblasts via TGF- β1 production (Figure 3.8, 3.9, and 3.12). Myofibroblasts are key cells in the regulation of tissue repair and wound healing through ECM deposition, maturation of granulation tissue, and vascular network development (95, 96). VEGF-A plays an important regulatory role in myofibroblast behavior because of its role as a mediator in the fibroblast-to-myofibroblast transformation process (7, 8). Specifically, VEGF-A-induced TGF-β1 expression leads to myofibroblast transformation through the SMAD-signaling pathway (97). In addition, HA also plays a key role in facilitating TGF-β1 dependent fibroblast differentiation through a CD44-mediated, MMP-dependent mechanism (47). Relocation of CD44, through interaction with HA, enhances the interaction with EGFR in lipid rafts to activate the SMAD pathway through intracellular signaling via both the MAPK/ERK pathway and CaMKII, leading to myofibroblast differentiation. I have observed indirect evidence of myofibroblast-like phenotype change of fibroblast through a lower proliferation rate of fibroblasts cultured in VEGF-GAHCM (Figure 3.6(A)). The data in Figures 3.8, 3.9, and 3.12 demonstrated that the sustained and engaged signals of VEGF-A and HA-CD44 using CMP-modified VEGF-GAHCM (50 CP) induced the highest levels of TGF-β1 production, leading to the increased α-SMA expression and myofibroblast-like phenotypic differentiation over at least 7 days.

Furthermore, in vivo studies using splinted excisional mouse wound models revealed the direct correlation between wound closure and α-SMA expression/potent myofibroblast activity (Figure 3.15 and Figure 3.18). In agreement with in vitro analyses (Figures 3.8 and 3.12), the 50 CP VEGF-GAHCM facilitated the highest levels of

wound closure, the highest levels of α-SMA expression, and the closest ratios of mature vs. immature collagen fibrils as compared with healthy native skin tissue. These results indicated that myofibroblasts transformed by 50 CP VEGF-GAHCM prompted granulation tissue formation and collagen deposition, and that these changes to fibroblast/myofibroblast behavior contributed to the observed improvements in wound closure and healing response. Also, as α-SMA is a marker for smooth muscle cells of blood vessels (71, 98), the α-SMA expression at day 14 could potentially indicate the presence of newly formed blood vessels in the wound bed. However, the enhancement of 50 CP VEGF-GAHCM in in vivo wound closure and α-SMA expression was not significantly different from PEI VEGF-GAHCM, despite the differences between these samples based on in vitro experiments. The different outcomes in vivo vs. in vitro for these samples may be a result of differences in the polyplex concentration in the in vivo (200 μg/mL of plasmid VEGF) vs. in vitro (20 μg/mL of plasmid VEGF) studies that resulted in increased in vivo transfection using the higher polyplex concentration (99, 100) and a corresponding masking of differences between samples. Alternatively, the different outcomes in vivo vs. in vitro could be due to the multiple cell types that are present in the in vivo environment (62, 101). Either of these effects, or combination of them both, could result in sufficient production of VEGF by both PEI VEGF-GAHCM and 50 CP VEGF-GAHCM to a level that exceeds a threshold for stimulating cells (102, 103), resulting in similar healing responses. Regardless, the wound closure induced by VEGF-GAHCM was directly correlated with increased α-SMA expression and myofibroblast-like phenotypic feature, and application of 50 CP VEGF-GAHCM resulted in the most efficient wound closure, the highest sustained levels of α-SMA

expression, and collagen deposition with the most similar structural properties as native skin tissue.

Altogether, these data demonstrate that the GAHCM induces not only efficient gene transfection but also enhanced pro-healing behaviors in fibroblasts for wound closure via the complementary effects of CMP gene delivery and HCM signaling. The CMP-gene delivery system controls the retention of polyplexes via CMP strand invasion with collagen. Furthermore, HCM-cell interactions facilitate cell mobility and ECM degradation, which triggers ECM-mediated endocytosis of CMP-polyplexes. Thus, harnessing CMP-HCM hydrogel interactions drives a sustained and efficient gene transfer process with a high degree of tunability based upon alteration of CMP modification. Despite the lower amounts of VEGF expressed versus the amount of rVEGF loaded in the HCM, the VEGF produced by cells in the VEGF-encoding GAHCM more effectively elicited cellular responses and sustained this activity for at least 7 days. These pro-healing responses successfully translated into more efficient wound repair in the in vivo wound healing model. The GAHCM thus has substantial promise for improved growth factor therapy in chronic wounds treatment with maximal cellular responses.

3.5 Conclusion

Despite the longstanding potential for growth factor treatment in wound repair, difficulties in controlling growth factor activity continue to limit the clinical translation of growth factor therapies. I developed a new strategy to exploit synergies in matrix-mediated gene delivery and matrix-signaling to drive enhanced fibroblast regenerative responses for wound closure. In this study, owing to the critical roles of VEGF-A and HA in the wound healing process, I have successfully incorporated HA in polyplex-

loaded collagen hydrogels (GAHCM) for an efficient gene transfer system to produce VEGF-A for wound repair. Although this study only focused on one of multifaceted roles of VEGF-A in the wound healing process, i.e., the healing responses driven by VEGF-A-triggered α-SMA expression and myofibroblast-like phenotype, the angiogenic effects of VEGF-A and TGF-β1 in our system also may benefit healing. Thus, our approaches may offer benefits to guiding multiple types of cells involved in wound healing, including not only fibroblasts, but also keratinocytes, endothelial cells, and leukocytes (5). Overall, this study provides further support recommending the use of ECM-based materials for long-term retention as well as efficient delivery of polyplexes to cells resulting in robust and localized gene transfer to stimulate wound healing.

REFERENCES

1. Sen CK. Human Wounds and Its Burden: An Updated Compendium of Estimates. Adv Wound Care (New Rochelle). 2019;8(2):39-48. Epub 2019/02/28. doi: 10.1089/wound.2019.0946. PubMed PMID: 30809421; PMCID: PMC6389759.

2. Leavitt T, Hu MS, Marshall CD, Barnes LA, Lorenz HP, Longaker MT. Scarless wound healing: finding the right cells and signals. Cell Tissue Res. 2016;365(3):483-93. Epub 2016/06/04. doi: 10.1007/s00441-016-2424-8. PubMed PMID: 27256396; PMCID: PMC5010960.

3. Fife CE, Carter MJ. Wound Care Outcomes and Associated Cost Among Patients Treated in US Outpatient Wound Centers: Data From the US Wound Registry. Wounds. 2012;24(1):10-7. Epub 2012/01/01. PubMed PMID: 25875947.

4. Farahani M, Shafiee A. Wound Healing: From Passive to Smart Dressings. Adv Healthc Mater. 2021;10(16):e2100477. Epub 2021/06/27. doi: 10.1002/adhm.202100477. PubMed PMID: 34174163.

5. Gurtner GC, Werner S, Barrandon Y, Longaker MT. Wound repair and regeneration. Nature. 2008;453(7193):314-21. Epub 2008/05/16. doi: 10.1038/nature07039. PubMed PMID: 18480812.

6. Barrientos S, Stojadinovic O, Golinko MS, Brem H, Tomic-Canic M. Growth factors and cytokines in wound healing. Wound Repair Regen. 2008;16(5):585-601. Epub 2009/01/09. doi: 10.1111/j.1524-475X.2008.00410.x. PubMed PMID: 19128254.

7. Gutpell KM, Hoffman LM. VEGF induces stress fiber formation in fibroblasts isolated from dystrophic muscle. J Cell Commun Signal. 2015;9(4):353-60. Epub 2015/07/30. doi: 10.1007/s12079-015-0300-z. PubMed PMID: 26219981; PMCID: PMC4715825.

8. Park HY, Kim JH, Park CK. VEGF induces TGF-beta1 expression and myofibroblast transformation after glaucoma surgery. Am J Pathol. 2013;182(6):2147-54. Epub 2013/05/21. doi: 10.1016/j.ajpath.2013.02.009. PubMed PMID: 23684430.

9. Larsson-Callerfelt A-K, Andersson Sjöland A, Hallgren O, Bagher M, Thiman L, Löfdahl C-G, Bjermer L, Westergren-Thorsson G. VEGF induces ECM synthesis and fibroblast activity in human lung fibroblasts. European Respiratory Journal. 2017;50(suppl 61):PA1045. doi: 10.1183/1393003.congress-2017.PA1045.

10. Li B, Wang JH. Fibroblasts and myofibroblasts in wound healing: force generation and measurement. J Tissue Viability. 2011;20(4):108-20. Epub 2009/12/10. doi: 10.1016/j.jtv.2009.11.004. PubMed PMID: 19995679; PMCID: PMC2891362.

11. Smiell JM, Wieman TJ, Steed DL, Perry BH, Sampson AR, Schwab BH. Efficacy and safety of becaplermin (recombinant human platelet-derived growth factor-BB) in patients with nonhealing, lower extremity diabetic ulcers: a combined analysis of four randomized studies. Wound Repair Regen. 1999;7(5):335-46. Epub 1999/11/17. doi: 10.1046/j.1524-475x.1999.00335.x. PubMed PMID: 10564562.

12. Niezgoda JA, Van Gils CC, Frykberg RG, Hodde JP. Randomized clinical trial comparing OASIS Wound Matrix to Regranex Gel for diabetic ulcers. Adv Skin Wound Care. 2005;18(5 Pt 1):258-66. Epub 2005/06/09. doi: 10.1097/00129334-200506000-00012. PubMed PMID: 15942317.

13. Niu Y, Li Q, Ding Y, Dong L, Wang C. Engineered delivery strategies for enhanced control of growth factor activities in wound healing. Adv Drug Deliv Rev. 2019;146:190-208. Epub 2018/06/08. doi: 10.1016/j.addr.2018.06.002. PubMed PMID: 29879493.

14. Lee K, Silva EA, Mooney DJ. Growth factor delivery-based tissue engineering: general approaches and a review of recent developments. J R Soc Interface. 2011;8(55):153-70. Epub 2010/08/20. doi: 10.1098/rsif.2010.0223. PubMed PMID: 20719768; PMCID: PMC3033020.

15. Caballero Aguilar LM, Silva SM, Moulton SE. Growth factor delivery: Defining the next generation platforms for tissue engineering. J Control Release. 2019;306:40-58. Epub 2019/06/01. doi: 10.1016/j.jconrel.2019.05.028. PubMed PMID: 31150750.

16. Giacca M, Zacchigna S. VEGF gene therapy: therapeutic angiogenesis in the clinic and beyond. Gene Ther. 2012;19(6):622-9. Epub 2012/03/02. doi: 10.1038/gt.2012.17. PubMed PMID: 22378343.

17. Wu P, Chen H, Jin R, Weng T, Ho JK, You C, Zhang L, Wang X, Han C. Non-viral gene delivery systems for tissue repair and regeneration. J Transl Med. 2018;16(1):29. Epub 2018/02/17. doi: 10.1186/s12967-018-1402-1. PubMed PMID: 29448962; PMCID: PMC5815227.

18. Martino MM, Briquez PS, Ranga A, Lutolf MP, Hubbell JA. Heparin-binding domain of fibrin(ogen) binds growth factors and promotes tissue repair when incorporated within a synthetic matrix. Proc Natl Acad Sci U S A. 2013;110(12):4563-8. Epub 2013/03/15. doi: 10.1073/pnas.1221602110. PubMed PMID: 23487783; PMCID: PMC3607046.

19. Martino MM, Tortelli F, Mochizuki M, Traub S, Ben-David D, Kuhn GA, Muller R, Livne E, Eming SA, Hubbell JA. Engineering the growth factor microenvironment with fibronectin domains to promote wound and bone tissue healing.

Sci Transl Med. 2011;3(100):100ra89. Epub 2011/09/16. doi: 10.1126/scitranslmed.3002614. PubMed PMID: 21918106.

20. Liu Y, Cai S, Shu XZ, Shelby J, Prestwich GD. Release of basic fibroblast growth factor from a crosslinked glycosaminoglycan hydrogel promotes wound healing. Wound Repair Regen. 2007;15(2):245-51. Epub 2007/03/14. doi: 10.1111/j.1524-475X.2007.00211.x. PubMed PMID: 17352757.

21. Sacchi V, Mittermayr R, Hartinger J, Martino MM, Lorentz KM, Wolbank S, Hofmann A, Largo RA, Marschall JS, Groppa E, Gianni-Barrera R, Ehrbar M, Hubbell JA, Redl H, Banfi A. Long-lasting fibrin matrices ensure stable and functional angiogenesis by highly tunable, sustained delivery of recombinant VEGF164. Proc Natl Acad Sci U S A. 2014;111(19):6952-7. Epub 2014/04/30. doi: 10.1073/pnas.1404605111. PubMed PMID: 24778233; PMCID: PMC4024904.

22. Martino MM, Briquez PS, Guc E, Tortelli F, Kilarski WW, Metzger S, Rice JJ, Kuhn GA, Muller R, Swartz MA, Hubbell JA. Growth factors engineered for super-affinity to the extracellular matrix enhance tissue healing. Science. 2014;343(6173):885-8. Epub 2014/02/22. doi: 10.1126/science.1247663. PubMed PMID: 24558160.

23. Ferraro B, Cruz YL, Coppola D, Heller R. Intradermal delivery of plasmid VEGF(165) by electroporation promotes wound healing. Mol Ther. 2009;17(4):651-7. Epub 2009/02/26. doi: 10.1038/mt.2009.12. PubMed PMID: 19240696; PMCID: PMC2835103.

24. Breitbart AS, Laser J, Parrett B, Porti D, Grant RT, Grande DA, Mason JM. Accelerated diabetic wound healing using cultured dermal fibroblasts retrovirally transduced with the platelet-derived growth factor B gene. Ann Plast Surg.

2003;51(4):409-14. Epub 2003/10/02. doi: 10.1097/01.SAP.0000084461.83554.71. PubMed PMID: 14520070.

25. Yin L, Zhao X, Ji S, He C, Wang G, Tang C, Gu S, Yin C. The use of gene activated matrix to mediate effective SMAD2 gene silencing against hypertrophic scar. Biomaterials. 2014;35(8):2488-98. Epub 2014/01/07. doi: 10.1016/j.biomaterials.2013.12.015. PubMed PMID: 24388384.

26. Tierney EG, Duffy GP, Cryan SA, Curtin CM, O'Brien FJ. Non-viral gene-activated matrices: next generation constructs for bone repair. Organogenesis. 2013;9(1):22-8. Epub 2013/03/30. doi: 10.4161/org.24329. PubMed PMID: 23538777; PMCID: PMC3674036.

27. Doukas J, Chandler LA, Gonzalez AM, Gu D, Hoganson DK, Ma C, Nguyen T, Printz MA, Nesbit M, Herlyn M, Crombleholme TM, Aukerman SL, Sosnowski BA, Pierce GF. Matrix immobilization enhances the tissue repair activity of growth factor gene therapy vectors. Hum Gene Ther. 2001;12(7):783-98. Epub 2001/05/08. doi: 10.1089/104303401750148720. PubMed PMID: 11339895.

28. Guo R, Xu S, Ma L, Huang A, Gao C. The healing of full-thickness burns treated by using plasmid DNA encoding VEGF-165 activated collagen-chitosan dermal equivalents. Biomaterials. 2011;32(4):1019-31. Epub 2010/11/13. doi: 10.1016/j.biomaterials.2010.08.087. PubMed PMID: 21071076.

29. Raftery RM, Walsh DP, Blokpoel Ferreras L, Mencia Castano I, Chen G, LeMoine M, Osman G, Shakesheff KM, Dixon JE, O'Brien FJ. Highly versatile cell-penetrating peptide loaded scaffold for efficient and localised gene delivery to multiple cell types: From development to application in tissue engineering. Biomaterials.

2019;216:119277. Epub 2019/06/30. doi: 10.1016/j.biomaterials.2019.119277. PubMed PMID: 31252371.

30. Urello MA, Kiick KL, Sullivan MO. A CMP-based method for tunable, cell-mediated gene delivery from collagen scaffolds. J Mater Chem B. 2014;2(46):8174-85. Epub 2014/12/14. doi: 10.1039/c4tb01435a. PubMed PMID: 32262095.

31. Urello MA, Kiick KL, Sullivan MO. Integration of growth factor gene delivery with collagen-triggered wound repair cascades using collagen-mimetic peptides. Bioeng Transl Med. 2016;1(2):207-19. Epub 2016/12/17. doi: 10.1002/btm2.10037. PubMed PMID: 27981245; PMCID: PMC5125401.

32. Urello MA, Kiick KL, Sullivan MO. ECM turnover-stimulated gene delivery through collagen-mimetic peptide-plasmid integration in collagen. Acta Biomater. 2017;62:167-78. Epub 2017/09/04. doi: 10.1016/j.actbio.2017.08.038. PubMed PMID: 28865990; PMCID: PMC5654588.

33. Thapa RK, Margolis DJ, Kiick KL, Sullivan MO. Enhanced wound healing via collagen-turnover-driven transfer of PDGF-BB gene in a murine wound model. ACS Appl Bio Mater. 2020;3(6):3500-17. Epub 2020/07/14. doi: 10.1021/acsabm.9b01147. PubMed PMID: 32656505; PMCID: PMC7351314.

34. Rohani MG, Parks WC. Matrix remodeling by MMPs during wound repair. Matrix Biol. 2015;44-46:113-21. Epub 2015/03/17. doi: 10.1016/j.matbio.2015.03.002. PubMed PMID: 25770908.

35. Amar S, Smith L, Fields GB. Matrix metalloproteinase collagenolysis in health and disease. Biochim Biophys Acta Mol Cell Res. 2017;1864(11 Pt A):1940-51.

Epub 2017/05/01. doi: 10.1016/j.bbamcr.2017.04.015. PubMed PMID: 28456643; PMCID: PMC5605394.

36. Hwang J, Sullivan MO, Kiick KL. Targeted Drug Delivery via the Use of ECM-Mimetic Materials. Front Bioeng Biotechnol. 2020;8:69. Epub 2020/03/07. doi: 10.3389/fbioe.2020.00069. PubMed PMID: 32133350; PMCID: PMC7040483.

37. Rainero E. Extracellular matrix endocytosis in controlling matrix turnover and beyond: emerging roles in cancer. Biochem Soc Trans. 2016;44(5):1347-54. Epub 2016/12/03. doi: 10.1042/BST20160159. PubMed PMID: 27911717.

38. Arora PD, Wang Y, Bresnick A, Dawson J, Janmey PA, McCulloch CA. Collagen remodeling by phagocytosis is determined by collagen substrate topology and calcium-dependent interactions of gelsolin with nonmuscle myosin IIA in cell adhesions. Mol Biol Cell. 2013;24(6):734-47. Epub 2013/01/18. doi: 10.1091/mbc.E12-10-0754. PubMed PMID: 23325791; PMCID: PMC3596245.

39. Madsen DH, Ingvarsen S, Jurgensen HJ, Melander MC, Kjoller L, Moyer A, Honore C, Madsen CA, Garred P, Burgdorf S, Bugge TH, Behrendt N, Engelholm LH. The non-phagocytic route of collagen uptake: a distinct degradation pathway. J Biol Chem. 2011;286(30):26996-7010. Epub 2011/06/10. doi: 10.1074/jbc.M110.208033. PubMed PMID: 21652704; PMCID: PMC3143658.

40. Nyman E, Henricson J, Ghafouri B, Anderson CD, Kratz G. Hyaluronic Acid Accelerates Re-epithelialization and Alters Protein Expression in a Human Wound Model. Plast Reconstr Surg Glob Open. 2019;7(5):e2221. Epub 2019/07/25. doi: 10.1097/GOX.0000000000002221. PubMed PMID: 31333952; PMCID: PMC6571313.

41. Gao F, Liu Y, He Y, Yang C, Wang Y, Shi X, Wei G. Hyaluronan oligosaccharides promote excisional wound healing through enhanced angiogenesis.

Matrix Biol. 2010;29(2):107-16. Epub 2009/11/17. doi: 10.1016/j.matbio.2009.11.002. PubMed PMID: 19913615.

42. Voinchet V, Vasseur P, Kern J. Efficacy and Safety of Hyaluronic Acid in the Management of Acute Wounds. American Journal of Clinical Dermatology. 2006;7(6):353-7. doi: 10.2165/00128071-200607060-00003.

43. Barrois B, Carles M, Rumeau M, Tell L, Toussaint J-F, Bonnefoy M, de Vathaire F. Efficacy and Tolerability of Hyaluronan (ialuset®) in the Treatment of Pressure Ulcers. Drugs in R & D. 2007;8(5):267-73. doi: 10.2165/00126839-200708050-00001.

44. Humbert P, Mikosinki J, Benchikhi H, Allaert FA. Efficacy and safety of a gauze pad containing hyaluronic acid in treatment of leg ulcers of venous or mixed origin: a double-blind, randomised, controlled trial. Int Wound J. 2013;10(2):159-66. Epub 2012/03/13. doi: 10.1111/j.1742-481X.2012.00957.x. PubMed PMID: 22405094.

45. Litwiniuk M, Krejner A, Speyrer MS, Gauto AR, Grzela T. Hyaluronic Acid in Inflammation and Tissue Regeneration. Wounds. 2016;28(3):78-88. Epub 2016/03/16. PubMed PMID: 26978861.

46. Chen WY, Abatangelo G. Functions of hyaluronan in wound repair. Wound Repair Regen. 1999;7(2):79-89. Epub 1999/05/07. doi: 10.1046/j.1524-475x.1999.00079.x. PubMed PMID: 10231509.

47. Midgley AC, Rogers M, Hallett MB, Clayton A, Bowen T, Phillips AO, Steadman R. Transforming growth factor-beta1 (TGF-beta1)-stimulated fibroblast to myofibroblast differentiation is mediated by hyaluronan (HA)-facilitated epidermal growth factor receptor (EGFR) and CD44 co-localization in lipid rafts. J Biol Chem.

2013;288(21):14824-38. Epub 2013/04/17. doi: 10.1074/jbc.M113.451336. PubMed PMID: 23589287; PMCID: PMC3663506.

48. Ghatak S, Maytin EV, Mack JA, Hascall VC, Atanelishvili I, Moreno Rodriguez R, Markwald RR, Misra S. Roles of Proteoglycans and Glycosaminoglycans in Wound Healing and Fibrosis. Int J Cell Biol. 2015;2015:834893. Epub 2015/10/09. doi: 10.1155/2015/834893. PubMed PMID: 26448760; PMCID: PMC4581578.

49. Graca MFP, Miguel SP, Cabral CSD, Correia IJ. Hyaluronic acid-Based wound dressings: A review. Carbohydr Polym. 2020;241:116364. Epub 2020/06/09. doi: 10.1016/j.carbpol.2020.116364. PubMed PMID: 32507198.

50. Nunzia Gallo HN, Luca Salvatore, Maria Lucia Natali, Lorena Campa, Mohamed Mahmoud, Loredana Capobianco, Alessandro Sannino, Marta Madaghiele,. Hyaluronic acid for advanced therapies: Promises and challenges. European Polymer Journal. 2019; 117:134-47. doi: https://doi.org/10.1016/j.eurpolymj.2019.05.007.

51. Mabry KM, Payne SZ, Anseth KS. Microarray analyses to quantify advantages of 2D and 3D hydrogel culture systems in maintaining the native valvular interstitial cell phenotype. Biomaterials. 2016;74:31-41. Epub 2015/10/05. doi: 10.1016/j.biomaterials.2015.09.035. PubMed PMID: 26433490; PMCID: PMC4661067.

52. Jeon JS, Bersini S, Whisler JA, Chen MB, Dubini G, Charest JL, Moretti M, Kamm RD. Generation of 3D functional microvascular networks with human mesenchymal stem cells in microfluidic systems. Integr Biol (Camb). 2014;6(5):555-63. Epub 2014/03/29. doi: 10.1039/c3ib40267c. PubMed PMID: 24676392; PMCID: PMC4307755.

53. Fan Z, Xu Z, Niu H, Gao N, Guan Y, Li C, Dang Y, Cui X, Liu XL, Duan Y, Li H, Zhou X, Lin PH, Ma J, Guan J. An Injectable Oxygen Release System to Augment Cell Survival and Promote Cardiac Repair Following Myocardial Infarction. Sci Rep. 2018;8(1):1371. Epub 2018/01/24. doi: 10.1038/s41598-018-19906-w. PubMed PMID: 29358595; PMCID: PMC5778078.

54. RI RI, do Amaral R, Reis RL, Marques AP, Murphy CM, O'Brien FJ. 3D-Printed Gelatin Methacrylate Scaffolds with Controlled Architecture and Stiffness Modulate the Fibroblast Phenotype towards Dermal Regeneration. Polymers (Basel). 2021;13(15). Epub 2021/08/11. doi: 10.3390/polym13152510. PubMed PMID: 34372114; PMCID: PMC8347286.

55. Scott RA, Kharkar PM, Kiick KL, Akins RE. Aortic adventitial fibroblast sensitivity to mitogen activated protein kinase inhibitors depends on substrate stiffness. Biomaterials. 2017;137:1-10. Epub 2017/05/21. doi: 10.1016/j.biomaterials.2017.05.010. PubMed PMID: 28527302; PMCID: PMC5554066.

56. Dunn L, Prosser HC, Tan JT, Vanags LZ, Ng MK, Bursill CA. Murine model of wound healing. J Vis Exp. 2013(75):e50265. Epub 2013/06/12. doi: 10.3791/50265. PubMed PMID: 23748713; PMCID: PMC3724564.

57. Yaron JR, Zhang L, Guo Q, Awo EA, Burgin M, Schutz LN, Zhang N, Kilbourne J, Daggett-Vondras J, Lowe KM, Lucas AR. Recombinant Myxoma Virus-Derived Immune Modulator M-T7 Accelerates Cutaneous Wound Healing and Improves Tissue Remodeling. Pharmaceutics. 2020;12(11). Epub 2020/10/28. doi: 10.3390/pharmaceutics12111003. PubMed PMID: 33105865; PMCID: PMC7690590.

58. Zhang L, Yaron JR, Guo Q, Kilbourne J, Awo EA, Burgin M, Schutz LN, Wallace SE, Lowe KM, Lucas AR. Topical Application of Virus-Derived Immunomodulating Proteins and Peptides to Promote Wound Healing in Mouse Models. Methods Mol Biol. 2021;2225:217-26. Epub 2020/10/28. doi: 10.1007/978-1-0716-1012-1_12. PubMed PMID: 33108665.

59. Wang X, Ge J, Tredget EE, Wu Y. The mouse excisional wound splinting model, including applications for stem cell transplantation. Nat Protoc. 2013;8(2):302-9. Epub 2013/01/19. doi: 10.1038/nprot.2013.002. PubMed PMID: 23329003.

60. Robinson KG, Scott RA, Hesek AM, Woodford EJ, Amir W, Planchon TA, Kiick KL, Akins RE. Reduced arterial elasticity due to surgical skeletonization is ameliorated by abluminal PEG hydrogel. Bioeng Transl Med. 2017;2(2):222-32. Epub 2017/09/22. doi: 10.1002/btm2.10060. PubMed PMID: 28932820; PMCID: PMC5579730.

61. Artym VV, Matsumoto K. Imaging cells in three-dimensional collagen matrix. Curr Protoc Cell Biol. 2010;Chapter 10:Unit 10 8 1-20. Epub 2010/09/21. doi: 10.1002/0471143030.cb1018s48. PubMed PMID: 20853341; PMCID: PMC2988473.

62. Bao P, Kodra A, Tomic-Canic M, Golinko MS, Ehrlich HP, Brem H. The role of vascular endothelial growth factor in wound healing. J Surg Res. 2009;153(2):347-58. Epub 2008/11/26. doi: 10.1016/j.jss.2008.04.023. PubMed PMID: 19027922; PMCID: PMC2728016.

63. Eppler SM, Combs DL, Henry TD, Lopez JJ, Ellis SG, Yi JH, Annex BH, McCluskey ER, Zioncheck TF. A target-mediated model to describe the pharmacokinetics and hemodynamic effects of recombinant human vascular endothelial

growth factor in humans. Clin Pharmacol Ther. 2002;72(1):20-32. Epub 2002/08/02. doi: 10.1067/mcp.2002.126179. PubMed PMID: 12152001.

64. Simon-Yarza T, Formiga FR, Tamayo E, Pelacho B, Prosper F, Blanco-Prieto MJ. Vascular endothelial growth factor-delivery systems for cardiac repair: an overview. Theranostics. 2012;2(6):541-52. Epub 2012/06/28. doi: 10.7150/thno.3682. PubMed PMID: 22737191; PMCID: PMC3381347.

65. Tijore A, Behr JM, Irvine SA, Baisane V, Venkatraman S. Bioprinted gelatin hydrogel platform promotes smooth muscle cell contractile phenotype maintenance. Biomed Microdevices. 2018;20(2):32. Epub 2018/03/30. doi: 10.1007/s10544-018-0274-8. PubMed PMID: 29594704.

66. Gabasa M, Duch P, Jorba I, Gimenez A, Lugo R, Pavelescu I, Rodriguez-Pascual F, Molina-Molina M, Xaubet A, Pereda J, Alcaraz J. Epithelial contribution to the profibrotic stiff microenvironment and myofibroblast population in lung fibrosis. Mol Biol Cell. 2017;28(26):3741-55. Epub 2017/10/20. doi: 10.1091/mbc.E17-01-0026. PubMed PMID: 29046395; PMCID: PMC5739292.

67. Caliari SR, Burdick JA. A practical guide to hydrogels for cell culture. Nat Methods. 2016;13(5):405-14. Epub 2016/04/29. doi: 10.1038/nmeth.3839. PubMed PMID: 27123816; PMCID: PMC5800304.

68. Jiang D, de Vries JC, Muschhammer J, Schatz S, Ye H, Hein T, Fidan M, Romanov VS, Rinkevich Y, Scharffetter-Kochanek K. Local and transient inhibition of p21 expression ameliorates age-related delayed wound healing. Wound Repair Regen. 2020;28(1):49-60. Epub 2019/10/02. doi: 10.1111/wrr.12763. PubMed PMID: 31571377.

69. Ren S, Chen J, Duscher D, Liu Y, Guo G, Kang Y, Xiong H, Zhan P, Wang Y, Wang C, Machens HG, Chen Z. Microvesicles from human adipose stem cells promote wound healing by optimizing cellular functions via AKT and ERK signaling pathways. Stem Cell Res Ther. 2019;10(1):47. Epub 2019/02/02. doi: 10.1186/s13287-019-1152-x. PubMed PMID: 30704535; PMCID: PMC6357421.

70. Wilkinson HN, Roberts ER, Stafford AR, Banyard KL, Matteucci P, Mace KA, Hardman MJ. Tissue Iron Promotes Wound Repair via M2 Macrophage Polarization and the Chemokine (C-C Motif) Ligands 17 and 22. Am J Pathol. 2019;189(11):2196-208. Epub 2019/08/30. doi: 10.1016/j.ajpath.2019.07.015. PubMed PMID: 31465751.

71. Yeh CJ, Chen CC, Leu YL, Lin MW, Chiu MM, Wang SH. The effects of artocarpin on wound healing: in vitro and in vivo studies. Sci Rep. 2017;7(1):15599. Epub 2017/11/17. doi: 10.1038/s41598-017-15876-7. PubMed PMID: 29142215; PMCID: PMC5688173.

72. Williams RM, Zipfel WR, Webb WW. Interpreting second-harmonic generation images of collagen I fibrils. Biophys J. 2005;88(2):1377-86. Epub 2004/11/10. doi: 10.1529/biophysj.104.047308. PubMed PMID: 15533922; PMCID: PMC1305140.

73. Xue M, Jackson CJ. Extracellular Matrix Reorganization During Wound Healing and Its Impact on Abnormal Scarring. Adv Wound Care (New Rochelle). 2015;4(3):119-36. Epub 2015/03/19. doi: 10.1089/wound.2013.0485. PubMed PMID: 25785236; PMCID: PMC4352699.

74. Mesquida P, Kohl D, Andriotis OG, Thurner PJ, Duer M, Bansode S, Schitter G. Evaluation of surface charge shift of collagen fibrils exposed to

glutaraldehyde. Sci Rep. 2018;8(1):10126. Epub 2018/07/06. doi: 10.1038/s41598-018-28293-1. PubMed PMID: 29973604; PMCID: PMC6031691.

75. Li Y, Asadi A, Monroe MR, Douglas EP. pH effects on collagen fibrillogenesis in vitro: Electrostatic interactions and phosphate binding. Materials Science and Engineering: C. 2009;29(5):1643-9.

76. Ito T, Iida-Tanaka N, Koyama Y. Efficient in vivo gene transfection by stable DNA/PEI complexes coated by hyaluronic acid. J Drug Target. 2008;16(4):276-81. Epub 2008/05/01. doi: 10.1080/10611860801900728. PubMed PMID: 18446606.

77. Ito T, Iida-Tanaka N, Niidome T, Kawano T, Kubo K, Yoshikawa K, Sato T, Yang Z, Koyama Y. Hyaluronic acid and its derivative as a multi-functional gene expression enhancer: protection from non-specific interactions, adhesion to targeted cells, and transcriptional activation. J Control Release. 2006;112(3):382-8. Epub 2006/05/02. doi: 10.1016/j.jconrel.2006.03.013. PubMed PMID: 16647780.

78. Ito T, Yoshihara C, Hamada K, Koyama Y. DNA/polyethyleneimine/hyaluronic acid small complex particles and tumor suppression in mice. Biomaterials. 2010;31(10):2912-8. Epub 2010/01/06. doi: 10.1016/j.biomaterials.2009.12.032. PubMed PMID: 20047759.

79. Aya KL, Stern R. Hyaluronan in wound healing: rediscovering a major player. Wound Repair Regen. 2014;22(5):579-93. Epub 2014/07/22. doi: 10.1111/wrr.12214. PubMed PMID: 25039417.

80. Bourguignon LY. Hyaluronan-mediated CD44 activation of RhoGTPase signaling and cytoskeleton function promotes tumor progression. Semin Cancer Biol. 2008;18(4):251-9. Epub 2008/05/03. doi: 10.1016/j.semcancer.2008.03.007. PubMed PMID: 18450475; PMCID: PMC2505114.

81. Dhaliwal A, Maldonado M, Lin C, Segura T. Cellular cytoskeleton dynamics modulates non-viral gene delivery through RhoGTPases. PLoS One. 2012;7(4):e35046. Epub 2012/04/18. doi: 10.1371/journal.pone.0035046. PubMed PMID: 22509380; PMCID: PMC3324413.

82. Dhaliwal A, Oshita V, Segura T. Transfection in the third dimension. Integr Biol (Camb). 2013;5(10):1206-16. Epub 2013/08/10. doi: 10.1039/c3ib40086g. PubMed PMID: 23929354; PMCID: PMC3798060.

83. Hsu SH, Ho TT, Tseng TC. Nanoparticle uptake and gene transfer efficiency for MSCs on chitosan and chitosan-hyaluronan substrates. Biomaterials. 2012;33(14):3639-50. Epub 2012/03/01. doi: 10.1016/j.biomaterials.2012.02.005. PubMed PMID: 22364729.

84. Yen J, Ying H, Wang H, Yin L, Uckun F, Cheng J. CD44 Mediated Nonviral Gene Delivery into Human Embryonic Stem Cells via Hyaluronic-Acid-Coated Nanoparticles. ACS Biomater Sci Eng. 2016;2(3):326-35. Epub 2016/03/14. doi: 10.1021/acsbiomaterials.5b00393. PubMed PMID: 33429536.

85. Park JS, Yi SW, Kim HJ, Park KH. Receptor-mediated gene delivery into human mesenchymal stem cells using hyaluronic acid-shielded polyethylenimine/pDNA nanogels. Carbohydr Polym. 2016;136:791-802. Epub 2015/11/18. doi: 10.1016/j.carbpol.2015.09.053. PubMed PMID: 26572414.

86. Kobayashi H, Terao T. Hyaluronic acid-specific regulation of cytokines by human uterine fibroblasts. Am J Physiol. 1997;273(4):C1151-9. Epub 1997/11/14. doi: 10.1152/ajpcell.1997.273.4.C1151. PubMed PMID: 9357758.

87. von Gersdorff K, Sanders NN, Vandenbroucke R, De Smedt SC, Wagner E, Ogris M. The internalization route resulting in successful gene expression depends

on both cell line and polyethylenimine polyplex type. Mol Ther. 2006;14(5):745-53. Epub 2006/09/19. doi: 10.1016/j.ymthe.2006.07.006. PubMed PMID: 16979385.

88. McMahon HT, Boucrot E. Molecular mechanism and physiological functions of clathrin-mediated endocytosis. Nat Rev Mol Cell Biol. 2011;12(8):517-33. Epub 2011/07/23. doi: 10.1038/nrm3151. PubMed PMID: 21779028.

89. Torreno-Pina JA, Castro BM, Manzo C, Buschow SI, Cambi A, Garcia-Parajo MF. Enhanced receptor-clathrin interactions induced by N-glycan-mediated membrane micropatterning. Proc Natl Acad Sci U S A. 2014;111(30):11037-42. Epub 2014/07/18. doi: 10.1073/pnas.1402041111. PubMed PMID: 25030450; PMCID: PMC4121791.

90. Reilly MJ, Larsen JD, Sullivan MO. Polyplexes traffic through caveolae to the Golgi and endoplasmic reticulum en route to the nucleus. Mol Pharm. 2012;9(5):1280-90. Epub 2012/03/17. doi: 10.1021/mp200583d. PubMed PMID: 22420286.

91. McLendon PM, Fichter KM, Reineke TM. Poly(glycoamidoamine) vehicles promote pDNA uptake through multiple routes and efficient gene expression via caveolae-mediated endocytosis. Mol Pharm. 2010;7(3):738-50. Epub 2010/03/31. doi: 10.1021/mp900282e. PubMed PMID: 20349982.

92. Doyle AD, Carvajal N, Jin A, Matsumoto K, Yamada KM. Local 3D matrix microenvironment regulates cell migration through spatiotemporal dynamics of contractility-dependent adhesions. Nat Commun. 2015;6:8720. Epub 2015/11/10. doi: 10.1038/ncomms9720. PubMed PMID: 26548801; PMCID: PMC4643399.

93. Even-Ram S, Yamada KM. Cell migration in 3D matrix. Curr Opin Cell Biol. 2005;17(5):524-32. Epub 2005/08/23. doi: 10.1016/j.ceb.2005.08.015. PubMed PMID: 16112853.

94. Shepard JA, Huang A, Shikanov A, Shea LD. Balancing cell migration with matrix degradation enhances gene delivery to cells cultured three-dimensionally within hydrogels. J Control Release. 2010;146(1):128-35. Epub 2010/05/11. doi: 10.1016/j.jconrel.2010.04.032. PubMed PMID: 20450944; PMCID: PMC2914156.

95. Darby IA, Laverdet B, Bonte F, Desmouliere A. Fibroblasts and myofibroblasts in wound healing. Clin Cosmet Investig Dermatol. 2014;7:301-11. Epub 2014/11/15. doi: 10.2147/CCID.S50046. PubMed PMID: 25395868; PMCID: PMC4226391.

96. Mayrand D, Laforce-Lavoie A, Larochelle S, Langlois A, Genest H, Roy M, Moulin VJ. Angiogenic properties of myofibroblasts isolated from normal human skin wounds. Angiogenesis. 2012;15(2):199-212. Epub 2012/02/22. doi: 10.1007/s10456-012-9253-5. PubMed PMID: 22350743.

97. Finnson KW, McLean S, Di Guglielmo GM, Philip A. Dynamics of Transforming Growth Factor Beta Signaling in Wound Healing and Scarring. Adv Wound Care (New Rochelle). 2013;2(5):195-214. Epub 2014/02/15. doi: 10.1089/wound.2013.0429. PubMed PMID: 24527343; PMCID: PMC3857355.

98. Murphy KC, Whitehead J, Falahee PC, Zhou D, Simon SI, Leach JK. Multifactorial Experimental Design to Optimize the Anti-Inflammatory and Proangiogenic Potential of Mesenchymal Stem Cell Spheroids. Stem Cells. 2017;35(6):1493-504. Epub 2017/03/10. doi: 10.1002/stem.2606. PubMed PMID: 28276602; PMCID: PMC5446296.

99. Luo D, Saltzman WM. Enhancement of transfection by physical concentration of DNA at the cell surface. Nat Biotechnol. 2000;18(8):893-5. Epub 2000/08/10. doi: 10.1038/78523. PubMed PMID: 10932162.

100. Tokatlian T, Cam C, Segura T. Porous hyaluronic acid hydrogels for localized nonviral DNA delivery in a diabetic wound healing model. Adv Healthc Mater. 2015;4(7):1084-91. Epub 2015/02/20. doi: 10.1002/adhm.201400783. PubMed PMID: 25694196; PMCID: PMC4433401.

101. Johnson KE, Wilgus TA. Vascular Endothelial Growth Factor and Angiogenesis in the Regulation of Cutaneous Wound Repair. Adv Wound Care (New Rochelle). 2014;3(10):647-61. Epub 2014/10/11. doi: 10.1089/wound.2013.0517. PubMed PMID: 25302139; PMCID: PMC4183920.

102. Jih YJ, Lien WH, Tsai WC, Yang GW, Li C, Wu LW. Distinct regulation of genes by bFGF and VEGF-A in endothelial cells. Angiogenesis. 2001;4(4):313-21. Epub 2002/08/29. doi: 10.1023/a:1016080321956. PubMed PMID: 12197476.

103. Yoshida A, Anand-Apte B, Zetter BR. Differential endothelial migration and proliferation to basic fibroblast growth factor and vascular endothelial growth factor. Growth Factors. 1996;13(1-2):57-64. Epub 1996/01/01. doi: 10.3109/08977199609034566. PubMed PMID: 8962720.

Chapter 4

VEGF-ENCODING, GENE-ACTIVATED COLLAGEN-BASED MATRICES PROMOTE BLOOD VESSEL FORMATION AND IMPROVED WOUND REPAIR

Disruption in vascularization during wound healing can severely impair healing. Pro-angiogenic growth factor therapies have shown great healing potential; however, controlling growth factor activity and cellular behavior over desired healing time scales remains challenging. In this study, I evaluated collagen mimetic peptide (CMP) tethers for their capacity to control growth factor gene transfer and growth factor activity using our recently developed gene-activated hyaluronic acid-collagen matrix (GAHCM). GAHCM was comprised of DNA/polyethyleneimine (PEI) polyplexes retained on hyaluronic acid (HA)-collagen hydrogels using CMPs. I hypothesized that using CMP-collagen tethers to control vascular endothelial growth factor-A (VEGF-A) gene delivery would provide a powerful strategy to modulate the pro-angiogenic behaviors of endothelial cells (ECs) for blood vessel formation, resulting in enhanced wound repair. Due to the ability of fibroblast remodeled collagen to induce tunable gene delivery in GAHCM with CMP modification, VEGF-A produced by fibroblast leads to the increased growth and persistent migration of ECs for at least 7 days, as compared to non-CMP modified GAHCM. Moreover, when ECs were exposed to fibroblast-containing VEGF-GAHCM with higher levels of CMP modification (50% CMP-PEI, or 50 CP), high CD31 expression was stimulated, resulting in formation of an interconnected EC network with a significantly higher network volume and a larger diameter network structure than controls. Application of VEGF-GAHCM with 50 CP in murine splinted excisional wounds facilitated prolonged pro-healing and pro-angiogenic responses resulting in increased blood vessel formation, improved granulation tissue formation, faster re-epithelialization, and overall enhanced repair.

These findings suggest the benefits of CMP-collagen tethers as useful tools to control gene transfer and growth factor activity for improved treatment of wounds.

4.1 Introduction

Impaired revascularization in injury sites can ultimately impede healing and lead to chronic non-healing wounds, which are a persistent societal and economic burden (1, 2). The estimated health care cost of chronic wounds in the U.S. alone is over $25 billion annually (3, 4), and inadequate healing in chronic wounds causes severe complications including limb amputations associated with elevated morbidity and mortality (5). Thus, enhancing vascularization is a major therapeutic target for developing new wound treatments.

The formation of new blood vessels via angiogenesis is a critical first step towards revascularization. During normal wound healing processes, angiogenic capillary sprouts form by endothelial cell (EC) migration, proliferation, and enhanced endothelial cell-cell interactions to allow leukocyte infiltration, supply growth factors and oxygen, and aid granulation tissue formation (1, 6, 7). The dynamic angiogenesis process is highly regulated by interactions between ECs, angiogenic soluble factors, and surrounding extracellular matrix (ECM). The ECM components such as fibronectin, collagen, laminin, and proteoglycans are involved in both normal vessel growth and maintenance by providing a scaffold for EC migration, and acting as a reservoir and modulator for pro-angiogenic growth factors (8). Pro-angiogenic growth factors, including vascular endothelial growth factor (VEGF), fibroblast growth factor (FGF), angiopoietins, and transforming growth factor (TGF-β) activate proangiogenic signals in ECs to stimulate angiogenesis and enhance wound healing (6, 8, 9). Hence,

manipulating ECM signaling and growth factor presentation offers a compelling strategy to regulate angiogenesis.

The topical application of growth factors in the wound milieu has emerged as a promising strategy to stimulate angiogenesis and catalyze other aspects of wound healing. In particular, the VEGF protein family is of key interest due to the role of VEGF as an angiogenic mediator during granulation tissue formation (8). VEGF induces EC proliferation, migration, and sprouting for blood vessel formation, and it plays a significant role in regulating the permeability of blood vessels, vasodilation, and stabilization of new blood vessel growth (9-11). The topical application of recombinant human VEGF (Telbermin, 72 μg/cm2) three times a week for up to six weeks showed promising efficacy and tolerability in the treatment of diabetic foot ulcers during a phase I trial (12); however, Telbermin was discontinued following a phase II trial (13). Clinical studies of growth factor therapies in wound repair have demonstrated that the short half-life and instability of recombinant growth factors in the wound environment result in high required doses, correspondingly high costs, and off-target side effects that limit the success of existing formulations (14, 15). Thereby, strategies to better control growth factor activity and provide a cellular microenvironment that maximizes growth factor signaling are desirable to overcome current limitations.

ECM-mimicking biomaterials including collagen, hyaluronic acid (HA), and fibrin have emerged as both delivery vehicles and cellular scaffolds that are able to control growth factor activity while providing a microenvironment conducive to cell recruitment and differentiation (16-24). For example, HA has been extensively utilized in wound healing to accelerate wound repair, decrease fibrosis, and improve the quality of healing by modulating inflammation, cellular recruitment, and angiogenesis (25, 26).

HA promotes angiogenesis via an interplay between two HA-specific receptors, CD44/PKCδ and RHAMM-ERK-TGFβRI, to induce PAI-1for MMP-2 expression, independent of proangiogenic factors (27, 28). This phenomenon has been leveraged in studies exploring the delivery of recombinant VEGF protein using HA-based hydrogels, which induced a synergistic angiogenic response that was greater than the sum of the separate responses produced by VEGF or HA hydrogel application individually (29).

Our groups previously developed biomaterials that employed the ECM for growth factor delivery in a new way, harnessing collagen mimetic peptides (CMPs) to retain growth factor-encoding plasmid DNA polyplexes in collagen-based hydrogels. CMP tethering improved DNA availability/lifetime and resulted in cell-mediated growth factor gene delivery, triggered by matrix metalloproteinase (MMP)-mediated collagen remodeling (30-33). Moreover, CMP-modified collagen-fibrin hydrogels encoding PDGF-BB promoted robust and tunable PDGF-BB expression in vivo, and resulted in enhanced cellular recruitment and improved healing responses within in vivo murine wounds (33). I recently built on these findings to develop a gene-activated hyaluronic acid-collagen matrix (GAHCM) comprising CMP-linked pVEGF polyplexes, and I demonstrated the advantages of this GAHCM for both efficient gene transfer and pro-healing phenotype modulation in fibroblasts (Chapter 3). CMP tethers and HA-CD44 interactions together increased the efficiency and duration of VEGF production, while simultaneously reprogramming the cellular microenvironment to stimulate TGF-β1-induced myofibroblast differentiation to a pro-healing phenotype.

Herein, I leveraged these materials to demonstrate the multifaceted and complex roles by which VEGF-A gene delivery via CMP tethering substantially improved wound healing by orchestrating the cellular processes underlying angiogenesis (34), including

pro-angiogenic behaviors in ECs as well as vessel maturation. Since fibroblasts are the primary cell type in skin dermis (35), and because our prior work showed that fibroblasts efficiently remodeled collagen to induce gene delivery in GAHCM (chapter 3), I assessed EC mechanistic responses in VEGF-A-encoding GAHCM that was pre-seeded with fibroblasts. I showed that CMP-collagen tethers in VEGF-A-encoding GAHCM sustained both mitogenic signaling and chemotactic signaling in ECs, resulting in increased EC growth and consistent EC migration for approximately one week of EC growth in GAHCM culture. Moreover, I showed that the prolonged VEGF activity induced by CMP-collagen tethering significantly improved the rate and extent of interconnected network formation in ECs, resulting in network structures at day 10 of fibroblast pre-incubation time, with a 4-fold larger volume and twice the network diameter as compared with the EC networks formed in rVEGF protein supplemented samples. Based on these promising findings, I applied VEGF-GAHCM topically in a murine splinted excisional wound model, and showed that VEGF-GAHCM with CMP modification triggered the development of a 1.7-fold greater number of mature blood vessels and a 3-fold higher quantity of granulation tissue formation after 7 days of treatment as compared to rVEGF treated wounds, resulting in robust wound repair. These findings strongly supported the potential of GAHCM as an effective treatment option to induce a comprehensive angiogenesis and wound healing response in poorly vascularized wounds.

4.2 Materials and Methods

4.2.1 Materials

FibriCol® (10 mg/mL) and Glycosil® were obtained from Advanced BioMatrix (San Diego, CA). pCMV3-VEGF-A plasmids were acquired from Sino Biological (Wayne, PA). Following the manufacturer's protocols, pCMV3-VEGF-A plasmids were amplified in MAX EfficiencyTM DH5α competent Escherichia coli (Thermo Fisher, Waltham, MA) and purified using a Qiagen Maxiprep Kit (Germantown, MD). Murine recombinant VEGF-A was obtained from Pepro Tech. (Cranbury, NJ). CellTiter 96® Aqueous One Solution Cell Proliferation Assay (MTS) was purchased from Promega (Madison, WI). GeltrexTM and Calcein-AM were acquired from ThermoFisher (Waltham, MA). Alexa Fluor® 555-conjugated Rabbit IgG-CD31 polyclonal antibody (PECAM-1) and Alexa Fluor® 555-conjugated Rabbit IgG Isotype Control were purchased from Bioss Antibodies Inc. (Woburn, MA). Mouse IgG2a monoclonal α-SMA-FITC antibody and mouse IgG2a-FITC antibody were obtained from Sigma-Aldrich (St. Louis, MO).

4.2.2 Animals

BALB/cJ mice (8-week-old, male) were procured from Jackson Laboratory (Bar Harbor, ME, USA). All experiments were performed in accordance with protocols and guidelines approved and established by the University of Delaware's Institutional Animal Care and Use Committee (IACUC).

4.2.3 Net growth of ECs treated with conditioned media from fibroblasts

Fibroblasts cultured in VEGF-GAHCM were prepared as described in our previous studies (Chapters 2 and 3). Briefly, After CMP-PEI was prepared via covalent linkage between CMP and PEI using a sulfo-SMCC bifunctional linker, the CMP-PEI was mixed with PEI at various percentages, and the CMP-PEI/PEI solution was mixed with pVEGF in 20 mM HEPES at pH 6 to prepare pVEGF/PEI (PEI), pVEGF/20% CMP modified PEI (20 CP), or pVEGF/50% CMP modified PEI (50 CP) complexes (N:P = 8, 20 μg/mL of pVEGF) through the electrostatic interaction between CMP-PEI/PEI and pVEGF. After the polyplexes were lyophilized with 20 mM sucrose, lyophilized pVEGF-A/PEI, pVEGF-A/20 CP, or pVEGF-A/50 CP polyplexes (20 μg/mL of pVEGF) were mixed into neutralized collagen. As the control samples, HCM or rVEGF-containing HCM samples was prepared with either only neutralized collagen or rVEGF (10 ng/μL) mixed in neutralized collagen. Then, all samples were incubated at 4 °C for 2 h. Fibroblasts (100,000 cells/mL) suspended in 1× DPBS were added into the neutralized collagen mixture without/with either polyplex or rVEGF, and Glycosil® was mixed into the fibroblast/neutralized collagen. After gelation at 37 °C for 45 min, the VEGF-GAHCM was incubated in complete DMEM at 37 °C with 5% CO2 for 7 days. The culture medium was collected and replaced with the fresh culture medium every two days.

ECs (3B-11 cells; ATCC, Manassas, VA) were cultured in complete DMEM containing 10% heat-inactivated fetal bovine serum (FBS) and 1% penicillin-streptomycin (P/S) at 37 °C with 5% CO2. Cells were passaged with 0.25% Trypsin containing 2.21 mM EDTA every 2-3 days. To evaluate the mitogenic effects of the conditioned media collected from fibroblasts cultured in VEGF-GAHCM, the net growth of ECs after treatment with the conditioned medium was determined. ECs

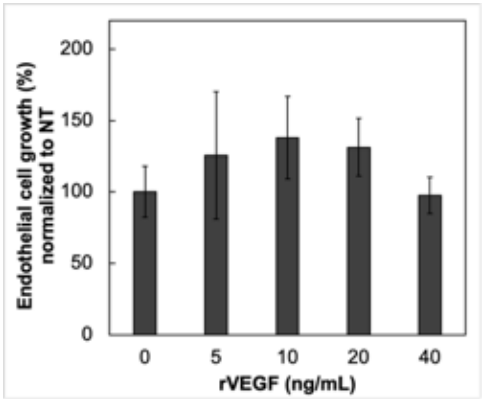

Figure 4.1. Endothelial cell growth after 24 h treatment with different concentrations of recombinant VEGF-A. Each data point represents the mean ± standard deviation for n=4.

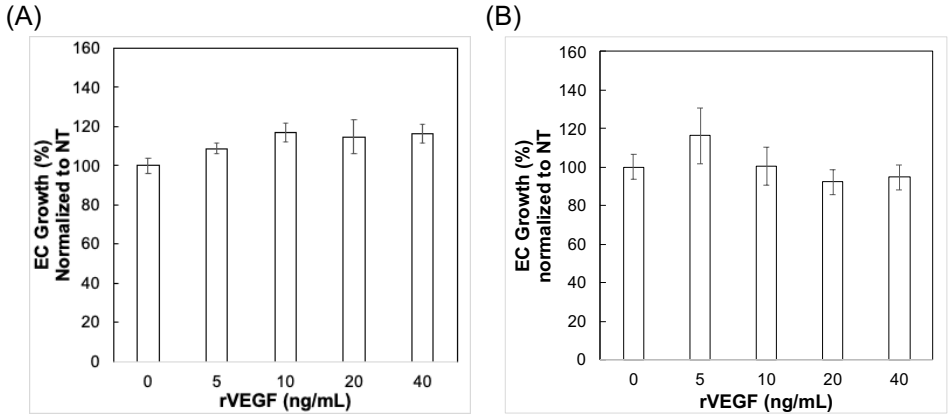

Figure 4.2. Endothelial cell growth on (A) tissue culture treated plate or (B) HCM hydrogel after 48 h treatment of different concentrations of recombinant VEGF-A. Each data point represents the mean ± standard deviation for n=4.

were plated at a density of 10,000 cells per cm2 for 7 h. ECs were treated with the conditioned medium collected from fibroblasts cultured in HCM, rVEGF-containing HCM, or VEGF-GAHCM (containing PEI polyplexes, 20 CP polyplexes, or 50 CP polyplexes) for 12h at 37 °C with 5% CO2. Then, conditioned media were removed, and ECs were washed and incubated with complete DMEM at 37 °C with 5% CO2 for 24 h. The growth of ECs was determined using an MTS assay, following the

manufacturer's procedure. Following the protocols above, the dependence of the growth of ECs on recombinant VEGF-A concentration (0, 5, 10, 20, and 40 ng/mL), incubation time, and culture in GAHCM vs. Tissue culture plates (TCPS) (Figures 4.1 and 4.2) were additionally investigated to expand our understanding of the effects of conditioned media treatment on the growth of ECs.

4.2.4 Chemotactic effect on ECs of VEGF-GAHCM containing fibroblasts

Prior to the study of EC invasion in fibroblasts cultured in VEGF-GAHCM, the chemotactic effects of VEGF-A-encoding polyplex-transfected fibroblasts on EC migratory behaviors were examined using an in vitro co-cultivation/invasion assays (Figure 4.3). Following the manufacturer's protocols, silicon culture-inserts with 2 wells (Ibidi Inc. USA) were placed on the tissue culture treated dish. Fibroblasts (10,000 cells/cm2) were seeded on one side of the well and ECs (10,000 cells/cm2) were seeded on the other side of the well. Fibroblasts were transfected with pVEGF/PEI, pVEGF/20 CP, or pVEGF/50 CP polyplexes for 1.5 h while the ECs on the other side were stained with calcein-AM (2 μM). Subsequently, the medium over both types of cells was removed and replaced with complete medium. After marking the outline of the culture insert on the dish with a permanent marker to define the initial gap between the ECs and the fibroblasts, the culture insert was carefully removed using tweezers. The cell invasion process to close the gap was monitored at 0, 6, 12, and 24 h after the removal of the culture insert using a Zeiss Axio Observer 7 inverted microscope with a 10× objective (Carl Zeiss Microscopy, LLC, White Plains, NY). The percentage of gap closure per time point for each group was analyzed manually using Fiji Image J software.

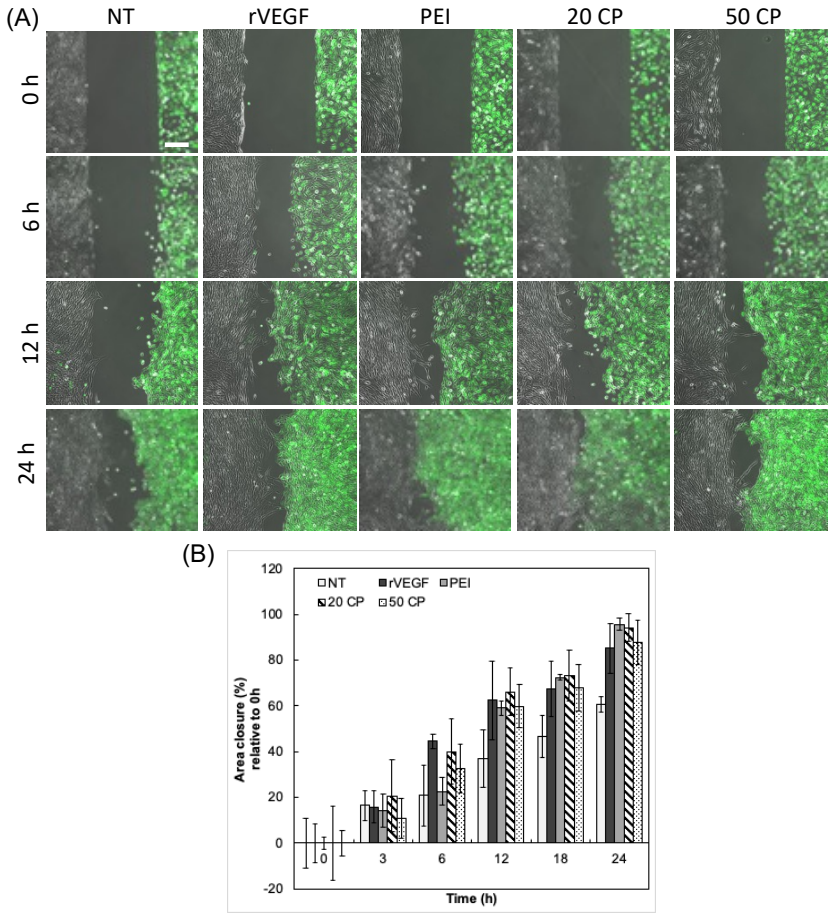

Figure 4.3. Fibroblasts transfection by VEGF encoding polyplexes mediated endothelial cell migration. (A) Representative microscopic images for migration of both fibroblasts (grey) and calcein-AM pre-stained endothelial cells (green) at different time points, 0, 6, 12, and 24 hr. Scale bar is 200 μm. (B) Image quantification for percentage of area closure relative to 0 h by both fibroblasts and endothelial cells migration. Each data point represents the mean ± standard deviation for n=4.

As described in our previous work (Chapters 2 and 3), VEGF-GAHCM was prepared and fibroblasts were cultured in the VEGF-GAHCM for 2, 4, or 6 days. Subsequently, ECs were added to the fibroblast-containing GAHCM, and the invasive behaviors of the ECs were examined during co-culture. Briefly, lyophilized VEGF-A-encoding polyplexes (PEI, 20 CP, or 50 CP; 20 μg/mL of pVEGF-A) were mixed into

neutralized collagen and incubated at 4 °C for 2 h. NIH/3T3 fibroblasts (100,000 cells/mL) suspended in 1× DPBS were added into the polyplex/neutralized collagen mixture and then Glycosil® was mixed into the fibroblast/neutralized collagen. After gelation, VEGF-GAHCM was incubated in complete DMEM at 37 °C with 5% CO2 for 2, 4, and 6 days. At each culture time point, calcein-AM (2 μM) pre-stained ECs (10,000 cells) were seeded on the top of the fibroblast-containing VEGF-GAHCM and incubated for an additional 24 hr. Calcein-AM-stained ECs were detected (λex. = 495 nm) with z-stack imaging of the full height of each hydrogel using a Zeiss LSM 880 confocal microscope with a EC Plan-Neofluar 10× objective (Carl Zeiss Microscopy, LLC, White Plains, NY). The mean intensity throughout the z-stack images was analyzed to determine the localization of ECs within the z-axis of each sample using Fiji ImageJ software.

4.2.5 Endothelial cell networks induced by growth in VEGF-GAHCM containing fibroblasts

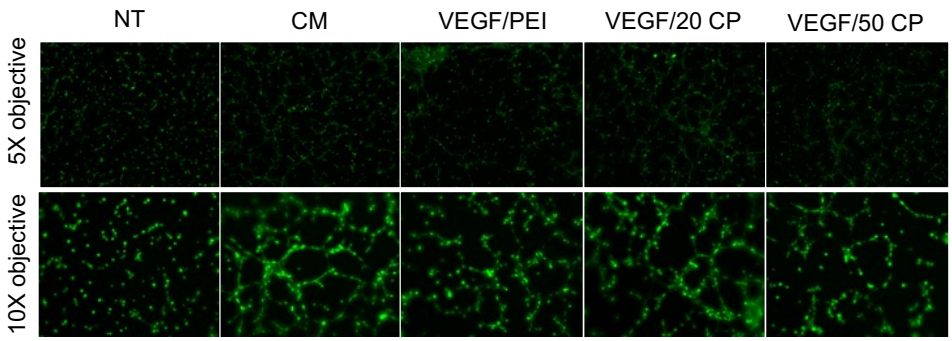

Figure 4.4. Representative microscopic images for Calcein-AM pre-stained endothelial cells (green) networks on Geltrex after 4 h treatment with fibroblasts condition media (CM), PEI-polyplex transfected fibroblasts condition media (VEGF/PEI), 20 CP-polyplex transfected fibroblasts condition media (VEGF/20 CP), and 50 CP-polyplex transfected fibroblasts condition media (VEGF/50 CP).

To evaluate pro-angiogenic potency, tube formation and EC reorganization into capillary-like structures were assessed in vitro following EC culture in VEGF-GAHCM containing fibroblasts. As described in previous literature (36-38), one day prior to the assay, ECs were starved in reduced serum DMEM containing 0.2% FBS and 1% P/S at 37 °C with 5% CO2 for 12 h. ECs were pre-stained with calcein-AM (2 µM) for 40 min to enable visualization under the confocal microscope, and cells were filtered through a 100 µm cell strainer to remove cell aggregates before seeding onto the hydrogels. In initial studies, the reduced growth factor basement membrane matrix GeltrexTM (12 mg/mL, 250 µL) was used to investigate the angiogenic potential of the conditioned media collected from fibroblasts that were bolus transfected with VEGF-A encoding polyplexes (Figure 4.4). In addition to GeltrexTM samples, hydrogels (250 µL) were prepared for analysis by mixing neutralized bovine collagen type I (Fibricol (4 mg/mL)) and Glycosil® at various concentrations of Glycosil® (0 mg/mL (Collagen only), 2 mg/mL (2HC = HCM), and 4 mg/mL (4HC)) to examine the effects of the hydrogel composition on EC network formation in conditioned media (Figure 4.5). After gelation at 37 °C on the 24-well plate, the ECs (75,000 cells) in 300 µL of conditioned media

were seeded on the top of the GeltrexTM or hydrogels and incubated at 37 °C with 5% CO2 for 4 h. Then, calcein-AM pre-stained EC networks on the GeltrexTM or hydrogels were visualized using a Zeiss LSM 880 confocal microscope with an EC Plan-Neofluar 10× objective.

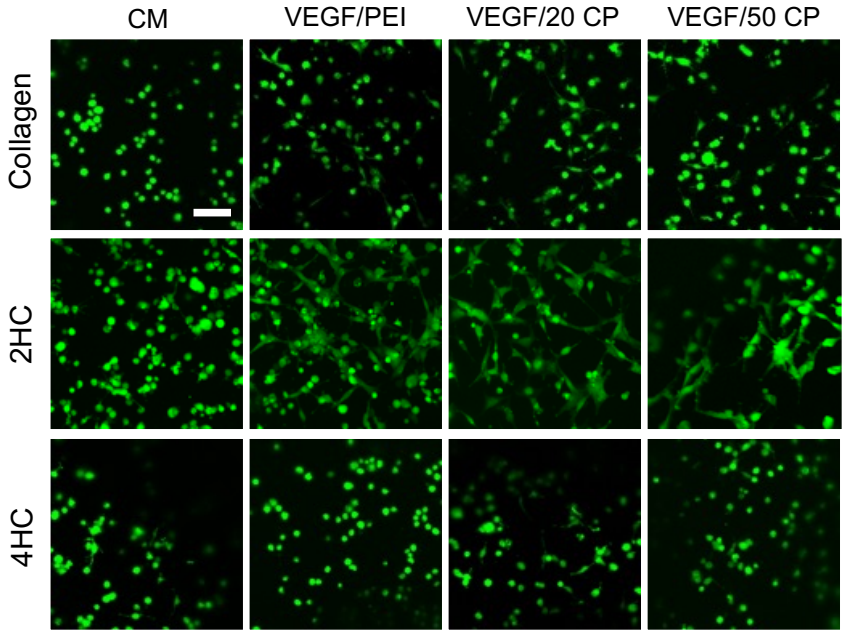

Figure 4.5. Representative confocal images of calcein-AM pre-stained endothelial cells (green) networks on collagen (0.4%), 2HC or HCM (0.2% HA + 0.4% Collagen), and 4HC (0.4% HA + 0.4% Collagen) after 4 h treatment with fibroblast culture condition media (CM), PEI-polyplex transfected fibroblast culture condition media (VEGF/PEI), 20 CP-polyplex transfected fibroblast culture condition media (VEGF/20 CP), and 50 CP-polyplex transfected fibroblast culture condition media (VEGF/50 CP). Scale bar is 80 μm.

As described in Section 2.4., fibroblasts (100,000 cells/mL) were cultured in an HCM hydrogel, HCM + rVEGF hydrogel, or VEGF-GAHCM with polyplexes (PEI, 20 CP, or 50 CP) (10 μL of each sample) for 2, 4, 6, or 10 days. Samples were prepared in a μ-Slide Angiogenesis (Ibidi Inc. USA) to evaluate the pro-angiogenic effects via analysis of EC differentiation into capillary-like networks. Half of the culture medium was replaced with fresh culture medium every two days. After a 12 h i ncubation in reduced serum DMEM containing 0.2% FBS and 1% P/S at 37 °C with 5% CO2,

calcein-AM pre-stained and filtered ECs (10,000 cells) were seeded on the top of each sample and incubated at 37 °C under 5% CO2 for an additional 24 h. The EC networks were visualized with z-stack imaging using a Zeiss LSM 880 confocal microscope with an EC Plan-Neofluar 10× objective. In addition, the pro-angiogenic potency of HCM hydrogels or fibroblast-containing HCM hydrogels with or without rVEGF was examined to screen the effects of the various samples on EC network formation at each incubation time point (days 2, 4, 6, and 10) (Figure 4.6). Furthermore, the pro-angiogenic potency of conditioned media from both fibroblasts that were bolus transfected with pVEGF/PEI polyplexes, and fibroblasts that were cultured in HCM hydrogels for 2, 4, 6, or 10 days of incubation was evaluated. The result showed that the presence of both fibroblast and rVEGF or VEGF in the condition media of fibroblast transfection exerted the greatest effects on EC network formation. The extent of EC network formation was different depending on the fibroblast culture time. But that at all incubation times, the samples with both fibroblast and rVEGF/VEGF showed greater EC network formation than the other samples.

The z-stack images for each sample were imported into Imaris software (Oxfold instruments) for 3-D visualization and analysis using a Filament Tracer function to reconstruct the filamentous microstructures and volume of the EC networks (39, 40). The filamentous microstructures were quantified for the total volume of the network using an automated method with the selected intensity threshold; the average of a total of five replicates per sample was reported. The average diameter of the network was calculated using a manual distance measurement function to quantify the average of the diameters of the individual branches in each image. Since the number of branches varied from image to image, the number of manual distance measurements also was different for each image.

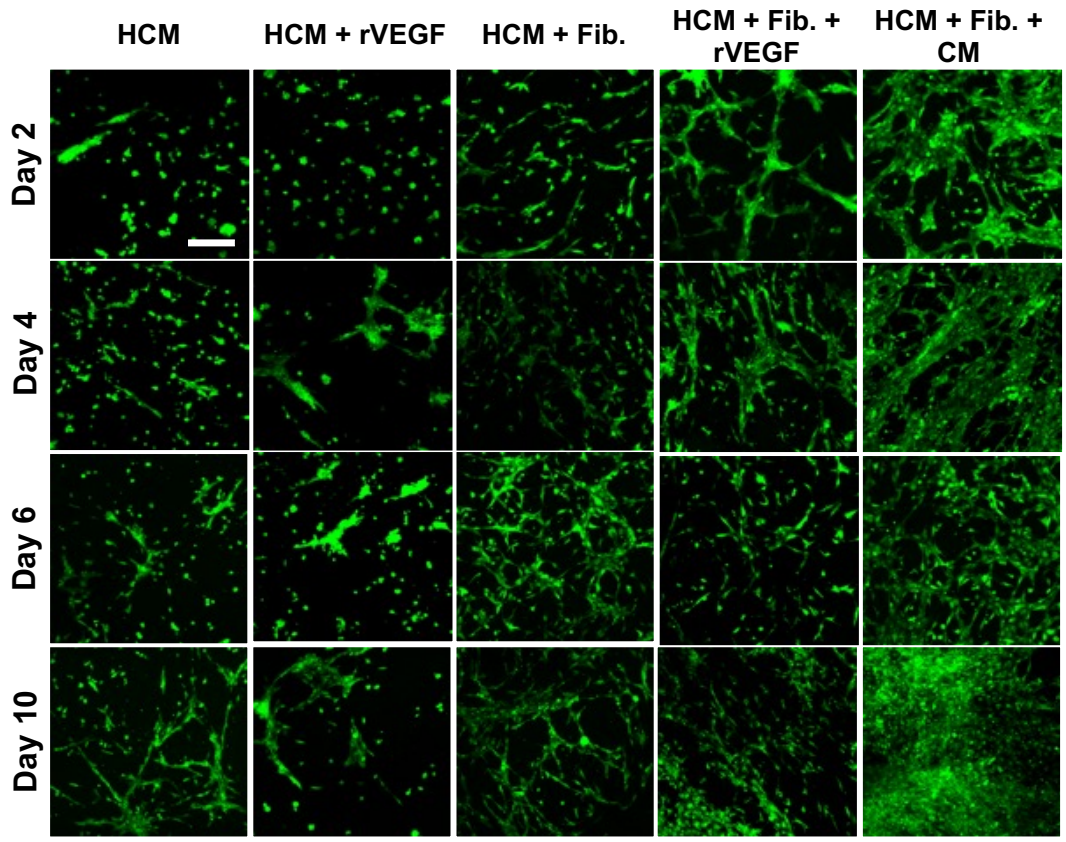

Figure 4.6. Representative confocal images of calcein-AM pre-stained endothelial cells (green) networks after 24 h incubation on HCM, HCM with recombinant VEGF in the media (HCM + rVEGF), fibroblast cultured in HCM (HCM + Fib.), fibroblast cultured in HCM with recombinant VEGF in the media (HCM + Fib. + rVEGF), and fibroblast cultured in HCM with VEGF/PEI polyplex transfected fibroblasts condition media (HCM + Fib. + CM) at days 2, 4, 6, and 10. Scale bar is 200 μm.

4.2.6 CD31 immunostaining and image analysis

The expression of CD31 by EC networks cultured on HCM hydrogels, HCM + rVEGF hydrogels, or VEGF-GAHCM hydrogels equipped with PEI, 20 CP, or 50 CP polyplexes (where fibroblasts were pre-cultured for 6 days prior to EC seeding) was evaluated via immunostaining for CD31. After a 24 h incubation of ECs on the samples, both EC networks and fibroblasts were fixed with 4% paraformaldehyde for 30 minutes, permeabilized with 0.2% Triton X-100 for 45 min, and blocked with 3% BSA in PBS at room temperature overnight. Samples were incubated for 2 days to ensure the antibody penetration into antigen of the cells within in the hydrogel at room temperature with Alexa Fluor® 555-conjugated Rabbit CD31 (PECAM-1) polyclonal antibody (1:100), Phalloidin-647 (1:100; Life Technologies), and the nuclear stain Hoechst 33258 (1:500; Life Technologies) in a 1% BSA PBS solution at room temperature with shaking. For control samples, Alexa Fluor® 555-conjugated Rabbit IgG Isotype Control

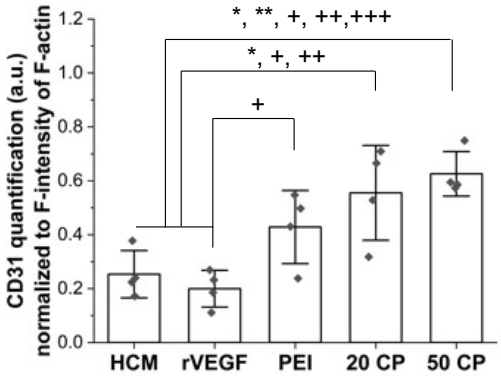

Figure 4.7. Image quantification for CD31 expression on the endothelial cells normalized to F-actin expression. Each data point represents the mean ± standard deviation for n=4. +P<0.05, ++P<0.001 compared to ECM, #P<0.05, ##P<0.001 compared to rVEGF, *P<0.05, **P<0.001 compared to PEI

(1:100) with Phalloidin-647 and Hoeschst 33258 were added and incubated with the cell

samples for 2 days. After incubation, the samples were rinsed by incubation in 3% BSA in 0.05% Tween-20 in PBS for 1 day, and cells were subsequently visualized by z-stack imaging using a Zeiss LSM 880 confocal microscope with a 10× objective. The z-stack images were analyzed as a z-projection with maximum intensity using Fiji ImageJ software. CD31 expression was quantified using the sum of the fluorescence intensity of CD31 and further normalization to the sum of the fluorescence intensity of F-actin in the same sample (Figure 4.7), with the same threshold setting for each channel to avoid complications from the background signal.

4.2.7 Murine splinted excisional wound healing studies and histological analysis

As described in our previous publication (Chapter 3), murine splinted excisional wound healing studies were performed to evaluate the capacity of VEGF-GAHCM to stimulate wound healing. Briefly, 8-week-old BALB/cJ mice were anesthetized using isoflurane and the fur on the back of each mouse was removed using an electric razor. After sterilizing the shaved regions, one wound per mouse was created at the mouse's midline at the level of the shoulders using a biopsy punch (D = 5 mm). Then, the wound was treated by application of 35 μL of saline, HCM gel with/without rVEGF (1 μg per wound), or VEGF-GAHCM with/without CMP tethering (200 μg/mL of pVEGF per wound formulated into PEI or 50 CP polyplexes). Subsequent to treatment, a silicone splint (O.D. = 14 mm and I.D. = 6.35 mm) was attached onto the top of each wound by dropwise addition of Krazy Glue® (41, 42), such that the inside orifice of the silicon ring encircled the wound; OpSite wound dressing was applied on the top side of the attached silicone ring. To further secure the splint, 6 to 8 interrupted sutures (5-0 Vicryl Suture with Cutting Needle, Ethicon Inc.) were placed around the outer edge of the O-ring. The splints were removed after 7 days, as mice typically self-remove the splints after this time period, which can result in secondary damage that complicates analysis of results (41). For the 7-day treatment groups, mice were euthanized immediately after

the splints were removed. Meanwhile, for the 14-day treatment groups, mice were monitored for an additional 7 days after splint removal, at which point they were euthanized (14 days after treatment). After the mice were euthanized, the wound skin tissue was collected using surgical scissors, and the tissue was fixed in 2% paraformaldehyde. For histology/immunohistochemistry analysis, the tissues were embedded in Tissue-Tek OCT compound for freezing and cut into 10 µm sections. Tissue sections on the glass slide were stained with Harris hematoxylin (Leica Biosystems, Deer Park, IL) and eosin (H&E) or Masson's trichrome (Figure 4.8) to investigate re-epithelialization, granulation tissue formation, and collagen deposition for wound repair analysis.

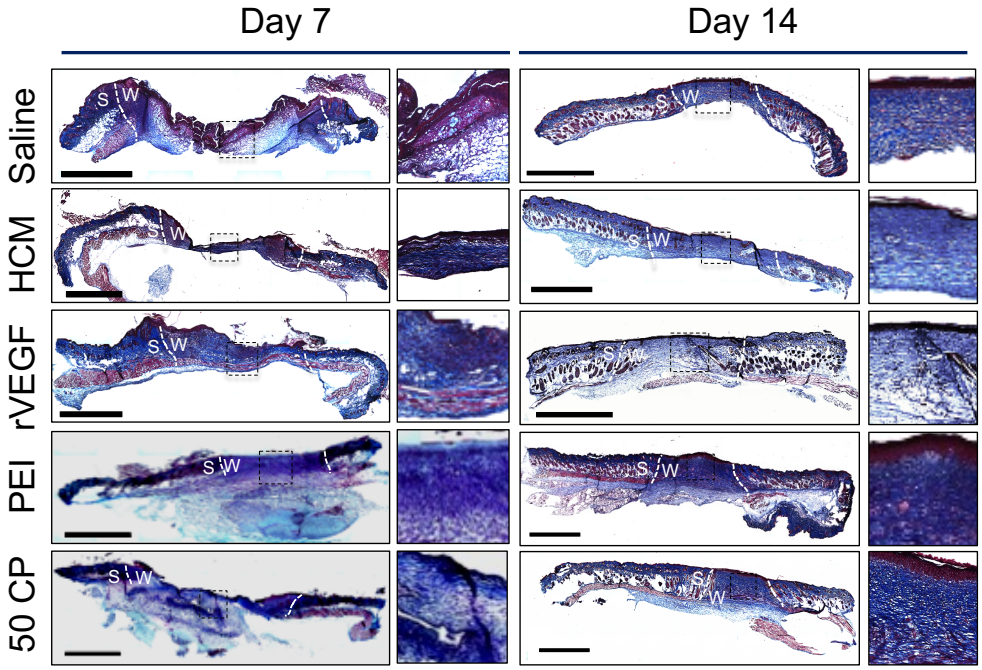

Figure 4.8. *In vivo* wound healing evaluation using histological analysis of mouse splinted excisional wounds treated with saline, HCM hydrogel, rVEGF+HCM hydrogel, and VEGF-GAECM with PEI, 20 CP, and 50 CP after 7 and 14 days. The tiled images of Masson's Trichrome stained mouse skin wound tissue section at 7 or 14 days of treatments and the zoom-in image of black-dotted box in the tiled images. s = native skin and w = wound. Black arrow indicates the scab. Scale bar is 1.5 mm and scale bar for zoom-in image is 250 µm.

4.2.8 CD31/α-SMA immunostaining and blood vessel analysis

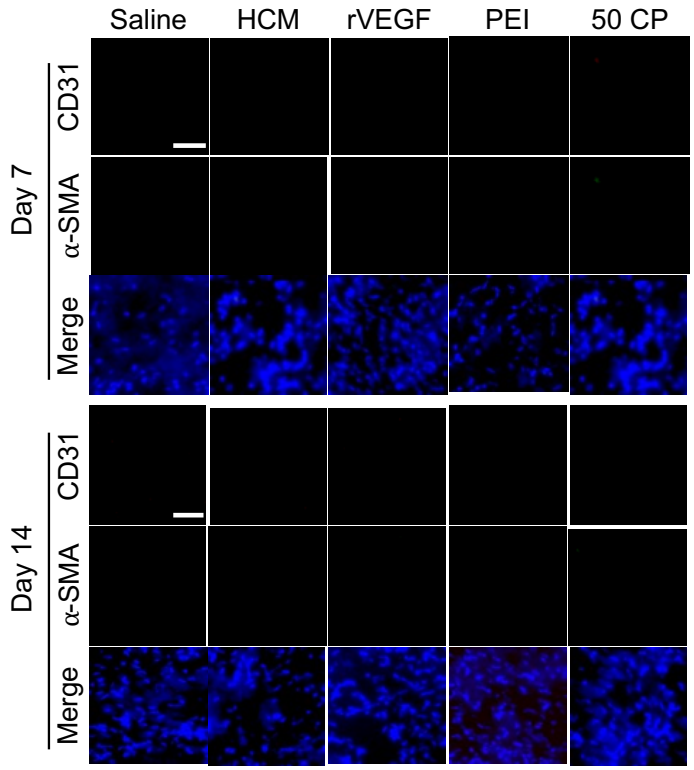

Figure 4.9. The representative confocal microscope images of IgG control antibodies for CD31/α-SMA immunostained mouse skin wound tissue section after 7 or 14 days of treatment with saline, HCM hydrogel, rVEGF+HCM hydrogel, and VEGF-GAECM with PEI, 20 CP, and 50 CP after 7 and 14 days. (CD31 for red, α-SMA for green, and nuclei for blue). Scale bar is 40 μm.

To assess blood vessel formation in the mouse wound tissue sections, tissue sections were stained for CD31, α-SMA, and nuclei as described in section 2.6. After permeabilization with 0.4% Triton X-100 in PBS and blocking with 5% goat serum, tissue section slides were incubated for 2 h with mouse anti-goat IgG (0.01 mg/mL, Sigma-Aldrich) in 1% goat serum in PBS at room temperature. After rinsing three times with PBS, tissue section slides were incubated with α-SMA-FITC antibody (1:250), Alexa Fluor®555-Conjugated Rabbit CD31(PECAM-1) polyclonal antibody (1:250),

and the nuclear stain Hoechst 33258 (1:500) overnight at 4 ºC (Figure 4.9). For control samples, tissue sections were incubated with mouse IgG2a-FITC control antibody (1:250), Alexa Fluor® 555-conjugated Rabbit IgG Isotype Control antibody (1:250), and the nuclear stain Hoechst 33258 (1:500) overnight at 4 ºC. After rinsing with PBS, the tissue sections were mounted with ProLongTM Gold Antifade mounting solution. The stained tissue sections were visualized using a Zeiss Axio Observer 7 inverted microscope with 10× objective. Using the tile function, entire tissue sections were analyzed for CD31/α-SMA expression to identify blood vessels in the wound tissue sections via Fiji ImageJ software. Five images per mouse (over the same area per mouse) were taken for each treatment group (N = 6 mice) to provide 30 images per group for analyzing the total number of blood vessels and the total number of mature blood vessels in each wound. As in the previous literature (43-45), the total number of blood vessels per image was manually counted based on the co-localization of signals for CD31 and nuclear stain to define a closed circle as an individual blood vessel. The number of mature blood vessels per image was manually counted based on the co-localization of CD31, α-SMA, and nuclear stain signals to identify vessels for which greater than half of the area in the closed circle was co-stained with CD31 and α-SMA.

4.2.9 Statistical Analysis

Unless indicated, all experimental data were expressed as the mean ± standard deviation of the mean. The statistical significance was analyzed using Origin (OriginLab Corporation). Sample groups were compared using either one-way (Figure 4.16(B) and 4.18(B)) for one independent variable or two-way (Figure. 4.10,4.15, 4.18 (A), and 4.19 (B-C)) for two independent variables analysis of variance (ANOVA) with a Tukey's post-hoc test for multiple comparison with a significance of 0.05

4.3 Results

4.3.1 EC mitogenesis

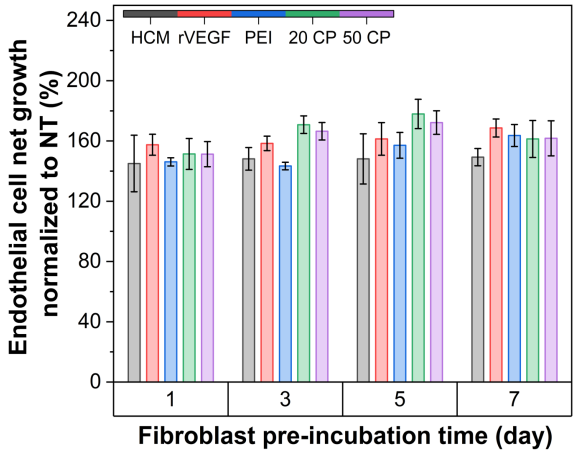

Figure 4.10. Endothelial cell net growth stimulated by the condition media collected from fibroblasts cultured in VEGF-GAHCM at days 1, 3, 5, and 7. The net growth (%) was normalized to the endothelial cell growth without the condition media treatment. Each data point represents the mean ± standard deviation for n=4. The statistically significant differences state +P<0.05 compared to HCM and *P<0.05 compared to PEI.

I predicted that the different levels of VEGF-A gene expression induced by the GAHCM biomaterials would result in EC mitogenic responses correlated with the level of gene expression. Therefore, I assessed the net growth of ECs stimulated by the conditioned medium collected from fibroblasts cultured in various biomaterial samples by measuring EC metabolic activity. Specifically, the conditioned medium was collected from fibroblasts cultured in VEGF-GAHCM hydrogels (containing PEI, 20 CP, or 50 CP polyplexes), HCM hydrogels, or HCM + rVEGF hydrogels after 1, 3, 5, or 7 days of fibroblast culture. This experimental design enabled analysis of how both fibroblast culture time and the mechanism of VEGF-A delivery affected the net growth of ECs (Figure. 4.10). As predicted, the conditioned medium collected from fibroblast

culture induced the growth of ECs in all samples. The conditioned medium collected from fibroblasts cultured for one day in either of the control HCM hydrogels or HCM + rVEGF hydrogels was pro-mitogenic, and stimulated the growth of the ECs by ~160%. Longer durations of fibroblast preculture in these control HCM or HCM + rVEGF hydrogels did not increase mitogenic activity, however, based on the lack of evolution in EC growth after stimulation with conditioned medium samples collected after extended preculture. Moreover, the lack of a significant difference in the activity of conditioned medium collected from fibroblasts grown with and without rVEGF stimulation indicated that the rVEGF protein lacked stability under the culture conditions.

On the other hand, for the VEGF-GAHCM groups, the fibroblast preculture time clearly influenced the growth of ECs induced by conditioned medium collected, suggesting that the activity and/or amount of VEGF produced by fibroblast transfection using VEGF-GAHCM changed as a function of fibroblast culture time. The conditioned medium collected from fibroblasts cultured for one day in all three of the VEGF-GAHCM samples was pro-mitogenic, and resulted in similar EC growth levels (~150%) as the conditioned medium collected from fibroblasts grown in HCM hydrogels and HCM + rVEGF hydrogels for one day. The growth of ECs induced by the conditioned medium from VEGF-GAHCM containing PEI polyplexes increased monotonically as the fibroblast preculture time was extended (e.g., there was a 5% increase in EC growth using conditioned medium collected after one day vs. five days of fibroblast preculture). Meanwhile, the growth of ECs induced by conditioned medium collected from VEGF-GAHCM containing either 20 CP or 50 CP polyplexes consistently increased as the fibroblast preculture time was extended up to five days of preculture, when it reached a

maximal level. Specifically, ECs exhibited 20 % more growth in five-day vs. one-day 20 CP precultured samples, and 15% more growth in five-day vs. one-day 50 CP precultured samples. Additionally, the growth of ECs induced by the day-3 conditioned medium from VEGF-GAHCM with 20 CP was significantly increased as compared to EC growth induced by day-3 conditioned medium from VEGF-GAHCM with PEI. This indicates that CMP modification enhanced VEGF gene transfer and/or the corresponding mitogenic activity of expressed VEGF.

4.3.2 EC chemotaxis

I predicted that the sustained VEGF production induced by GAHCM with CMP modification would result in prolonged VEGF activity resulting in EC chemotaxis. Therefore, I assessed VEGF-A stimulated EC chemotaxis by monitoring the migratory behaviors of ECs grown on the fibroblast-containing biomaterials. After I confirmed the chemotactic activity of the fibroblast-expressed VEGF gene product on ECs (Figure 4.3), I applied ECs on the top of fibroblast-containing HCM hydrogels, HCM + rVEGF hydrogels, or VEGF-GAHCM hydrogels containing PEI, 20 CP, or 50 CP polyplexes. In all experiments, fibroblasts were pre-cultured in the hydrogels for 3, 5, or 7 days prior to the addition of ECs to enable analysis of the invasive behaviors of ECs as a function of fibroblast-mediated VEGF-A gene expression (Figure 4.11). Since the VEGF was produced by transfected fibroblasts within the VEGF-GAHCM samples, I expected that the fibroblast distribution within the samples would influence the migratory behaviors of the ECs. Fibroblast distribution in the matrices was therefore also characterized; based on the results of Figure 4.12, the schematics of fibroblast distribution within each sample at the various culture time points were placed on the EC migration plots for each group. Briefly, fibroblasts in the HCM hydrogel or in the rVEGF-HCM hydrogel were

dispersed uniformly in the z-direction of the gels over 5 days of culture, and then the fibroblasts gradually migrated to the top of the hydrogels by day 7. On the other hand, the fibroblast distribution in VEGF-GAHCM showed fibroblasts migrating toward the bottom of the hydrogel starting from day 3; in particular, approximately 90% of the fibroblasts were located on the bottom of the hydrogel in the 50 CP VEGF-GAHCM at day 7 of culture.

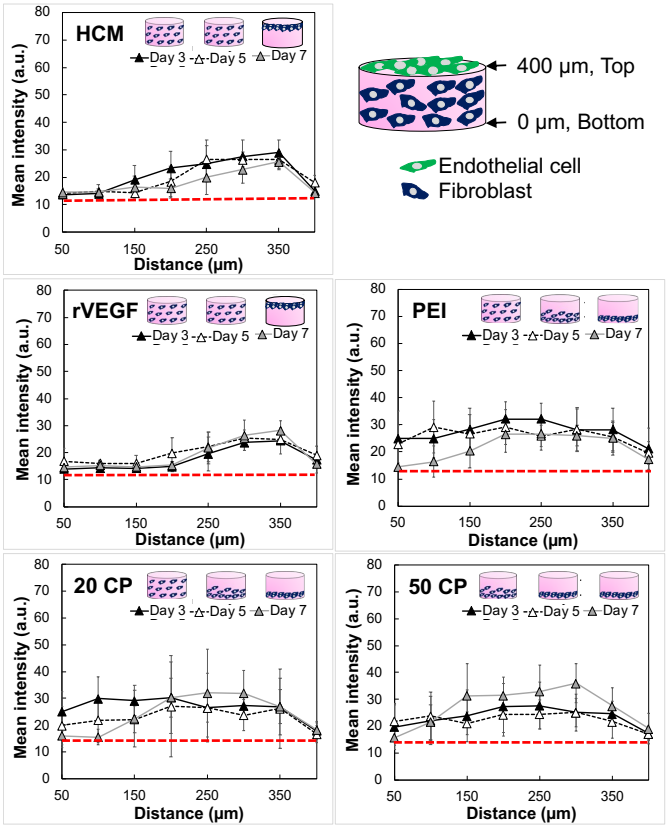

Figure 4.11. Endothelial cell invasion in fibroblasts cultured in HCM hydrogel, rVEGF-HCM hydrogel, VEGF-GAHCM with PEI, 20 CP, or 50 CP at days 3, 5, and 7. The schematics in the graph are fibroblast location in VEGF-GAHCM at days 3, 5, and 7. The red dotted line is the minimum threshold used to detect signal of calcein-AM pre-stained endothelial cells on the z-stack images of full thickness of samples. Each data point represents the mean ± standard deviation for n=7.

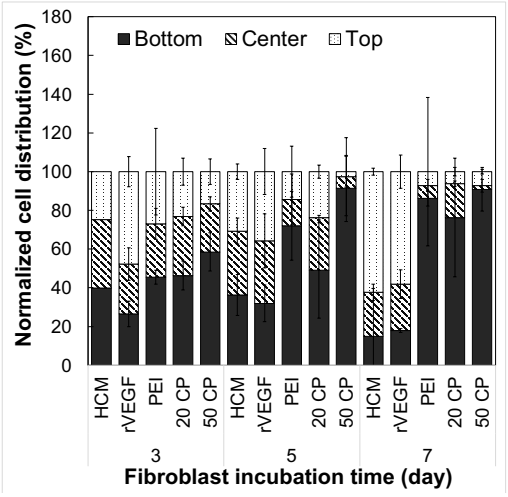

Figure 4.12. NIH 3T3 Fibroblast distribution within VEGF-GAHCM for 3, 5, or 7 days of culture at three different z-stack (30 μm) location (Top (Dotted), Center (Stripe), Bottom (Dark Grey)) using normalized to total fibroblast count. Each data point represents the mean ± standard deviation for n=4.

ECs on both HCM and HCM + rVEGF hydrogels mostly were localized in the top portion of the hydrogels, consistent with the fact that the fibroblasts did not produce VEGF and they also were distributed near the top of the hydrogels throughout the preculture time, indicating that the ECs were less invasive in the HCM and HCM + rVEGF hydrogels. On the other hand, fibroblasts migrated towards the bottom of the VEGF-GAHCM hydrogels throughout the preculture time, and therefore the ECs on the VEGF-GAHCM groups similarly tended to migrate into the hydrogels. The invasive behavior of ECs into the 50 CP VEGF-GAHCM was persistent even at 7 days of fibroblast preculture, suggesting that not only that the location of the fibroblasts within the 50 CP VEGF-GAHCM, but also the VEGF amounts produced by the transfected fibroblasts, might guide the migratory behaviors of ECs within VEGF-GAHCM.

4.3.3 *In vitro* pro-angiogenic potency in ECs

I predicted that the sustained VEGF production by fibroblasts cultured in VEGF-GAHCM with CMP modification would support prolonged pro-angiogenic activity. Therefore, I analyzed EC network formation by seeding the ECs on the fibroblast-containing matrices (HCM hydrogel, HCM + rVEGF hydrogel, or VEGF-GAHCM hydrogels with PEI, 20 CP, or 50 CP polyplexes) after fibroblasts were cultured in the matrices for 2, 4, 6, or 10 days. After 24 h of EC culture on the fibroblast-containing matrices, EC network formation was assessed (Figure 4.13). As predicted, the

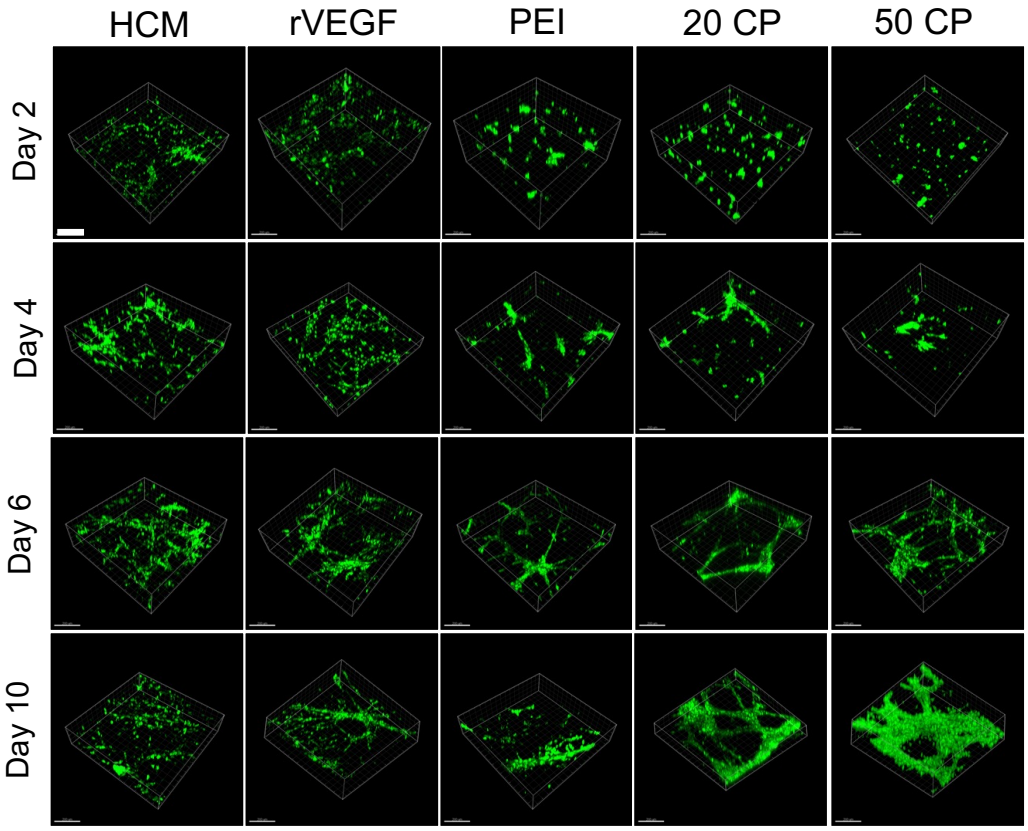

Figure 4.13. Endothelial cellular networks on fibroblast cultured in HCM hydrogel, rVEGF-HCM hydrogel, VEGF-GAHCM with PEI, 20 CP, or 50 CP at days 2,4,6, and 10. The representative 3D plot of z-stack images for calcein-AM pre-stained endothelial cells (Green). Scale bar is 200 μm.

representative 3D plots of z-stack images demonstrated network formation by the ECs, with the extent of network formation dependent on the fibroblast culture time and type of matrix. On the fibroblast-containing HCM and HCM + rVEGF hydrogels, ECs formed mainly web-like clusters of connecting spindle-shaped cells, and the density of these web-like EC networks increased as a function of the fibroblast culture time. In contrast, ECs on fibroblast-containing VEGF-GAHCM hydrogels progressively formed networks as the fibroblast preculture time was lengthened (Figure 4.13). On all VEGF-GAHCM matrices precultured for 2 days, ECs formed clusters of cobblestone-like cells, while on the VEGF-GAHCM matrices precultured for 4 days, ECs began to sprout and connect with neighboring cell clusters. On the VEGF-GAHCM matrices precultured for 6 days, ECs formed a defined set of web-like clusters of connecting spindle-shaped cells, but the networks were visually different among the different VEGF-GAHCM groups (PEI, 20 CP, or 50 CP polyplexes). Lastly, on VEGF-GAHCM matrices precultured for 10 days, VEGF-GAHCM with CMP modification (20 CP and 50 CP) continued to stimulate the formation of EC networks, indicating that the sustained production of VEGF by fibroblasts transfection using VEGF-GAHCM with CMP modification extended VEGF activity to stimulate the EC network formation (chapter 2).

The EC networks shown in Figure 4.13 were analyzed via image quantification to determine the overall interconnected network volumes (38, 46, 47), identify the overall features of the network, and measure the average diameter of the tube-like structure (48, 49) (Figure. 4.14). The total volume of an EC network is defined as the sum of all volumes between two branch points or between a branch point and a terminal point. EC networks formed on fibroblast-containing hydrogel samples after 2 days of fibroblast preculture exhibited significantly larger network volumes in the HCM

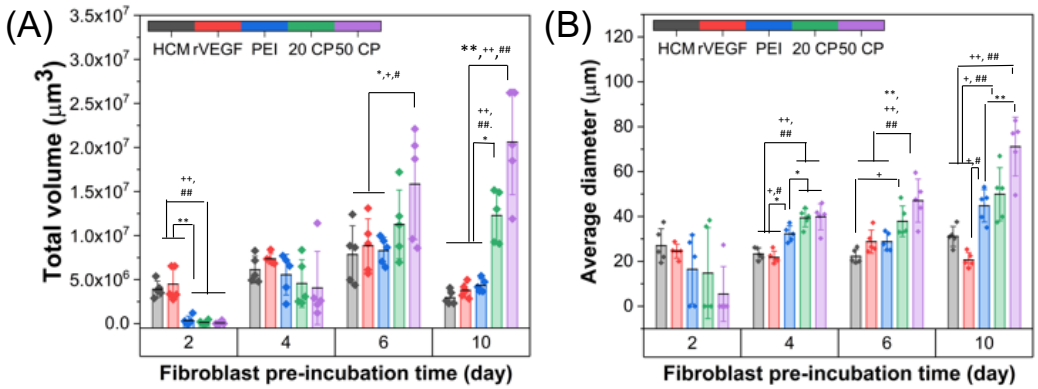

Figure 4.14. Image quantification for endothelial cellular networks on fibroblast cultured in HCM hydrogel, rVEGF-HCM hydrogel, VEGF-GAHCM with PEI, 20 CP, or 50 CP at days 2,4,6, and 10. (A) The total volume of capillary network. (B) The average diameter of capillary network. Each data point represents the mean ± standard deviation for n=5. +P<0.05, ++P<0.001 compared to HCM, #P<0.05, ##P<0.001 compared to rVEGF, *P<0.05, **P<0.001 compared to PEI

hydrogel and the HCM + rVEGF hydrogel as compared with the VEGF-GAHCM hydrogel groups, presumably due to the smaller number of viable fibroblasts from the mild cytotoxic effects of polyplex present in the VEGF-GAHCM groups at the initial culture timepoint (chapter 2). After 4 days of fibroblast preculture, the total volume of the EC networks in the VEGF-GAHCM groups was increased by approximately 6-fold as compared to the EC network volume in the VEGF-GAHCM samples in which fibroblasts were precultured for 2 days; furthermore, at the 4 days preculture timepoint, EC network volumes in VEGF-GAHCM exhibited a similar size as the EC network volumes in HCM hydrogel and HCM + rVEGF hydrogel. Moreover, when fibroblasts were precultured for 6 days, the total EC network volumes consistently increased in all groups versus the EC network volumes on 4-day fibroblast precultured samples, and, in particular, VEGF-GAHCM with 50 CP polyplexes stimulated the most significantly increased total volume of EC network at this preculture timepoint, as compared to HCM

hydrogel, HCM + rVEGF hydrogel, and VEGF-GAHCM with PEI polyplexes. In addition, fibroblast containing VEGF-GAHCM with CMP modification cultured for 10 days sustained the formation of EC networks with significantly larger volumes than those observed for the HCM hydrogel, HCM + rVEGF hydrogel, and VEGF-GAHCM with PEI polyplexes. This quantification analysis agreed with our visual observation in Figure 4.13 that the sustained production of VEGF by fibroblasts in VEGF-GAHCM with CMP modification cultured for 6 and 10 days supported the formation of EC networks with a larger volume. Moreover, quantitative analysis of the average diameter of the EC networks indicated that the sustained VEGF activity by VEGF-GAHCM, especially with CMP modification (chapter 2), resulted in EC networks with larger diameters. For instance, the average diameters of EC networks on VEGF-GAHCM with 50 CP after 24 h incubation of ECs on fibroblasts precultured for 4, 6, or 10 days were significantly larger than those in the HCM hydrogel, HCM + rVEGF hydrogel, and VEGF-GAHCM with PEI polyplexes. These data suggest that the sustained VEGF gene transfer to fibroblasts in the VEGF-GAHCM with 50 CP promoted the enhanced duration of VEGF activity (chapter 2) and stimulated the formation of EC networks with larger volumes and bigger diameters.

To confirm the presence of EC intercellular connections in the observed EC networks, the networks formed on fibroblast-containing HCM hydrogels, HCM + rVEGF hydrogels, or VEGF-GAHCM hydrogels with PEI, 20 CP, or 50 CP polyplexes precultured for 6 days were evaluated to detect the expression of CD31 (PECAM-1), which is an EC cell-cell adhesion molecule and an important factor during angiogenesis (50) (Figure 4.15). The representative confocal images showed the CD31-labeling of

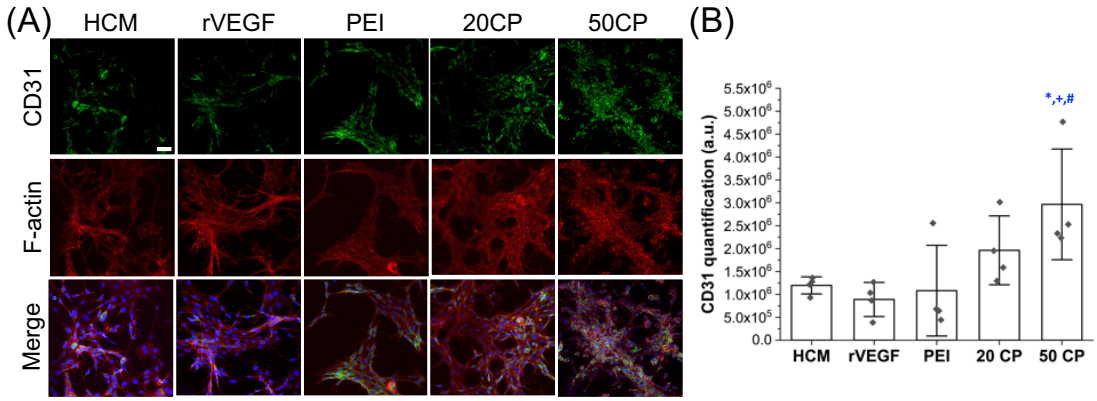

Figure 4.15. CD31 immunostaining on the endothelial cells network formed on fibroblast cultured in HCM hydrogel, rVEGF-HCM hydrogel, VEGF-GAHCM with PEI, 20 CP, or 50 CP at day 6. (A) The representative confocal microscope images of CD31 expressed endothelial cells within the capillary network. CD31 (Green) and F-actin (Red). Scale bar is 50 µm. (B) Image quantification for CD31 expression on the endothelial cells within the capillary network. Each data point represents the mean ± standard deviation for n=4. +P<0.05 compared to HCM, #P<0.05 compared to rVEGF, and *P<0.05, compared to PEI

ECs and F-actin/Hoechst labeling of both fibroblasts and ECs within the samples. EC networks on VEGF-GAHCM with CMP modification demonstrated more positive CD31 signals in the formed networks as compared with other groups. Additionally, the quantification of CD31 expression on EC networks using the integrated density of fluorescence intensity calculation revealed that CD31 expression was greater for VEGF-GAHCM with CMP modification. In particular, CD31 expression in 20 CP polyplex containing samples was not statistically different from expression in other groups; by contrast, CD31 expression in 50 CP polyplex containing samples was significantly greater as compared to expression in HCM hydrogel, HCM + rVEGF hydrogel, and VEGF-GAHCM with PEI polyplexes, suggesting that the networks formed on VEGF-GAHCM with 50 CP occurred through the formation of stable intercellular connections between ECs.

4.3.4 *In vivo* wound healing analysis

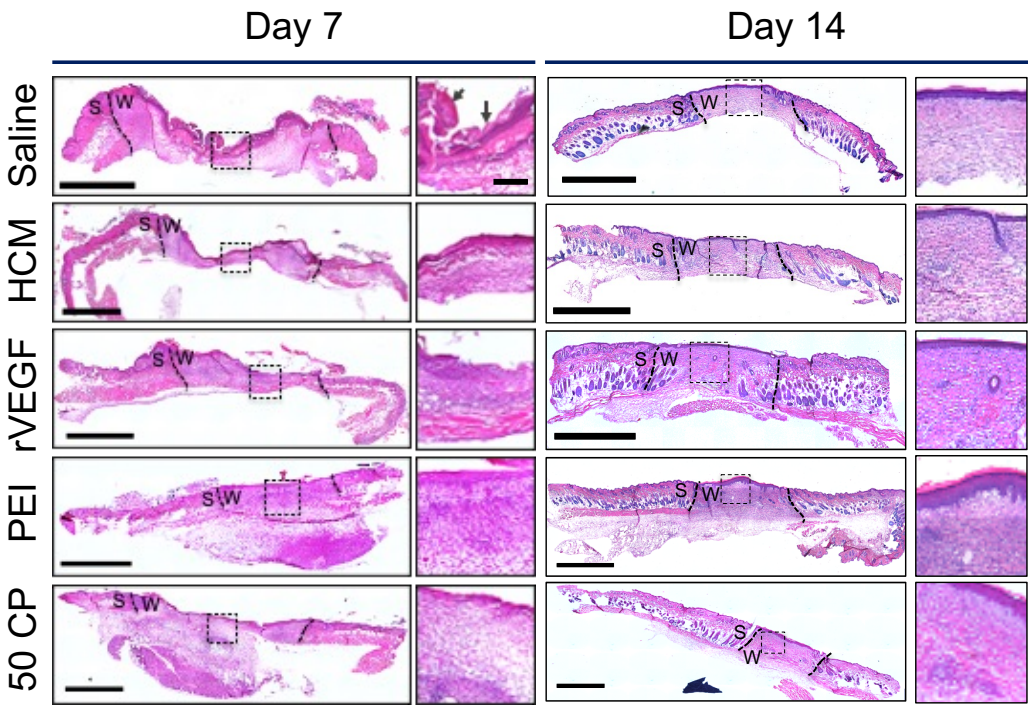

Figure 4.16. In vivo wound healing evaluation using histological analysis of mouse splinted excisional wounds treated with saline, HCM hydrogel, rVEGF+HCM hydrogel, and VEGF-GAHCM with PEI, 20 CP, and 50 CP after 7 and 14 days. The tiled images of H&E stained mouse skin wound tissue section at 7 or 14 days of treatments and the zoom-in image of black-dotted box in the tiled images. s = native skin and w = wound. Black arrow indicates the scab. Scale bar is 1.5 mm and scale bar for zoom-in image is 250 μm.

To characterize possible VEGF-GAHCM-stimulated improvements in wound healing responses, I analyzed histological stained tissues which were harvested from murine excisional splinted skin wounds after 7 or 14 days of treatment with saline, HCM hydrogel, HCM + rVEGF hydrogel, or VEGF-GAHCM hydrogel with PEI, 20 CP, or 50 CP polyplexes. Our previous studies (chapter 3) demonstrated that no adverse effects arose from the surgical procedure and materials, and the extended VEGF bioactivity induced by 50 CP VEGF-GAHCM treatment triggered sustained α-SMA expression,

resulting in accelerated closure. Figure 4.16 shows representative images of H&E-stained tissue sections after 7 or 14 days of treatment. At day 7, granulation tissue formation initiated to fill the wound in all groups, although scab formation (indicated by the black arrow) was evident in the saline group. Moreover, the wounds were completely closed in all groups at day 14, with granulation tissue formation. The formation of granulation tissue was further confirmed by Masson's Trichrome staining, indicating collagen deposition in the healed wounds (Figure 4.8).

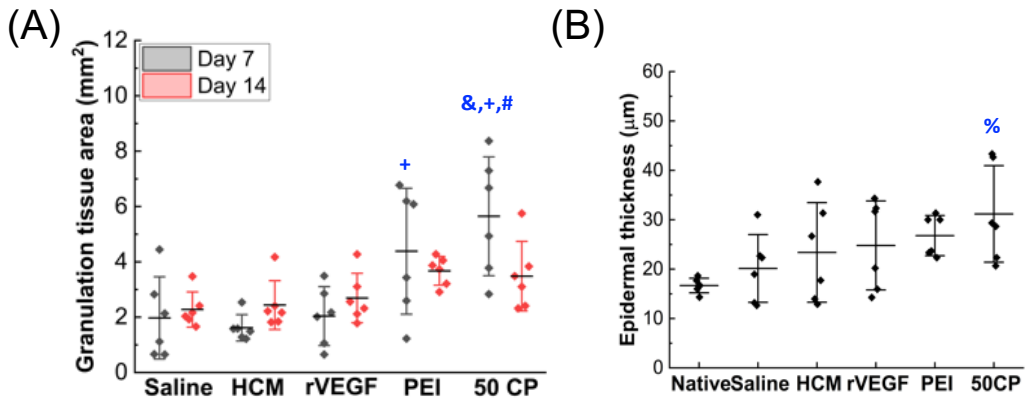

Figure 4.17. In vivo wound healing evaluation using image analysis of histological stained mouse splinted excisional wounds treated with saline, HCM hydrogel, rVEGF+HCM hydrogel, and VEGF-GAHCM with PEI, 20 CP, and 50 CP. (A) Granulation tissue area quantification after 7 and 14 days of treatment. Each data point represents the granulation tissue area for each mouse per group. (B) Epidermal thickness measurements after 14 days of treatment. Each data point represents the average of epidermal thickness in the wound per field of image for three images per each mouse. The horizontal line represents the mean ± standard deviation for total 6 mouse per group. The statistically significant differences state $^{\%}P<0.05$ for samples relative to Native, $^{\&}P<0.05$ for samples relative to Saline, $^{+}P<0.05$ for samples relative to HCM, and $^{\#}P<0.05$ for samples relative to rVEGF.

Additionally, H&E-stained tissue sections were analyzed to quantify the area of granulation tissue after days 7 or 14 of treatments in each group (Figure 4.17(A)). The area of granulation tissue was greater at day 14 than at day 7 in the saline, HCM

hydrogel, and HCM + rVEGF hydrogel treatment groups. On the other hand, the area of granulation tissue was decreased from day 7 to day 14 in the VEGF-GAHCM with PEI and 50 CP polyplex groups. The area of granulation tissue formed for the 50 CP VEGF-GAHCM at day 7 was significantly larger than that in the saline, HCM hydrogel, and HCM + rVEGF hydrogel treatment groups, but there was no statistically significant difference relative to the PEI VEGF-GAHCM group. At day 14, there was no statistically significant difference in the extent of granulation tissue formation between any of the groups. The thickness of the epidermal layer formed at day 14 was also determined to evaluate the re-epithelialization of the healed wounds (Figure 4.17(B)). The epidermis of wounds treated with 50 CP VEGF-GAHCM was thicker than that observed for the other groups, and the epidermis in this sample was also significantly thicker than the native epidermis of skin tissue, consistent with the normal morphology in newly formed epidermis. Altogether, 50 CP VEGF-GAHCM induced both a larger area of granulation tissue formation at the initial stage of healing and a reduction in the area of granulation tissue at the later stage of healing to support improved re-epithelialization, indicative of the improved wound repair.

4.3.5 *In vivo* angiogenesis analysis

To evaluate correlations between blood vessel formation and wound healing, the blood vessels in the healed wounds after 7 or 14 days of treatment with saline, HCM hydrogel, HCM + rVEGF hydrogel, or VEGF-GAHCM hydrogel with PEI, 20 CP, or 50 CP polyplexes were determined with immunostaining for CD31 (PECAM-1) to detect ECs and staining of α-SMA to detect vascular smooth muscle cells on the blood vessel walls within the tissue sections. Figure 4.18(A) shows representative images of

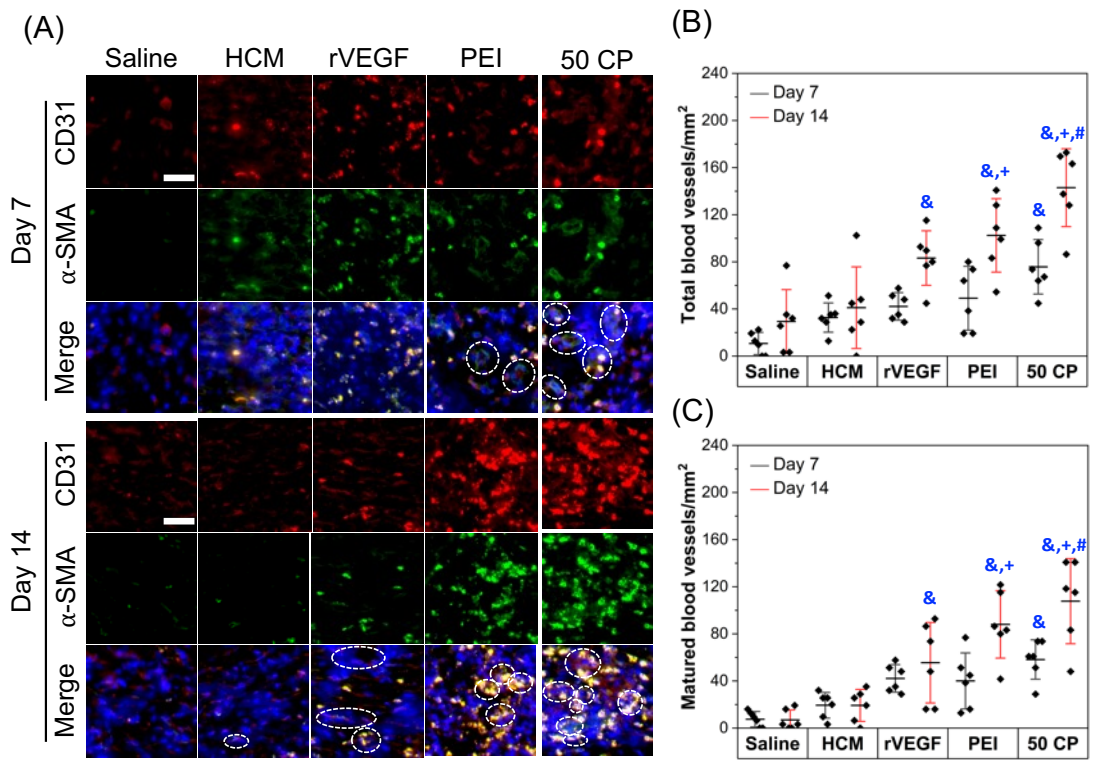

Figure 4.18. Blood vessels formation analysis of mouse wounds treated with saline, HCM hydrogel, rVEGF+HCM hydrogel, and VEGF-GAHCM with PEI, 20 CP, and 50 CP after 7 and 14 days. . (A) The representative confocal microscope images of CD31/α-SMA Immunostained mouse skin wound tissue section after 7 or 14 days of treatment (CD31 for red, α-SMA for green, and nuclei for blue). Scale bar is 40 μm. The white dotted circles indicate blood vessels on the images. (B) Total blood vessels counts per field of image. (C) The number of matured blood vessels within the total blood vessels counts per field of image. Each data point represents the average of number of blood vessels in the wound per field of image for five images per each mouse. The horizontal line represents the mean ± standard deviation for total 6 mouse per group. The statistically significant differences state $^{\&}P<0.05$ for samples relative to Saline, $^{+}P<0.05$ for samples relative to HCM, and $^{\#}P<0.05$ for samples relative to rVEGF.

CD31- and α-SMA-positive tissue sections for each group after 7 or 14 days of treatment. At day 7, interconnected EC networks with positive CD31 and α-SMA staining were observed in the wounds treated with VEGF-GAHCM with PEI or 50 CP

polyplexes, and the signals from CD31 and α-SMA were visually more intense at day 14. As a result of the poor structural integrity of the frozen tissue compared to paraffin-processed tissue (51, 52), individual blood vessels in the image were identified in regions where CD31 and Hoeschst 33258 signals were colocalized within both enclosed circular and circular-like shapes on the representative images (53-55). Individual blood vessels (that met either of these criteria) in the field of the image were counted and the total blood vessels per area were determined for each group (Figure 4.18(B)). At day 7, a greater number of blood vessels were formed in the wounds treated with 50 CP VEGF-GAHCM than for the other groups, with a statistically significant increase versus the saline group. At day 14, the overall number of blood vessels was increased for all of the groups. The increase in the total number of blood vessels formed in wounds treated with 50 CP VEGF-GAHCM was statistically significant relative to the saline, HCM hydrogel, and HCM + rVEGF hydrogel groups, but not statistically significant relative to the PEI VEGF-GAHCM group. Mature blood vessels were defined as those in which greater than half of the detected α-SMA was co-localized with the CD31 and nuclear stains (Fig. 4.18(C)) (56). This observed trend in the formation of mature blood vessels was similar to that observed in the quantitation of total blood vessels. The number of mature blood vessels increased from day 7 to day 14 of treatment for all groups. At day 14, a significantly greater number of mature blood vessels was measured for the 50 CP VEGF-GAHCM than in the other groups (with the exception of the PEI VEGF-GAHCM).

4.4 Discussion

Despite the great potential for pro-angiogenic growth factor therapy, limitations in growth factor stability and activity continue to limit clinical translation. To further

evaluate a CMP-mediated gene delivery approach, I assessed the ability our multifunctional therapeutic biomaterial, VEGF-A-encoding GAHCM (VEGF-GAHCM) to control VEGF production and activity and to enhance pro-healing and pro-angiogenic effects mediated by fibroblasts and ECs both in vitro and in vivo.

It is well recognized that the both VEGF-A and fibroblasts play a key role in physiological and pathological angiogenesis (57); in response to angiogenic stimuli mediated by VEGF-A and fibroblasts, ECs proliferate, migrate, and interconnect to form tubular networks. As a heparin-binding polypeptide mitogen, VEGF-A is an essential regulator of vessel formation and function by mediating EC survival, proliferation, adhesion, and migration (58, 59). Fibroblasts secrete various collagens, heparin sulfate proteoglycans, matricellular proteins (e.g., SPARC [secreted protein acidic and rich in cysteine] and tenascin), connective tissue growth factors, and angiogenic growth factors (e.g.,VEGF, TGF-β, and PDGF) involved in EC tubulogenesis (60-63). Both VEGF-A and other fibroblast-derived factors are critically involved in stimulating the proangiogenic response of ECs.

I observed maximal growth for ECs cultured on fibroblast-containing, VEGF-encoding GAHCM with CMP modification, at all of fibroblast culture time points, versus all other groups (Figure. 4.10), indicating the enhanced mitogenic effects of the conditioned media collected from the cultured fibroblasts. In particular, the conditioned media from fibroblasts precultured for three or five days in 20 CP VEGF-GAHCM induced more EC growth than the conditioned media from fibroblasts precultured in 50 CP VEGF-GAHCM, due to the too high amounts of VEGF-A in 50 CP VEGF-GAHCM than 20 CP VEGF-GAHCM which might be above the threshold concentration of VEGF-A for its activity. In our previous studies, I have determined the VEGF-A

amounts produced by fibroblast cultured in VEGF-GAHCM with and without CMP modification for 7 days of culture and I have observed that the VEGF-A amount produced by each fibroblast (pg/cell) in 50 CP VEGF-GAHCM after three or five days of pre-culture was higher than the VEGF-A production by fibroblasts precultured in the 50 CP VEGF-GAHCM (Figure 3.7). The VEGF-A concentration in the conditioned media collected from fibroblasts cultured in 50 CP VEGF-GAHCM might exceed the threshold concentration at which VEGF-A activity is known to peak. In particular, multiple studies have reported the presence of a threshold VEGF concentration that maximizes EC proliferation, migration, and angiogenic network formation, and decreased EC proliferation at VEGF concentrations higher than the threshold can occur due to the loss of detectable spatial differences in cytokine concentration (64-66). The phenomenon of decreased EC proliferation at high VEGF concentrations also agreed with our observation that rVEGF at a concentration of 10 ng/mL stimulated maximal EC proliferation, but proliferation was lower at concentrations above 10 ng/mL (Figure. 4.1 and 4.2(A)). Altogether, the conditioned media from fibroblasts cultured in CMP-modified, VEGF-encoding GAHCM effectively triggered the growth of ECs.

Moreover, I observed enhanced persistence of EC migratory behavior with sustained VEGF production by fibroblasts cultured in VEGF-encoding GAHCM with greater CMP modification (50 CP) (Figure. 4.11). Cells typically migrate either randomly or directionally toward a chemotactic stimulus (67). Most growth factors such as VEGF, platelet-derived growth factor (PDGF), and fibroblast growth factor (FGF) stimulate directional cell migration, with VEGF serving as a chemoattractant that directs EC migration along a gradient (68). Consistent with this phenomenon, I observed limited EC migratory behaviors in the rVEGF hydrogel group (Figure. 4.11), likely

because rVEGF was homogeneously distributed in these hydrogels during sample preparation. On the other hand, in all of the VEGF-GAHCM groups, VEGF was gradually produced by transfected fibroblasts, such that the directionality of EC migration depended directly on fibroblast location within the hydrogels. Because fibroblasts in the 50 CP VEGF-GAHCM sample, in particular, exhibited sustained VEGF production for 7 days and were located near the bottom of the hydrogel (Figure 3.7], ECs exhibited the most invasive behavior in the 50 CP VEGF-GAHCM. In agreement of our result, the sustained VEGF presence via covalently conjugation into PEG hydrogel promoted the 2-fold higher expression of activated c-Src, protein kinase involved in cell migration, in ECs as compared to the non-sustained VEGF control sample (69).

I also observed that the pro-angiogenic signaling of VEGF produced by fibroblasts cultured in VEGF-encoding GAHCM with CMP modification stimulated robust network formation resulting in stably interconnected ECs (Figure. 4.13, 4.14, and 4.15). While ECs typically exhibit a cobblestone morphology during in vitro culture, increased concentrations of angiogenic signals can trigger EC proliferation, migration, and differentiation leading to the formation of EC networks or capillary-like tubes in Matrigel, fibrin, or collagen (37, 38, 70). Due to the sustained and enhanced production of VEGF by fibroblasts cultured in 50 CP VEGF-GAHCM, the formation of EC networks showed 20-fold and 14-fold increases in total volume and average diameter, respectively, as a function of fibroblast preculture time from day 2 to day 10 (Figure. 4.14). These findings are consistent with prior studies from the Hughes group, which reported that VEGF concentration regulated the diameter of vessels formed by human umbilical vein ECs in fibrin gels (48). For instance, long and thin vessels were formed

at low concentrations of VEGF, whereas vessels with a larger diameter were formed at higher concentration of VEGF. Increased vessel diameters were linked to MEK1-mitogen activated protein kinase (MAP Kinase)/extracellular regulated kinase (ERK)1/2-triggered cell proliferation and migration. Other studies have shown that myofibroblasts stimulate angiogenic signaling leading to vascular network development. For example, Moulin and co-workers demonstrated that human dermal microvascular ECs developed significantly more capillary networks when they were co-cultured with myofibroblasts as compared with fibroblasts (71). Although there was no difference in secretion of VEGF and bFGF by the myofibroblasts vs. fibroblasts in their study, myofibroblast co-culture induced decreased matrix metalloproteinase activity and increased tissue inhibitor of metalloproteinase (TIMP)-1 and TIMP-3 activity, leading to more capillary-like network formation. Our results are aligned with this report, in that larger-volume EC networks were formed in 50 CP VEGF-GAHCM in which high levels of fibroblast-to-myofibroblast differentiation were observed (Figure. 3.8].

Although the EC networks formed by fibroblasts cultured in 50 CP VEGF-GACHM exhibited a larger volume and diameter, lumen formation was not clearly defined. Vascular lumen formation by ECs is critical for the transformation of EC cords into perfusable vascular tubes during the angiogenic process (72-74). Vascular lumen formation is regulated by complex cellular processes including angiogenic sprouting and intracellular vacuolation that relies on the expression of multiple molecules such as integrins, cdc42 and Rac, and proteinase (72). In particular, the activities of MMPs including MT1-MMP, TIMP-2, and TIMP-3, have been involved in the lumen expansion (75, 76). During vascular network development and lumen formation in wound healing, myofibroblasts have shown to lead a more favorable environment for

angiogenic development than fibroblasts (71, 77). This could be different levels of MMP activities such as TIMPs-1 and -3 in myofibroblasts vs. fibroblasts to stabilize the vascular network for the lumen formation (71, 76). I previously reported myofibroblast differentiation by fibroblasts cultured in VEGF-GAHCM, with increased myofibroblast signaling stemming from VEGF-GAHCM with greater CMP modification (Chapter 3). While increased myofibroblast signaling would be expected to stabilize lumen formation and expansion in these materials, 24 h might be a relatively short incubation time period to enable ECs to respond to the effects of the myofibroblasts (76, 78, 79).

Splinted murine excisional wound healing studies demonstrated a direct correlation between wound healing, EC activation, and blood vessel formation in the healed wounds (Figure. 4.16, 4.17, and 4.18). During wound healing, the proliferation phase mainly encompasses coverage of the wound via formation of granulation tissue and restoration of the vascular network (80). Granulation tissue formation is a particularly critical step that generates new connective tissue and microscopic vessels via a complex interplay between multiple cell types such as fibroblasts, keratinocytes, and ECs at the wound site (81). Thicker granulation tissue is typically present at earlier time points and reduced at later time points to trigger re-epithelialization and wound closure (33, 82, 83). In agreement with this phenomenon, I observed that VEGF-GAHCM stimulated increased granulation tissue formation in wounds at day 7, as compared to other groups, and the area of granulation tissue decreased by day 14 consistent with the kinetics of wound closure (Figure. 4.16 and 4.17) (33, 82, 83). Granulation tissue also supports the recruitment of keratinocytes for re-epithelialization (84), resulting in newly formed epidermis that is typically relatively thicker and flatter than the epidermis of normal skin (85). Our findings also mirrored this phenomenon, as

I observed significantly enhanced thickness in the epidermal layer 14 days after wound treatment with VEGF-GAHCM with 50 CP, indicating freshly formed epidermis.

Moreover, angiogenesis plays an important role in wound healing via angiogenic capillary sprouting, capillary invasion of the fibrin/fibronectin-rich wound clot, and organization of a microvascular network to support newly formed granulation tissue (6). In response to angiogenic stimuli such as VEGF, ECs proliferate, migrate, and coalesce to form primitive vascular labyrinths that undergo maturation by recruitment of smooth muscle cells to form mature blood vessels. Although previous studies reported that topical treatment of rodent skin wound models with rVEGF protein or VEGF-encoding DNA resulted in increased healing, these studies did not demonstrate a significant increase in vessel formation following treatment (86-88). On the other hand, in our study, I demonstrated that application of VEGF-GAHCM with 50 CP increased both the total number of blood vessels and the number of mature blood vessels in the wound, presumably due to the capacity of these materials to sustain VEGF production for extended time periods. However, the enhancement of 50 CP VEGF-GAHCM in in vivo healing and angiogenesis evaluations was not statistical significantly different from VEGF-GAHCM with no CMP modification, despite the significant differences observed between these samples based on in vitro EC networks formation experiments. Similarly, I have observed this outcome for wound closure and α-SMA expression in in vitro vs. in vivo our previous studies (Chapter 3). I explained that the 10-fold higher polyplex concentration in the in vivo than in vitro studies (43) and the presence of multiple cell types in vivo environment (89) might result in the production of VEGF by PEI VEGF-GAHCM and 50 CP VEGF-GAHCM, which exceeds a threshold for stimulating cells and similar proangiogenic and prohealing responses (66). Overall, the

increased wound healing resulting from 50 CP VEGF-GAHCM correlated with increases in the total number of blood vessels and mature blood vessels, along with corresponding changes to granulation tissue formation and re-epithelialization.

4.5 Conclusion

Due to the difficulties in controlling growth factor activity and corresponding cellular signals in the wound microenvironment, growth factor therapies have historically results in insufficient healing outcomes. Our recent design employs synergies in CMP-collagen tether-mediated growth factor gene delivery and matrix signaling to improve cellular responses for wound repair. In this study, VEGF-A activity controlled by fibroblasts cultured in VEGF-GAHCM with CMP modification stimulates both mitogenic and chemotactic responses to ECs for proliferation and migration. Additionally, the pro-angiogenic effects of sustained VEGF production directly on ECs, coupled with its synergistic effects on fibroblasts (including myofibroblast differentiation that improves EC network formation), resulted in the formation of large-diameter and large-volume networks of stably interconnected ECs. These pro-angiogenic responses monitored in vitro also translated into more efficient blood vessel formation and wound repair in an in vivo wound healing model. Therefore, VEGF-GAHCM is a potential therapeutic option for chronic wound treatment to improve vascularization and wound healing. This study suggests the broad benefits of using CMP-collagen tethers to regulate the efficient transfer of genes for a variety of growth factors, which could serve to orchestrate improved cellular healing signals for the treatment of chronically impaired wounds.

REFERENCES

1. Demidova-Rice TN, Durham JT, Herman IM. Wound Healing Angiogenesis: Innovations and Challenges in Acute and Chronic Wound Healing. Adv Wound Care (New Rochelle). 2012;1(1):17-22. Epub 2012/02/01. doi: 10.1089/wound.2011.0308. PubMed PMID: 24527273; PMCID: PMC3623570.

2. Veith AP, Henderson K, Spencer A, Sligar AD, Baker AB. Therapeutic strategies for enhancing angiogenesis in wound healing. Adv Drug Deliv Rev. 2019;146:97-125. Epub 2018/09/30. doi: 10.1016/j.addr.2018.09.010. PubMed PMID: 30267742; PMCID: PMC6435442.

3. Sen CK, Gordillo GM, Roy S, Kirsner R, Lambert L, Hunt TK, Gottrup F, Gurtner GC, Longaker MT. Human skin wounds: a major and snowballing threat to public health and the economy. Wound Repair Regen. 2009;17(6):763-71. Epub 2009/11/12. doi: 10.1111/j.1524-475X.2009.00543.x. PubMed PMID: 19903300; PMCID: PMC2810192.

4. Richmond NA, Maderal AD, Vivas AC. Evidence-based management of common chronic lower extremity ulcers. Dermatol Ther. 2013;26(3):187-96. Epub 2013/06/08. doi: 10.1111/dth.12051. PubMed PMID: 23742279.

5. Frykberg RG, Banks J. Challenges in the Treatment of Chronic Wounds. Adv Wound Care (New Rochelle). 2015;4(9):560-82. Epub 2015/09/05. doi: 10.1089/wound.2015.0635. PubMed PMID: 26339534; PMCID: PMC4528992.

6. Tonnesen MG, Feng X, Clark RA. Angiogenesis in wound healing. J Investig Dermatol Symp Proc. 2000;5(1):40-6. Epub 2001/01/09. doi: 10.1046/j.1087-0024.2000.00014.x. PubMed PMID: 11147674.

7. DiPietro LA. Angiogenesis and wound repair: when enough is enough. J Leukoc Biol. 2016;100(5):979-84. Epub 2016/11/02. doi: 10.1189/jlb.4MR0316-102R. PubMed PMID: 27406995; PMCID: PMC6608066.

8. Li J, Zhang YP, Kirsner RS. Angiogenesis in wound repair: angiogenic growth factors and the extracellular matrix. Microsc Res Tech. 2003;60(1):107-14. Epub 2002/12/25. doi: 10.1002/jemt.10249. PubMed PMID: 12500267.

9. Ucuzian AA, Gassman AA, East AT, Greisler HP. Molecular mediators of angiogenesis. J Burn Care Res. 2010;31(1):158-75. Epub 2010/01/12. doi: 10.1097/BCR.0b013e3181c7ed82. PubMed PMID: 20061852; PMCID: PMC2818794.

10. Barrientos S, Stojadinovic O, Golinko MS, Brem H, Tomic-Canic M. Growth factors and cytokines in wound healing. Wound Repair Regen. 2008;16(5):585-601. Epub 2009/01/09. doi: 10.1111/j.1524-475X.2008.00410.x. PubMed PMID: 19128254.

11. Ferrara N, Gerber HP, LeCouter J. The biology of VEGF and its receptors. Nat Med. 2003;9(6):669-76. Epub 2003/06/05. doi: 10.1038/nm0603-669. PubMed PMID: 12778165.

12. Hanft JR, Pollak RA, Barbul A, van Gils C, Kwon PS, Gray SM, Lynch CJ, Semba CP, Breen TJ. Phase I trial on the safety of topical rhVEGF on chronic neuropathic diabetic foot ulcers. J Wound Care. 2008;17(1):30-2, 4-7. Epub 2008/01/24. doi: 10.12968/jowc.2008.17.1.27917. PubMed PMID: 18210954.

13. Berry-Kilgour C, Cabral J, Wise L. Advancements in the Delivery of Growth Factors and Cytokines for the Treatment of Cutaneous Wound Indications. Adv Wound Care (New Rochelle). 2021;10(11):596-622. Epub 2020/10/23. doi: 10.1089/wound.2020.1183. PubMed PMID: 33086946; PMCID: PMC8392095.

14. Smiell JM, Wieman TJ, Steed DL, Perry BH, Sampson AR, Schwab BH. Efficacy and safety of becaplermin (recombinant human platelet-derived growth factor-BB) in patients with nonhealing, lower extremity diabetic ulcers: a combined analysis of four randomized studies. Wound Repair Regen. 1999;7(5):335-46. Epub 1999/11/17. doi: 10.1046/j.1524-475x.1999.00335.x. PubMed PMID: 10564562.

15. Niezgoda JA, Van Gils CC, Frykberg RG, Hodde JP. Randomized clinical trial comparing OASIS Wound Matrix to Regranex Gel for diabetic ulcers. Adv Skin Wound Care. 2005;18(5 Pt 1):258-66. Epub 2005/06/09. doi: 10.1097/00129334-200506000-00012. PubMed PMID: 15942317.

16. Niu Y, Li Q, Ding Y, Dong L, Wang C. Engineered delivery strategies for enhanced control of growth factor activities in wound healing. Adv Drug Deliv Rev. 2019;146:190-208. Epub 2018/06/08. doi: 10.1016/j.addr.2018.06.002. PubMed PMID: 29879493.

17. Lee K, Silva EA, Mooney DJ. Growth factor delivery-based tissue engineering: general approaches and a review of recent developments. J R Soc Interface. 2011;8(55):153-70. Epub 2010/08/20. doi: 10.1098/rsif.2010.0223. PubMed PMID: 20719768; PMCID: PMC3033020.

18. Caballero Aguilar LM, Silva SM, Moulton SE. Growth factor delivery: Defining the next generation platforms for tissue engineering. J Control Release. 2019;306:40-58. Epub 2019/06/01. doi: 10.1016/j.jconrel.2019.05.028. PubMed PMID: 31150750.

19. Giacca M, Zacchigna S. VEGF gene therapy: therapeutic angiogenesis in the clinic and beyond. Gene Ther. 2012;19(6):622-9. Epub 2012/03/02. doi: 10.1038/gt.2012.17. PubMed PMID: 22378343.

20. Wu P, Chen H, Jin R, Weng T, Ho JK, You C, Zhang L, Wang X, Han C. Non-viral gene delivery systems for tissue repair and regeneration. J Transl Med. 2018;16(1):29. Epub 2018/02/17. doi: 10.1186/s12967-018-1402-1. PubMed PMID: 29448962; PMCID: PMC5815227.

21. Martino MM, Briquez PS, Ranga A, Lutolf MP, Hubbell JA. Heparin-binding domain of fibrin(ogen) binds growth factors and promotes tissue repair when incorporated within a synthetic matrix. Proc Natl Acad Sci U S A. 2013;110(12):4563-8. Epub 2013/03/15. doi: 10.1073/pnas.1221602110. PubMed PMID: 23487783; PMCID: PMC3607046.

22. Liu Y, Cai S, Shu XZ, Shelby J, Prestwich GD. Release of basic fibroblast growth factor from a crosslinked glycosaminoglycan hydrogel promotes wound healing. Wound Repair Regen. 2007;15(2):245-51. Epub 2007/03/14. doi: 10.1111/j.1524-475X.2007.00211.x. PubMed PMID: 17352757.

23. Sacchi V, Mittermayr R, Hartinger J, Martino MM, Lorentz KM, Wolbank S, Hofmann A, Largo RA, Marschall JS, Groppa E, Gianni-Barrera R, Ehrbar M, Hubbell JA, Redl H, Banfi A. Long-lasting fibrin matrices ensure stable and functional angiogenesis by highly tunable, sustained delivery of recombinant VEGF164. Proc Natl Acad Sci U S A. 2014;111(19):6952-7. Epub 2014/04/30. doi: 10.1073/pnas.1404605111. PubMed PMID: 24778233; PMCID: PMC4024904.

24. Martino MM, Briquez PS, Guc E, Tortelli F, Kilarski WW, Metzger S, Rice JJ, Kuhn GA, Muller R, Swartz MA, Hubbell JA. Growth factors engineered for super-affinity to the extracellular matrix enhance tissue healing. Science. 2014;343(6173):885-8. Epub 2014/02/22. doi: 10.1126/science.1247663. PubMed PMID: 24558160.

25. Nyman E, Henricson J, Ghafouri B, Anderson CD, Kratz G. Hyaluronic Acid Accelerates Re-epithelialization and Alters Protein Expression in a Human Wound Model. Plast Reconstr Surg Glob Open. 2019;7(5):e2221. Epub 2019/07/25. doi: 10.1097/GOX.0000000000002221. PubMed PMID: 31333952; PMCID: PMC6571313.

26. Gao F, Liu Y, He Y, Yang C, Wang Y, Shi X, Wei G. Hyaluronan oligosaccharides promote excisional wound healing through enhanced angiogenesis. Matrix Biol. 2010;29(2):107-16. Epub 2009/11/17. doi: 10.1016/j.matbio.2009.11.002. PubMed PMID: 19913615.

27. Park D, Kim Y, Kim H, Kim K, Lee YS, Choe J, Hahn JH, Lee H, Jeon J, Choi C, Kim YM, Jeoung D. Hyaluronic acid promotes angiogenesis by inducing RHAMM-TGFbeta receptor interaction via CD44-PKCdelta. Mol Cells. 2012;33(6):563-74. Epub 2012/05/23. doi: 10.1007/s10059-012-2294-1. PubMed PMID: 22610405; PMCID: PMC3887750.

28. Pardue EL, Ibrahim S, Ramamurthi A. Role of hyaluronan in angiogenesis and its utility to angiogenic tissue engineering. Organogenesis. 2008;4(4):203-14. Epub 2009/04/02. doi: 10.4161/org.4.4.6926. PubMed PMID: 19337400; PMCID: PMC2634325.

29. Peattie RA, Nayate AP, Firpo MA, Shelby J, Fisher RJ, Prestwich GD. Stimulation of in vivo angiogenesis by cytokine-loaded hyaluronic acid hydrogel implants. Biomaterials. 2004;25(14):2789-98. Epub 2004/02/14. doi: 10.1016/j.biomaterials.2003.09.054. PubMed PMID: 14962557.

30. Urello MA, Kiick KL, Sullivan MO. A CMP-based method for tunable, cell-mediated gene delivery from collagen scaffolds. J Mater Chem B.

2014;2(46):8174-85. Epub 2014/12/14. doi: 10.1039/c4tb01435a. PubMed PMID: 32262095.

31. Urello MA, Kiick KL, Sullivan MO. Integration of growth factor gene delivery with collagen-triggered wound repair cascades using collagen-mimetic peptides. Bioeng Transl Med. 2016;1(2):207-19. Epub 2016/12/17. doi: 10.1002/btm2.10037. PubMed PMID: 27981245; PMCID: PMC5125401.

32. Urello MA, Kiick KL, Sullivan MO. ECM turnover-stimulated gene delivery through collagen-mimetic peptide-plasmid integration in collagen. Acta Biomater. 2017;62:167-78. Epub 2017/09/04. doi: 10.1016/j.actbio.2017.08.038. PubMed PMID: 28865990; PMCID: PMC5654588.

33. Thapa RK, Margolis DJ, Kiick KL, Sullivan MO. Enhanced wound healing via collagen-turnover-driven transfer of PDGF-BB gene in a murine wound model. ACS Appl Bio Mater. 2020;3(6):3500-17. Epub 2020/07/14. doi: 10.1021/acsabm.9b01147. PubMed PMID: 32656505; PMCID: PMC7351314.

34. Gurtner GC, Werner S, Barrandon Y, Longaker MT. Wound repair and regeneration. Nature. 2008;453(7193):314-21. Epub 2008/05/16. doi: 10.1038/nature07039. PubMed PMID: 18480812.

35. Rognoni E, Watt FM. Skin Cell Heterogeneity in Development, Wound Healing, and Cancer. Trends Cell Biol. 2018;28(9):709-22. Epub 2018/05/29. doi: 10.1016/j.tcb.2018.05.002. PubMed PMID: 29807713; PMCID: PMC6098245.

36. Montesano R, Orci L, Vassalli P. In vitro rapid organization of endothelial cells into capillary-like networks is promoted by collagen matrices. J Cell Biol. 1983;97(5 Pt 1):1648-52. Epub 1983/11/01. doi: 10.1083/jcb.97.5.1648. PubMed PMID: 6630296; PMCID: PMC2112683.

37. Arnaoutova I, Kleinman HK. In vitro angiogenesis: endothelial cell tube formation on gelled basement membrane extract. Nat Protoc. 2010;5(4):628-35. Epub 2010/03/13. doi: 10.1038/nprot.2010.6. PubMed PMID: 20224563.

38. DeCicco-Skinner KL, Henry GH, Cataisson C, Tabib T, Gwilliam JC, Watson NJ, Bullwinkle EM, Falkenburg L, O'Neill RC, Morin A, Wiest JS. Endothelial cell tube formation assay for the in vitro study of angiogenesis. J Vis Exp. 2014(91):e51312. Epub 2014/09/17. doi: 10.3791/51312. PubMed PMID: 25225985; PMCID: PMC4540586.

39. Whittington CF, Yoder MC, Voytik-Harbin SL. Collagen-polymer guidance of vessel network formation and stabilization by endothelial colony forming cells in vitro. Macromol Biosci. 2013;13(9):1135-49. Epub 2013/07/09. doi: 10.1002/mabi.201300128. PubMed PMID: 23832790; PMCID: PMC3787951.

40. Zhou Q, Kiosses WB, Liu J, Schimmel P. Tumor endothelial cell tube formation model for determining anti-angiogenic activity of a tRNA synthetase cytokine. Methods. 2008;44(2):190-5. Epub 2008/02/05. doi: 10.1016/j.ymeth.2007.10.004. PubMed PMID: 18241800; PMCID: PMC3835186.

41. Zhang L, Yaron JR, Guo Q, Kilbourne J, Awo EA, Burgin M, Schutz LN, Wallace SE, Lowe KM, Lucas AR. Topical Application of Virus-Derived Immunomodulating Proteins and Peptides to Promote Wound Healing in Mouse Models. Methods Mol Biol. 2021;2225:217-26. Epub 2020/10/28. doi: 10.1007/978-1-0716-1012-1_12. PubMed PMID: 33108665.

42. Yaron JR, Zhang L, Guo Q, Awo EA, Burgin M, Schutz LN, Zhang N, Kilbourne J, Daggett-Vondras J, Lowe KM, Lucas AR. Recombinant Myxoma Virus-Derived Immune Modulator M-T7 Accelerates Cutaneous Wound Healing and

Improves Tissue Remodeling. Pharmaceutics. 2020;12(11). Epub 2020/10/28. doi: 10.3390/pharmaceutics12111003. PubMed PMID: 33105865; PMCID: PMC7690590.

43. Tokatlian T, Cam C, Segura T. Porous hyaluronic acid hydrogels for localized nonviral DNA delivery in a diabetic wound healing model. Adv Healthc Mater. 2015;4(7):1084-91. Epub 2015/02/20. doi: 10.1002/adhm.201400783. PubMed PMID: 25694196; PMCID: PMC4433401.

44. Tokatlian T, Cam C, Segura T. Non-viral DNA delivery from porous hyaluronic acid hydrogels in mice. Biomaterials. 2014;35(2):825-35. Epub 2013/11/12. doi: 10.1016/j.biomaterials.2013.10.014. PubMed PMID: 24210142; PMCID: PMC3941464.

45. Qiu M, Chen D, Shen C, Shen J, Zhao H, He Y. Platelet-Rich Plasma-Loaded Poly(d,l-lactide)-Poly(ethylene glycol)-Poly(d,l-lactide) Hydrogel Dressing Promotes Full-Thickness Skin Wound Healing in a Rodent Model. Int J Mol Sci. 2016;17(7). Epub 2016/06/28. doi: 10.3390/ijms17071001. PubMed PMID: 27347938; PMCID: PMC4964377.

46. Aranda E, Owen GI. A semi-quantitative assay to screen for angiogenic compounds and compounds with angiogenic potential using the EA.hy926 endothelial cell line. Biol Res. 2009;42(3):377-89. Epub 2009/11/17. doi: /S0716-97602009000300012. PubMed PMID: 19915746.

47. Xie D, Ju D, Speyer C, Gorski D, Kosir MA. Strategic Endothelial Cell Tube Formation Assay: Comparing Extracellular Matrix and Growth Factor Reduced Extracellular Matrix. J Vis Exp. 2016(114). Epub 2016/09/02. doi: 10.3791/54074. PubMed PMID: 27585062; PMCID: PMC5091872.

48. Nakatsu MN, Sainson RC, Perez-del-Pulgar S, Aoto JN, Aitkenhead M, Taylor KL, Carpenter PM, Hughes CC. VEGF(121) and VEGF(165) regulate blood vessel diameter through vascular endothelial growth factor receptor 2 in an in vitro angiogenesis model. Lab Invest. 2003;83(12):1873-85. Epub 2003/12/24. doi: 10.1097/01.lab.0000107160.81875.33. PubMed PMID: 14691306.

49. Pauty J, Usuba R, Cheng IG, Hespel L, Takahashi H, Kato K, Kobayashi M, Nakajima H, Lee E, Yger F, Soncin F, Matsunaga YT. A Vascular Endothelial Growth Factor-Dependent Sprouting Angiogenesis Assay Based on an In Vitro Human Blood Vessel Model for the Study of Anti-Angiogenic Drugs. EBioMedicine. 2018;27:225-36. Epub 2018/01/01. doi: 10.1016/j.ebiom.2017.12.014. PubMed PMID: 29289530; PMCID: PMC5828365.

50. DeLisser HM, Christofidou-Solomidou M, Strieter RM, Burdick MD, Robinson CS, Wexler RS, Kerr JS, Garlanda C, Merwin JR, Madri JA, Albelda SM. Involvement of endothelial PECAM-1/CD31 in angiogenesis. Am J Pathol. 1997;151(3):671-7. Epub 1997/09/01. PubMed PMID: 9284815; PMCID: PMC1857836.

51. Shi SR, Liu C, Pootrakul L, Tang L, Young A, Chen R, Cote RJ, Taylor CR. Evaluation of the value of frozen tissue section used as "gold standard" for immunohistochemistry. Am J Clin Pathol. 2008;129(3):358-66. Epub 2008/02/21. doi: 10.1309/7CXUYXT23E5AL8KQ. PubMed PMID: 18285257.

52. Liou W, Geuze HJ, Slot JW. Improving structural integrity of cryosections for immunogold labeling. Histochem Cell Biol. 1996;106(1):41-58. Epub 1996/07/01. doi: 10.1007/BF02473201. PubMed PMID: 8858366.

53. Yi C, Wu W, Zheng D, Peng G, Huang H, Shen Z, Teng X. Targeted inhibition of endothelial calpain delays wound healing by reducing inflammation and angiogenesis. Cell Death Dis. 2020;11(7):533. Epub 2020/07/16. doi: 10.1038/s41419-020-02737-x. PubMed PMID: 32665543; PMCID: PMC7360547.

54. Michalczyk ER, Chen L, Fine D, Zhao Y, Mascarinas E, Grippo PJ, DiPietro LA. Pigment Epithelium-Derived Factor (PEDF) as a Regulator of Wound Angiogenesis. Sci Rep. 2018;8(1):11142. Epub 2018/07/26. doi: 10.1038/s41598-018-29465-9. PubMed PMID: 30042381; PMCID: PMC6057962.

55. An Y, Liu WJ, Xue P, Ma Y, Zhang LQ, Zhu B, Qi M, Li LY, Zhang YJ, Wang QT, Jin Y. Autophagy promotes MSC-mediated vascularization in cutaneous wound healing via regulation of VEGF secretion. Cell Death Dis. 2018;9(2):58. Epub 2018/01/21. doi: 10.1038/s41419-017-0082-8. PubMed PMID: 29352190; PMCID: PMC5833357.

56. Kim SJ, Kim SA, Choi YA, Park DY, Lee J. Alpha-Smooth Muscle Actin-Positive Perivascular Cells in Diabetic Retina and Choroid. Int J Mol Sci. 2020;21(6). Epub 2020/04/05. doi: 10.3390/ijms21062158. PubMed PMID: 32245120; PMCID: PMC7139401.

57. Newman AC, Nakatsu MN, Chou W, Gershon PD, Hughes CC. The requirement for fibroblasts in angiogenesis: fibroblast-derived matrix proteins are essential for endothelial cell lumen formation. Mol Biol Cell. 2011;22(20):3791-800. Epub 2011/08/26. doi: 10.1091/mbc.E11-05-0393. PubMed PMID: 21865599; PMCID: PMC3192859.

58. Yamamoto H, Rundqvist H, Branco C, Johnson RS. Autocrine VEGF Isoforms Differentially Regulate Endothelial Cell Behavior. Front Cell Dev Biol.

2016;4:99. Epub 2016/10/07. doi: 10.3389/fcell.2016.00099. PubMed PMID: 27709112; PMCID: PMC5030275.

59. Ferrara N, Houck KA, Jakeman LB, Winer J, Leung DW. The vascular endothelial growth factor family of polypeptides. J Cell Biochem. 1991;47(3):211-8. Epub 1991/11/01. doi: 10.1002/jcb.240470305. PubMed PMID: 1791185.

60. Chang HY, Sneddon JB, Alizadeh AA, Sood R, West RB, Montgomery K, Chi JT, van de Rijn M, Botstein D, Brown PO. Gene expression signature of fibroblast serum response predicts human cancer progression: similarities between tumors and wounds. PLoS Biol. 2004;2(2):E7. Epub 2004/01/23. doi: 10.1371/journal.pbio.0020007. PubMed PMID: 14737219; PMCID: PMC314300.

61. Kellouche S, Mourah S, Bonnefoy A, Schoevaert D, Podgorniak MP, Calvo F, Hoylaerts MF, Legrand C, Dosquet C. Platelets, thrombospondin-1 and human dermal fibroblasts cooperate for stimulation of endothelial cell tubulogenesis through VEGF and PAI-1 regulation. Exp Cell Res. 2007;313(3):486-99. Epub 2006/11/28. doi: 10.1016/j.yexcr.2006.10.023. PubMed PMID: 17126831.

62. Paunescu V, Bojin FM, Tatu CA, Gavriliuc OI, Rosca A, Gruia AT, Tanasie G, Bunu C, Crisnic D, Gherghiceanu M, Tatu FR, Tatu CS, Vermesan S. Tumour-associated fibroblasts and mesenchymal stem cells: more similarities than differences. J Cell Mol Med. 2011;15(3):635-46. Epub 2010/02/27. doi: 10.1111/j.1582-4934.2010.01044.x. PubMed PMID: 20184663; PMCID: PMC3922385.

63. Antoniades HN, Galanopoulos T, Neville-Golden J, Kiritsy CP, Lynch SE. Injury induces in vivo expression of platelet-derived growth factor (PDGF) and PDGF receptor mRNAs in skin epithelial cells and PDGF mRNA in connective tissue

fibroblasts. Proc Natl Acad Sci U S A. 1991;88(2):565-9. Epub 1991/01/15. doi: 10.1073/pnas.88.2.565. PubMed PMID: 1846446; PMCID: PMC50852.

64. Jih YJ, Lien WH, Tsai WC, Yang GW, Li C, Wu LW. Distinct regulation of genes by bFGF and VEGF-A in endothelial cells. Angiogenesis. 2001;4(4):313-21. Epub 2002/08/29. doi: 10.1023/a:1016080321956. PubMed PMID: 12197476.

65. Soker S, Gollamudi-Payne S, Fidder H, Charmahelli H, Klagsbrun M. Inhibition of vascular endothelial growth factor (VEGF)-induced endothelial cell proliferation by a peptide corresponding to the exon 7-encoded domain of VEGF165. J Biol Chem. 1997;272(50):31582-8. Epub 1998/02/12. doi: 10.1074/jbc.272.50.31582. PubMed PMID: 9395496.

66. Yoshida A, Anand-Apte B, Zetter BR. Differential endothelial migration and proliferation to basic fibroblast growth factor and vascular endothelial growth factor. Growth Factors. 1996;13(1-2):57-64. Epub 1996/01/01. doi: 10.3109/08977199609034566. PubMed PMID: 8962720.

67. Michaelis UR. Mechanisms of endothelial cell migration. Cell Mol Life Sci. 2014;71(21):4131-48. Epub 2014/07/21. doi: 10.1007/s00018-014-1678-0. PubMed PMID: 25038776.

68. Lamalice L, Le Boeuf F, Huot J. Endothelial cell migration during angiogenesis. Circ Res. 2007;100(6):782-94. Epub 2007/03/31. doi: 10.1161/01.RES.0000259593.07661.1e. PubMed PMID: 17395884.

69. Porter AM, Klinge CM, Gobin AS. Covalently grafted VEGF(165) in hydrogel models upregulates the cellular pathways associated with angiogenesis. Am J Physiol Cell Physiol. 2011;301(5):C1086-92. Epub 2011/07/29. doi: 10.1152/ajpcell.00090.2011. PubMed PMID: 21795519.

70. Arnaoutova I, George J, Kleinman HK, Benton G. The endothelial cell tube formation assay on basement membrane turns 20: state of the science and the art. Angiogenesis. 2009;12(3):267-74. Epub 2009/04/29. doi: 10.1007/s10456-009-9146-4. PubMed PMID: 19399631.

71. Mayrand D, Laforce-Lavoie A, Larochelle S, Langlois A, Genest H, Roy M, Moulin VJ. Angiogenic properties of myofibroblasts isolated from normal human skin wounds. Angiogenesis. 2012;15(2):199-212. Epub 2012/02/22. doi: 10.1007/s10456-012-9253-5. PubMed PMID: 22350743.

72. Iruela-Arispe ML, Davis GE. Cellular and molecular mechanisms of vascular lumen formation. Dev Cell. 2009;16(2):222-31. Epub 2009/02/17. doi: 10.1016/j.devcel.2009.01.013. PubMed PMID: 19217424; PMCID: PMC8606173.

73. Lammert E, Axnick J. Vascular lumen formation. Cold Spring Harb Perspect Med. 2012;2(4):a006619. Epub 2012/04/05. doi: 10.1101/cshperspect.a006619. PubMed PMID: 22474612; PMCID: PMC3312398.

74. Charpentier MS, Conlon FL. Cellular and molecular mechanisms underlying blood vessel lumen formation. Bioessays. 2014;36(3):251-9. Epub 2013/12/11. doi: 10.1002/bies.201300133. PubMed PMID: 24323945; PMCID: PMC4187360.

75. Stratman AN, Saunders WB, Sacharidou A, Koh W, Fisher KE, Zawieja DC, Davis MJ, Davis GE. Endothelial cell lumen and vascular guidance tunnel formation requires MT1-MMP-dependent proteolysis in 3-dimensional collagen matrices. Blood. 2009;114(2):237-47. Epub 2009/04/03. doi: 10.1182/blood-2008-12-196451. PubMed PMID: 19339693; PMCID: PMC2714200.

76. Saunders WB, Bohnsack BL, Faske JB, Anthis NJ, Bayless KJ, Hirschi KK, Davis GE. Coregulation of vascular tube stabilization by endothelial cell TIMP-2 and pericyte TIMP-3. J Cell Biol. 2006;175(1):179-91. Epub 2006/10/13. doi: 10.1083/jcb.200603176. PubMed PMID: 17030988; PMCID: PMC2064509.

77. Kirk TZ, Mark ME, Chua CC, Chua BH, Mayes MD. Myofibroblasts from scleroderma skin synthesize elevated levels of collagen and tissue inhibitor of metalloproteinase (TIMP-1) with two forms of TIMP-1. J Biol Chem. 1995;270(7):3423-8. Epub 1995/02/17. doi: 10.1074/jbc.270.7.3423. PubMed PMID: 7852429.

78. Chun TH, Sabeh F, Ota I, Murphy H, McDonagh KT, Holmbeck K, Birkedal-Hansen H, Allen ED, Weiss SJ. MT1-MMP-dependent neovessel formation within the confines of the three-dimensional extracellular matrix. J Cell Biol. 2004;167(4):757-67. Epub 2004/11/17. doi: 10.1083/jcb.200405001. PubMed PMID: 15545316; PMCID: PMC2172577.

79. Andree B, Ichanti H, Kalies S, Heisterkamp A, Strauss S, Vogt PM, Haverich A, Hilfiker A. Formation of three-dimensional tubular endothelial cell networks under defined serum-free cell culture conditions in human collagen hydrogels. Sci Rep. 2019;9(1):5437. Epub 2019/04/02. doi: 10.1038/s41598-019-41985-6. PubMed PMID: 30932006; PMCID: PMC6443732.

80. Reinke JM, Sorg H. Wound repair and regeneration. Eur Surg Res. 2012;49(1):35-43. Epub 2012/07/17. doi: 10.1159/000339613. PubMed PMID: 22797712.

81. Alhajj M, Goyal A. Physiology, Granulation Tissue. StatPearls. Treasure Island (FL)2022.

82. Shinozaki M, Okada Y, Kitano A, Ikeda K, Saika S, Shinozaki M. Impaired cutaneous wound healing with excess granulation tissue formation in TNFalpha-null mice. Arch Dermatol Res. 2009;301(7):531-7. Epub 2009/06/23. doi: 10.1007/s00403-009-0969-z. PubMed PMID: 19543902.

83. Druecke D, Lamme EN, Hermann S, Pieper J, May PS, Steinau HU, Steinstraesser L. Modulation of scar tissue formation using different dermal regeneration templates in the treatment of experimental full-thickness wounds. Wound Repair Regen. 2004;12(5):518-27. Epub 2004/09/30. doi: 10.1111/j.1067-1927.2004.012504.x. PubMed PMID: 15453834.

84. Evans ND, Oreffo RO, Healy E, Thurner PJ, Man YH. Epithelial mechanobiology, skin wound healing, and the stem cell niche. J Mech Behav Biomed Mater. 2013;28:397-409. Epub 2013/06/12. doi: 10.1016/j.jmbbm.2013.04.023. PubMed PMID: 23746929.

85. Kuo TY, Huang CC, Shieh SJ, Wang YB, Lin MJ, Wu MC, Huang LLH. Skin wound healing assessment via an optimized wound array model in miniature pigs. Sci Rep. 2022;12(1):445. Epub 2022/01/12. doi: 10.1038/s41598-021-03855-y. PubMed PMID: 35013386; PMCID: PMC8748672.

86. Ferraro B, Cruz YL, Coppola D, Heller R. Intradermal delivery of plasmid VEGF(165) by electroporation promotes wound healing. Mol Ther. 2009;17(4):651-7. Epub 2009/02/26. doi: 10.1038/mt.2009.12. PubMed PMID: 19240696; PMCID: PMC2835103.

87. O'Toole G, MacKenzie D, Lindeman R, Buckley MF, Marucci D, McCarthy N, Poole M. Vascular endothelial growth factor gene therapy in ischaemic

rat skin flaps. Br J Plast Surg. 2002;55(1):55-8. Epub 2002/01/11. doi: 10.1054/bjps.2001.3741. PubMed PMID: 11783969.

88. Zhang F, Lei MP, Oswald TM, Pang Y, Blain B, Cai ZW, Lineaweaver WC. The effect of vascular endothelial growth factor on the healing of ischaemic skin wounds. Br J Plast Surg. 2003;56(4):334-41. Epub 2003/07/23. doi: 10.1016/s0007-1226(03)00175-9. PubMed PMID: 12873460.

89. Johnson KE, Wilgus TA. Vascular Endothelial Growth Factor and Angiogenesis in the Regulation of Cutaneous Wound Repair. Adv Wound Care (New Rochelle). 2014;3(10):647-61. Epub 2014/10/11. doi: 10.1089/wound.2013.0517. PubMed PMID: 25302139; PMCID: PMC4183920.

Chapter 5

CONTROLLED DELIVERY OF VANCOMYCIN FROM COLLAGEN-TETHERED PEPTIDE VEHICLES FOR TREATMENT OF WOUND INFECTIONS

Despite the great promise for antibiotic therapy in wound infections, antibiotic resistance stemming from frequent dosing diminishes drug efficacy and contributes to recurrent infection. To overcome the limitations of current antibiotic therapies, it would be useful to develop new antibiotic delivery systems that maximize pharmacological activity and minimize side effects. In this study, I developed elastin-like peptide and collagen-like peptide (ELP-CLP) nanovesicles (ECnVs) tethered to collagen-containing matrices to control vancomycin delivery and provide extended antibacterial effects against methicillin-resistant Staphylococcus aureus (MRSA). I observed that ECnVs showed enhanced entrapment efficacy of vancomycin by 3-fold as compared to liposome formulations. Additionally, ECnVs enabled the controlled release of vancomycin at a constant rate with zero-order kinetics, whereas liposomes exhibited first-order release kinetics. Moreover, ECnVs could be retained on both collagen-fibrin (co-gel) matrices and collagen-only matrices, with differential retention on the two biomaterials resulting in different local concentrations of released vancomycin. Overall, the biphasic release profiles of vancomycin from ECnVs/co-gel and ECnVs/collagen more effectively inhibited the growth of MRSA for 18 h and 24 h, respectively, even after repeated bacterial inoculation as compared to matrices containing free vancomycin, which just delayed the growth of MRSA. Thus, this newly developed antibiotic delivery system exhibited distinct advantages for controlled vancomycin delivery and prolonged antibacterial activity relevant to the treatment of wound infections.

5.1 Introduction

Wound infection is one of the major healing impediments in chronic wounds, leading to serious life-threatening complications such as tissue necrosis, hemorrhage, and low-extremity amputations (1-3). Wound infection is usually characterized by an excessive inflammatory response involving immune cells, which are recruited by the release of toxins from bacteria colonizing the wound (4, 5). Further, colonies of pathogenic bacteria, including the Gram-negative bacterium Pseudomonas aeruginosa and the Gram-positive bacterium Staphylococcus aureus, form fibrous biofilms, which make it more challenging for host clearance mechanisms to eradicate bacterial colonies from the wound and stimulate wound repair (6-8). Thus, approaches to inhibit the growth of the bacterial populations in wound beds has been a target of drug delivery therapies for the treatment and prevention of wound infection while promoting wound healing.

Numerous topical formulations for wounds have been developed to manage and prevent wound infection (9-11). Synthetic and natural materials-based wound dressings in the form of hydrogels and films have been applied on the wound site to provide a moist environment, maintain the tissue temperature, and aid the wound healing process (12-14). Wound dressings containing antimicrobial/antibacterial agents enable control over local infections in situations where high concentrations of antibiotics are required, although the use of high antibiotic concentrations can lead to adverse effects such as renal toxicity and antibiotic resistance (15, 16). In addition, the presence of multidrug-resistant microorganisms (e.g., methicillin-resistant Staphylococcus aureus, or MRSA) in the wound diminishes the efficacy of common antibiotics, leading to infection recurrence and antibiotic resistance (17). Thus, the sustained local delivery of the minimum inhibitory concentrations (MIC) of antibiotics against MRSA is necessary to actively eradicate bacterial populations while minimizing adverse effects.

Nanoscale particles have been widely employed to encapsulate small-molecule therapeutics and control the release of these molecules over extended time periods. Due to the advantages of liposomes as a drug delivery system, including improved

pharmacokinetics and biodistribution, liposomes have demonstrated their effectiveness in antibiotic delivery and bacterial growth inhibition for a number of decades (18-22). Indeed, liposomes have shown a capacity to enhance the efficacy of antibiotics through their ability to fuse with the bacterial cell membrane and thereby increase the local concentration of antibiotics within the bacterial cells (23-25). As a result, antibiotics delivered by liposomes have shown efficacy against antibiotic-resistant microorganisms (26, 27). For example, liposomal delivery has been shown to increase the amount of intracellular methicillin accumulation and reduce bacterial populations by 96%, as compared to 40% for free methicillin (28). Likewise, liposomal delivery has also been shown to reduce the MIC of vancomycin against MRSA to 2- to 4-fold lower than that of free vancomycin (29, 30). Moreover, vancomycin-loaded liposomes have been shown to significantly reduced MRSA populations in a mouse surgical wound model relative to that of free vancomycin at the end of the 9th and 14th days of treatment (31).

Owing to the effectiveness of liposomes for antibiotic delivery to inhibit MRSA growth, our group previously demonstrated the potential utility of employing collagen-like peptide (CLP; also known as collagen-mimetic peptide or CMP)-modified vancomycin-liposomes, tethered to collagen/fibrin hydrogels (co-gels), for the treatment of MRSA-infected wounds in vivo (32). CLPs, composed of $(GXY)_n$ units, can fold into triple-helix structures at temperatures below their melting temperature, Tm, but disassemble into single strands above their Tm (33, 34), which enables them to hybridize with native collagen molecules through strand invasion at temperatures below the CLP T_m (35). I demonstrated that CLP modification of liposomes improved liposome retention on the co-gels, enhancing the sustained release of vancomycin and providing robust antibacterial effects against MRSA, as compared to liposome-containing co-gels without CLP modification (32). At the same time, the bioactivity of the co-gels stimulated cellular healing responses and improved the wound repair process in an in vivo murine wound model (36). While these results are promising, liposomal antibiotic delivery systems suffer limitations such as a short shelf-life and low

encapsulation efficiency (ca. 2.7-5.7%) for hydrophilic antibiotics (19, 37, 38), which motivated our evaluation of alternative collagen-binding carriers.

In this study, I employed the thermoresponsive assembly/disassembly of extracellular-matrix (ECM)-inspired elastin-like peptide and collagen-like peptide (ELP-CLP) nanovesicles (ECnVs) to improve the encapsulation efficiency of hydrophilic drugs, and to leverage the ability of ECnVs to tether to collagen-based matrices to extend the controlled delivery of vancomycin for prolonged antibacterial effects. Our group developed ELP-CLP conjugates whose design facilitated the triple helical assembly of CLPs, as well as corresponding reductions in the inverse transition temperature of the short ELP. This design approach resulted in assembly of stable vesicle-like nanostructures above the inverse transition temperature of the ELP domain (Tt), and disassembly above the Tm of the CLP domain (39-45). Our previous studies demonstrated that the ECnVs induced a minimal inflammatory response from macrophages, exhibited high cytocompatibility for murine fibroblasts, offered the ability to hybridize with collagen, and thermally controlled the delivery of a model drug (40). Thus, ECnVs offer significant potential owing to their high biocompatibility, tunable properties, and bioactivity of the peptide building blocks.

The overall goal of this study was to evaluate improvements in the efficacy of ECnVs tethered to collagen-containing matrices (collagen and co-gel) for vancomycin delivery and antibacterial activity against MRSA. ECnVs controlled vancomycin release at a constant rate to maintain the drug concentration within the therapeutic window for an extended period. Moreover, the different retention of ECnVs on collagen vs. co-gel affected the rates of ECnVs release from the matrices, leading to variations in the rate of biphasic vancomycin release depending on the matrix. The sustained release of vancomycin from the matrix-bound ECnVs extended the duration of antibacterial activity of vancomycin against MRSA, even with re-inoculation. Our finding suggests the potential for ECnVs in collagen-containing matrices as a potential treatment option for wound infections to prevent recurrence of infection and aid wound repair.

5.2 Materials and Methods

5.2.1 Materials

Low loading (LL) Rink Amide ProTide® Resin, ethyl cyanohydroxyiminoacetate (Oxyma), and diisopropylcarbodiimide (DIC) were procured from CEM Corporation (Matthews, NC). Fmoc-protected amino acids including 4-azidobutyric acid and Fmoc-propargylglycine-OH, as well as O-benzotriazole-N,N,N′,N′-tetramethyl-uronium-hexafluoro-phosphate (HBTU) were purchased from ChemPep Inc. (Wellington, FL). trifluoroacetic acid (TFA), N,N-dimethyl formamide (DMF), acetonitrile, methanol, and anhydrous ethyl ether were acquired from Fisher Scientific (Fairlawn, NJ). Piperidine, N,N-diisopropylethylamine (DIPEA), ethanethiol, triisopropylsilane, and tris-hydroxypropyltriazolylmethylamine (THPTA), (+)-sodium L-ascorbate, and copper (II) sulfate were procured from Sigma Aldrich (St. Louis, MO). Cy3 maleimide was obtained from Click Chemistry Tools LLC (Scottsdale, AZ). 1,2-dipalmitoyl-sn-glycero-3-phosphocholine (DPPC), 1,2-distearoyl-sn-glycero-3-phosphoethanolamine-N-[methoxy(polyethylene glycol)−2000-maleimide] (DSPE-PEG-Mal), and cholesterol were procured from Avanti Polar Lipids, Inc. (Alabama, USA), Sigma Aldrich (St. Louis, MO, USA), and Nanocs Inc. (New York, USA), respectively. Type I bovine collagen (10 mg/mL) was obtained from Advanced BioMatrix (San Diego, CA). A luminescent strain of Staphylococcus aureus (SAP231, luminescent version of USA300 MRSA strain NRS384) was a kind gift from Dr. Roger Plaut (42). All experiments using MRSA culture were performed in accordance with biosafety level 2 practices. The proper laboratory PPE and BSL-2 operation practices were carefully used to avoid any potential MRSA infection. Vancomycin, tryptic soy broth, tryptic soy agar, and chloramphenicol were purchased from Sigma Aldrich (St. Louis MO, USA).

5.2.2 Synthesis of ELP-CLP conjugates

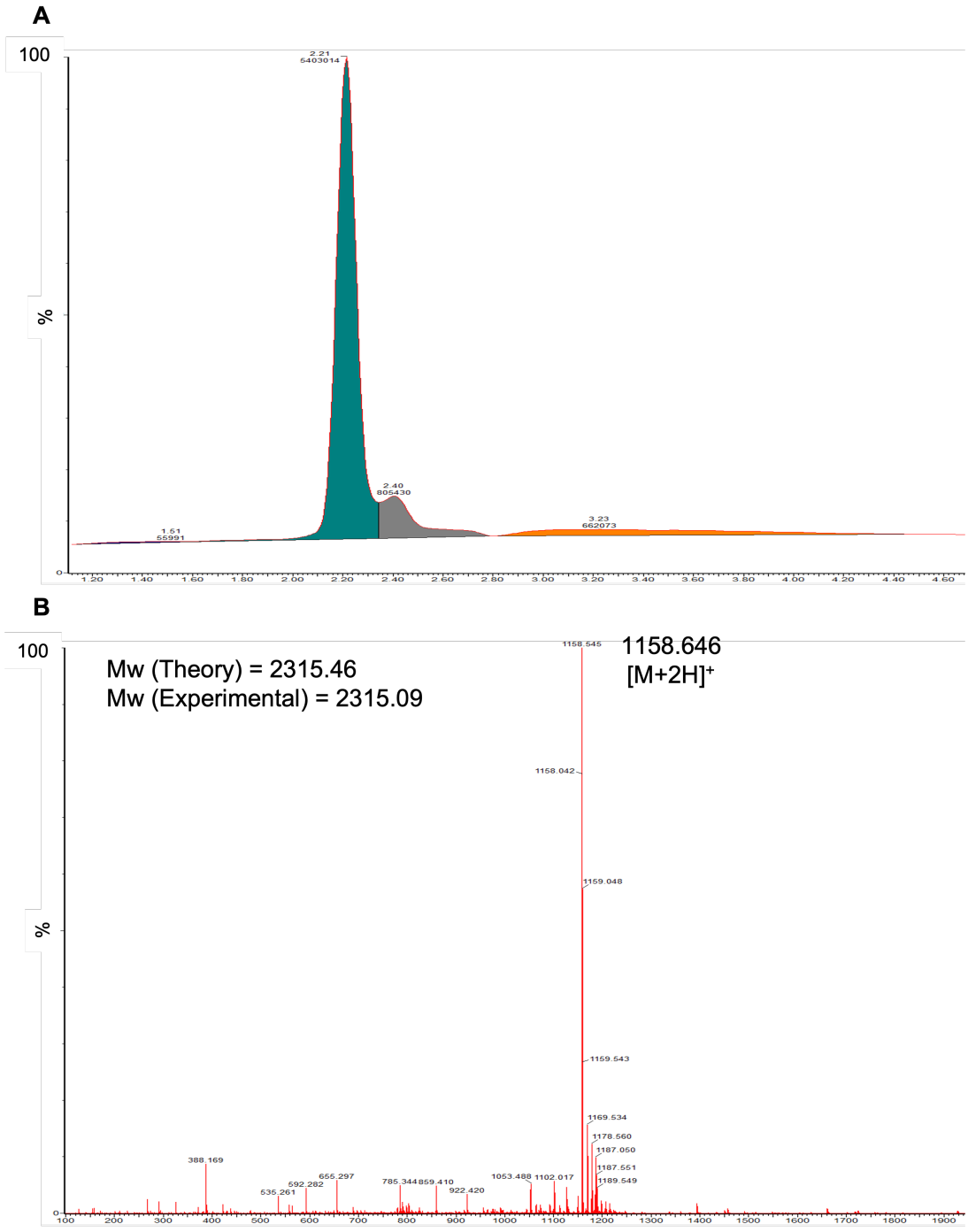

Figure 5.1. LC-MS of the purified $(GPO)_8GC$: (A) UPLC trace; (B) ESI-MS spectra.

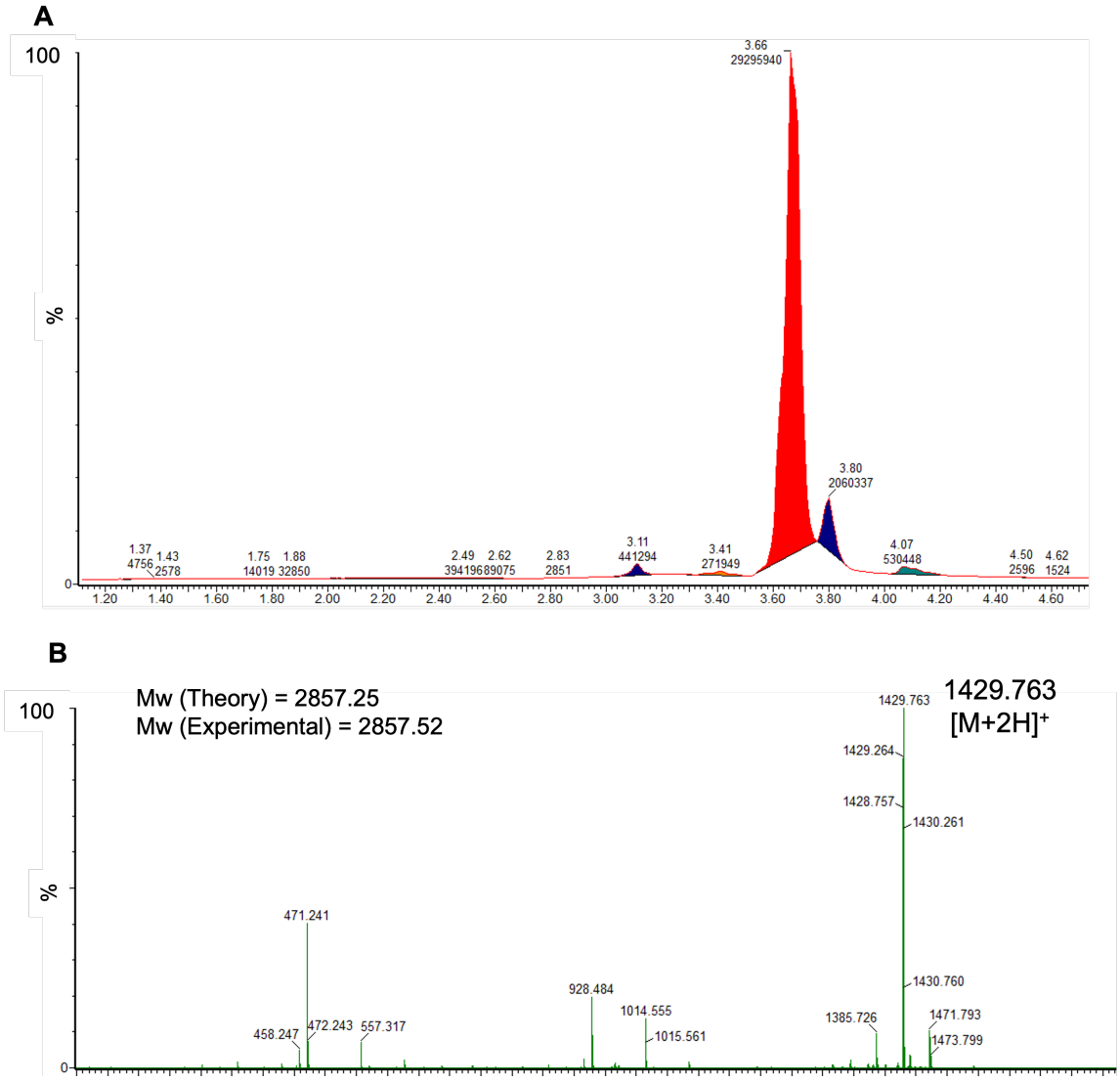

Figure 5.2. LC-MS of the purified F_6: (A) UPLC trace; (B) ESI-MS spectra for peak 3.66.

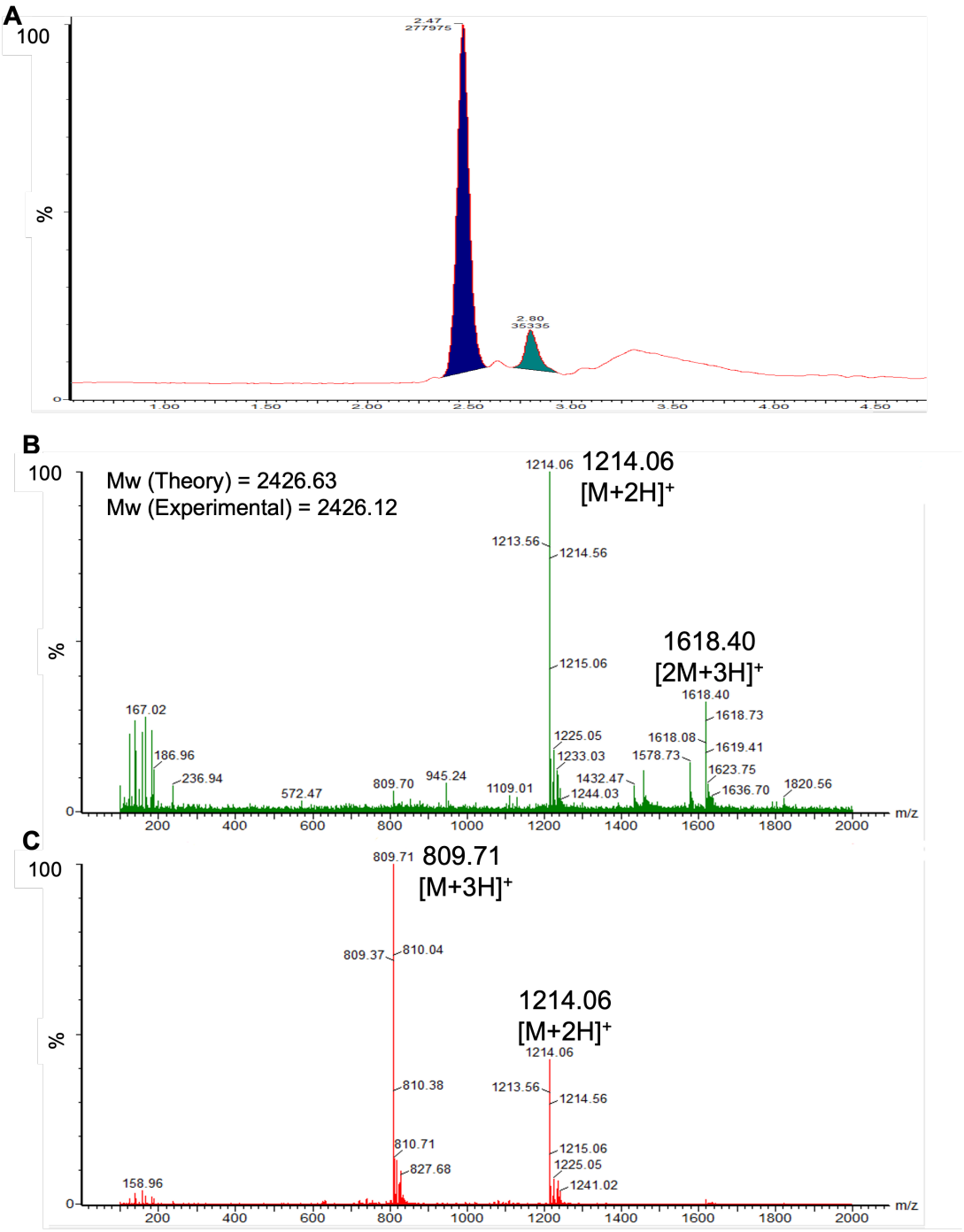

Figure 5.3. LC-MS of the purified azide-$(GPO)_8$GC: (A) UPLC trace (2.47 peak is pure CLP and 2.80 peak is a mixture of monomer CLP with dimer CLP); (B) ESI-MS spectra for peak 2.80; (C) ESI-MS spectra for peak 2.47.

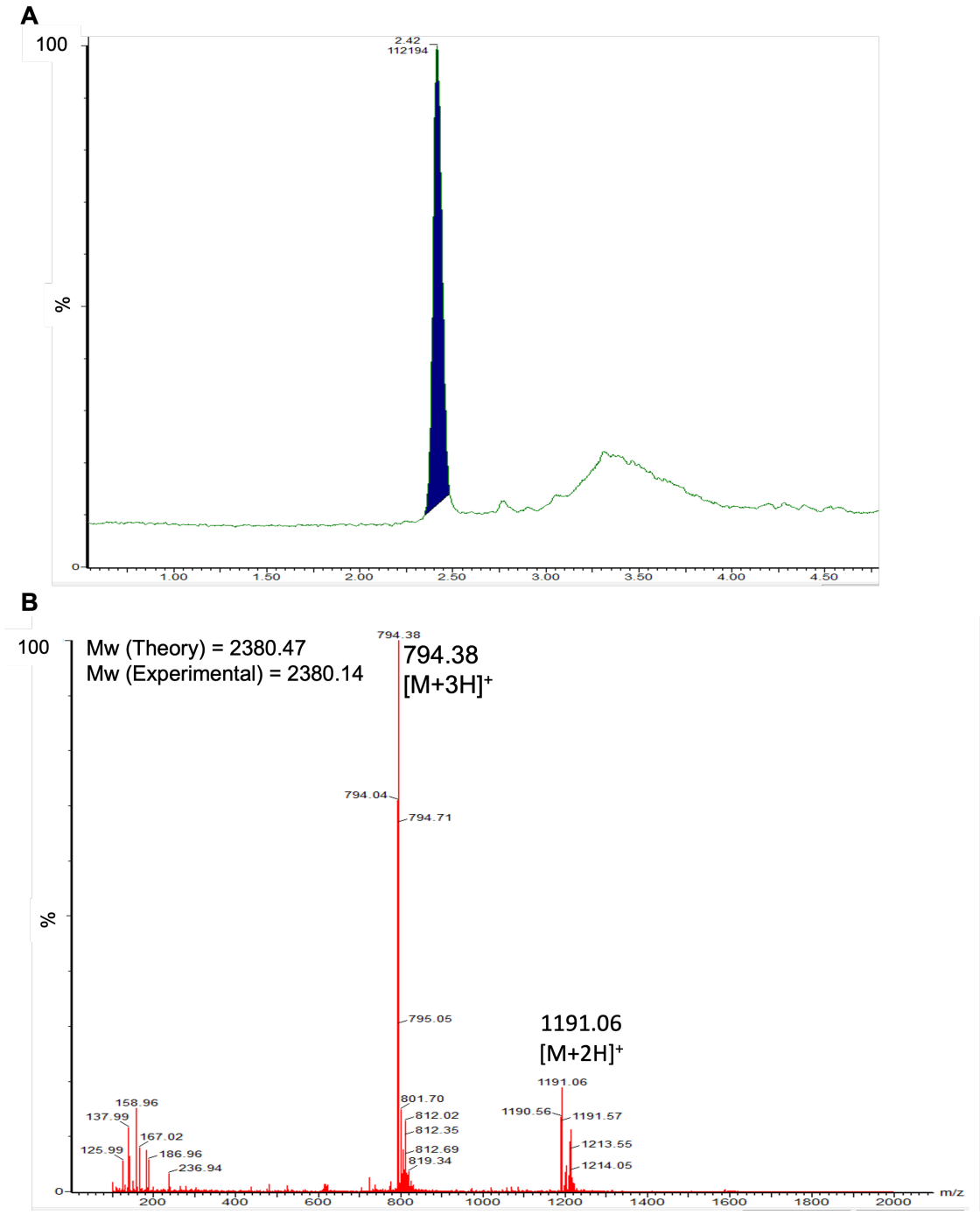

Figure 5.4. LC-MS of the purified azide-$(GPO)_8$GG: (A) UPLC trace; (B) ESI-MS spectra.

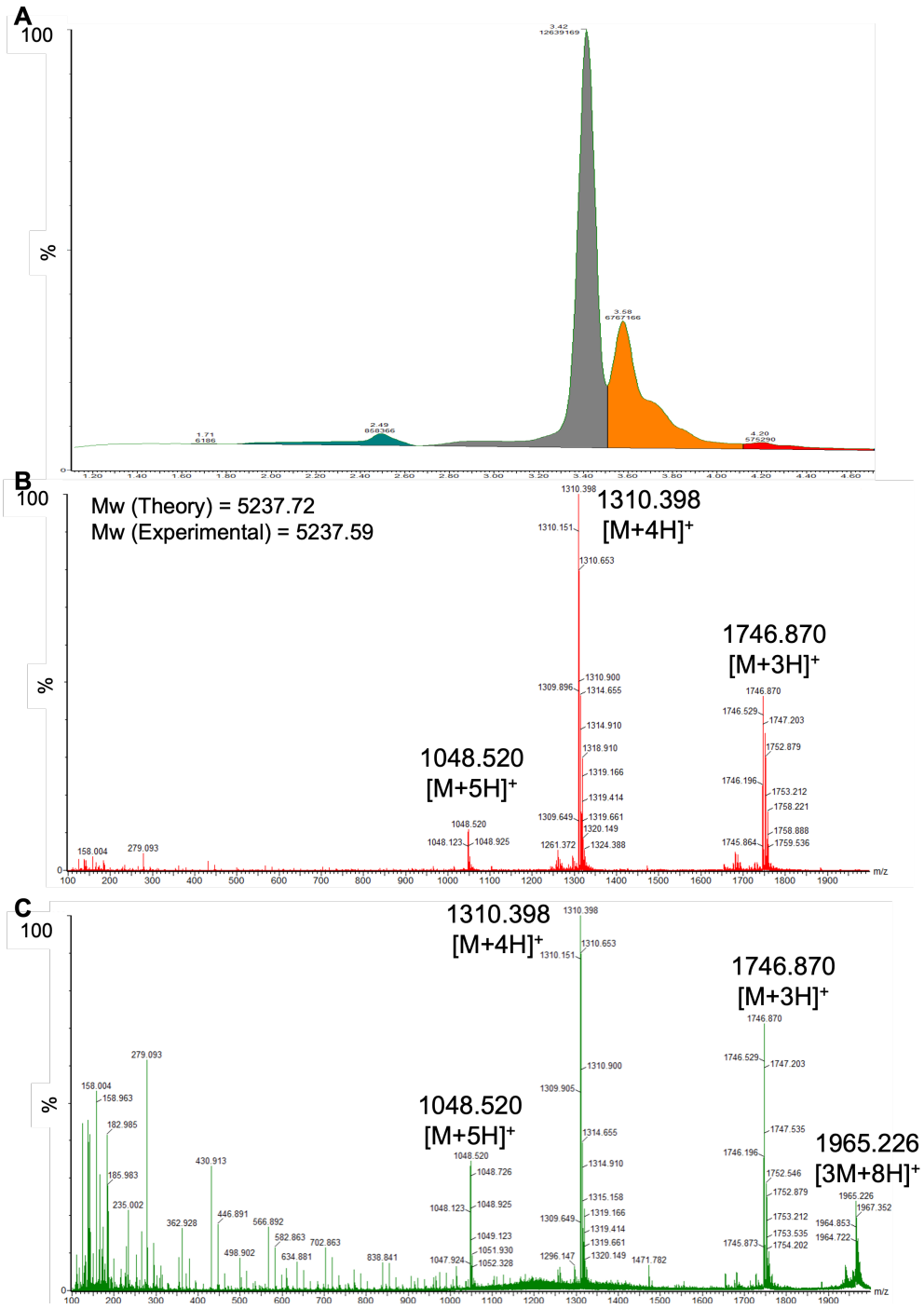

Figure 5.5. LC-MS of the purified F6-(GPO)8GG: (A) UPLC trace (3.42 peak is pure CLP and 3.58 peak is a mixture of monomer ELP-CLP with trimer ELP-CLP); (B) ESI-MS spectra for peak 3.42; (C) ESI-MS spectra for peak 3.58.

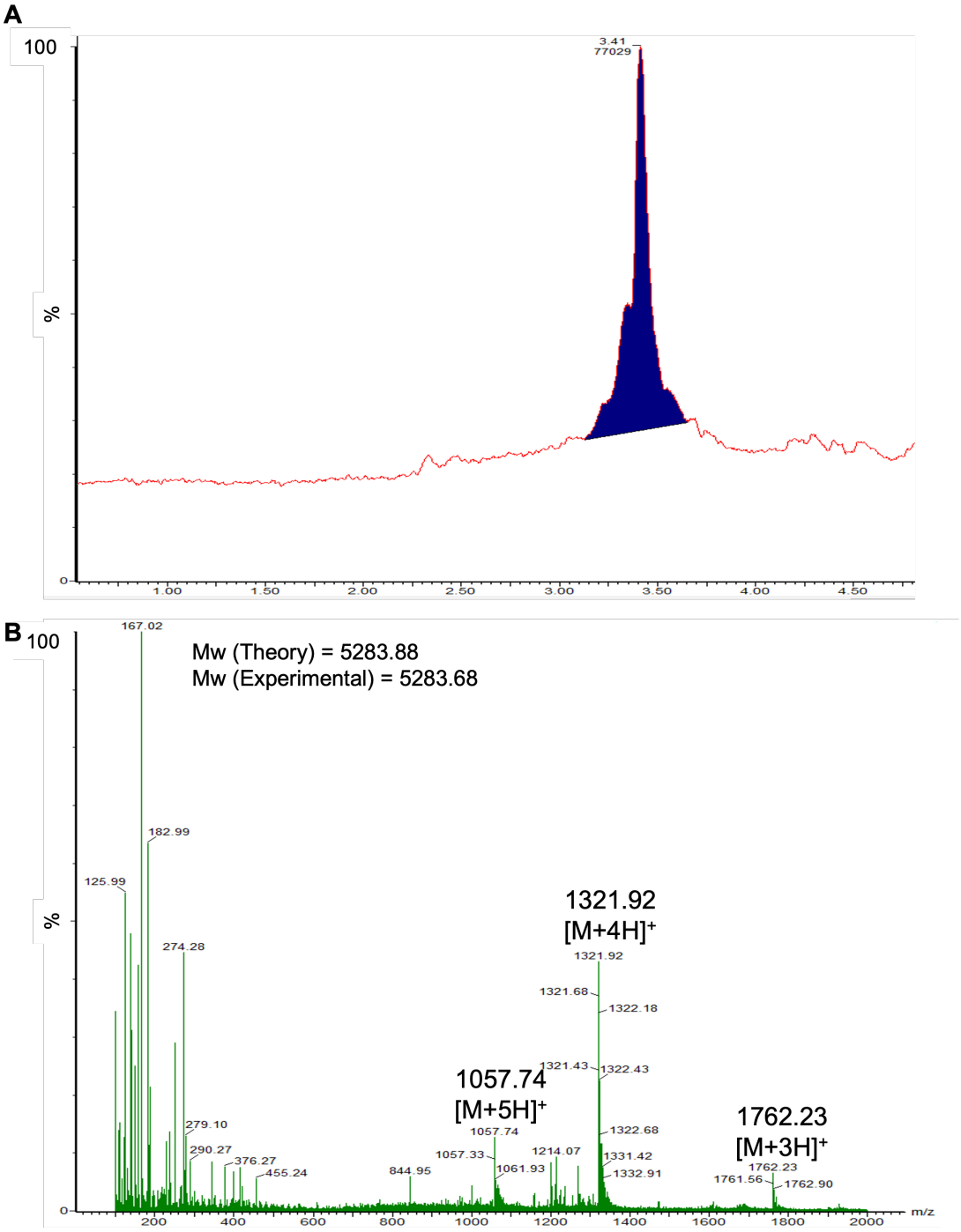

Figure 5.6. LC-MS of the purified F_6-$(GPO)_8$GC: (A) UPLC trace; (B) ESI-MS spectra.

The peptides [CLP (G_8): $(GPO)_8GG$, $(GPO)_8GC$, ELP (F_6): $(VPGFG)_6G'$ (G' = propargyl glycine)] were synthesized via standard Fmoc solid-phase peptide synthesis using a Liberty Blue Automated Microwave Peptide Synthesizer (CEM Corporation, Charlotte, NC) as described in our previous reports (41). Briefly, each amino acid (4 molar equivalents) was added by double coupling at 90 ºC for 10 min with Oxyma (4 molar equivalents) and DIC (12 molar equivalents). For azido functionalization of the CLP, 4-azidobutyric acid (6 molar equivalents) was coupled to the N-terminus of the CLP on resin via a 2 h reaction with HBTU (6 molar equivalents) and DIPEA (12 molar equivalents). The peptides were cleaved from the resin after 2 h by incubation in 95:2.5:2.5 TFA:TIS:water (v:v:v). The crude peptides were purified via reverse-phase HPLC (Waters Inc., Milford, MA) on a Waters XBridge BEH130 Prep C-18 column using a linear gradient mixture of water (0.1% TFA) and acetonitrile (0.1% TFA) with ultraviolet detection at 214 nm. The molecular weights and purities of each of the purified peptides were confirmed via ultra-performance liquid chromatography, in line with electrospray ionization mass spectrometry (Xevo G2-S QTof mass spectrometer; Waters Inc., Milford, MA) (Figure 5.1-5.4). The purified CLP (6 µmol) and ELP (3 µmol) were conjugated via the copper (I)-mediated azide-alkyne cycloaddition reaction as described in our previous papers (39). Briefly, ELP, CLP, Cu (II) sulfate (6 µmol), THPTA ligand (35.1 µmol), and (+)-sodium L-ascorbate (400 µmol) in 70:30 water:DMSO (v:v) were incubated for 1 h with stirring at 70 ºC. Then, the ELP-CLP conjugate (F_6-G_8GG) was purified via HPLC at 70 ºC and confirmed by UPLC-MS (Figure 5.5&5.6).

5.2.3 Characterization of ELP-CLP conjugates

The melting temperature (T_m) of the ELP-CLP F6-G8GG (T_m = 57.9 ºC; Figure 5.7A) and the transition temperature (Tt) of the same ELP-CLP (T_t = 21.20 ºC) were identified in previous study (41). ELP-CLP conjugate dissolved in water (1 mg/mL) was incubated at 37 ºC overnight after 30 min of heating the solution at 80 ºC to completely dissociate the ELP-CLP conjugate (Figure 5.7B). The resulting ELP-CLP nanovesicles

sizes were analyzed via DLS on a ZetaSizer Nano Series (Nano ZS, Malvern Instruments, UK) at 173 º as a scattering angle. The cumulant method was used for data fitting. The cross-sectional morphology of the ELP-CLP nanovesicles was evaluated via Thermo ScientificTM TalosTM -TEM (Thermo Fisher scientific, Waltham, MA) operated at 200 kV. The ELP-CLP sample (5 µL) was drop-casted onto the carbon-coated copper grids (CF300-Cu, Electron Microscopy Sciences Inc.) and blotted after 1 min. Samples were stained using 1% PTA at pH 7 (3 µL) for 10 s and blotted. Then, samples were air-dried for at least 2 h before TEM imaging.

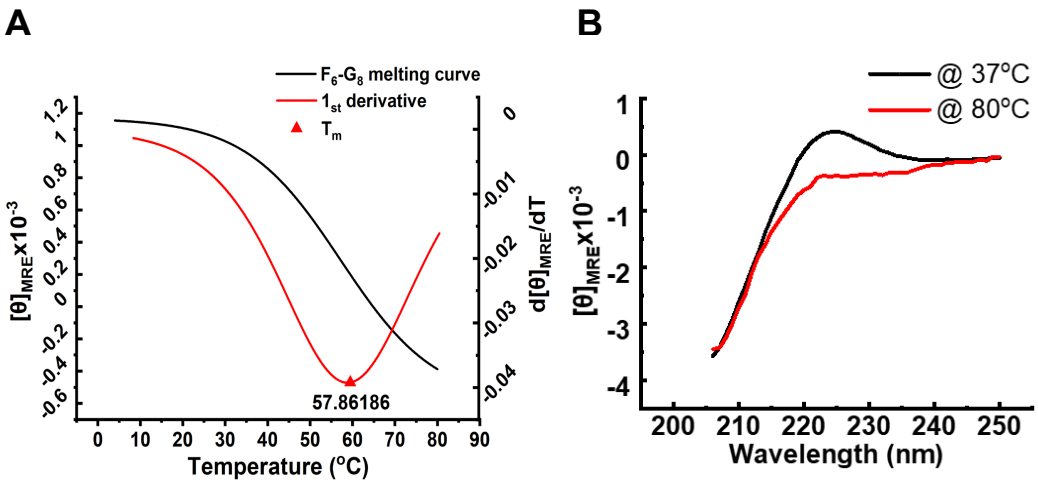

Figure 5.7. Circular dichroism measurement of F_6-$(GPO)_8GG$ (A) Variable temperature measurement at 225 nm for Tm determination (B) Spectra measurement from 205 to 250 nm at 37 ºC and 80 ºC.

5.2.4 Vancomycin encapsulation in ECnVs

First, the ELP-CLP conjugate (dissolved in water) was heated at 80 ºC for 30 min to completely disassemble the ELP-CLP conjugate. Vancomycin (1 molar ratio to ELP-CLP conjugate) in PBS at pH 7 was added to the solution of ELP-CLP conjugate. Vancomycin and the ELP-CLP conjugate were then mixed with a vortex mixer and incubated at 37 ºC overnight to enable loading of vancomycin into the ECnVs during

nanovesicle formation. Then, 10x PBS (Corning®, Corning, NY) was added to yield a final 1x PBS solution. For determining the encapsulation efficiency (EE) and loading capacity (LC) of vancomycin (van) in the ECnVs, each nanovesicle sample was centrifuged at 15K rpm for 10 min to separate the vancomycin loaded ECnVs from any unencapsulated vancomycin in the supernatant; subsequently, the ECnVs were resuspended in PBS. The concentration of unloaded vancomycin in the collected supernatant was determined using absorbance measurements on the collected supernatant. Comparison of the concentration of vancomycin in the supernatant to the initial concentration of vancomycin in solution yielded an assessment of the concentration of vancomycin encapsulated in the ECnVs. The EE of vancomycin (van) in ECnVs was calculated using the following formula:

$$EE = \frac{M_{\text{van loaded in ECnVs}}}{M_{\text{van initial}}} \times 100 \quad (1)$$

where $M_{\text{van loaded in ECnVs}}$ = mass of vancomycin-loaded in ECnVs, and $M_{\text{van initial}}$ = initial mass of vancomycin added to the ELP-CLP solution for encapsulation.

The LC of vancomycin (van) in ECnVs was calculated using the following formula:

$$LC = \frac{M_{\text{van loaded in ECnVs}}}{M_{\text{ECnvs}}} \times 100 \quad (2)$$

where $M_{\text{van loaded in ECnVs}}$ = mass of vancomycin-loaded in ECnVs, and M_{ECnvs} = mass of ECnVs.

5.2.5 Vancomycin encapsulation in liposomes

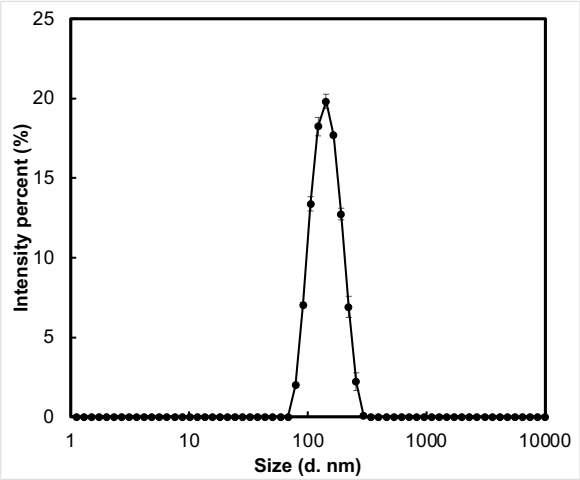

Figure 5.8. Size measurement of vancomycin loaded liposome using dynamic light scattering.

The liposomes were prepared by a traditional thin-film dehydration-rehydration protocol, followed by sequential extrusion through membrane filters with pore sizes of 200 nm and 100 nm, respectively (47). Lipids with a molar ratio of 73:24:3 (DPPC:Cholesterol:DSPE-PEG-Mal) were mixed in 4:1 chloroform and methanol (v:v) and added into a round-bottom flask. The lipid film was formed after evaporation of the organic solvent for at least 2 h via rotary evaporation at 40 ºC and 400 psi. The vancomycin in PBS at pH 7 was added to the flask at a 3-fold excess of vancomycin:total mass of lipids, and the flask was rotated for 15 min at 60 ºC for rehydration. The samples were then sonicated for 2 min before extrusion. The lipid and vancomycin suspension was first extruded through a polycarbonate membrane with a pore size of 200 nm (15 times), and subsequently, through a membrane with pore size of 100 nm (10 times). The diameters of the vancomycin-loaded liposomes were evaluated via DLS with a ZetaSizer Nano Series (Nano ZS, Malvern Instruments, UK) with a scattering angle of 173º (Figure. 5.8). In order to determine the encapsulation efficiency (EE) and loading capacity (LC) of vancomycin in the liposomes, the sample was centrifuged at 15 K rpm for 10 min for precipitation of vancomycin-loaded liposomes to remove any unencapsulated vancomycin, and the concentration of the unencapsulated vancomycin

was determined via evaluation of the absorbance of the supernatant. The EE and LC of vancomycin in the liposomes was calculated using Formula 1 and 2 above. The vancomycin-loaded liposomes were re-suspended in PBS, and lyophilized with 20 mM sucrose prior to incorporation into collagen-containing matrices.

5.2.6 Vancomycin release kinetics from nanocarriers

Vancomycin release rates from vancomycin-loaded liposomes and vancomycin-loaded ELP-CLP nanovesicles were evaluated using Slide-A-Lyzer™ Mini dialysis device with 10K molecular weight cutoff (Thermo Scientific™, Waltham, MA), using the rate of free vancomycin transport across the dialysis membrane as a control. 100 µL aliquots of each formulation (free vancomycin, vancomycin-loaded liposomes, and vancomycin-loaded ELP-CLP) were placed in the dialysis cup and immersed in 2 mL of PBS buffer in a glass vial. The samples were incubated at 37 ºC with a shaking at 225 rpm. The PBS, containing released vancomycin (400 µL) was collected and replaced with fresh PBS at 2, 4, 8, 24, 48, 72, 96, 120, 144, and 168 h. At 168 h, the samples were incubated at 80 ºC for 30 min to recover the vancomycin from the disassembled ELP-CLP (Figure 5.7B) and liposome and collected as the 168.5 h time point. The concentrations of released vancomycin in PBS were determined using an absorbance measurement at 280 nm on a Nanodrop spectrometer (Thermo Scientific™, Waltham, MA), and the cumulative percentage release of vancomycin per sample was calculated using the following equation (44):

$$P = \frac{V_e \sum_1^{n-1} C_i + V_0 C_n}{M_{van-loaded}} \times 100\% \qquad (3)$$

Where $M_{van\text{-}loaded}$ represents the amount of vancomycin encapsulated in ELP-CLP or liposome, V_0 is the total volume of the release media, V_e is the volume of each sample that is being collected at each time point, C_i is the concentration of vancomycin measured by UV absorbance in the i^{th} sample, and C_n represents the concentration of vancomycin in n^{th} sample.

In order to assess the diffusion of any free vancomycin, that remained in the encapsulated samples, across the dialysis membrane, free vancomycin controls were formulated based on the calculation of encapsulation efficiency (EE) for the liposome and ECnVs. Because the EE for the liposomes was 15.2% of the initial vancomycin employed during formulation, free vancomycin controls with 84.8% of the initial vancomycin were employed for the liposome. And, free vancomycin controls with 51.8% of the initial vancomycin were employed for ECnVs since the EE for the ECnVs was 48.2 % of the initial vancomycin employed during formulation. Then, the release profiles of free vancomycin were subtracted from the data in Figure 5.12A to acquire the data presented in Figure 5.12B.

5.2.7 Collagen and co-gel matrix retention and release of nanovesicles

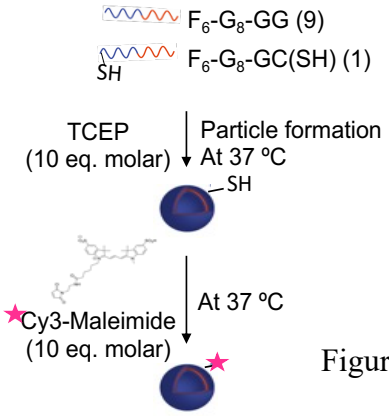

Figure 5.9. The reaction schematic for Cy3 labeled ECnVs.

First, ECnVs were labelled with Cy3-Maleimide using a Michael-type addition reaction (Figure. 5.9). Briefly, a 1:9 $(VPGFG)_6$-$(GPO)_8GC$:$(VPGFG)_6$-$(GPO)_8GG$ mass ratio in PBS was heated at 80 ºC to completely dissociate the ELP-CLP assembly, and the heated samples were subsequently mixed thoroughly. Then, the ECnVs were allowed to form by incubation at 37 ºC overnight. Cy3-Maleimide (10 molar equivalents as compared to $(VPGFG)_6$-$(GPO)_8GC$) was added into the ECnV solution and the mixture was rotated at 50 rpm for 2 h at 37 ºC. The unreacted Cy3-Malemide was removed by centrifugation at 15K rpm for 10 min, and the labeled ECnVs were suspended in PBS. The Cy3-labeled ECnVs were lyophilized with 20 mM sucrose. For

the control experiment, fluorescently labeled liposomes were prepared (DPPC : Cholesterol : DSPE-PEG-Maleimide : NBD-PC (72.6:24:3:0.4)) as described in our previous work (49). Additionally, CLP-functionalized, fluorescently labeled liposomes were prepared through one of two methods: post-surface modification with CLP, or pre-surface modification with CLP. For post-surface modification, CLP was added to the fluorescently labeled liposome using a Michael-type addition reaction between DSPE-PEG-Maleimide of the fluorescently labeled liposome and thiol groups on the cysteine residue of the CLP ($(GPO)_8GC$). For pre-surface modification, prior to liposome formulation, CLP ($(GPO)_8GC$)) was conjugated with DSPE-PEG-Maleimide lipid to prepare DSPE-PEG-CLP lipid, which was confirmed by MALDI-ToF (Fig. S10), as described in the literature (50, 51). CLP functionalized, fluorescently labeled liposomes

were prepared (DPPC : Cholesterol : DSPE-PEG-CLP : NBD-PC (72.6:24:3:0.4)) following the same protocol to prepare fluorescently labeled liposome.

The pre-gel mixtures of collagen or co-gel were prepared separately. The pre-gel collagen was composed of 4 mg/mL neutralized bovine collagen type I (Fibricol®) with 10X PBS and 0.1N NaOH, and the pre-gel co-gel was composed of 4 mg/mL neutralized bovine collagen type I in PBS, 1.25 mg/mL fibrinogen in 20 mM HEPES pH 6, and 0.156 IU/mL thrombin in 20 mM HEPES pH 6. The lyophilized Cy3-labeled

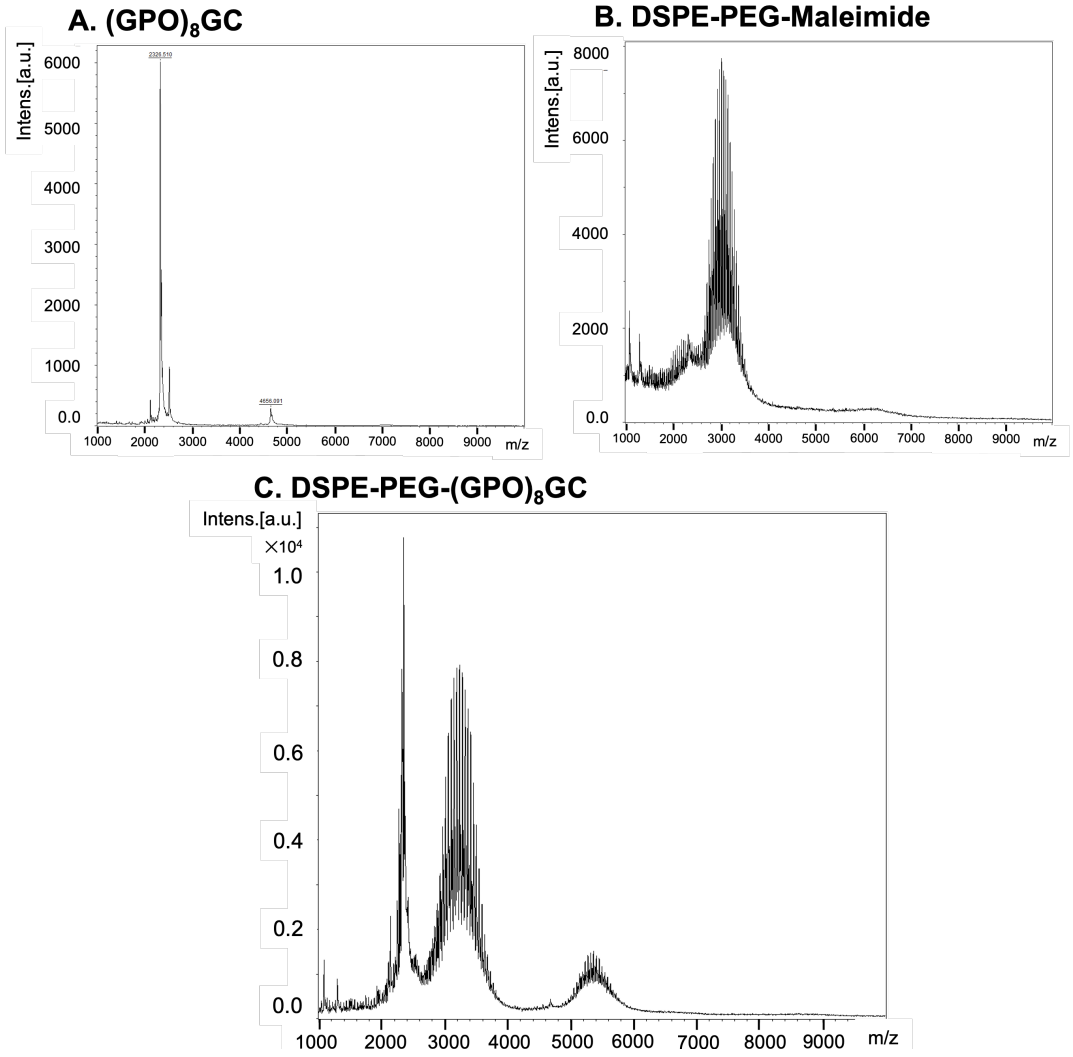

Figure 5.10. MALDI-ToF with a linear mode of A. $(GPO)_8GC$ B. DSPE-PEG-Maleimide C. DSEP-PEG-$(GPO)_8GC$.

ECnVs or fluorescently labeled liposomes were suspended in the pre-gel mixtures of collagen or co-gel. Then, samples were added to a microscope slide for gelation overnight. The Cy3 labelled ECnVs (λ_{ex} 532 nm and λ_{em} 568 nm) or fluorescently labeled liposomes (λ_{ex} 564 nm and λ_{em} 531 nm) and autofluorescence of collagen fibers (reflected light at 405 nm) within the matrices were visualized both before and after washing (with PBS overnight at 37 ºC) using a Zeiss LSM 880 confocal microscope with C-Apochromat 40x water objective. The 3D image plot and image analysis were performed using Volocity Imaging software (Quorum Tech. Inc., Canada). In addition, in vitro Cy3-labeled ECnV release from the matrices (collagen vs. co-gel) was measured for matrix samples containing Cy3-labeled ECnVs. Lyophilized Cy3-labeled ECnVs were suspended and mixed well into the pre-gel mixture, and 100 µL samples were transferred into non-coated 48-well plate wells for gelation at 37 ºC overnight. Then, 500 µL of PBS was added to visually turbid hydrogel samples in each well to initiate the release experiments with the (unloaded) ECnV-loaded matrices. The release samples (100 µL) were collected at 0.5, 1, 2, 4, 8, 24, 48, 72, and 96 h at 37 ºC. The cumulative ECnVs release was determined using fluorescent measurements at λ_{ex} 532 nm and λ_{em} 568 nm using a SpectraMax i3x multi-mode microplate reader (Molecular Devices, LLC. San Jose, CA) and using equation (3).

5.2.8 Vancomycin release kinetics from matrices

Similar to the study of Cy3-labeled ECnVs release from matrices, in vitro vancomycin release from the matrices (collagen vs. co-gel) was measured for matrix samples containing free vancomycin, vancomycin-loaded liposomes, and vancomycin-loaded ECnVs. Collagen matrices were prepared with a neutralized 4 mg/mL bovine type I collagen, and co-gels were prepared by mixing 4 mg/mL neutralized bovine type I collagen, 1.25 mg/mL fibrinogen in 20 mM HEPES at pH 6, and 0.156 IU/mL thrombin in 20 mM HEPES at pH 6. In these pre-gel mixtures of collagen or co-gel, the lyophilized free vancomycin, vancomycin-loaded liposomes, or vancomycin-loaded ELP-CLP ECnVs were suspended and mixed well. Then, 100 µL samples were

transferred into non-coated 48-well plate wells before gelation by incubation at 37 ºC overnight. After overnight gelation, 500 µL of PBS at 37 ºC was added to visually turbid hydrogel samples in each well to initiate vancomycin release. The released samples were collected at 0.5, 1, 2, 4, 8, 24, 48, 72, and 96 h at 37 ºC. After the last time point of release, samples were heated at 80 ºC for 30 min to completely dissolve the matrices for the recovery of remaining vancomycin, and these samples were collected as the 96.5 h time point. The cumulative vancomycin release was determined using absorbance measurements at 280 nm using a Nanodrop spectrophotometer (Thermo ScientificTM, Waltham, MA) and using equation (3).

5.2.9 Antibacterial activity of vancomycin-loaded in ECnVs in matrices

Similar to the re-inoculation protocols employed in our previous study (32), collagen gel or co-gel (100 µL) was loaded with free vancomycin or vancomycin-loaded ECnVs at concentrations of 4, 7, or 10 µg/mL vancomycin per gel. Gels were added to the wells of black 96-well plates. The plates were incubated at 37 ºC overnight for gelation. After gelation, samples of the luminescent MRSA strain (SAP231, luminescent version of USA300 MRSA strain NRS384) were diluted in tryptic soy broth with chloramphenicol (10 µg/mL) to prepare solutions of 5 × 105 cfu/mL of MRSA. 200 µL of MRSA (5 × 105 cfu/mL) were added to each well of a 96-well plate; the final concentrations of vancomycin in the MRSA cultures were 1, 2, and 3 µg/mL. The plate was incubated at 37 ºC with shaking at 150 rpm for 16 h, and the optical density (O.D.) at 600 nm and luminescence of luminescent MRSA with no excitation set-up were measured using absorbance module and photomultiplier tubes (PMT) detector of luminescence modules, respectively, of a SpectraMax i3x multi-mode microplate reader (Molecular Devices, LLC. San Jose, CA) every two hours. Sixteen hours after the first inoculation, the bacterial cultures were removed from the wells and the wells were rinsed with the culture broth. Then, a fresh aliquot of 200 µL of MRSA (5 × 105 cfu/mL) was added into each well of the 96-well plate for re-inoculation. The

bacterial growth was evaluated using O.D. and luminescence measurements every 2 h for an additional 16 h.

5.2.10 Mathematical model fitting and statistical analysis

The vancomycin or ECnV release profiles were analyzed using the fitting functions BoxLucas1 for first-order release and Allometric2 for Korsmeyer-Peppas kinetics with the max number of iterations set to 500 and the tolerance set to 1-6 in OriginLab (Northampton, MA).

Unless indicated, all experimental data were expressed as the mean ± standard deviation of the mean. The statistical significance was analyzed using OriginLab software (Northampton, MA). Sample groups were compared using a Student's t-test with a significance level of 0.05.

5.3 Results

5.3.1 Characterization of vancomycin- loaded ELP-CLP

To evaluate whether the loading of vancomycin in ECnVs influenced the physical properties of the ECnVs, the diameters and morphology of ECnVs before and after vancomycin encapsulation were examined using DLS and TEM imaging, respectively. The ECnVs (D_h = 157.0 ± 5.0 nm) exhibited a decreased diameter (D_h = 122.3 ± 6.2 nm) after the loading of vancomycin (Figure. 5.11A), which was similar behavior to that of liposomes after vancomycin loading (32), and also similar behavior to that of ECnVs after hydrophobic fluorescein loading (40). Furthermore, the morphology of the ECnVs was similar before and after loading of vancomycin (Figure.

5.11B), indicating that the encapsulation of vancomycin in the nanovesicles did not disrupt ELP-CLP assembly.

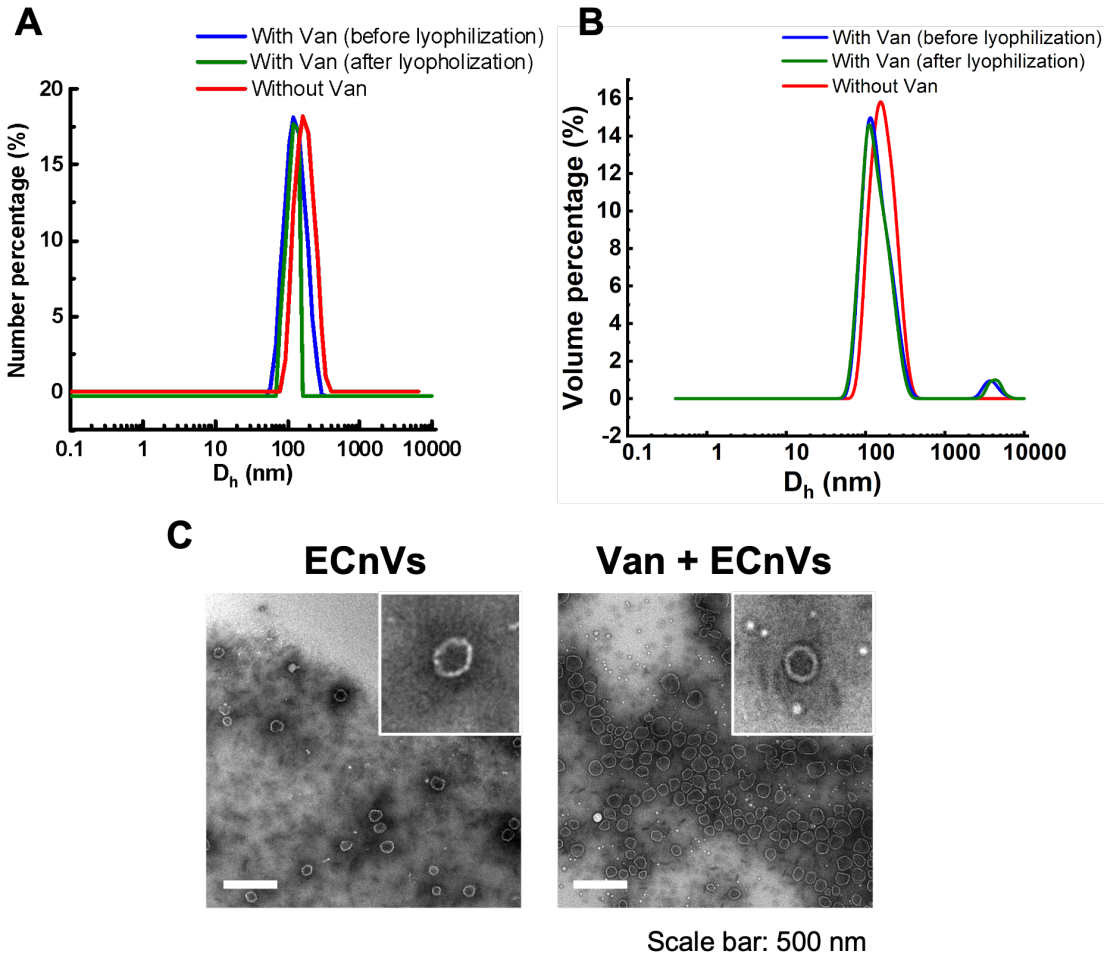

Figure 5.11. Characterization of vancomycin loaded ECnVs (A) Size measurements of ECnVs using DLS (number percentage and volume percentage) before and after vancomycin loading and after lyophilization. (B) Representative TEM images of ECnVs before and after Vancomycin loading. Scale bar is 500 nm.

5.3.2 Vancomycin release kinetics from nanocarriers

To determine the release kinetics of vancomycin from ECnVs, in vitro vancomycin release studies were conducted using a dialysis method under physiologically relevant conditions. The release kinetics of vancomycin from ECnVs

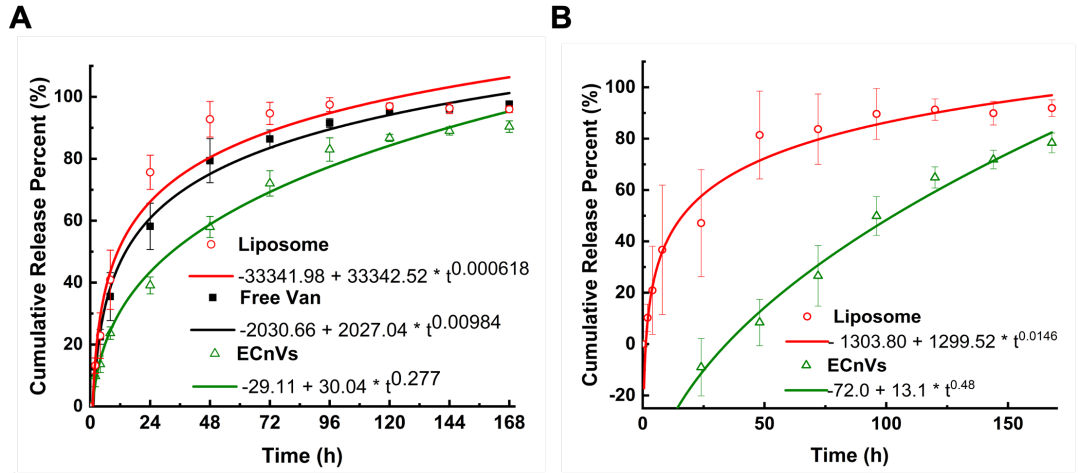

C

	EE (%)	LC (%)	K_{kp}	n	R^2
Van. + Liposome	15.2 ± 0.6	45.6 ± 1.8	-1303.80	0.0146	0.969
				Quasi Fickian	
Van. + ECnVs	48.2 ± 3.2	144.6 ± 9.6	-71.97	0.480	0.985
				Non-Fickian	

Figure 5.12. Vancomycin release from nanocarriers (A) without removing or (B) with mathematically removing the unloaded Vancomycin at 37 ºC. The release profiles were fitted with Korsmeyer-Peppas model. (C) Table for encapsulation efficiency (E.E.), loading capacity (L.C.) of vancomycin in liposome and ELP-CLP and constants for Korsmeyer-Peppas model fitting. K_{kp} indicates Korsmeyer release rate constant and n indicates diffusional exponent. Each data represents mean ± standard deviation for n=6.

were calculated as the cumulative release percentage over a period of 7 days. As a control, vancomycin-loaded liposomes (D_h = 136.6 ± 1.0 nm) of similar diameter as the vancomycin-loaded ECnVs (Figure. 5.8) were used. The vancomycin release data from the liposomes and ECnVs is presented in Figure. 5.12A; it is obvious from the data that the release of vancomycin from ECnVs was much slower than the release of vancomycin from the liposomes. The data were fit to a Korsmeyer-Peppas model, and the numeric coefficient (n) from this model (which describes the mechanism of release), was less than 0.45 for both nanocarriers, indicating a similar mechanism of release of vancomycin from the ECnVs and liposomes (Figure. 5.12A). The release kinetics of

free vancomycin were also determined and mathematically subtracted from the overall release profiles to account for the diffusion of vancomycin across the dialysis membrane and to allow a more direct comparison of the release rates and mechanisms of the carriers (Figure. 5.12B and 5.12C). To better capture the mechanism of vancomycin release from ECnVs and liposomes, the Korsmeyer-Peppas model was then utilized to characterize the release kinetics of these corrected release profiles (Figure. 5.12B). And, since the initial three data points at 2h, 4h, and 8h for ECnVs represented no vancomycin release from ECnVs during the lag-time, these three data points were excluded for fitting with Korsmeyer-Peppas model. Based on the data in Figure. 5.12B, the vancomycin was released from liposomes largely via diffusion ($n < 0.45$), whereas the release of vancomycin from ECnVs occured mainly via both diffusion and dissolution mechanisms ($0.45 < n < 0.8$) (Figure. 5.12C). These data confirm not only that the release kinetics of vancomycin can be controlled by the type of nanocarriers, but the release mechanism is also depending on the types of nanocarriers.

5.3.3 ELP-CLP retention and release on/from matrices

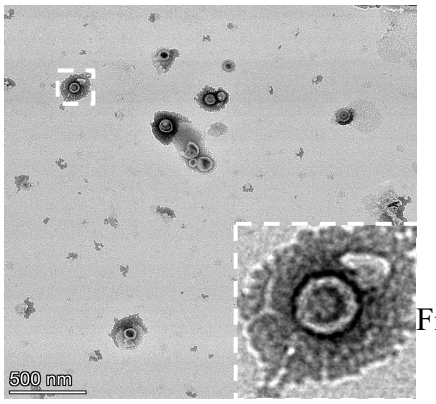

Figure 5.13. TEM images of Cy3 labeled ECnVs at 37 ºC

In order to characterize the retention of ECnVs on collagen-containing matrices, fluorescently labeled ECnVs in collagen vs. co-gel matrices were detected using confocal microscopy via comparison of the fluorescence before and after rinsing the ECnV-loaded matrices with PBS at 37 ºC. Prior to conducting these experiments, I confirmed via TEM imaging that the addition of the fluorescent label, Cy3, did not

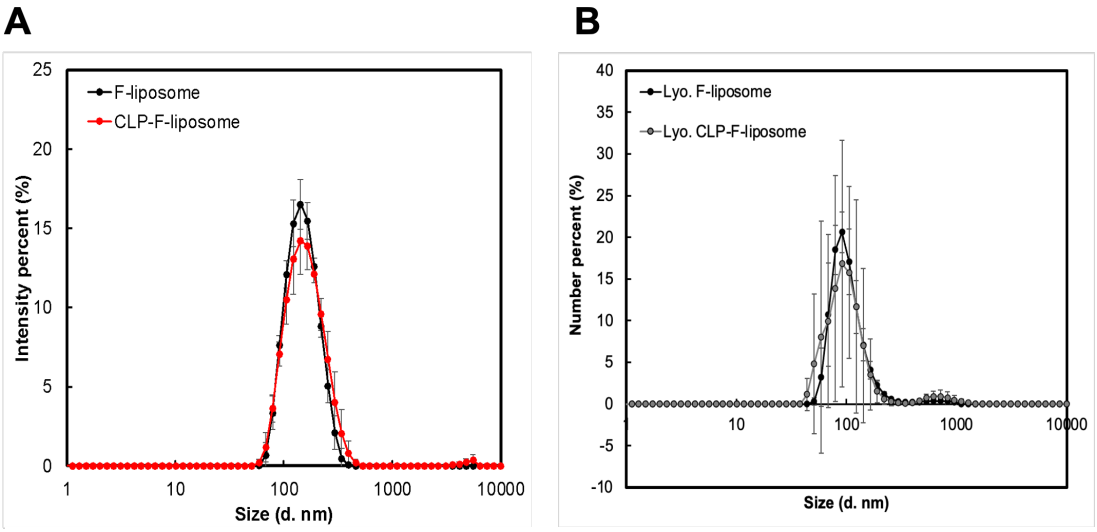

Figure 5.14. Size measurement of F-liposome (A) before and after CLP conjugation and (B) before and after lyophilization using dynamic light scattering.

disturb the assembly of the ECnVs (Figure. 5.13). Additionally, I prepared liposomes and CLP-liposomes to enable evaluation of the effect of the CLP on hybridization/matrix retention, since such studies to directly probe the effect of the CLP could not be conducted with ECnVs as ECnVs cannot be prepared in the absence of CLP. The diameters of the lyophilized liposomes and CLP-liposomes were assessed after resuspension in PBS using dynamic light scattering, which confirmed that the liposomes and CLP-liposomes were not aggregated before incorporation in the matrices (Figure. 5.14). The fluorescence retained after washing the ECnV in co-gel samples (36.0 ± 4.0 %) was significantly greater than the fluorescence observed for collagen hydrogels (14.2 ± 3.3 %) (Figure. 5.15), which agrees with the observation that CLP-liposomes incorporated in both collagen and co-gel matrices showed slightly greater retention of CLP-liposome in co-gels than collagen gels (Figure. 5.16). Since I have demonstrated that the shear storage moduli of the two hydrogel matrices were similar ($G'_{Collagen+ELP-CLP}$ = 40.5 ± 5.8 Pa and $G'_{Co-gel+ELP-CLP}$ = 47.3 ± 2.4 Pa as determined via

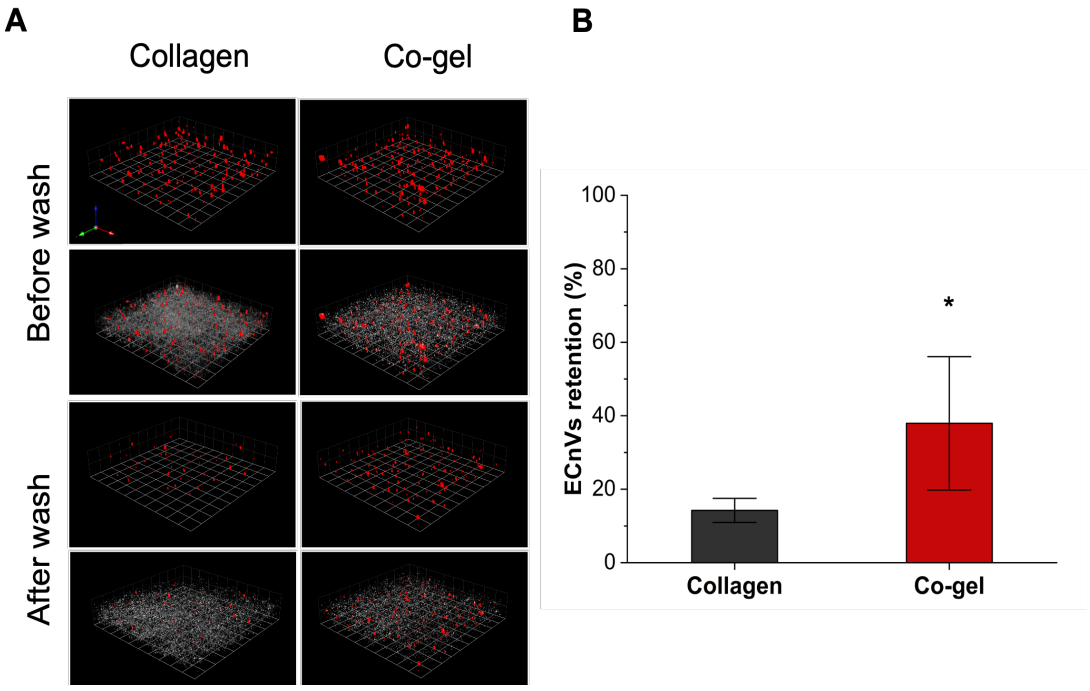

Figure 5.15. ECnVs retention on matrices at 37 ºC. (A) Representative 3D plotted confocal images of ECnVs-Cy3 (Red) and collagen (Grey) in Collagen matrix or Co-gel matrix before and after wash. 1 unit is 25 µm. (B) Image quantification for fluorescent intensity of ECnVs after wash normalized to the intensity before wash. Each data represents mean ± standard deviation for n=6. An unpaired student's t-test with equal variance was used to detect statistical significance. *$p<0.0001$ for co-gel relative to collagen.

oscillatory rheology (Figure. 5.17), the difference in retention of ECnVs in collagen vs co-gel most likely resulted from differences in the interactions of the ECnVs with the collagen in these substrates. Additionally, the lower retention of liposomes within and on the of surfaces of the matrices, as compared with CLP-liposomes (Figure. 5.16 and 5.18), confirmed that the retention of both ECnVs and CLP-liposomes likely occurred via triple helix formation with collagen of the matrices. Thus, these results suggest that

triple helix formation of the CLPs with collagen is more facile in the co-gel than the collagen.

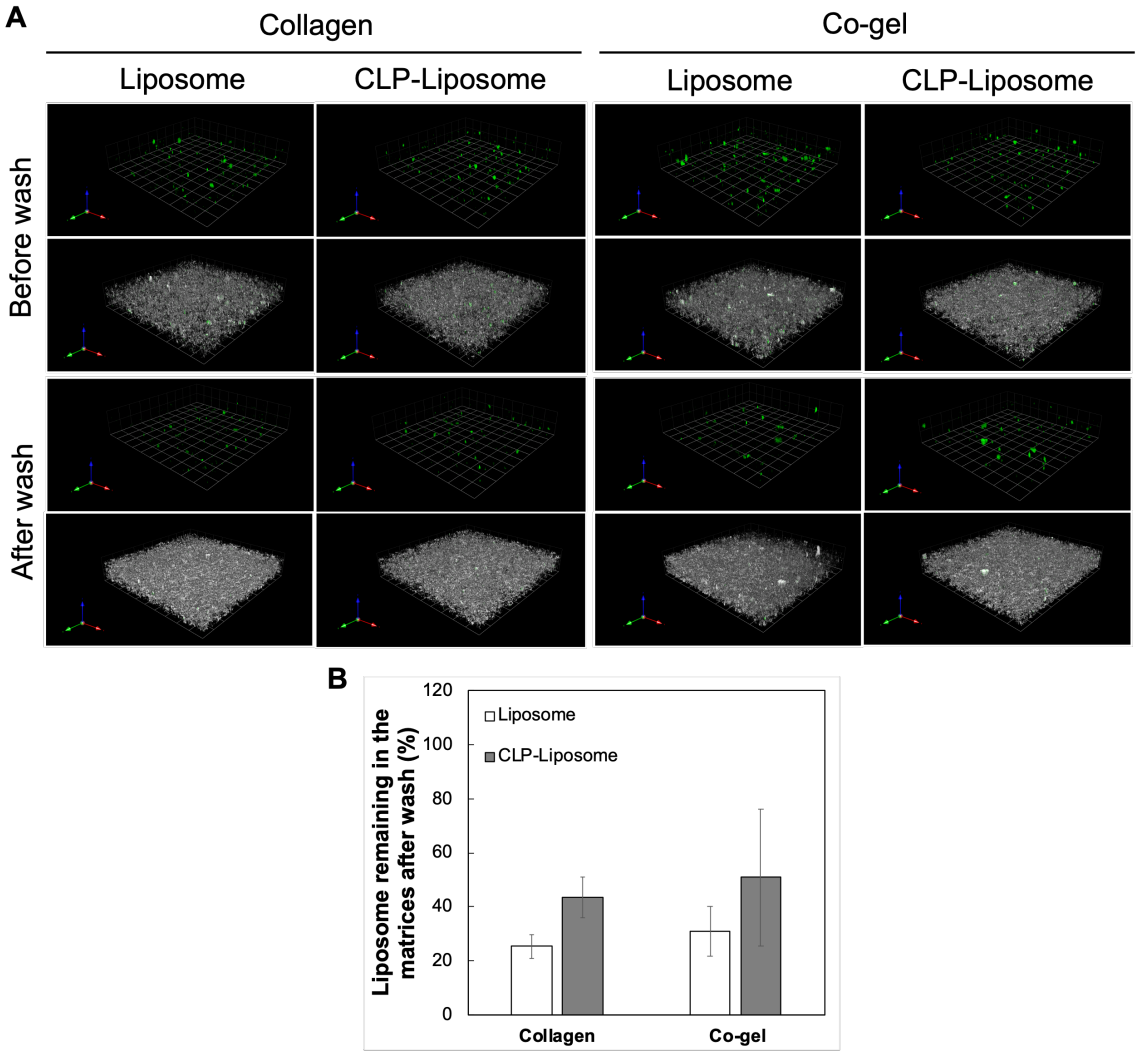

Figure 5.16. Fluorescently labeled liposome with/without CLP modification retention in collagen/co-gel matrices. (A) Representative 3D plot of confocal images of F-liposome and CLP conjugated F-liposome (green) and collagen (grey). (B) Liposome retention quantification. Each data represents mean ± standard deviation for n=4.

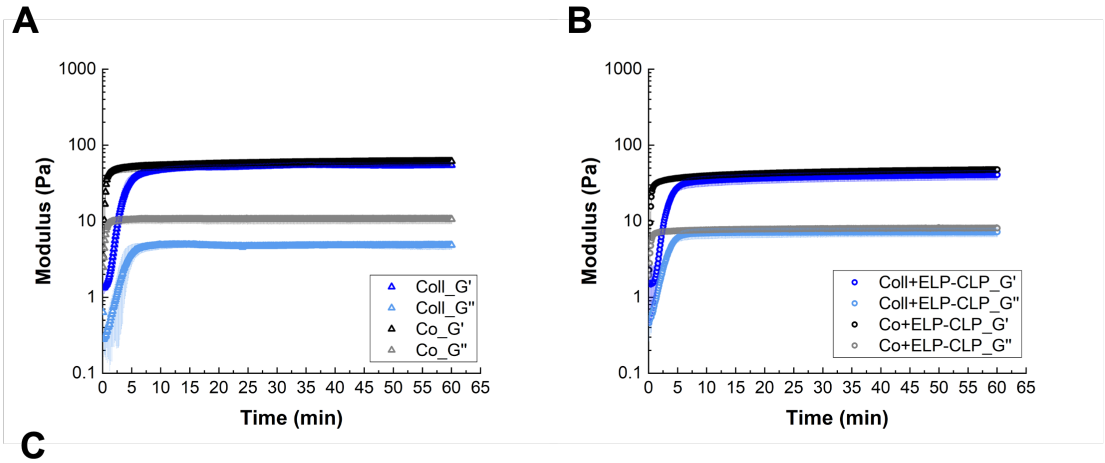

C

	Collagen	Co-gel	Coll + ECnVs	Co + ECnVs
Storage modulus (G')	53.9 ± 3.0	61.0 ± 7.7	40.5 ± 5.8	47.3 ± 2.4
Loss modulus (G")	6.1 ± 5.3	10.6 ± 1.4	7.19 ± 1.0	8.12 ± 0.4

Figure 5.17. Mechanical properties of Collagen, Co-gel, ECnVs (1 mg/mL) loaded collagen and ECnVs (1 mg/mL) loaded co-gel. (A) Time sweep of rheological measurement of collagen and co-gel, (B) ECnVs loaded collagen and ECnVs loaded co-gel. Each data represents mean ± standard deviation for n=3.

Moreover, to understand how ECnV release from the matrices influenced vancomycin release from the ECnVs-containing matrices, the cumulative release profiles of Cy3-labeled ECnVs from collagen vs. co-gel were determined using fluorescent measurements (Figure. 5.19). Mathematical fitting of the cumulative release over 96 h with the Korsmeyer-Peppas model suggested that the overall rate of release of ECnVs from the co-gel (K_{kp} = 29000) was 1.6-fold slower than the rate of release from collagen (K_{kp} = 46500), indicating that ECnV sequestration in the co-gel was significantly greater than on collagen gels, likely due to a different extent of CLP hybridization based on the different physical features of collagen fibers in co-gels vs. collagen gels (52, 53).

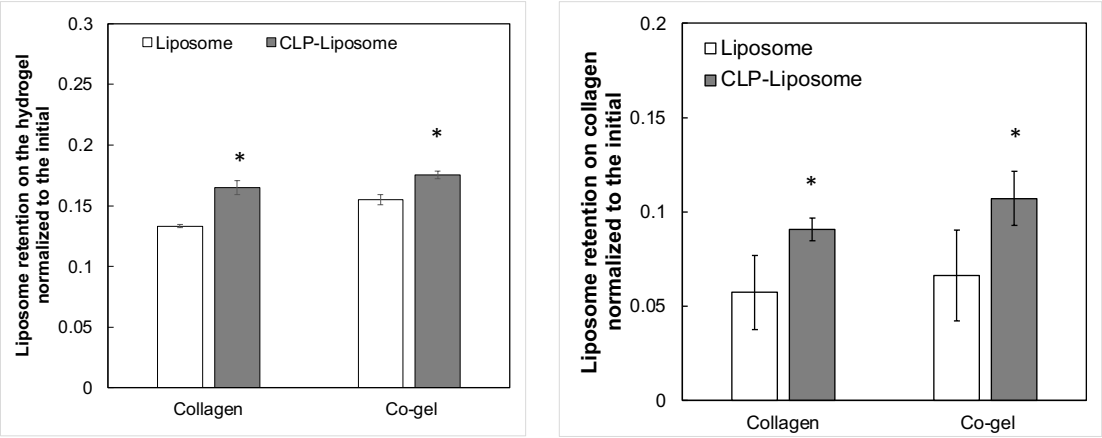

Figure 5.18. Fluorescently labeled liposome with/without CLP modification retention on collagen/co-gel matrices. A) CLP was functionalized after fluorescently labeled liposome was formulated B) The liposome was formulated using pre-CLP functionalized lipid (DSPE-PEG-CLP). Each data represents mean ± standard deviation for N=3. One way-ANOVA was used to detect statistical significance. *p<0.05 for CLP-liposome relative to liposome.

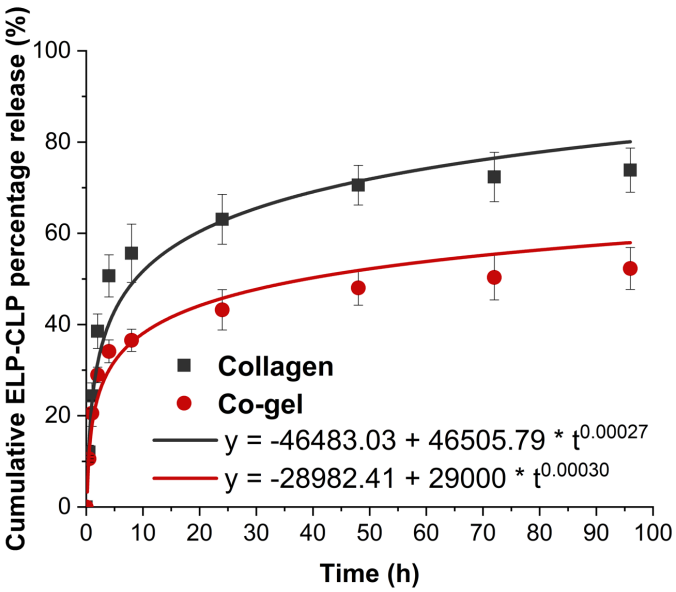

Figure 5.19. ECnVs release from matrices at 37 °C for 96 h. Release profile were fitted Kormeyer-Peppas model. Each data represents mean ± standard deviation for n=3.

5.3.4 Vancomycin release from ELP-CLP tethered in matrices

The cumulative release of vancomycin from vancomycin-loaded ECnVs tethered in the matrices was determined. Mathematical fitting of the cumulative release with either the Korsmeyer-Peppas (fitting failed) or 1st order release models (Figure. 5.20) alone yielded poor fits to the data, suggesting that there could be multiple behaviors mediating vancomycin release. The initial burst release of vancomycin from ECnVs in the matrices was fit with high fidelity to the 1st order release model up to 8 h (Figure. 5.21); subsequently, data were fit to the Korsmeyer-Peppas model from 8 h to day 4, with the expectation that release in this window would be dominated by the vancomycin release from the ECnVs tethered in the matrices. The cumulative release of

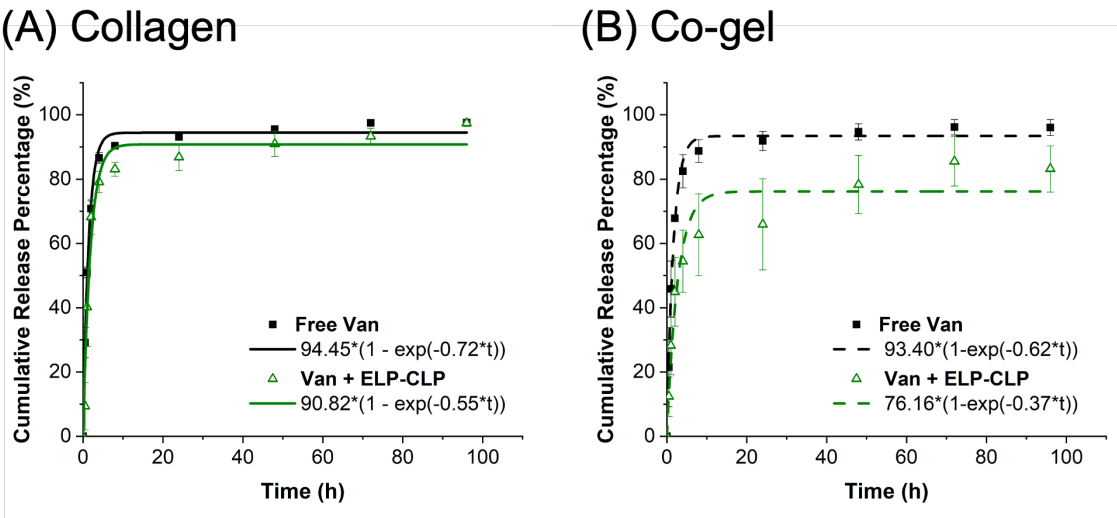

Figure 5.20. Vancomycin release from ECnVs tethered in (A) collagen or (B) co-gel matrix. Release profiles of free vancomycin (black line (solid and dotted)) and vancomycin in ECnVs (green line (solid line and dotted) were fitted by first-order kinetics.

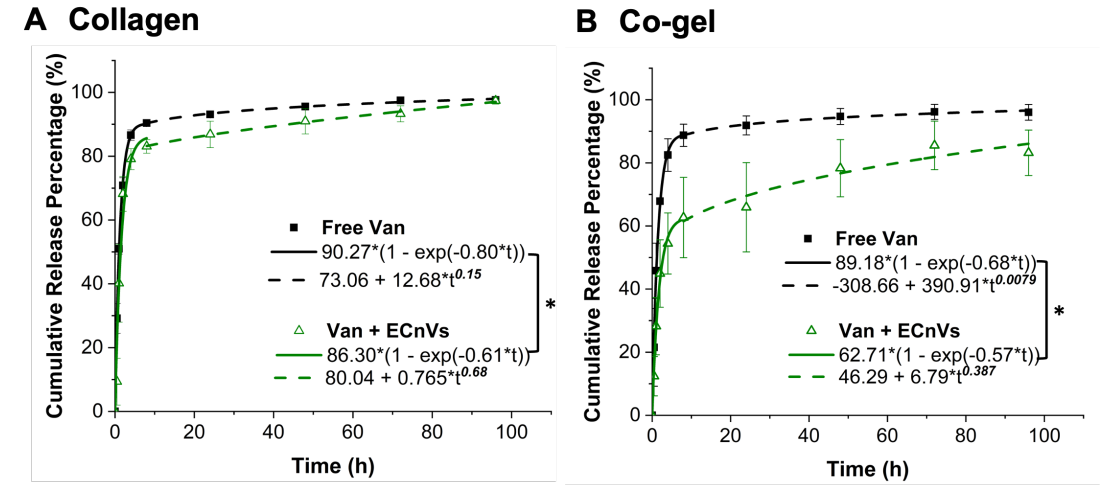

C

	Collagen		Co-gel	
	Free-Van	Van + ECnVs	Free-Van	Van + ECnVs
K_i	0.80	0.61	0.68	0.57
R_i^2	0.999	0.983	0.995	0.993
n	0.15	0.68	0.01	0.39
	Quasi Fickian	Non-Fickian	Quasi Fickian	Quasi Fickian
R_{kb}^2	0.986	0.994	0.981	0.908

Figure 5.21. Vancomycin release from ECnVs tethered in (A) collagen or (B) co-gel matrix. (C) Release profile were fitted by first-order kinetics from 0 to 8 h (solid line) and Kormeyer-Peppas model from 8 h to 96 h (dotted line). K_i = first order constant, K_{kp} = Korsmeyer release rate constant, and n = diffusional exponent. Each data represents mean ± standard deviation for n=4. The statistical difference of K_i states *$p<0.05$.

free vancomycin from the matrices was close to 70-80% at the initial 8 h time point, similar to observations of vancomycin release profiles from collagen-based scaffolds in the literature (32, 54, 55). In contrast, the vancomycin release from ECnVs, over the initial 8 hours, from both collagen (K_i = 0.61) and co-gel (K_i = 0.57) matrices was significantly slower than free vancomycin release from the matrices (collagen (K_i = 0.80) and co-gel (K_i = 0.68)). These data suggest that the early release of the vancomycin from the loaded ECnVs likely resulted from non-tethered vancomycin-loaded carriers

on matrices rather than from the presence of free vancomycin. In addition, after the initial burst release of vancomycin from the released ECnVs from the matrices, the cumulative release of vancomycin from the vancomycin-loaded ECnVs in the co-gel (63%) at the 8 h time point was significantly less than that observed from the collagen gel (83%). However, I have observed that the release of vancomycin at 8 h time point from non-tethered liposomes loaded in the collagen gel (67%) and co-gel (69%) was nearly identical (Figure. 5.22). Thus, the results indicate slower vancomycin release from the vancomycin-loaded ECnVs in the co-gel matrices relative to that from collagen gels was likely due to a greater retention and slower release of ECnVs in the co-gel (Figure. 5.15 and 5.19).

After the initial 8 h release, the data from 8 h to day 4 were fit to the Korsmeyer-Peppas model with the expectation that release in this time period was mainly from the vancomycin release from the ECnVs tethered in the matrices. The diffusional exponent (n) of the Korsmeyer-Peppas model fitting revealed differences in the release mechanism, with $n < 0.45$ indicating diffusion-controlled release, $0.45 < n < 0.8$ indicating both diffusion- and dissolution-controlled release, and $0.8 < n$ indicating dissolution-controlled release. Vancomycin release from ECnVs in collagen gels ($n = 0.679$) was classified as both diffusion- and dissolution-controlled, and vancomycin release from co-gels ($n = 0.387$) was classified as diffusion-controlled. Altogether, the data indicate that ECnVs enable the delay of vancomycin release, while the different retention of ECnVs on different collagen-containing matrices can also be leveraged to fine tune release profiles.

A Collagen

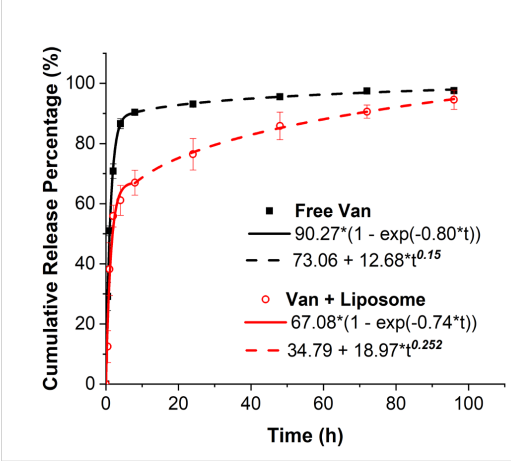

B Co-gel

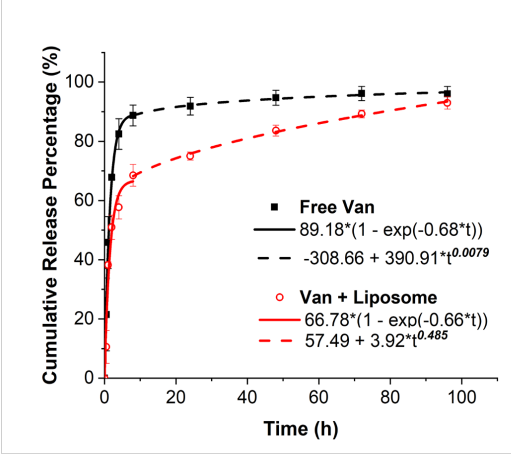

C

	Collagen		Co-gel	
	Free-Van	Van + Lipo.	Free-Van	Van +Lipo.
K_i	0.797	0.740	0.680	0.661
R_i^2	0.999	0.973	0.995	0.973
n	0.148	0.252	0.00788	0.486
	Quasi Fickian	Quasi Fickian	Quasi Fickian	Non-Fickian
R_{kb}^2	0.986	0.998	0.981	0.997

Figure 5.22. Vancomycin release from liposome in (A) collagen or (B) co-gel matrix. (C) Release profile were fitted by first-order kinetics from 0 to 8 h (solid line) and Kormeyer-Peppas model from 8 h to 96 h (dotted line). K_i = first order constant, K_{kp} = Korsmeyer release rate constant, and n = diffusional exponent.

5.3.5 Antibacterial effect of vancomycin-loaded ECnVs tethered matrices against MRSA

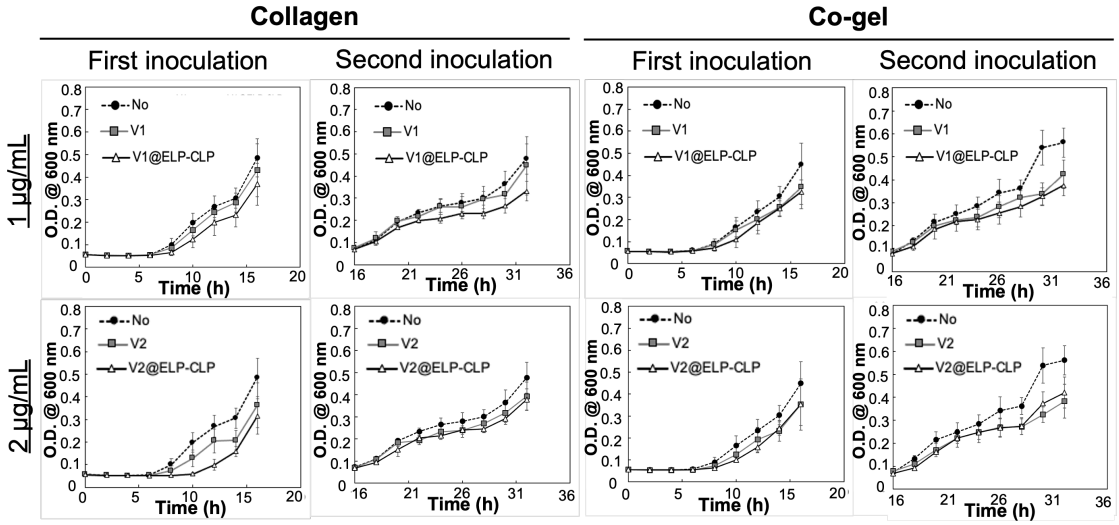

Figure 5.23. Anti-bacterial activity of vancomycin loaded ECnVs tethered collagen/co-gel matrices against MRSA . Optical density measurement of MRSA cultures grown in blank collagen/co-gel (black circle), vancomycin (1 or 2 µg/mL) loaded collagen/co-gel (grey square), and vancomycin (1 or 2 µg/mL) loaded ECnVs tethered collagen/c-gel (white triangle) with a total of two bacterial inoculations (16 h per inoculation). Each data represents mean ± standard deviation for n = 9.

To evaluate possible improvements in the antibacterial activity of vancomycin when delivered from ECnVs tethered to collagen or co-gel matrices, the growth of luminescent MRSA cultured on vancomycin-loaded ECnV-tethered matrices was monitored for 16 hours post-inoculation. To simulate a recurrent bacterial infection (1, 56), an additional inoculation of MRSA was made at the 16 h timepoint, and bacterial growth monitored after an additional 16 h of culture. Vancomycin-loaded ECnVs were tethered in the collagen or co-gel matrices at a final vancomycin concentration of 2 µg/mL, which is the minimum inhibitory concentration (MIC) for MRSA (5 × 105 cfu/mL) (32). The vancomycin-loaded ECnVs matrices inhibited the growth of MRSA for 14 h (collagen) and 10 h (co-gel) after the first inoculation, while free vancomycin

in either matrix failed to inhibit MRSA (Figure. 5.23 & 5.24). Increasing the concentration of tethered, vancomycin-loaded ECnVs (in collagen and in the co-gel) to 3 µg/mL extended the antibacterial effects to inhibit the growth of MRSA (Figure. 5.25), although free vancomycin at this concentration also delayed (but did not halt) MRSA growth. The vancomycin-loaded ECnVs in the collagen matrix completely inhibited the growth of MRSA for 16 h with the first inoculation and an additional 8 h after the second inoculation (for a total time of 24 h). Vancomycin-loaded ECnVs in the co-gel matrix also completely inhibited the growth of MRSA for 16 h with the first inoculation and delayed the growth of MRSA additional 2 h after the second inoculation (for a total 18

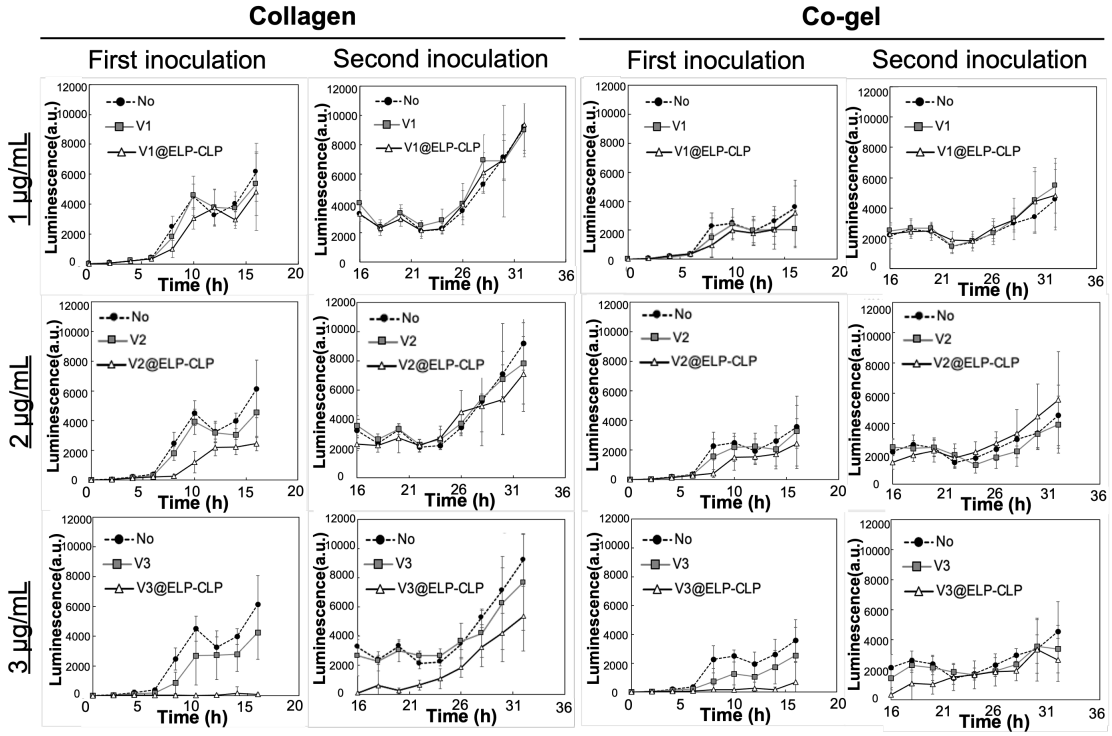

Figure 5.24. Anti-bacterial activity of vancomycin loaded ECnVs tethered collagen/co-gel matrices against MRSA . Luminescence measurement of MRSA cultures grown in blank collagen/co-gel (black circle), vancomycin (1, 2, 3 µg/mL) loaded collagen/co-gel (grey square), and vancomycin (1, 2, 3 µg/mL) loaded ECnVs tethered collagen/co-gel (white triangle) with a total of two bacterial inoculations (16 h per inoculation). Each data represents mean ± standard deviation for n = 9.

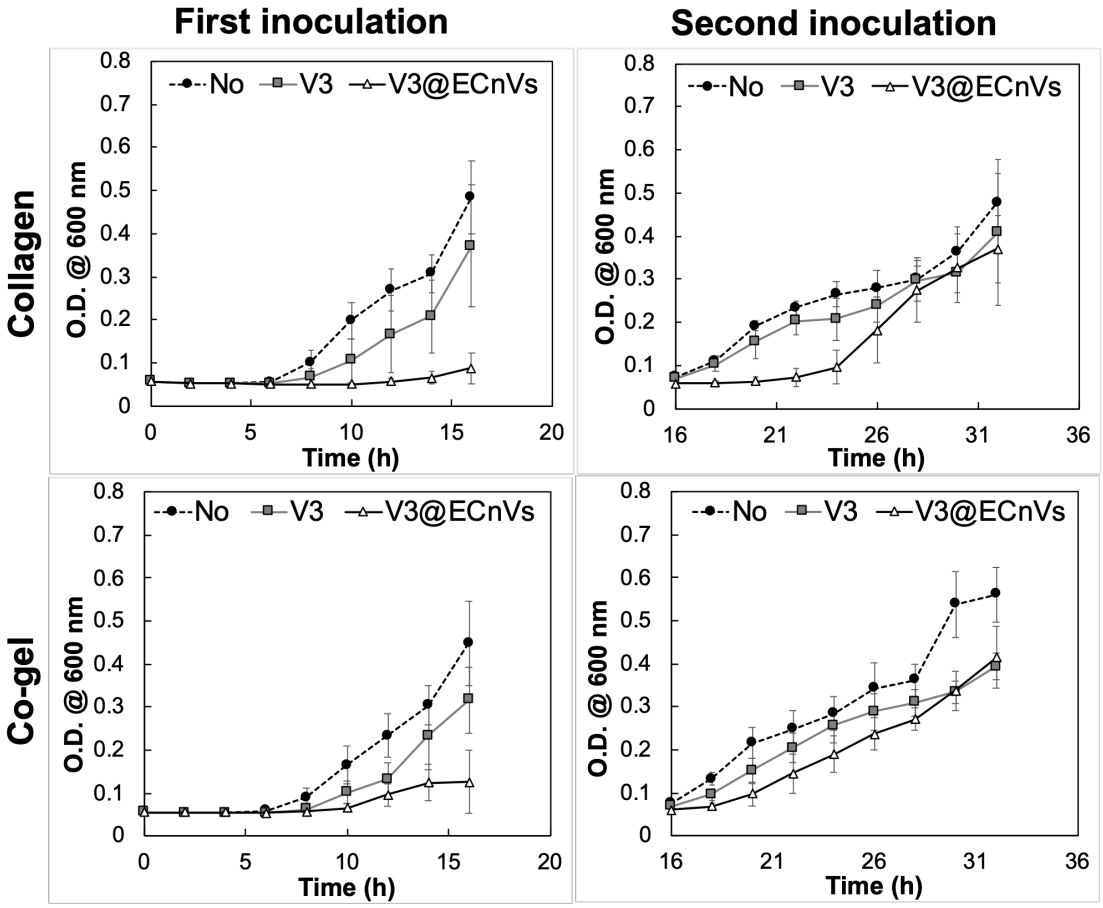

Figure 5.25. Anti-bacterial activity of vancomycin loaded ECnVs tethered collagen/co-gel matrices against MRSA . Optical density measurement of MRSA cultures grown in blank collagen/co-gel (black circle), vancomycin (3 µg/mL) loaded collagen/co-gel (grey square), and vancomycin (3 µg/mL) loaded ECnVs tethered collagen/c-gel (white triangle) with a total of two bacterial inoculations (16 h per inoculation). Each data represents mean ± standard deviation for n = 3.

h). This study indicated that the ECnVs, both released and tethered in matrices, maintained a sufficiently high local concentration of vancomycin to inhibit the growth of MRSA, as compared to release of free vancomycin from matrices. In addition, the different release kinetics of vancomycin from ECnVs in collagen vs. co-gel controlled the duration of the antibacterial effect.

5.4 Discussion

The eradication of MRSA populations from the wounds using commercially available antibiotics is a persistent challenge, leading to incomplete wound healing and potential risks of further antibiotic resistance. As a potential approach to improve antibiotic efficacy, I developed a peptide-based nanocarrier, ECnVs, taking advantage of the stability and specific interactions of these nanoparticles with native collagen as a means to control the delivery of vancomycin for inhibition of MRSA growth at the first time.

The peptide-based nanocarrier enabled improved encapsulation efficiency and controlled delivery of vancomycin in solution when compared with liposome nanocarriers, suggesting that physical chemistry between drugs and nanocarriers is a key factor in determining encapsulation efficiency and release kinetics from the carriers. ECnVs encapsulated a greater amount of vancomycin (EE = 48.2% and LC = 144.6%) and facilitated both dissolution and diffusion mediated sustained delivery of vancomycin; in contrast, the liposome nanocarrier encapsulated significantly less cargo (EE = 15.2% and LC = 45.6%) and delivered vancomycin with more rapid first-order kinetics with diffusion mechanism. Generally speaking, encapsulation of drugs in nanocarriers protects the drug against degradation and enhances sustained drug release, resulting in improved pharmacokinetics (57, 58). However, the high water solubility of hydrophilic drugs makes it difficult to encapsulate/sequester hydrophilic drugs in liposomes, hydrogels, nanoparticles, and/or fiber-based carriers, thus resulting in undesired and rapid burst release (59-62). In addition, the steric hindrance from the inclusion of cholesterol in liposomal carriers (which is necessary to improve liposome stability for use in vivo), can result in low encapsulation efficiency of hydrophilic cargo. These general difficulties are reproduced in our control studies, in which low E.E. of vancomycin in the liposome is observed (EE = 15.2% and LC = 45.6%) along with rapid first-order diffusive release of the vancomycin cargo (n = 0.1) (Figure. 5.12) (19, 37, 38, 63).

The use of our peptide-based ECnV carriers, in contrast, enabled efficient encapsulation of vancomycin, by exploiting the thermal responsiveness of these carriers as a mechanism for loading. Vancomycin can be solubilized at elevated concentrations along with the monomeric ELP-CLP above its Tm; thermally-induced assembly of ELP-CLP into vesicles upon cooling leads to high efficiency of drug loading, which is one of advantages of peptide self-assembled nanocarriers (64, 65). For example, elastin-based protein diblock copolymer nanoparticles achieved approximately 50% of encapsulation efficiency for the anti-proliferative hydrophobic drug, rapamycin, for cancer treatment (66). In addition, the nanoparticles formed by the conjugate of low molecular weight polylactide and the self-assembled lipid-like V6K2 peptides enabled the efficient encapsulation of both hydrophilic doxorubicin (44 ± 9%) and hydrophobic paclitaxel (>90%) in the nanoparticles (67). The additional barrier from the attractive interactions between V6K2 peptide and drugs delayed the release of doxorubicin and paclitaxel from V6K2 peptide assembled polylactide nanoparticles as compared with the release from ethylene glycol polylactide nanoparticles. Similarly, the hydrophobic coacervation of ELP block in the ECnVs could behave as an additional barrier for vancomycin release. Due to the hydrophobic interaction with the addition of pi-pi stacking, hydrogen bonding, and charge-charge interaction from the side chains of the ELP sequence, the ELP block has been shown to collapse tightly to reduce the pore size within the ELP block, which is able to effectively shed water (68-70). On the other hand, only hydrophobic interactions of alkyl chains and cholesterol form the hydrophobic barriers in liposome bilayers to reduce water penetration (71, 72). Thus, the coacervation of the ELP layer in the vesicle bilayer provides a more stable barrier to diffusion relative to the liposome bilayer, supporting sustained vancomycin release with both diffusion and dissolution mechanisms as compared to with mainly diffusion mechanisms for vancomycin release from the liposome. Such sustained release behavior of drug from ECnVs could expand the performance of therapeutics by minimizing adverse off-target effects and the toxicity with burst release of high concentrations of cargo (73).

Next, I observed that different levels of ECnV retention on the different matrices, which might influence the release kinetics of vancomycin from ECnVs-loaded matrices. ECnVs tended to be retained to a greater extent on the co-gel compared to the collagen matrix (Figure. 5.15 and 5.19), suggesting that the collagen in the co-gel may be more accessible for triple helix formation with the CLPs that are on the exterior of the ECnVs. Both collagen and fibrin contribute to hydrogel formation via fibrillogenesis driven by physico-chemical interactions between peptide chains that can be triggered with stimuli such as pH, temperature, and ionic strength (74). The Barocas group reported a related collagen-fibrin co-gel with high concentrations of collagen (68-83%) that comprised two interpenetrating but non-interacting networks (e.g., 'parallel networks'); the reported conditions in those studies are similar to those of our co-gels in this report (76% collagen in our co-gel) (53). The mechanical properties of the parallel co-gel networks were driven by the competition between the extensibility of fibrin and stiffness of collagen. For example, although the tangent modulus of fibrin gel alone was much smaller than that of the co-gel, the tangent moduli of co-gel and collagen with the same collagen concentration were similar, consistent with our observation of similar shear storage moduli for the co-gel and collagen matrices (Figure. 5.17) (52). SEM and confocal imaging analysis revealed that the morphological structure of collagen fibrin networks were altered to have the average collagen fiber diameters smaller in the co-gel than pure collagen gels, and this physical feature alone would be expected to provide more sites for interaction, on a surface area-per-volume basis, with the collagen in the co-gel formulations (Figure 5.16 and 5.18) (32, 36), consistent with our observations of significantly greater ECnVs retention on the co-gel than collagen gel (Figure. 5.15 and 5.19).

In addition, ECnVs retention on matrices would be necessary to support controlled release of vancomycin from either matrix, and enhanced retention on the co-gel would be expected to reduce vancomycin release from the co-gel versus the collagen matrix (Figure. 5.21). The pore sizes of both collagen and fibrin gels have been reported to be on the micron length scale, which is much larger than the nanometer-scale of

ECnVs (75, 76). Thus, the initial burst release of vancomycin likely results from the rapid release of non-tethered ECnVs from the matrices (Figure. 5.19). Moreover, our previous studies showed that the CLP-modification of liposomes, and their incorporation into co-gel matrices, enhanced the sustained release of vancomycin, as compared to non-CLP liposomes in the same matrices (32). After the initial burst release of vancomycin, the release of vancomycin from ECnVs in collagen and co-gel matrices was sustained, although via different release mechanisms (Figure. 5.21). These different mechanisms might result from differences in vancomycin release from either tethered van-loaded ECnVs in collagen and in co-gel or from the released van-loaded ECnVs from the matrices over the incubation time.

The release kinetics of vancomycin from ECnVs in the matrices regulated the duration of antibacterial effects against MRSA. Vancomycin is one of the most effective options for treatment of MRSA infections, which is one of the major Gram-positive microorganisms found in chronic wounds (77). However, wound infections by MRSA are often recurring, leading to the critical need for the better antibiotic delivery systems to enhance the prolonged duration of its antibacterial effect against MRSA (78, 79). A biphasic drug-release profile has been reported to have significant practical advantages in managing MRSA infections, including implant-associated infections (80, 81), bone infection (82), and wound infection (83). The biphasic drug-release profiles demonstrate an initial 10 h burst release of vancomycin at least above its MIC to completely eradicate bacterial colonies, followed by a sustained release of 0.36% per h for 24 h, a prolonged period to eliminate any remaining bacteria (84, 85). In agreement of this observation, I demonstrated that vancomycin release profile from ECnV-tethered both collagen and co-gel followed the biphasic drug-release profiles; an initial 8 h burst release of vancomycin followed by a sustained release of vancomycin. The released vancomycin-loaded ECnVs from matrices during the initial burst release would result in the localized high concentration of vancomycin, entrapped in the released ECnV, near to the MRSA, leading to more efficient inhibition of the MRSA growth than freely diffused vancomycin from matrices.

I observed that the difference in the duration of MRSA inhibition by vancomycin release from ECnV-tethered collagen vs. co-gel. In fact that the maintenance at the infection site, of antibiotic above its MIC (2 μg/mL for MRSA (5 ✕ 105 cfu/mL)), is a key factor in mediating antibacterial effects. Due to the slower release of ECnVs from co-gel than collagen-gel, the local concentration of vancomycin was not maintained above the MIC (~60% cumulative release at 8 h = 3 μg/mL × 0.6 = ~1.8 μg/mL, which is less than the reported MIC), resulting in the incomplete eradication of MRSA at the initial time and a shorter duration of the inhibition of MRSA growth than for the vancomycin-loaded ECnVs released from the collagen matrix (~81% cumulative release at 8 h = 3 μg/mL × 0.83 = ~2.43 μg/mL, which is more than the reported MIC) (Figure. 5.21 and 5.25). In addition, the sustained release of vancomycin both with released ECnVs and from ECnVs tethered matrices (0.0024 μg/mL release per h for collagen and 0.006 μg/mL release per h for co-gel from 8 h to 32 h) further extended the duration of antibacterial effects even after a MRSA re-inoculation.

Moreover, I have demonstrated that antibiotic delivery using ECnVs performed the pro-longed antibacterial effects as effective as the liposomal delivery system. As compared to freely applied antibiotic, antibiotic delivery using liposome has been reported their effectiveness to inhibit MRSA growth [28-31] and their effectiveness were further enhanced by CMP-collagen tether strategies in the system. For example, vancomycin-loaded CMP-modified liposome tethered co-gel in the previous study facilitated the inhibition of MRSA growth at least 36 h even with the third inoculation, while vancomycin loaded liposome incorporated in co-gel inhibited the MRSA growth at least 26 h [32]. Similarly, I have observed the prolonged duration of antibacterial activities at least 18 h by vancomycin-loaded ECnVs tethered co-gel against MRSA, as compared to the antibacterial duration at least 8 h with free vancomycin loaded co-gel. However, the duration of antibacterial activities by vancomycin-loaded ECnVs tethered co-gel (at least 18h) were shorter than vancomycin-loaded CMP-modified liposome tethered co-gel (at least 36 h) [32]. This can be the fact that the different levels of retention of CMP-liposome (95% after 24 h) vs. ECnV (60% after 24 h) on co-gel

because of different CMP sequences in CMP-liposome vs. ECnV. Thus, as similar with liposomal delivery system, ECnVs improved the antibacterial activity, and its duration can be potentially tuned by the level of CLP-collagen tethers.

Altogether, these results demonstrated that the combination of peptide-based nanocarriers and their interaction with collagen-containing matrices manipulated the delivery of vancomycin for its extended efficacy in inhibiting MRSA growth. Non-cytotoxic ECnVs (Figure. 5.26) improved not only entrapment efficiency of vancomycin but also resulted in release kinetics using a zero-order mechanism. The ability of ECnVs to be retained on collagen-containing matrices facilitates sustained release of vancomycin and its antibacterial effects against MRSA for a prolonged period. Thus, the delivery of vancomycin with an optimal concentration using ECnVs, collagen-based matrices has a great potential for the effective treatment of wound infections.

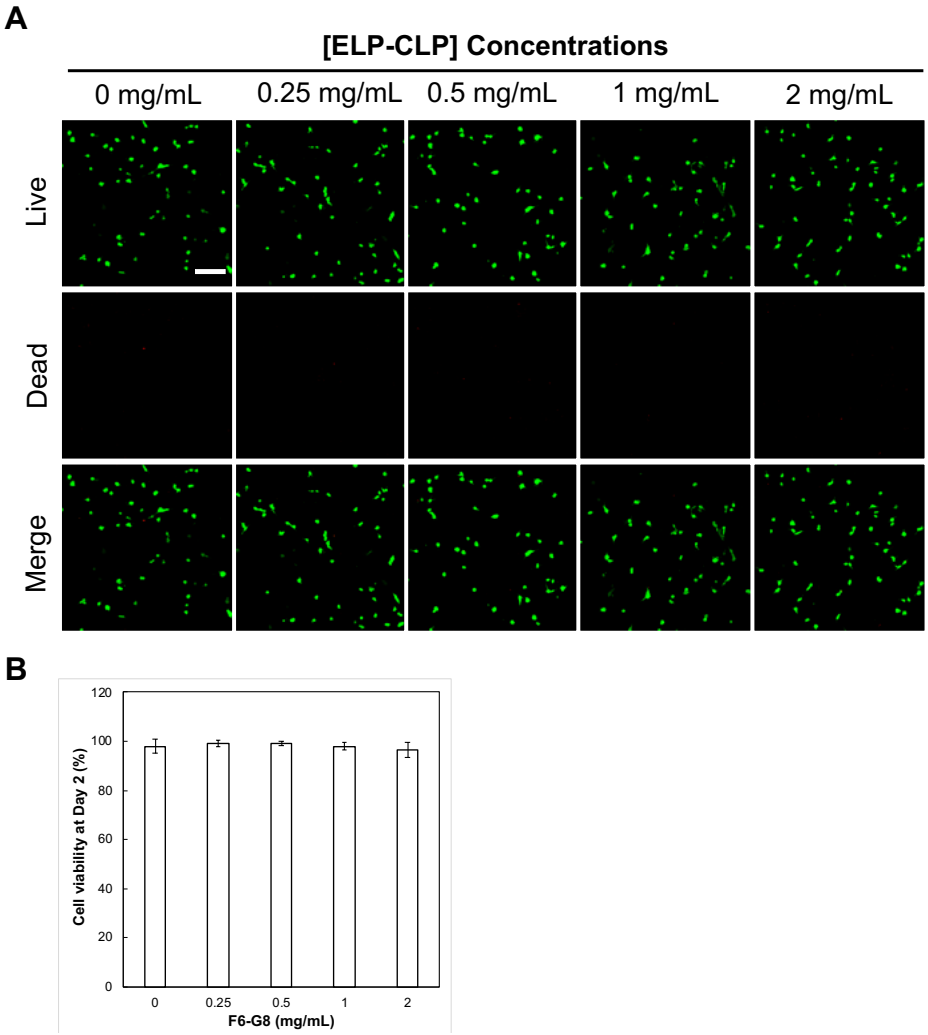

Figure 5.26. The viability of NIH 3T3 cells in [F_6-G_8] tethered collagen gel (4 mg/mL) after 2 days of culture. (A) Representative confocal microscope images of Calcein AM stained live cells (Green) and Ethidium homodimer-stained dead cells (Red). Scale bar is 150 μm. (B) Image quantification to determine viability of fibroblast. Each data represents mean ± standard deviation for n=8.

5.5 Conclusion

To overcome the prolonged challenge in treatment of wounds infections by MRSA, I developed a novel antibiotic delivery system using the combination of ELP-CLP self-assembled nanovesicles and collagen-containing matrices for the topical

delivery of antibiotic with controlled release. This ECM-based material system exploits synergies in peptide nanocarriers and their interaction with the scaffold to improve the efficacy of the commercially available antibiotic, vancomycin, and the extended duration of its antibacterial effects against MRSA after repeated inoculation. Our system may offer benefits to manage chronic wound infections while stimulating wound-healing potency.

REFERENCES

1. Leaper D, Assadian O, Edmiston CE. Approach to chronic wound infections. Br J Dermatol. 2015;173(2):351-8. Epub 2015/03/17. doi: 10.1111/bjd.13677. PubMed PMID: 25772951.

2. Jarbrink K, Ni G, Sonnergren H, Schmidtchen A, Pang C, Bajpai R, Car J. Prevalence and incidence of chronic wounds and related complications: a protocol for a systematic review. Syst Rev. 2016;5(1):152. Epub 2016/09/10. doi: 10.1186/s13643-016-0329-y. PubMed PMID: 27609108; PMCID: PMC5017042.

3. Tan TW, Shih CD, Concha-Moore KC, Diri MM, Hu B, Marrero D, Zhou W, Armstrong DG. Disparities in outcomes of patients admitted with diabetic foot infections. PLoS One. 2019;14(2):e0211481. Epub 2019/02/05. doi: 10.1371/journal.pone.0211481. PubMed PMID: 30716108; PMCID: PMC6361439.

4. Leaper D, Assadian O, Edmiston CE. Approach to chronic wound infections. British Journal of Dermatology. 2015;173(2):351-8 %@ 0007-963.

5. Falcone M, De Angelis B, Pea F, Scalise A, Stefani S, Tasinato R, Zanetti O, Dalla Paola L. Challenges in the management of chronic wound infections. J Glob Antimicrob Resist. 2021;26:140-7. Epub 2021/06/19. doi: 10.1016/j.jgar.2021.05.010. PubMed PMID: 34144200.

6. Robson MC. Wound infection. A failure of wound healing caused by an imbalance of bacteria. Surg Clin North Am. 1997;77(3):637-50. Epub 1997/06/01. doi: 10.1016/s0039-6109(05)70572-7. PubMed PMID: 9194884.

7. Eming SA, Martin P, Tomic-Canic M. Wound repair and regeneration: mechanisms, signaling, and translation. Sci Transl Med. 2014;6(265):265sr6. Epub 2014/12/05. doi: 10.1126/scitranslmed.3009337. PubMed PMID: 25473038; PMCID: PMC4973620.

8. Pastar I, Nusbaum AG, Gil J, Patel SB, Chen J, Valdes J, Stojadinovic O, Plano LR, Tomic-Canic M, Davis SC. Interactions of methicillin resistant Staphylococcus aureus USA300 and Pseudomonas aeruginosa in polymicrobial wound infection. PLoS One. 2013;8(2):e56846. Epub 2013/03/02. doi: 10.1371/journal.pone.0056846. PubMed PMID: 23451098; PMCID: PMC3579943.

9. Stotts NA. Wound infection: diagnosis and management. Acute and Chronic Wounds-E-Book. 2015:283 %@ 0323316220.

10. Lipsky BA, Hoey C. Topical antimicrobial therapy for treating chronic wounds. Clin Infect Dis. 2009;49(10):1541-9. Epub 2009/10/22. doi: 10.1086/644732. PubMed PMID: 19842981.

11. White RJ, Cooper R, Kingsley A. Wound colonization and infection: the role of topical antimicrobials. Br J Nurs. 2001;10(9):563-78. Epub 2002/06/18. doi: 10.12968/bjon.2001.10.9.9387. PubMed PMID: 12066030.

12. Negut I, Grumezescu V, Grumezescu AM. Treatment Strategies for Infected Wounds. Molecules. 2018;23(9). Epub 2018/09/21. doi: 10.3390/molecules23092392. PubMed PMID: 30231567; PMCID: PMC6225154.

13. Tavakoli S, Klar AS. Advanced Hydrogels as Wound Dressings. Biomolecules. 2020;10(8). Epub 2020/08/17. doi: 10.3390/biom10081169. PubMed PMID: 32796593; PMCID: PMC7464761.

14. Liang Y, He J, Guo B. Functional Hydrogels as Wound Dressing to Enhance Wound Healing. ACS Nano. 2021. Epub 2021/08/11. doi: 10.1021/acsnano.1c04206. PubMed PMID: 34374515.

15. Punjataewakupt A, Napavichayanun S, Aramwit P. The downside of antimicrobial agents for wound healing. Eur J Clin Microbiol Infect Dis. 2019;38(1):39-54. Epub 2018/10/07. doi: 10.1007/s10096-018-3393-5. PubMed PMID: 30291466.

16. Lovering AM, Reeves DS. Antibiotic and Chemotherapy (Ninth Edition). Roger G. Finch DG, S. Ragnar Norrby, Richard J. Whitley,, editor: W.B. Saunders; 2011. Pages 145-69 p.

17. Pray L. Antibiotic resistance, mutation rates and MRSA. Nature Education. 2008;1(1):30.

18. Kim HG, E. L. M.; Jones, M. N.;. The adsorption of cationic liposomes to Staphylococcus aureus biofilms. Colloids and Surfaces A: Physicochemical and Engineering Aspects. 1999;149(1-3):561-70. doi: 10.1016/S0927-7757(98)00765-1.

19. Drulis-Kawa Z, Dorotkiewicz-Jach A. Liposomes as delivery systems for antibiotics. Int J Pharm. 2010;387(1-2):187-98. Epub 2009/12/09. doi: 10.1016/j.ijpharm.2009.11.033. PubMed PMID: 19969054.

20. Gonzalez Gomez A, Hosseinidoust Z. Liposomes for Antibiotic Encapsulation and Delivery. ACS Infect Dis. 2020;6(5):896-908. Epub 2020/03/27. doi: 10.1021/acsinfecdis.9b00357. PubMed PMID: 32208673.

21. Ferreira M, Pinto SN, Aires-da-Silva F, Bettencourt A, Aguiar SI, Gaspar MM. Liposomes as a Nanoplatform to Improve the Delivery of Antibiotics into Staphylococcus aureus Biofilms. Pharmaceutics. 2021;13(3). Epub 2021/04/04. doi: 10.3390/pharmaceutics13030321. PubMed PMID: 33801281; PMCID: PMC7999762.

22. Lankalapalli S, Tenneti V, Nimmali SK. Design and development of vancomycin liposomes. Indian Journal of Pharm Education Research. 2015;49:208-15.

23. Wang Z, Ma Y, Khalil H, Wang R, Lu T, Zhao W, Zhang Y, Chen J, Chen T. Fusion between fluid liposomes and intact bacteria: study of driving parameters and in vitro bactericidal efficacy. Int J Nanomedicine. 2016;11:4025-36. Epub 2016/08/31. doi: 10.2147/IJN.S55807. PubMed PMID: 27574430; PMCID: PMC4993285.

24. Jones MN, Song YH, Kaszuba M, Reboiras MD. The interaction of phospholipid liposomes with bacteria and their use in the delivery of bactericides. J Drug Target. 1997;5(1):25-34. Epub 1997/01/01. doi: 10.3109/10611869708995855. PubMed PMID: 9524311.

25. Scriboni AB, Couto VM, Ribeiro LNM, Freires IA, Groppo FC, de Paula E, Franz-Montan M, Cogo-Muller K. Fusogenic Liposomes Increase the Antimicrobial Activity of Vancomycin Against Staphylococcus aureus Biofilm. Front Pharmacol. 2019;10:1401. Epub 2019/12/19. doi: 10.3389/fphar.2019.01401. PubMed PMID: 31849660; PMCID: PMC6895244.

26. Mat Rani NNI, Mustafa Hussein Z, Mustapa F, Azhari H, Sekar M, Chen XY, Mohd Amin MCI. Exploring the possible targeting strategies of liposomes against methicillin-resistant Staphylococcus aureus (MRSA). Eur J Pharm Biopharm. 2021;165:84-105. Epub 2021/05/12. doi: 10.1016/j.ejpb.2021.04.021. PubMed PMID: 33974973.

27. Pumerantz AS. PEGylated liposomal vancomycin: a glimmer of hope for improving treatment outcomes in MRSA pneumonia. Recent Pat Antiinfect Drug Discov. 2012;7(3):205-12. Epub 2012/06/30. doi: 10.2174/157489112803521904. PubMed PMID: 22742394.

28. Bartomeu Garcia C, Shi D, Webster TJ. Tat-functionalized liposomes for the treatment of meningitis: an in vitro study. Int J Nanomedicine. 2017;12:3009-21. Epub 2017/04/27. doi: 10.2147/IJN.S130125. PubMed PMID: 28442909; PMCID: PMC5396966.

29. Sande L, Sanchez M, Montes J, Wolf AJ, Morgan MA, Omri A, Liu GY. Liposomal encapsulation of vancomycin improves killing of methicillin-resistant Staphylococcus aureus in a murine infection model. J Antimicrob Chemother. 2012;67(9):2191-4. Epub 2012/06/05. doi: 10.1093/jac/dks212. PubMed PMID: 22661572.

30. Huang CM, Chen CH, Pornpattananangkul D, Zhang L, Chan M, Hsieh MF, Zhang L. Eradication of drug resistant Staphylococcus aureus by liposomal oleic acids. Biomaterials. 2011;32(1):214-21. Epub 2010/10/01. doi: 10.1016/j.biomaterials.2010.08.076. PubMed PMID: 20880576; PMCID: PMC2987540.

31. Hajiahmadi F, Alikhani MY, Shariatifar H, Arabestani MR, Ahmadvand D. The bactericidal effect of lysostaphin coupled with liposomal vancomycin as a dual combating system applied directly on methicillin-resistant Staphylococcus aureus infected skin wounds in mice. Int J Nanomedicine. 2019;14:5943-55. Epub 2019/08/27. doi: 10.2147/IJN.S214521. PubMed PMID: 31447553; PMCID: PMC6683660.

32. Thapa RK, Kiick KL, Sullivan MO. Encapsulation of collagen mimetic peptide-tethered vancomycin liposomes in collagen-based scaffolds for infection control in wounds. Acta Biomater. 2020;103:115-28. Epub 2019/12/18. doi: 10.1016/j.actbio.2019.12.014. PubMed PMID: 31843720; PMCID: PMC7044801.

33. Li Y, Yu SM. Targeting and mimicking collagens via triple helical peptide assembly. Curr Opin Chem Biol. 2013;17(6):968-75. Epub 2013/11/12. doi: 10.1016/j.cbpa.2013.10.018. PubMed PMID: 24210894; PMCID: PMC3863647.

34. Luo T, Kiick KL. Collagen-like peptides and peptide-polymer conjugates in the design of assembled materials. Eur Polym J. 2013;49(10):2998-3009. Epub 2013/09/17. doi: 10.1016/j.eurpolymj.2013.05.013. PubMed PMID: 24039275; PMCID: PMC3770267.

35. Urello M, Kiick K, Sullivan M. A CMP-based method for tunable, cell-mediated gene delivery from collagen scaffolds. Journal of Materials Chemistry B. 2014;2(46):8174-85.

36. Thapa RK, Margolis DJ, Kiick KL, Sullivan MO. Enhanced wound healing via collagen-turnover-driven transfer of PDGF-BB gene in a murine wound model. ACS Appl Bio Mater. 2020;3(6):3500-17. Epub 2020/07/14. doi: 10.1021/acsabm.9b01147. PubMed PMID: 32656505; PMCID: PMC7351314.

37. Gubernator J, Drulis-Kawa Z, Dorotkiewicz-Jach A, Doroszkiewicz W, Kozubek A. In vitro antimicrobial activity of liposomes containing ciprofloxacin, meropenem and gentamicin against gram-negative clinical bacterial strains. Letters in Drug Design & Discovery. 2007;4(4):297-304.

38. Kshirsagar NA, Pandya SK, Kirodian GB, Sanath S. Liposomal drug delivery system from laboratory to clinic. J Postgrad Med. 2005;51 Suppl 1:S5-15. Epub 2006/03/08. PubMed PMID: 16519249.

39. Luo T, Kiick KL. Noncovalent Modulation of the Inverse Temperature Transition and Self-Assembly of Elastin-b-Collagen-like Peptide Bioconjugates. J Am

Chem Soc. 2015;137(49):15362-5. Epub 2015/12/04. doi: 10.1021/jacs.5b09941. PubMed PMID: 26633746; PMCID: PMC4930074.

40. Luo T, David MA, Dunshee LC, Scott RA, Urello MA, Price C, Kiick KL. Thermoresponsive Elastin-b-Collagen-Like Peptide Bioconjugate Nanovesicles for Targeted Drug Delivery to Collagen-Containing Matrices. Biomacromolecules. 2017;18(8):2539-51. Epub 2017/07/19. doi: 10.1021/acs.biomac.7b00686. PubMed PMID: 28719196; PMCID: PMC5815509.

41. Qin J, Luo T, Kiick KL. Self-Assembly of Stable Nanoscale Platelets from Designed Elastin-like Peptide-Collagen-like Peptide Bioconjugates. Biomacromolecules. 2019;20(4):1514-21. Epub 2019/02/23. doi: 10.1021/acs.biomac.8b01681. PubMed PMID: 30789709.

42. Prhashanna A, Taylor PA, Qin J, Kiick KL, Jayaraman A. Effect of Peptide Sequence on the LCST-Like Transition of Elastin-Like Peptides and Elastin-Like Peptide-Collagen-Like Peptide Conjugates: Simulations and Experiments. Biomacromolecules. 2019;20(3):1178-89. Epub 2019/02/05. doi: 10.1021/acs.biomac.8b01503. PubMed PMID: 30715857.

43. Dunshee LC, Sullivan MO, Kiick KL. Manipulation of the dually thermoresponsive behavior of peptide-based vesicles through modification of collagen-like peptide domains. Bioeng Transl Med. 2020;5(1):e10145. Epub 2020/01/29. doi: 10.1002/btm2.10145. PubMed PMID: 31989034; PMCID: PMC6971430.

44. Qin J, Sloppy JD, Kiick KL. Fine structural tuning of the assembly of ECM peptide conjugates via slight sequence modifications. Sci Adv. 2020;6(41). Epub

2020/10/09. doi: 10.1126/sciadv.abd3033. PubMed PMID: 33028534; PMCID: PMC7541060.

45. Taylor PA, Huang H, Kiick KL, Jayaraman A. Placement of Tyrosine Residues as a Design Element for Tuning the Phase Transition of Elastin-peptide-containing Conjugates: Experiments and Simulations. Mol Syst Des Eng. 2020;5(7):1239-54. Epub 2021/04/03. doi: 10.1039/d0me00051e. PubMed PMID: 33796336; PMCID: PMC8009313.

46. Plaut RD, Mocca CP, Prabhakara R, Merkel TJ, Stibitz S. Stably luminescent Staphylococcus aureus clinical strains for use in bioluminescent imaging. PLoS One. 2013;8(3):e59232. Epub 2013/04/05. doi: 10.1371/journal.pone.0059232. PubMed PMID: 23555002; PMCID: PMC3595258.

47. Palmese LL, Fan M, Scott RA, Tan H, Kiick KL. Multi-stimuli-responsive, liposome-crosslinked poly(ethylene glycol) hydrogels for drug delivery. J Biomater Sci Polym Ed. 2021;32(5):635-56. Epub 2020/11/25. doi: 10.1080/09205063.2020.1855392. PubMed PMID: 33231137; PMCID: PMC8659393.

48. Liang Y, Coffin MV, Manceva SD, Chichester JA, Jones RM, Kiick KL. Controlled release of an anthrax toxin-neutralizing antibody from hydrolytically degradable polyethylene glycol hydrogels. J Biomed Mater Res A. 2016;104(1):113-23. Epub 2015/08/01. doi: 10.1002/jbm.a.35545. PubMed PMID: 26223817; PMCID: PMC4933017.

49. Liang YX. Engineering polymeric matrices for controlled drug delivery applications: From bulk gels to nanogels: University of Delaware; 2016.

50. Chen CW, Lu DW, Yeh MK, Shiau CY, Chiang CH. Novel RGD-lipid conjugate-modified liposomes for enhancing siRNA delivery in human retinal pigment

epithelial cells. Int J Nanomedicine. 2011;6:2567-80. Epub 2011/12/01. doi: 10.2147/IJN.S24447. PubMed PMID: 22128247; PMCID: PMC3225218.

51. Sekhon UDS, Swingle K, Girish A, Luc N, de la Fuente M, Alvikas J, Haldeman S, Hassoune A, Shah K, Kim Y, Eppell S, Capadona J, Shoffstall A, Neal MD, Li W, Nieman M, Sen Gupta A. Platelet-mimicking procoagulant nanoparticles augment hemostasis in animal models of bleeding. Sci Transl Med. 2022;14(629):eabb8975. Epub 2022/01/27. doi: 10.1126/scitranslmed.abb8975. PubMed PMID: 35080915.

52. Lai VK, Frey CR, Kerandi AM, Lake SP, Tranquillo RT, Barocas VH. Microstructural and mechanical differences between digested collagen-fibrin co-gels and pure collagen and fibrin gels. Acta Biomater. 2012;8(11):4031-42. Epub 2012/07/26. doi: 10.1016/j.actbio.2012.07.010. PubMed PMID: 22828381; PMCID: PMC3462241.

53. Lai VK, Lake SP, Frey CR, Tranquillo RT, Barocas VH. Mechanical behavior of collagen-fibrin co-gels reflects transition from series to parallel interactions with increasing collagen content. J Biomech Eng. 2012;134(1):011004. Epub 2012/04/10. doi: 10.1115/1.4005544. PubMed PMID: 22482659; PMCID: PMC3717315.

54. Riau AK, Mondal D, Aung TT, Murugan E, Chen L, Lwin NC, Zhou L, Beuerman RW, Liedberg B, Venkatraman SS, Mehta JS. Collagen-Based Artificial Corneal Scaffold with Anti-Infective Capability for Prevention of Perioperative Bacterial Infections. ACS Biomater Sci Eng. 2015;1(12):1324-34. Epub 2015/12/14. doi: 10.1021/acsbiomaterials.5b00396. PubMed PMID: 33429679.

55. Hartinger JM, Lukac P, Mitas P, Mlcek M, Popkova M, Suchy T, Supova M, Zavora J, Adamkova V, Benakova H, Slanar O, Sima M, Bartos M, Chlup H, Grus T. Vancomycin-releasing cross-linked collagen sponges as wound dressings. Bosn J Basic Med Sci. 2021;21(1):61-70. Epub 2019/11/30. doi: 10.17305/bjbms.2019.4496. PubMed PMID: 31782696; PMCID: PMC7861629.

56. Siddiqui AR, Bernstein JM. Chronic wound infection: facts and controversies. Clin Dermatol. 2010;28(5):519-26. Epub 2010/08/28. doi: 10.1016/j.clindermatol.2010.03.009. PubMed PMID: 20797512.

57. Vrignaud S, Benoit JP, Saulnier P. Strategies for the nanoencapsulation of hydrophilic molecules in polymer-based nanoparticles. Biomaterials. 2011;32(33):8593-604. Epub 2011/08/13. doi: 10.1016/j.biomaterials.2011.07.057. PubMed PMID: 21831421.

58. Eloy JO, Claro de Souza M, Petrilli R, Barcellos JP, Lee RJ, Marchetti JM. Liposomes as carriers of hydrophilic small molecule drugs: strategies to enhance encapsulation and delivery. Colloids Surf B Biointerfaces. 2014;123:345-63. Epub 2014/10/05. doi: 10.1016/j.colsurfb.2014.09.029. PubMed PMID: 25280609.

59. Li Q, Li X, Zhao C. Strategies to Obtain Encapsulation and Controlled Release of Small Hydrophilic Molecules. Front Bioeng Biotechnol. 2020;8:437. Epub 2020/06/02. doi: 10.3389/fbioe.2020.00437. PubMed PMID: 32478055; PMCID: PMC7237580.

60. Yu L, Ci T, Zhou S, Zeng W, Ding J. The thermogelling PLGA-PEG-PLGA block copolymer as a sustained release matrix of doxorubicin. Biomater Sci. 2013;1(4):411-20. Epub 2013/04/05. doi: 10.1039/c2bm00159d. PubMed PMID: 32481906.

61. Ramazani F, Chen W, van Nostrum CF, Storm G, Kiessling F, Lammers T, Hennink WE, Kok RJ. Strategies for encapsulation of small hydrophilic and amphiphilic drugs in PLGA microspheres: State-of-the-art and challenges. Int J Pharm. 2016;499(1-2):358-67. Epub 2016/01/23. doi: 10.1016/j.ijpharm.2016.01.020. PubMed PMID: 26795193.

62. Sultanova Z, Kaleli G, Kabay G, Mutlu M. Controlled release of a hydrophilic drug from coaxially electrospun polycaprolactone nanofibers. Int J Pharm. 2016;505(1-2):133-8. Epub 2016/03/26. doi: 10.1016/j.ijpharm.2016.03.032. PubMed PMID: 27012983.

63. Briuglia ML, Rotella C, McFarlane A, Lamprou DA. Influence of cholesterol on liposome stability and on in vitro drug release. Drug Deliv Transl Res. 2015;5(3):231-42. Epub 2015/03/20. doi: 10.1007/s13346-015-0220-8. PubMed PMID: 25787731.

64. Fan T, Yu X, Shen B, Sun L. Peptide Self-Assembled Nanostructures for Drug Delivery Applications. Journal of Nanomaterials. 2017;2017:4562474. doi: 10.1155/2017/4562474.

65. Lee S, Trinh THT, Yoo M, Shin J, Lee H, Kim J, Hwang E, Lim YB, Ryou C. Self-Assembling Peptides and Their Application in the Treatment of Diseases. Int J Mol Sci. 2019;20(23). Epub 2019/11/27. doi: 10.3390/ijms20235850. PubMed PMID: 31766475; PMCID: PMC6928719.

66. Shi P, Aluri S, Lin YA, Shah M, Edman M, Dhandhukia J, Cui H, MacKay JA. Elastin-based protein polymer nanoparticles carrying drug at both corona and core suppress tumor growth in vivo. J Control Release. 2013;171(3):330-8. Epub

2013/05/30. doi: 10.1016/j.jconrel.2013.05.013. PubMed PMID: 23714121; PMCID: PMC3795821.

67. Jabbari E, Yang X, Moeinzadeh S, He X. Drug release kinetics, cell uptake, and tumor toxicity of hybrid VVVVVVKK peptide-assembled polylactide nanoparticles. Eur J Pharm Biopharm. 2013;84(1):49-62. Epub 2013/01/01. doi: 10.1016/j.ejpb.2012.12.012. PubMed PMID: 23275111; PMCID: PMC3626769.

68. Rodriguez-Cabello JC, Arias FJ, Rodrigo MA, Girotti A. Elastin-like polypeptides in drug delivery. Adv Drug Deliv Rev. 2016;97:85-100. Epub 2015/12/26. doi: 10.1016/j.addr.2015.12.007. PubMed PMID: 26705126.

69. Betre H, Setton LA, Meyer DE, Chilkoti A. Characterization of a genetically engineered elastin-like polypeptide for cartilaginous tissue repair. Biomacromolecules. 2002;3(5):910-6. Epub 2002/09/10. doi: 10.1021/bm0255037. PubMed PMID: 12217035.

70. Adams Jr. SB, Shamji MF, Nettles DL, Hwang P, Setton LA. Sustained release of antibiotics from injectable and thermally responsive polypeptide depots. Journal of Biomedical Materials Research Part B: Applied Biomaterials. 2009;90B(1):67-74. doi: https://doi.org/10.1002/jbm.b.31254.

71. Subczynski WK, Wisniewska A, Yin JJ, Hyde JS, Kusumi A. Hydrophobic barriers of lipid bilayer membranes formed by reduction of water penetration by alkyl chain unsaturation and cholesterol. Biochemistry. 1994;33(24):7670-81. Epub 1994/06/21. doi: 10.1021/bi00190a022. PubMed PMID: 8011634.

72. Nasr G, Greige-Gerges H, Elaissari A, Khreich N. Liposomal membrane permeability assessment by fluorescence techniques: Main permeabilizing agents,

applications and challenges. Int J Pharm. 2020;580:119198. Epub 2020/03/15. doi: 10.1016/j.ijpharm.2020.119198. PubMed PMID: 32169353.

73. Laracuente ML, Yu MH, McHugh KJ. Zero-order drug delivery: State of the art and future prospects. J Control Release. 2020;327:834-56. Epub 2020/09/16. doi: 10.1016/j.jconrel.2020.09.020. PubMed PMID: 32931897.

74. Coradin T, Wang K, Law T, Trichet L. Type I Collagen-Fibrin Mixed Hydrogels: Preparation, Properties and Biomedical Applications. Gels. 2020;6(4):36. PubMed PMID: doi:10.3390/gels6040036.

75. Moreno-Arotzena O, Meier JG, Del Amo C, Garcia-Aznar JM. Characterization of Fibrin and Collagen Gels for Engineering Wound Healing Models. Materials (Basel). 2015;8(4):1636-51. Epub 2015/08/21. doi: 10.3390/ma8041636. PubMed PMID: 26290683; PMCID: PMC4538789.

76. Lang NR, Munster S, Metzner C, Krauss P, Schurmann S, Lange J, Aifantis KE, Friedrich O, Fabry B. Estimating the 3D pore size distribution of biopolymer networks from directionally biased data. Biophys J. 2013;105(9):1967-75. Epub 2013/11/12. doi: 10.1016/j.bpj.2013.09.038. PubMed PMID: 24209841; PMCID: PMC3824714.

77. Wang F, Zhou H, Olademehin OP, Kim SJ, Tao P. Insights into Key Interactions between Vancomycin and Bacterial Cell Wall Structures. ACS Omega. 2018;3(1):37-45. Epub 2018/02/06. doi: 10.1021/acsomega.7b01483. PubMed PMID: 29399648; PMCID: PMC5793038.

78. Creech CB, Al-Zubeidi DN, Fritz SA. Prevention of Recurrent Staphylococcal Skin Infections. Infect Dis Clin North Am. 2015;29(3):429-64. Epub

2015/08/28. doi: 10.1016/j.idc.2015.05.007. PubMed PMID: 26311356; PMCID: PMC4552962.

79. Frykberg RG, Banks J. Challenges in the Treatment of Chronic Wounds. Adv Wound Care (New Rochelle). 2015;4(9):560-82. Epub 2015/09/05. doi: 10.1089/wound.2015.0635. PubMed PMID: 26339534; PMCID: PMC4528992.

80. Bertazzoni Minelli E, Benini A, Magnan B, Bartolozzi P. Release of gentamicin and vancomycin from temporary human hip spacers in two-stage revision of infected arthroplasty. J Antimicrob Chemother. 2004;53(2):329-34. Epub 2003/12/23. doi: 10.1093/jac/dkh032. PubMed PMID: 14688051.

81. Zhang L, Yan J, Yin Z, Tang C, Guo Y, Li D, Wei B, Xu Y, Gu Q, Wang L. Electrospun vancomycin-loaded coating on titanium implants for the prevention of implant-associated infections. Int J Nanomedicine. 2014;9:3027-36. Epub 2014/07/17. doi: 10.2147/IJN.S63991. PubMed PMID: 25028544; PMCID: PMC4077604.

82. Stravinskas M, Nilsson M, Vitkauskiene A, Tarasevicius S, Lidgren L. Vancomycin elution from a biphasic ceramic bone substitute. Bone Joint Res. 2019;8(2):49-54. Epub 2019/03/28. doi: 10.1302/2046-3758.82.BJR-2018-0174.R2. PubMed PMID: 30915210; PMCID: PMC6397329.

83. Abdel-Rahman LM, Eltaher HM, Abdelraouf K, Bahey-El-Din M, Ismail C, Kenawy E-RS, El-Khordagui LK. Vancomycin-functionalized Eudragit-based nanofibers: Tunable drug release and wound healing efficacy. Journal of Drug Delivery Science and Technology. 2020;58:101812.

84. Krishnan AG, Biswas R, Menon D, Nair MB. Biodegradable nanocomposite fibrous scaffold mediated local delivery of vancomycin for the treatment

of MRSA infected experimental osteomyelitis. Biomater Sci. 2020;8(9):2653-65. Epub 2020/04/07. doi: 10.1039/d0bm00140f. PubMed PMID: 32249281.

85. Singh S, Alrobaian MM, Molugulu N, Agrawal N, Numan A, Kesharwani P. Pyramid-Shaped PEG-PCL-PEG Polymeric-Based Model Systems for Site-Specific Drug Delivery of Vancomycin with Enhance Antibacterial Efficacy. ACS Omega. 2020;5(21):11935-45. Epub 2020/06/18. doi: 10.1021/acsomega.9b04064. PubMed PMID: 32548372; PMCID: PMC7271022.

Chapter 6

CONCLUSIONS and FUTURE PERSPECTIVE

6.1 Conclusions

Due to the enormous economic and societal burdens associated with the management of chronic wounds, there is a critical need for better approaches to engineer the wound microenvironment to promote the improved healing. The primary factors to develop chronic wounds are the lack of growth factors activity, as well as the wound infection caused by inefficiently clearance of microorganism from the wound site. Current treatments such as wound dressings, topical application of growth factors or antibiotics, and the combination approaches enable the increased accessibility of growth factors while eradicating microorganisms in the wound bed. However, the topically administered therapeutics often fail to reach the sufficient local concentration in harsh wound environment, leading to the reduced overall effectiveness of therapeutics. In this dissertation, to overcome the limitation of topically applied therapeutics in harsh wound environment, I have utilized CMP-collagen tethers to control the delivery of therapeutics and extend the duration of therapeutic effects.

In Chapter 2 and 3, GAHCM composed of CMP modified DNA/PEI polyplex and hyaluronic acid and collagen matrix was developed to improve the efficiency of growth factor gene transfer and maximize the growth factor activities to regulate cellular phenotypes for the improved wound repair. Both CMP modification to improve the retention of polyplex on GAHCM and HA-CD44 cellular interaction increased the gene transfer to fibroblasts. The sustained VEGF production by fibroblast transfection using VEGF encoding GAHCM stimulated not only pro-healing myofibroblasts differentiation and but also pro-angiogenic endothelial cellular network formation *in vitro*. Moreover, application of VEGF encoding GAHCM promoted the robust repair on

murine splinted excisional wounds through increased the myofibroblast differentiation and more numbers of blood vessel formation in the healed wounds.

In Chapter 4, ELP-CLP nanovesicle tethered collagen containing matrices (either collagen or collagen-fibrin (Co-gel)) were utilized to improve the control delivery of vancomycin and extend the duration of antibiotic effects against MRSA for wound infection treatment. As compared to liposome formulations, ELP-CLP enabled more efficient encapsulation of vancomycin and better control over the release profile of vancomycin as a zero-order kinetics. And, ELP-CLP had a different level of affinity to collagen vs co-gel and release rate from collagen vs co-gel. Due to the enhanced retention and slower release of ELP-CLP with co-gel than collagen, the vancomycin release from ELP-CLP with co-gel were more sustained than with collagen. Additionally, the biphasic release profiles of vancomycin from ELP-CLP tethered collagen/co-gel more effectively inhibited and delayed the growth of MRSA even after repeated bacterial inoculation for pro-longed duration as compared to free vancomycin loaded matrices.

In conclusions, CMP-collagen tethers approach has demonstrated tremendous potential in overcoming the limitations of topically administrated therapeutics for wound management. Overall, this dissertation provides further support recommending the use of CMP-collagen tethers approach to extend the duration and level of therapeutic effects for regenerative medicine and tissue engineering applications.

6.2 Future perspective

6.2.1 GAHCM – Multi-therapeutics delivery approach depending on the wound phases

Throughout the wound healing phases, multiple growth factors are present in the various processes to regulate interactions between cells, soluble cytokines, blood elements, and the extracellular matrix (1). The application of a single growth factor may

have only a temporary effect in enhancing wound healing, rather than a terminant solution. The proper growth factors must be available at the correct time and in effective concentrations to achieve favorable outcomes. Thus, strategies to deliver multiple growth factors to support cellular behaviors during the corresponding phase of wound healing cascade are needed.

Previous studies have demonstrated the benefits of delivering multiple growth factors, proteins, or genes, in which there is acceleration of wound repair seen through in vivo diabetic animal models (2-5). In details, sequential delivery of multiple angiogenic growth factors, including VEGF, PDGF, bFGF, and EGF, in diabetic rats revealed accelerated wound closure rate and increased collagen deposition and vessel maturation (6). Based on these findings, which validate advantages of sustained and sequential delivery of multiple growth factors in chronic wound repair, I propose to engineer the delivery of PDGF-BB and VEGF-A genes using the combined pPDGF-BB encoding PEI polyplex and pVEGF encoding CMP modified polyplex to prepare GAHCM for the precise control of their signaling times. PDGF-BB activity in early proliferation phase using pPDGF-BB PEI polyplex to proliferate fibroblasts to maximize transfection capacity to increase concentration of VEGF in the middle proliferation phase using pVEGF encoding CMP modified polyplex within GAHCM will help facilitate angiogenesis and wound healing.

6.2.2 GAHCM – Controlling the collagen degradation to extend the gene transfer profile

During chronic wound healing, the imbalance of proteases in the prolonged inflammatory phase delays the healing process via de-regulating essential growth factors including PDGF, VEGF, and FGF (7-9). Due to the high degradation rate and rapid clearance of growth factors in chronic wounds, the approach to improve the duration of growth factors activity is a key question to be addressed (10).

In my dissertation works, I have observed CMP modification on GAHCM enabled the extension of both duration and level of gene transfer due to the retention of

CMP modified polyplex on HCM hydrogel. Additionally, the previous work by our groups reported that CMP modified on polyplex tethered collagen containing matrices were released as CMP modified polyplex tethered collagen fragments in response of matrix metalloproteinase activity and delivered into cells using collagen cellular receptor mediated more efficient caveolae endocytic pathway(11, 12). Thus, the manipulating collagen matrix degradation rate would control the gene transfer kinetics. And the degradation rate of collagen can be delayed by addition of chemical crosslinks. In details, the various chemical crosslinks include carbodiimide coupling between -NH2 group and -COOH group in native collagen molecule(13) and photo-crosslink with collagen with additional methacrylate/acrylate groups modification(14). Thus, I propose to control the gene transfer kinetics of CMP modified polyplex via manipulating collagen matrix degradation rate using addition of chemical crosslink. This study will be beneficial to apply the temporal delivery of multiple growth factors depending on the wound healing phase. The combination of collagen and slow degrading collagen can be utilized to deliver different growth factor encoding CMP polyplexes depending on growth factor activity during the healing time frame. For example, the sustained activity of PDGF-BB throughout the entire healing phases can be regulated by PDGF-BB encoding CMP-polyplex tethered slow degrading collagen while the VEGF activity during the proliferation phase can be controlled by VEGF encoding CMP-polyplex tethered collagen formulation. Thus, the manipulating collagen degradation for CMP-collagen tether system would be a great potential to control the temporal delivery of multiple growth factor gene.

6.2.3 ELP-CLP nanovesicle collagen tether system to target intracellular bacterial

Staphylococcus aureus (S. aureus) is predominantly found in bacteria isolation from multiple patients with chronic wounds(15-18). Recurrence of S. Aureus infection may result from less effective antibiotic action due to the lack of access of the antibiotic

to the site of infection, especially, to the intracellular niche. Several studies have reported ability of S. aureus to adhere to, invade into, and grow on mammalian cells including macrophages, keratinocytes, endothelial cells, and fibroblasts(19-22). These intracellular forms of S. aureus have been shown to become resistant to antibiotic action (ex. Methicillin-resistant S. aureus (MRSA))(23, 24). Thus, the strategy to localize antibiotic agents into the intracellular sites where MRSA inhabit will effectively eradicate MRSA population to treat wound infection and prevent the recurrence of wound infection. The proposed strategy utilizes the CMP-collagen interaction mediated intracellular pathway via elastin like peptides and collagen like peptides (ELP-CLP) nanocarrier for the delivery of antibiotics to enhance the efficacy of antibiotics through targeting the intracellular bacterial population. I hypothesize that the manipulating ELP-CLP sequence, in particularly CLP sequence, to control the level of collagen tether of ELP-CLP nanocarriers enable the control of intracellular delivery of antibiotics. As the length of CLP repeat unit is increased, the melting temperature of CLP is increased, which means that the triple helix formation of CLP is more stable and CLP hybridization with collagen would be more enhanced. Thus, the comparison of ELP-CLP ($Tm > 37^{o}$) vs. ELP-CLP ($Tm < 37^{o}$) incorporated collagen-based hydrogel systems would explain the advantage of cellular uptake pathway and antibiotic effectiveness of ELP-CLP and collage tether ($Tm > 37^{o}$) vs. ELP-CLP ($Tm < 37^{o}$) at physiological condition. Through this study, I expect establish the ELP-CLP nanovesicles to improve the effectiveness of antibiotic through the CLP hybridization to collagen mediated intracellular localization and release of the antibiotics in its active concentration for the potential control of intracellular bacterial population.

REFERENCES

1. Branski LK, Pereira CT, Herndon DN, Jeschke MG. Gene therapy in wound healing: present status and future directions. Gene Ther. 2007;14(1):1-10. Epub 2006/08/25. doi: 10.1038/sj.gt.3302837. PubMed PMID: 16929353.

2. Shi R, Lian W, Han S, Cao C, Jin Y, Yuan Y, Zhao H, Li M. Nanosphere-mediated co-delivery of VEGF-A and PDGF-B genes for accelerating diabetic foot ulcers healing in rats. Gene Ther. 2018;25(6):425-38. Epub 2018/06/30. doi: 10.1038/s41434-018-0027-6. PubMed PMID: 29955127.

3. Ishihara J, Ishihara A, Fukunaga K, Sasaki K, White MJV, Briquez PS, Hubbell JA. Laminin heparin-binding peptides bind to several growth factors and enhance diabetic wound healing. Nat Commun. 2018;9(1):2163. Epub 2018/06/06. doi: 10.1038/s41467-018-04525-w. PubMed PMID: 29867149; PMCID: PMC5986797.

4. Martino MM, Briquez PS, Ranga A, Lutolf MP, Hubbell JA. Heparin-binding domain of fibrin(ogen) binds growth factors and promotes tissue repair when incorporated within a synthetic matrix. Proc Natl Acad Sci U S A. 2013;110(12):4563-8. Epub 2013/03/15. doi: 10.1073/pnas.1221602110. PubMed PMID: 23487783; PMCID: PMC3607046.

5. Martino MM, Tortelli F, Mochizuki M, Traub S, Ben-David D, Kuhn GA, Muller R, Livne E, Eming SA, Hubbell JA. Engineering the growth factor microenvironment with fibronectin domains to promote wound and bone tissue healing. Sci Transl Med. 2011;3(100):100ra89. Epub 2011/09/16. doi: 10.1126/scitranslmed.3002614. PubMed PMID: 21918106.

6. Lai HJ, Kuan CH, Wu HC, Tsai JC, Chen TM, Hsieh DJ, Wang TW. Tailored design of electrospun composite nanofibers with staged release of multiple angiogenic growth factors for chronic wound healing. Acta Biomater.

2014;10(10):4156-66. Epub 2014/05/13. doi: 10.1016/j.actbio.2014.05.001. PubMed PMID: 24814882.

7. Trengove NJ, Bielefeldt-Ohmann H, Stacey MC. Mitogenic activity and cytokine levels in non-healing and healing chronic leg ulcers. Wound Repair Regen. 2000;8(1):13-25. Epub 2000/04/12. doi: 10.1046/j.1524-475x.2000.00013.x. PubMed PMID: 10760211.

8. Berse B, Brown LF, Van de Water L, Dvorak HF, Senger DR. Vascular permeability factor (vascular endothelial growth factor) gene is expressed differentially in normal tissues, macrophages, and tumors. Mol Biol Cell. 1992;3(2):211-20. Epub 1992/02/01. doi: 10.1091/mbc.3.2.211. PubMed PMID: 1550962; PMCID: PMC275520.

9. Powers CJ, McLeskey SW, Wellstein A. Fibroblast growth factors, their receptors and signaling. Endocr Relat Cancer. 2000;7(3):165-97. Epub 2000/10/06. doi: 10.1677/erc.0.0070165. PubMed PMID: 11021964.

10. Losi P, Briganti E, Magera A, Spiller D, Ristori C, Battolla B, Balderi M, Kull S, Balbarini A, Di Stefano R, Soldani G. Tissue response to poly(ether)urethane-polydimethylsiloxane-fibrin composite scaffolds for controlled delivery of pro-angiogenic growth factors. Biomaterials. 2010;31(20):5336-44. Epub 2010/04/13. doi: 10.1016/j.biomaterials.2010.03.033. PubMed PMID: 20381861.

11. Urello MA, Kiick KL, Sullivan MO. ECM turnover-stimulated gene delivery through collagen-mimetic peptide-plasmid integration in collagen. Acta Biomater. 2017;62:167-78. Epub 2017/09/04. doi: 10.1016/j.actbio.2017.08.038. PubMed PMID: 28865990; PMCID: PMC5654588.

12. Urello MA, Kiick KL, Sullivan MO. A CMP-based method for tunable, cell-mediated gene delivery from collagen scaffolds. J Mater Chem B. 2014;2(46):8174-85. Epub 2014/12/14. doi: 10.1039/c4tb01435a. PubMed PMID: 32262095.

13. Ahn JI, Kuffova L, Merrett K, Mitra D, Forrester JV, Li F, Griffith M. Crosslinked collagen hydrogels as corneal implants: effects of sterically bulky vs. non-bulky carbodiimides as crosslinkers. Acta Biomater. 2013;9(8):7796-805. Epub 2013/04/27. doi: 10.1016/j.actbio.2013.04.014. PubMed PMID: 23619290.

14. Sarrigiannidis SO, Rey JM, Dobre O, Gonzalez-Garcia C, Dalby MJ, Salmeron-Sanchez M. A tough act to follow: collagen hydrogel modifications to improve mechanical and growth factor loading capabilities. Mater Today Bio. 2021;10:100098. Epub 2021/03/26. doi: 10.1016/j.mtbio.2021.100098. PubMed PMID: 33763641; PMCID: PMC7973388.

15. Frank DN, Wysocki A, Specht-Glick DD, Rooney A, Feldman RA, St Amand AL, Pace NR, Trent JD. Microbial diversity in chronic open wounds. Wound Repair Regen. 2009;17(2):163-72. Epub 2009/03/27. doi: 10.1111/j.1524-475X.2009.00472.x. PubMed PMID: 19320883.

16. Kirketerp-Moller K, Jensen PO, Fazli M, Madsen KG, Pedersen J, Moser C, Tolker-Nielsen T, Hoiby N, Givskov M, Bjarnsholt T. Distribution, organization, and ecology of bacteria in chronic wounds. J Clin Microbiol. 2008;46(8):2717-22. Epub 2008/05/30. doi: 10.1128/JCM.00501-08. PubMed PMID: 18508940; PMCID: PMC2519454.

17. Brackman G, De Meyer L, Nelis HJ, Coenye T. Biofilm inhibitory and eradicating activity of wound care products against Staphylococcus aureus and

Staphylococcus epidermidis biofilms in an in vitro chronic wound model. J Appl Microbiol. 2013;114(6):1833-42. Epub 2013/03/16. doi: 10.1111/jam.12191. PubMed PMID: 23490006.

18. Wolcott RD, Hanson JD, Rees EJ, Koenig LD, Phillips CD, Wolcott RA, Cox SB, White JS. Analysis of the chronic wound microbiota of 2,963 patients by 16S rDNA pyrosequencing. Wound Repair Regen. 2016;24(1):163-74. Epub 2015/10/16. doi: 10.1111/wrr.12370. PubMed PMID: 26463872.

19. Chiller K, Selkin BA, Murakawa GJ. Skin microflora and bacterial infections of the skin. J Investig Dermatol Symp Proc. 2001;6(3):170-4. Epub 2002/04/02. doi: 10.1046/j.0022-202x.2001.00043.x. PubMed PMID: 11924823.

20. Kintarak S, Whawell SA, Speight PM, Packer S, Nair SP. Internalization of Staphylococcus aureus by human keratinocytes. Infect Immun. 2004;72(10):5668-75. Epub 2004/09/24. doi: 10.1128/IAI.72.10.5668-5675.2004. PubMed PMID: 15385465; PMCID: PMC517534.

21. Tuchscherr L, Heitmann V, Hussain M, Viemann D, Roth J, von Eiff C, Peters G, Becker K, Loffler B. Staphylococcus aureus small-colony variants are adapted phenotypes for intracellular persistence. J Infect Dis. 2010;202(7):1031-40. Epub 2010/08/19. doi: 10.1086/656047. PubMed PMID: 20715929.

22. Schnaith A, Kashkar H, Leggio SA, Addicks K, Kronke M, Krut O. Staphylococcus aureus subvert autophagy for induction of caspase-independent host cell death. J Biol Chem. 2007;282(4):2695-706. Epub 2006/12/01. doi: 10.1074/jbc.M609784200. PubMed PMID: 17135247.

23. Krut O, Sommer H, Kronke M. Antibiotic-induced persistence of cytotoxic Staphylococcus aureus in non-phagocytic cells. J Antimicrob Chemother. 2004;53(2):167-73. Epub 2004/01/20. doi: 10.1093/jac/dkh076. PubMed PMID: 14729736.

24. Peyrusson F, Varet H, Nguyen TK, Legendre R, Sismeiro O, Coppee JY, Wolz C, Tenson T, Van Bambeke F. Intracellular Staphylococcus aureus persisters upon antibiotic exposure. Nat Commun. 2020;11(1):2200. Epub 2020/05/06. doi: 10.1038/s41467-020-15966-7. PubMed PMID: 32366839; PMCID: PMC7198484.

Appendix A

REAL-TIME ELASTIC MODULUS MEASUREMENTS OF HYALURONIC ACID AND COLLAGEN-BASED HYDROGEL DEGRADATION USING ATOMIC FORCE MICROSCOPY

The mechanical property of hydrogel, which provides microenvironment for cell growth, is important contributing factor to modulate the cellular functions. The study to determine the mechanical property of local cellular microenvironment is desired to understand better control over cellular behaviors using biomaterials. I have applied the atomic force microscope (AFM) to leverage its ability to detect the mechanical stiffness properties on the local surface of soft hydrogel. I have recently developed gene-activated hyaluronic acid (HA) and collagen matrix (GAHCM) containing collagen mimetic peptide (CMP) modified VEGF encoding polyplex and hyaluronic acid and collagen matrix (HCM), which has the bulk storage modulus as below 100 Pa. Whereas the oscillatory rheology measured the bulk mechanical stiffness of GAHCM samples, AFM technique enable the detection of difference in the mechanical stiffness depending on the local surface on GAHCM, where collagen/HA might be heterogeneously distributed. Moreover, I have demonstrated at the first time utilizing the AFM to measure the real-time change in the local elastic modulus of HCM sample during its degradation process by collagenase. These finding suggests that the potential advantage of AFM technique to understand the mechanical property of local cellular microenvironment for gene/drug delivery and tissue regeneration applications.

A.1 Introduction

The mechanical properties of native extracellular matrix mimicking polymeric hydrogel have significantly contributed with the fate of cellular behaviors in the broad range of biomedical applications (1, 2). In details, the varying the mechanical stiffness

of hydrogel guides cellular spreading (3), migration (4, 5), proliferation (6, 7), and differentiation (8, 9). Additionally, the cellular microenvironment modulated by mechanical stiffness of hydrogel regulates cellular uptake behavior of therapeutics loaded nanoparticles within the hydrogel (10, 11). Thus, the study to determine the local mechanical stiffness within the hydrogel will be desired to modulate sophistically the local cellular microenvironment to maximize the delivery efficiency of therapeutics.

However, due to the low rigidity of hydrogel with a typical elastic modulus as <1 kPa to mimic the mechanical property of the natural soft tissue (12), the detecting the local mechanical stiffness of the hydrogel is more challenging using typical traction or bending assays. Meanwhile, oscillatory rheological measurements allow the characterization of bulk mechanical properties of in situ fabricated hydrogel, but this technique has difficulty in measurements for the mechanical properties of the local spatial variation within hydrogel (13). On the other hand, atomic force microscope (AFM) can be equipped with nano- or micro- sized probe to determine the local surface modulus of hydrogel using the force versus distance data at specific point on the surface of hydrogel (14). Moreover, AFM technique enables the measurement of change in the modulus on the surface of the local spatial variable hydrogel over the time. This would be a significant tool to investigate the progression of change in mechanical properties of hydrogel by cellular secreted enzymes or growth factors.

I recently developed a gene-activated hyaluronic acid-collagen matrix (GAHCM) comprising collagen mimetic peptide (CMP) functionalized pVEGF polyplexes tethering natural polymeric HCM hydrogel to study cellular gene transfer kinetics and produced VEGF mediated cellular behaviors (chapter 3). However, the correlation between these studies and the impact of microenvironmental mechanical cues of GAHCM is still unexplored.

Herein, I leveraged AFM technique to investigate the local mechanical properties of GAHCM samples and their change in local mechanical properties during

collagenase triggered degradation process. These findings show great potential of AFM applications on the study of soft hydrogels and cellular interaction in the future.

A.2 Results and Discussion

A.2.1 Bulk mechanical stiffness of sample

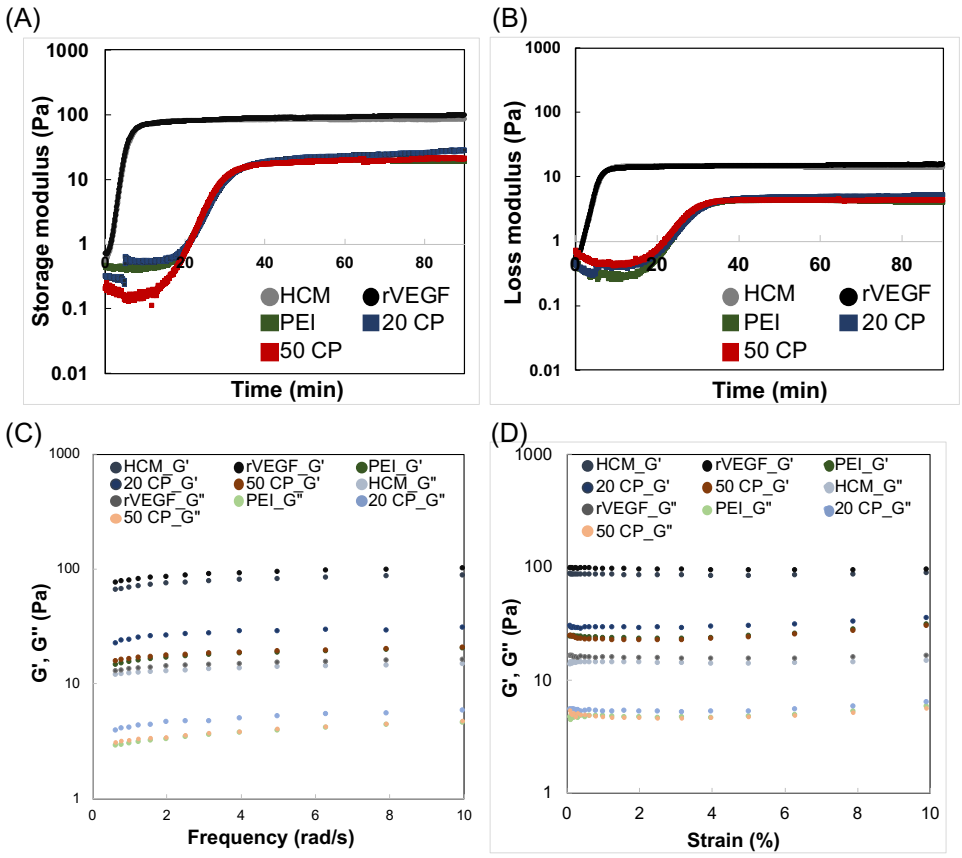

Figure A.1. The mechanical properties of measurements of bulk GAHCM using oscillatory shear rheology. Time sweep of (A) Storage modulus (G') and (B) Loss modulus (G") measurements. (C) Frequency sweep and (D) strain sweep measurements.

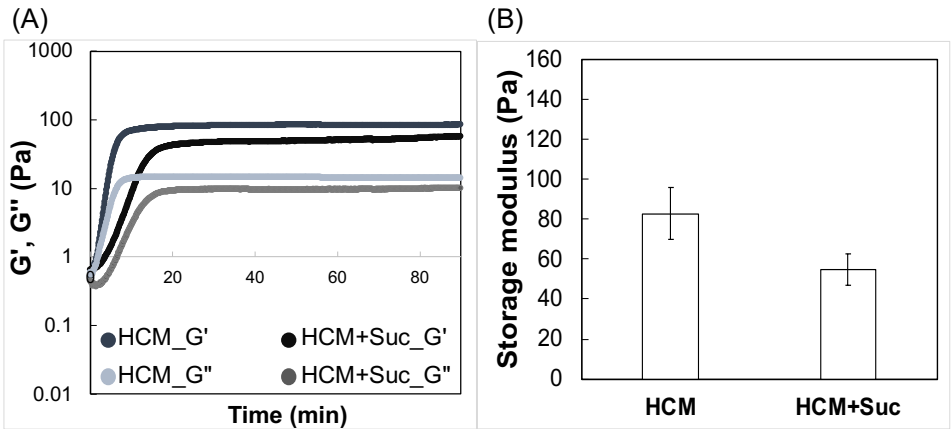

Figure A.2. The mechanical properties of measurements of bulk HCM hydrogel with and without sucrose using oscillatory shear rheology. (A) Time sweep of Storage modulus (G') and Loss modulus (G") measurements. (B) The average of storage modulus of HCM hydrogels. Each data represents mean ± standard deviation for n=3.

In order to investigate whether the presence of recombinant protein or polyplex nanoparticles influences on the overall bulk mechanical properties of HCM hydrogel, the bulk mechanical modulus of samples was determined using an oscillatory rheology (Figures A.1 and A.2). The average of storage modulus of both HCM hydrogel (80 Pa), which was 4-fold larger value than GAHCM samples (~ 20 Pa), indicating that the sucrose treated polyplex nanoparticles in GAHCM might interrupt the stiffness of HCM hydrogel (Figure A.3). Also, I have examined that the presence of sucrose in HCM hydrogel reduced the storage modulus (50 Pa) by 1.6-fold lower than HCM hydrogel without sucrose, but it did not reduce completely 4-fold lower as GAHCM than HCM hydrogel (Figure A.2). This suggested that the presence of polyplex within HCM hydrogel also contributed with the decreasing the modulus of HCM hydrogel. On the other hand, I have observed the similar average storage moduli of HCM + rVEGF hydrogel with no sucrose presence (~80 Pa), as HCM hydrogel.

The HCM hydrogel is formed by fibrillogenesis of acid solubilized collagen molecules via physical driver forces including physiological temperature, neutral pH, and ionic strength (15) and the disulfide bond cross-linked between thiol functionalized hyaluronic acid molecules via air oxidation (16). The mass ratio of Polyplex: HCM:

Sucrose (1: 12.5: 171.25) indicated that the mass composition of poly-plex and sucrose was occupied the 14-fold larger portion than HCM, which might significantly influence on the physical property of HCM hydrogel. In particular, sucrose has been reported as an inhibitor for collagen fibrillation even if it preserved the triple helical structure of collagen molecules (17). Thus, the sucrose treated polyplex might prevent collagen fibrillation process, which remarkably contributes on the mechanical properties of HCM hydrogel, leading to the decreased bulk modulus of HCM hydrogel.

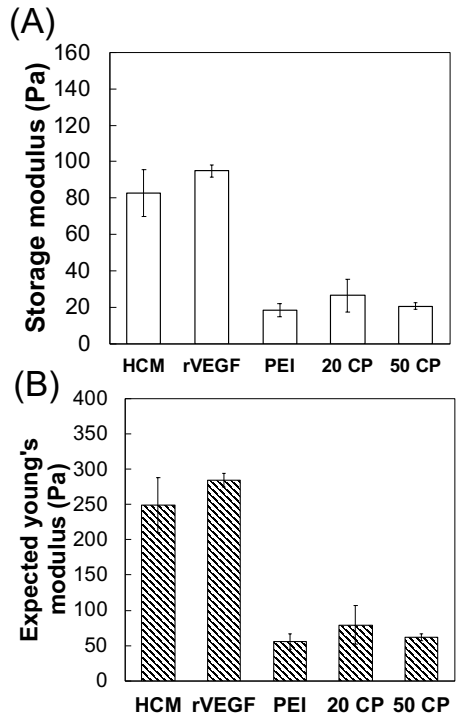

Figure A.3. The bulk mechanical properties of GAHCM using oscillatory shear rheology. (A) Storage modulus (G') measurements. (B) Expected young's modulus calculated using $2G'(1 + \nu) = E$, $\nu = Poisson\ ratio$, assuming 0.5. Each data represents mean $\pm$ standard deviation for n=3

A.2.2 Local mechanical stiffness of sample

In order to evaluate the comparison between bulk and local mechanical stiffness of samples, the local surface modulus of samples was determined via the contact mode

measurement using AFM. As compared to the expected young's modulus based on the bulk storage modulus of samples under the assumption of poisson ratio of sample as 0.5 (Figure A.3), the overall local young's modulus for local surface of samples was enhanced by twice but following with the same trend (Figure A.4). However, unexpectedly, the young's modulus for local surface of HCM hydrogel with rVEGF samples (100 Pa) was lower than HCM hydrogel (480 Pa) and the expected bulk young's modulus of HCM hydrogel with rVEGF (280 Pa). Due to the fact that AFM measurement was performed under the fluidic condition, the typical fast release profile of rVEGF, physically entrapped in the HCM hydrogel (30% of rVEGF was released from HA/collagen gel within 1 h (18) might influence on the mechanical stiffness in the local surface of HCM hydrogel, resulting in this unexpected young's modulus value. These results suggested that the bulk and local mechanical stiffness cannot be comparable.

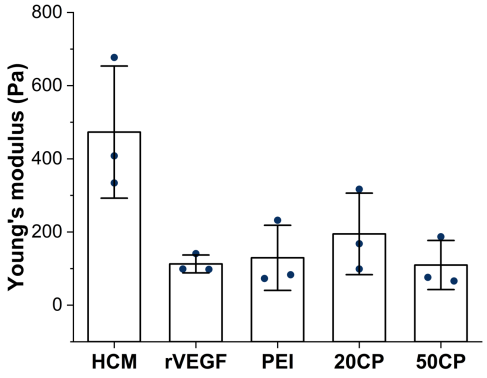

Figure A.4. Young's modulus measurements of GAHCM using atomic force microscopy. Each data represents mean ± standard deviation for three samples (N > 20 measurements per each sample).

I have observed that young's modulus values were varied depending on the location on the surface of HCM hydrogel (Figure A.5). This could be the fact that the different physical structure of hydrogel depending on the local area caused by the heterogenous distribution of HA-SH along with collagen fibers in HCM hydrogel. Kaufman and coworker demonstrated that HA in HA/collagen gels can both deposit on

collagen fibrils and disperse throughout the medium (19). Moreover, when the more amounts of HA were located on the collagen fibrils with temperature control during the gelation process, the collagen fibril diameter was decreased, leading to the reduced elastic modulus. Thus, the locally variable physical structure of HCM hydrogel might explain our observation on the larger variation in young's modulus of local surface of each sample.

A.2.3 Change in local stiffness of sample during degradation

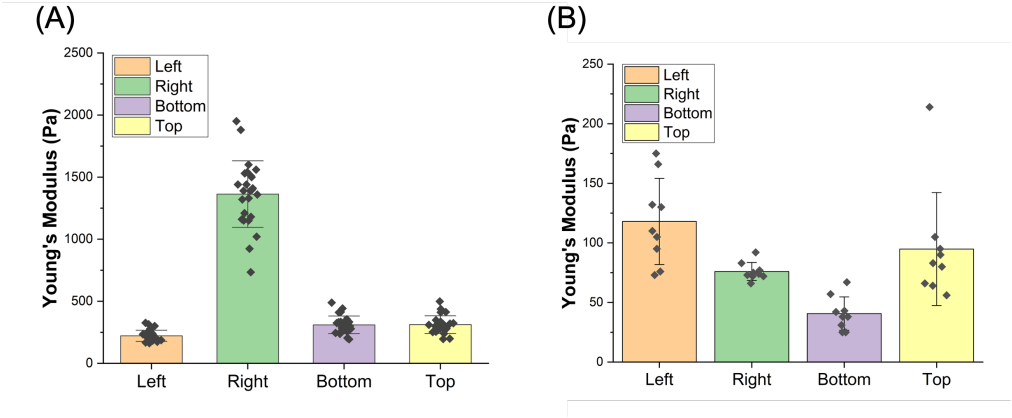

Figure A.5. The local young's modulus measurements of different area (displacement as 2 mm) on the surface of HCM hydrogel using atomic force microscope. (A) HCM sample #1. (B) HCM sample #2. Each data represents mean ± standard deviation for n>9 measurements per the location.

To evaluate the ability of AFM technique to monitor the progress of change in the local mechanical properties of samples in response to the external cues, I have determined the young's modulus of a specific point on the surface of HCM sample during degradation by collagenase. Only HCM hydrogel sample was selected in this study because of the highest young's modulus among samples that could behave the broad range of change in the young's modulus. First, I have demonstrated young's modulus measurements of HCM sample for 30 min (Figure A.6(A)) to confirm that the change in Young's modulus of HCM sample after collagenase treatment was not from the deformation of hydrogel during the overtime measurements on one particular

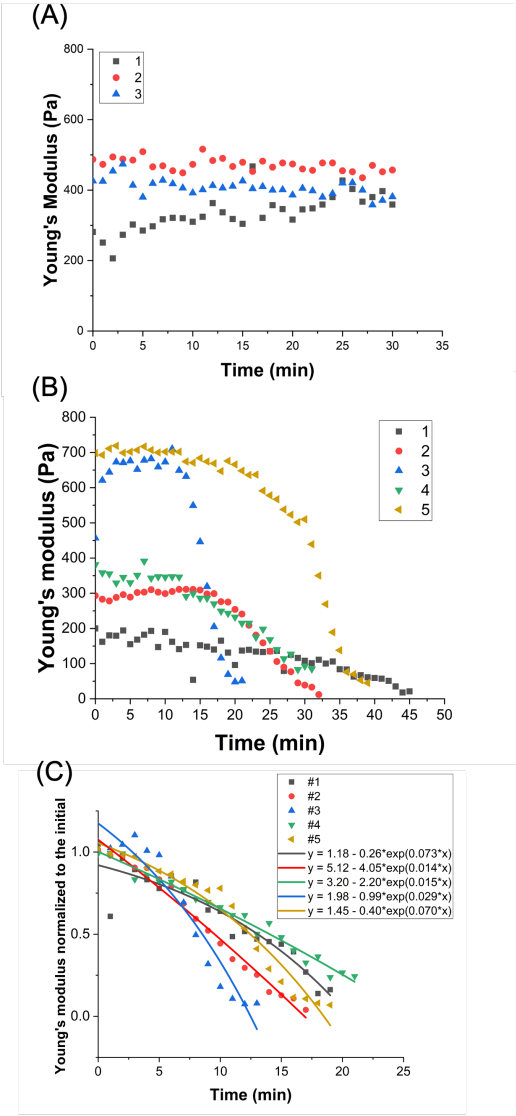

Figure A.6. Real-time young's modulus measurements using Atomic force microscopy of (A) HCM hydrogels (#1-5) for three samples and (B) HCM hydrogels with collagenase (100 unit/mL) for five samples. (C) The change in young's modulus of HCM which normalized to the initial, over time after collagenase treatment at 0 min. The data was fitted with mathematical exponential function to determine the rate of the change in young's modulus of HCM

location of sample (Figure A.6(B)). As expected, due to the variation in young's modulus from the difference in the local physical structure of HCM sample, each HCM sample showed the different initial young's modulus value before degradation (Figure

A.6(B)). However, I represented the wide range of the change in young's modulus of HCM hydrogel, normalized to the initial young's modulus, over the time (4.02 ± 2.9 %/min) during degradation (Figure A.6(C)). The reason why I have observed such a large variation could be the local point that I probed might be composed of different portion of collagen fibers and HA-SH. In fact, collagenase only degrades collagen in HCM hydrogel, which have shown the main structure within HA/collagen mixed gel (20). If the local point has rich HA-SH, it will additionally require more time for the diffusion of collagenase to the collagen surrounding the local point to trigger the complete degradation. Otherwise, if the local point has rich collagen, it will take relatively shorter time to break down the collagen structure by collagenase, resulting in the faster rate of change in young's modulus over time.

Taken together, these data demonstrate that the advantages of using the contact mode of AFM technique to determine the local mechanical property of soft hydrogels, which is not comparable to the bulk mechanical property. And our work is the first time to utilize the AFM to monitor the change in the local mechanical properties of soft hydrogel during the degradation by enzyme in real-time. Thus, the technique and method I present in here would be potentially beneficial to evaluate the mechanical property of local cellular microenvironment for gene/drug delivery and tissue regeneration applications.

A.3 Methods

A.3.1 Sample preparation

As described in a-SMA paper, VEGF encoding polyplexes (20 μg/mL of pVEGF) with PEI, 20% collagen mimetic peptides (CMP) modified PEI (20 CP), or 50% CMP modified PEI (50 CP) were lyophilized with 20 mM sucrose to stabilize polyplex during freezing. The lyophilized VEGF-encoding polyplexes or Murine recombinant VEGF-A (10 ng/mL) (Pepro Tech., NJ) were mixed into neutralized Type I bovine collagen (8 mg/mL) (Advanced BioMatrix, CA) and incubated at ice bath for 1 h. 1×

DPBS were added into the polyplex/neutralized collagen mixture, and Glycosil® (HA-SH, 20 mg/mL) (Advanced BioMatrix, CA was mixed into the polyplex/neutralized collagen. The final concentrations of collagen and Glycosil® in the pre-gel mixture were 4 mg/mL and 2 mg/mL, respectively. For atomic force microscope (AFM) samples preparation, the pre-gel mixture were placed within the silicon chamber (10 mm diameter and 2 mm thickness) on the glass slide and proceed the gelation with moisture chamber at 37 °C overnight.

A.3.2 Oscillatory rheology measurements

The oscillatory rheology experiments were conducted on an DHR3 rheometer (TA Instruments, New Castle, DE) with a 20 mm diameter stainless steel parallel-plate geometry. The 160 μL of pre-gel mixture was placed on the quartz rheometer stage, and the geometry was set at a 500 μm gap. Mineral oil was used to seal the geometry and prevent the dehydration of the hydrogel during the measurement. The mechanical properties of the hydrogels were measured in the linear viscoelastic regime where the modulus is independent of the level of applied stress or strain, confirmed with a frequency sweep from 0.1 to 10 rad/s at 1% strain and amplitude sweep from 0.1% to 10% strain at 6.25 rad/s (Figure A.1). The gelation of hydrogels was monitored using a time sweep conducted in the linear viscoelastic regime at 1% strain and an angular frequency of 6.25 rad/s for 90 min (Figures A.1 and A.2).

A.3.3 AFM measurements

The samples were additionally hydrated with applying PBS on the top of samples before/during AFM measurement. Operating under the assumption that the hydrogels are linear elastic materials, the Young's moduli of hydrogels were measured using a Bruker Catalyst atomic force microscope (AFM). I used a relatively large AFM probe with a 10 micron diameter tip and spring force constants measured by the manufacturer (Bruker, SAA-SPH-10UM, nominal k = 0.200 N/m). Typical

measurements consisted of taking multiple force-extension measurements at a rate of 2 μm/s, arranged in a 5-by-5 grid with 10 micron spacing between measurements, on at least two distant regions of the hydrogel (Figure A.4). For the collagenase degradation study, collagenase (1000 unit/mL) (Advanced BioMatrix, CA) in PBS was added on the PBS on the top of samples to make the final collagenase concentration as 100 unit/mL, without disrupting the AFM probe. The measurement consisted of taking one force-extension measurement at a rate of 2 μm/s per every one minute within the identical location until the measurement was failed due to the degradation of hydrogel by collagenase. The Young's modulus was approximated from fits of the approach curve with force boundaries of 10-70% of the maximum using a spherical Hertzian model curve fits with $R^2<0.98$ were excluded from analysis. All fits were per-formed in the NanoScope Analysis software package (v1.5) provided by the manufacturer.

REFERENCES

1. Yi B, Xu Q, Liu W. An overview of substrate stiffness guided cellular response and its applications in tissue regeneration. Bioact Mater. 2022;15:82-102. Epub 2022/04/08. doi: 10.1016/j.bioactmat.2021.12.005. PubMed PMID: 35386347; PMCID: PMC8940767.

2. Ma Y, Lin M, Huang G, Li Y, Wang S, Bai G, Lu TJ, Xu F. 3D Spatiotemporal Mechanical Microenvironment: A Hydrogel-Based Platform for Guiding Stem Cell Fate. Adv Mater. 2018;30(49):e1705911. Epub 2018/08/01. doi: 10.1002/adma.201705911. PubMed PMID: 30063260.

3. Ahearne M. Introduction to cell-hydrogel mechanosensing. Interface Focus. 2014;4(2):20130038. Epub 2014/04/22. doi: 10.1098/rsfs.2013.0038. PubMed PMID: 24748951; PMCID: PMC3982445.

4. Ehrbar M, Sala A, Lienemann P, Ranga A, Mosiewicz K, Bittermann A, Rizzi SC, Weber FE, Lutolf MP. Elucidating the role of matrix stiffness in 3D cell migration and remodeling. Biophys J. 2011;100(2):284-93. Epub 2011/01/20. doi: 10.1016/j.bpj.2010.11.082. PubMed PMID: 21244824; PMCID: PMC3021668.

5. Dietrich M, Le Roy H, Bruckner DB, Engelke H, Zantl R, Radler JO, Broedersz CP. Guiding 3D cell migration in deformed synthetic hydrogel microstructures. Soft Matter. 2018;14(15):2816-26. Epub 2018/03/30. doi: 10.1039/c8sm00018b. PubMed PMID: 29595213.

6. Banerjee A, Arha M, Choudhary S, Ashton RS, Bhatia SR, Schaffer DV, Kane RS. The influence of hydrogel modulus on the proliferation and differentiation of encapsulated neural stem cells. Biomaterials. 2009;30(27):4695-9. Epub 2009/06/23. doi: 10.1016/j.biomaterials.2009.05.050. PubMed PMID: 19539367; PMCID: PMC2743317.

7. Scott RA, Kharkar PM, Kiick KL, Akins RE. Aortic adventitial fibroblast sensitivity to mitogen activated protein kinase inhibitors depends on substrate

stiffness. Biomaterials. 2017;137:1-10. Epub 2017/05/21. doi: 10.1016/j.biomaterials.2017.05.010. PubMed PMID: 28527302; PMCID: PMC5554066.

8. Scott RA, Kiick KL, Akins RE. Substrate stiffness directs the phenotype and polarization state of cord blood derived macrophages. Acta Biomater. 2021;122:220-35. Epub 2020/12/29. doi: 10.1016/j.actbio.2020.12.040. PubMed PMID: 33359292; PMCID: PMC7904389.

9. Scott RA, Robinson KG, Kiick KL, Akins RE. Human Adventitial Fibroblast Phenotype Depends on the Progression of Changes in Substrate Stiffness. Adv Healthc Mater. 2020;9(8):e1901593. Epub 2020/02/28. doi: 10.1002/adhm.201901593. PubMed PMID: 32105417; PMCID: PMC7274877.

10. Wang Y, Gong T, Zhang ZR, Fu Y. Matrix Stiffness Differentially Regulates Cellular Uptake Behavior of Nanoparticles in Two Breast Cancer Cell Lines. ACS Appl Mater Interfaces. 2017;9(31):25915-28. Epub 2017/07/19. doi: 10.1021/acsami.7b08751. PubMed PMID: 28718278.

11. Huang C, Butler PJ, Tong S, Muddana HS, Bao G, Zhang S. Substrate stiffness regulates cellular uptake of nanoparticles. Nano Lett. 2013;13(4):1611-5. Epub 2013/03/15. doi: 10.1021/nl400033h. PubMed PMID: 23484640.

12. Gandin A, Murugesan Y, Torresan V, Ulliana L, Citron A, Contessotto P, Battilana G, Panciera T, Ventre M, Netti AP, Nicola L, Piccolo S, Brusatin G. Simple yet effective methods to probe hydrogel stiffness for mechanobiology. Sci Rep. 2021;11(1):22668. Epub 2021/11/24. doi: 10.1038/s41598-021-01036-5. PubMed PMID: 34811382; PMCID: PMC8608946.

13. Kloxin AM, Kloxin CJ, Bowman CN, Anseth KS. Mechanical properties of cellularly responsive hydrogels and their experimental determination. Adv Mater. 2010;22(31):3484-94. Epub 2010/05/18. doi: 10.1002/adma.200904179. PubMed PMID: 20473984; PMCID: PMC3890982.

14. Norman MDA, Ferreira SA, Jowett GM, Bozec L, Gentleman E. Measuring the elastic modulus of soft culture surfaces and three-dimensional hydrogels

using atomic force microscopy. Nat Protoc. 2021;16(5):2418-49. Epub 2021/04/16. doi: 10.1038/s41596-021-00495-4. PubMed PMID: 33854255.

15. Antoine EE, Vlachos PP, Rylander MN. Review of collagen I hydrogels for bioengineered tissue microenvironments: characterization of mechanics, structure, and transport. Tissue Eng Part B Rev. 2014;20(6):683-96. Epub 2014/06/14. doi: 10.1089/ten.TEB.2014.0086. PubMed PMID: 24923709; PMCID: PMC4241868.

16. Summonte S, Racaniello GF, Lopedota A, Denora N, Bernkop-Schnurch A. Thiolated polymeric hydrogels for biomedical application: Cross-linking mechanisms. J Control Release. 2021;330:470-82. Epub 2020/12/29. doi: 10.1016/j.jconrel.2020.12.037. PubMed PMID: 33359581.

17. Thankachan SN, Ilamaran M, Ayyadurai N, Shanmugam G. Insights into the effect of artificial sweeteners on the structure, stability, and fibrillation of type I collagen. Int J Biol Macromol. 2020;164:748-58. Epub 2020/07/22. doi: 10.1016/j.ijbiomac.2020.07.152. PubMed PMID: 32693139.

18. Rother S, Ruiz-Gomez G, Balamurugan K, Koehler L, Fiebig KM, Galiazzo VD, Hempel U, Moeller S, Schnabelrauch M, Waltenberger J, Pisabarro MT, Scharnweber D, Hintze V. Hyaluronan/Collagen Hydrogels with Sulfated Glycosaminoglycans Maintain VEGF165 Activity and Fine-Tune Endothelial Cell Response. ACS Appl Bio Mater. 2021;4(1):494-506. Epub 2022/01/12. doi: 10.1021/acsabm.0c01001. PubMed PMID: 35014301.

19. Yang YL, Kaufman LJ. Rheology and confocal reflectance microscopy as probes of mechanical properties and structure during collagen and collagen/hyaluronan self-assembly. Biophys J. 2009;96(4):1566-85. Epub 2009/02/17. doi: 10.1016/j.bpj.2008.10.063. PubMed PMID: 19217873; PMCID: PMC2717242.

20. Segura T, Anderson BC, Chung PH, Webber RE, Shull KR, Shea LD. Crosslinked hyaluronic acid hydrogels: a strategy to functionalize and pattern. Biomaterials. 2005;26(4):359-71. Epub 2004/07/28. doi: 10.1016/j.biomaterials.2004.02.067. PubMed PMID: 15275810.

Appendix B

IN SITU ASSESSMENT OF TISSUE REMODELING WITH COLLAGEN MIMETIC PEPTIDE (CMP) MODIFIED POLYSTYRENE PARTICLES

The overall goal of this appendix is to demonstrate the application of CMP functionalized polystyrene particles to localize on the tissue remodeling site for the potential targeted drug delivery and imaging tool. In this study, I have prepared CMP modified polystyrene particle (PS-CMP), through NHS chemistry between N-terminus of (GPO)7-GG and carboxylic acid group on the surface Nile red fluorescent encapsulated polystyrene nanoparticles, to investigate the binding of PS-CMP on the mouse tail tendon and human cholesteatoma tissues.

Both tissue types contain collagen, in particular, the major component of mouse tail tendon is collagen Type I. The mouse tail tendon tissue was further physically damaged using a surgical scalpel to mimic collagen denaturation during the tendon injury. I have optimized the condition for PS-CMP to apply on tissue for detecting the specific binding to damaged tendon vs. healthy tendon. The study revealed that PS-CMP localized more on the damaged tendon at both 4 ºC and 37 ºC incubation than the healthy tendon. In addition, the heating PS-CMP to disassemble the triple helix of CMP to single strand, prior to adding into tissue, did not necessary for the localization of PS-CMP more on the damaged tendon than the healthy tendon. Altogether, this result demonstrated the specific localization of PS-CMP on the tissue with denatured collagen, leading to the potential use of PS-CMP to target tissue remodeling sites.

Next, I have applied PS-CMP to the human cholesteatoma tissue, abnormal skin growth in the middle ear, to evaluate the potential use of PS-CMP as the imaging tool to identify cholesteatoma during the surgical removal of cholesteatoma and drug delivery vehicle to prevent the re-growth of cholesteatoma. I have investigated the presence of collagen in human cholesteatoma tissue from six patients and correlation

with the localization of PS-CMP within the cholesteatoma tissue. The results showed that cholesteatoma tissues contained the different levels of collagen and keratin depending on the patient and PS-CMP tended to localize more on the cholesteatoma tissue with a rich collagen. Moreover, PS-CMP had less tendency to bind to the cholesteatoma surrounding collagen rich tissues such as ossicle, mucosa membrane, and nerve, indicative of the specific targeting of PS-CMP to cholesteatoma. In addition, I have evaluated the presence of microorganisms on the cholesteatoma tissues characterized with inflamed and infected using gram staining, revealing that all of cholesteatoma tissue had gram-positive microorganisms accumulated on the keratin of cholesteatoma. This study suggests that the potential of use PS-CMP as a delivery system for antibiotic, which enable the localization on cholesteatoma residual and eradication of the microorganisms in cholesteatoma to prevent the recurrence of cholesteatoma.

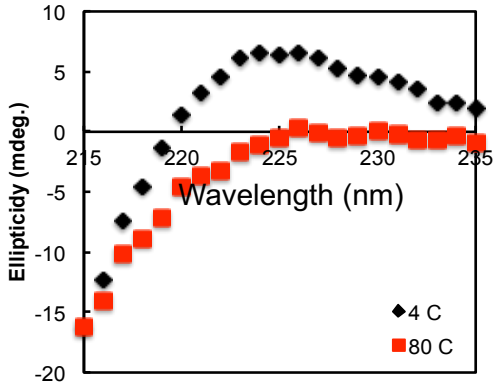

Figure B.1. Circular dichroism (CD) spectra wavelength measurement of CMP, $(GPO)_7GG$, at 4 ºC (Black diamond) and 80 ºC (Red square) to evaluate the ability of CMP for thermal responsive triple helix assembly and single strand disassembly. $(GPO)_7GG$ (150 µM) in PBS were incubated at 4 ºC overnight prior to CD measurement. The maximal peak at 225 nm indicated the triple helix assembly of CMP at 4 ºC, while the lack of peak at 225 nm suggested the thermally disassembly into a single strand of CMP at 80 ºC.

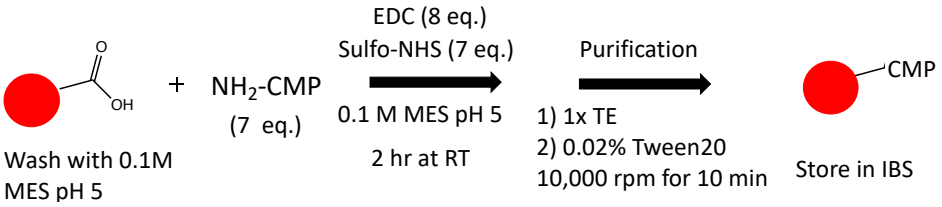

Figure B.2. Schematic of CMP, $(GPO)_7GG$, conjugation on carboxylic group functionalized Nile red encapsulated polystyrene nanoparticle (d = 300 nm). The carboxylic group functionalized Nile red encapsulated polystyrene (PS) nanoparticle were suspended in 0.1 M MES buffer at pH 5. 1-Ethyl-3-(3-dimethylaminopropyl)carbodiimide (EDC) (8 eq.) in MES was added into PS nanoparticle and incubated at RT for 15 min while rotating to activate the carboxylic acid groups on PS. Then, CMP (7 eq.) and Sulfo-NHS (7 eq.) were added into EDC and PS mixture and incubated at RT for 2 h while rotating. CMP conjugated PS nanoparticle were purified by centrifugation method for two runs with TE and 0.02% tween 20 in TE. CMP-PS nanoparticles were stored in isotonic buffered saline (IBS) at 4 ºC for future use.

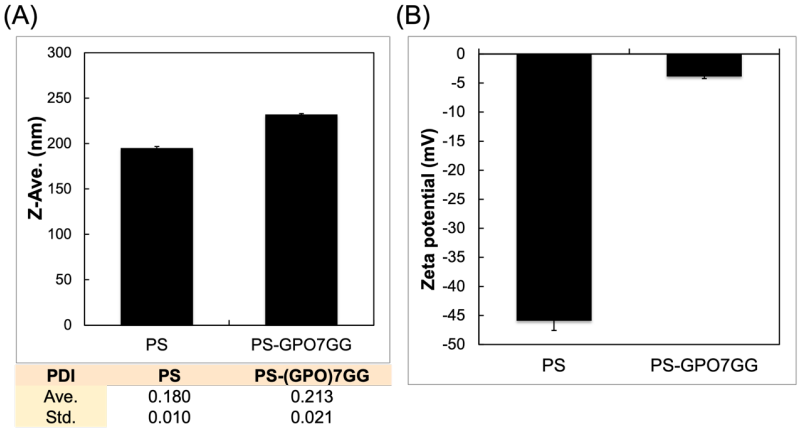

PDI	PS	PS-(GPO)7GG
Ave.	0.180	0.213
Std.	0.010	0.021

Figure B.3. Dynamic light scattering measurements to confirm the CMP functionalization on PS nanoparticles. (A) Size measurement of z-average diameter of PS nanoparticle before and after CMP conjugation. Z-average diameter was enhanced for CMP functionalized PS nanoparticle than PS nanoparticle. (B) Zeta-potential measurement to demonstrate the change in surface charge before and after CMP conjugation. Due to the presence of carboxylic acid on the surface of PS nanoparticle, PS nanoparticle exhibited -45 mV as zeta potential. After CMP conjugation on the surface of PS nanoparticle, zeta potential of CMP functionalized PS nanoparticle was closed to 0 mV.

B.1 Protocol for CMP functionalized PS nanoparticles binding on tissue and detection using the multi-photon microscope

After CMP functionalized PS nanoparticles (PS-CMP) in deionized water (0.1 mg/mL) was heated at 65 ºC for 5 min or non-heated, PS-CMP was applied on the tissue and was incubated at either 4 ºC or 37 ºC overnight. PS-CMP solution was removed from the tissue and the tissue was rinsed with 0.05% Tween-20 in PBS for three times at room temperature. To detect the PS-CMP binding on the tissue, the multi-photon microscope was used with both reverse and forward second harmonic generation (SHG) signals generated from collagen fibers in tissue using a 400 ± 10 nm emission filter and two-photon excited fluorescence (TPEF) of PS-(GPO)7GG (Nile red) was detected using 550 ± 50 nm emission filter at 800 nm as an excitation.

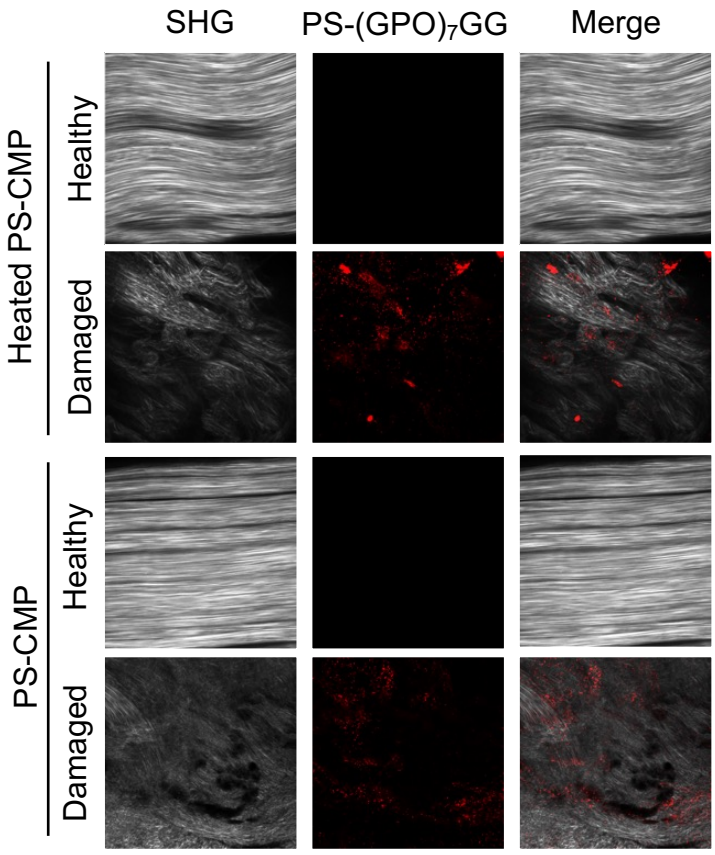

Figure B.4. The representative images of *in situ* binding of CMP functionalized PS nanoparticle (PS-CMP, red) on healthy, or physically damaged mouse tail tendon (collagen, grey) to mimic the denatured collagen during the tendon remodeling process. The figure showed more tendency of PS-CMP binding to physically disrupted collagen in mouse tail tendon and no binding of PS-CMP to healthy mouse tail tendon. PS-CMP were applied to the mouse tail tendons after heating at 65 ºC for 5 min to make sure CMP disassembled to single strand, or no heating. Although PS-CMP with heating showed more binding signal than PS-CMP without heating on the physically damaged tail tendon, PS-CMP without heating had still more affinity to the damaged tendon than healthy tendon.

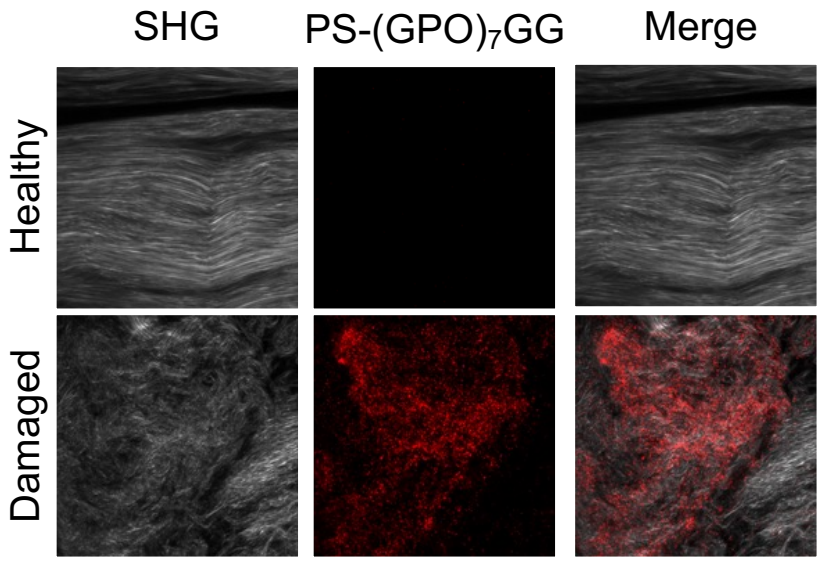

Figure B.5. The representative images of *in situ* binding of CMP functionalized PS nanoparticle (PS-CMP, red) on healthy or physically damaged mouse tail tendon (collagen, grey). CMP functionalized PS nanoparticles were applied to the mouse tail tendons and incubated at 37 ºC for binding to mimic the physiological condition. The figure showed similar as binding at 4 ºC, PS-CMP bound more on the physically damaged tail tendon than the healthy even at physiological condition. This suggested that the potential for PS-CMP to use as drug delivery systems to localize the tendon for repair.

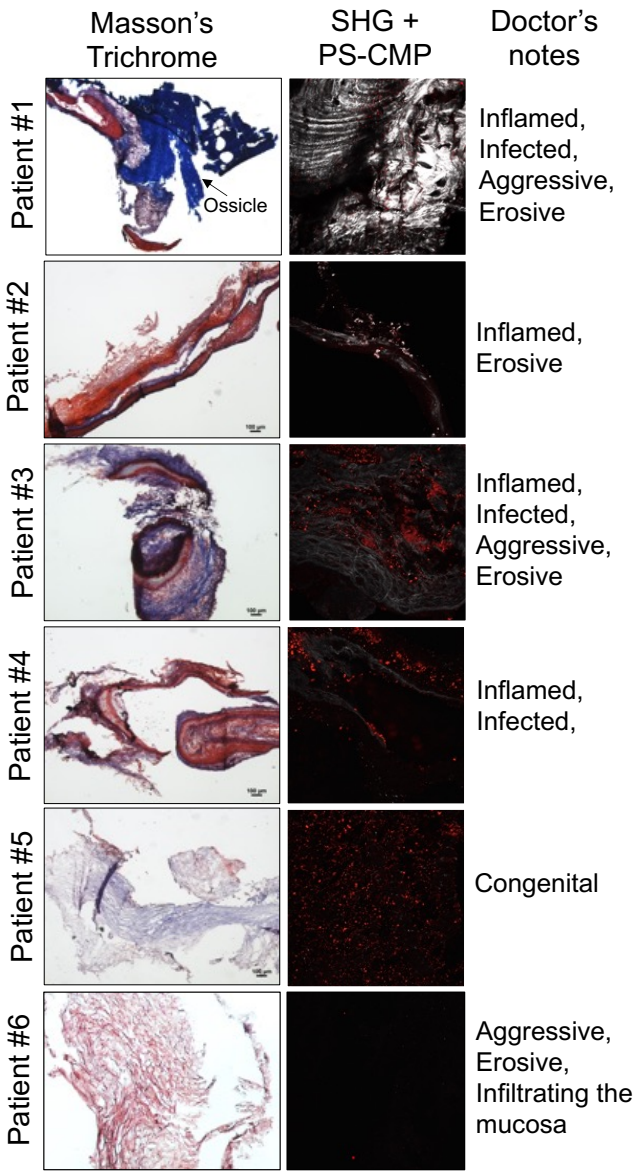

Figure B.6. The representative images of cholesteatoma tissue sections from six human patients. Each tissue was characterized by Doctor's observation during the removal surgery. Masson's trichrome staining (Blue-Collagen and Red- Keratin) and SHG imaging (grey) were used to evaluate the presence of collagen in cholesteatoma. The collagen signals were correlated with the localization of PS-CMP (red) signals within the cholesteatoma tissue. PS-CMP signals were low for the tissue with less collagen composed (Patient #2 and #6), while the PS-CMP signals were stronger where the collagen present on the tissue.

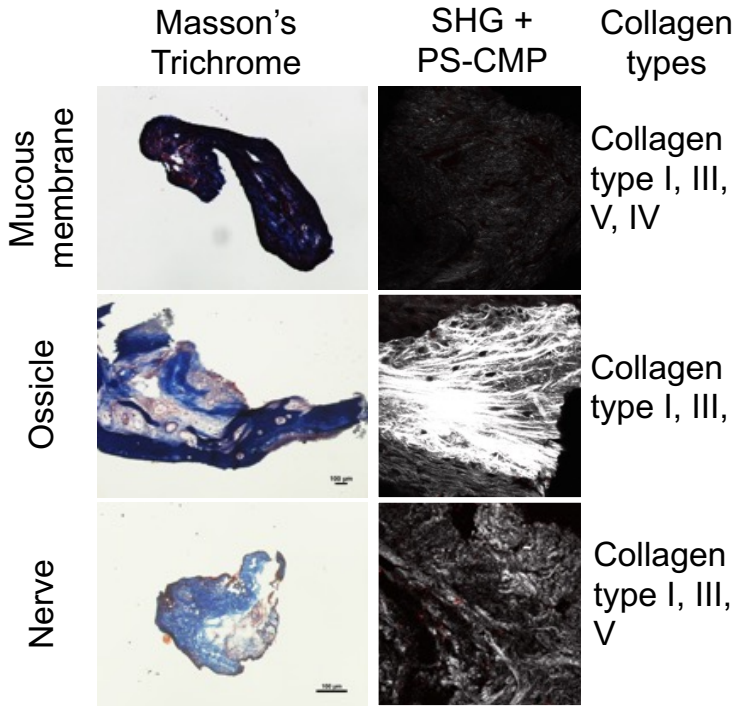

Figure B.7. The representative images of tissues sections (mucous membrane, ossicle, and nerve) surrounding the cholesteatoma to evaluate PS-CMP for specific targeting the cholesteatoma. Each tissue was composed of collagen but different types (1-3). Masson's trichrome staining (Blue-Collagen and Red- Keratin) and SHG imaging (grey) were used to confirm the presence of collagen in cholesteatoma. The collagen signals were correlated with the localization of PS-CMP (red) signals within the different types of tissues. Overall, PS-CMP signals were minimum for all of the testing tissue types, indicating that the potential use of PS-CMP to localize the collagen rich cholesteatoma.

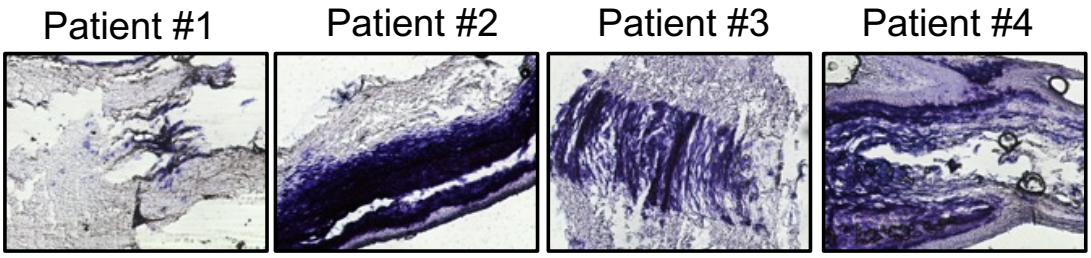

Figure B.8. The representative gram staining images of Cholesteatoma tissues sections with inflamed and infected (Patient #1,2,3, and 4) to detect the presence of microorganism (Gram-positive (dark blue-violet) and gram-negative (red)). All of tissue sections where Keratin were located, were stained positive for gram-positive. This result suggest that the potential use of PS-CMP as a delivery vehicle for antibiotic to eradicate the microorganism on cholesteatoma, leading to the prevention of the recurrence of cholesteatoma growth.

REFERENCES

1. Nerlich AG. Collagen types in the middle ear mucosa. Eur Arch Otorhinolaryngol. 1995;252(7):443-6; discussion 7-9. Epub 1995/01/01. doi: 10.1007/BF00167317. PubMed PMID: 8562042.

2. Stenfeldt K, Johansson C, Hellstrom S. The collagen structure of the tympanic membrane: collagen types I, II, and III in the healthy tympanic membrane, during healing of a perforation, and during infection. Arch Otolaryngol Head Neck Surg. 2006;132(3):293-8. Epub 2006/03/22. doi: 10.1001/archotol.132.3.293. PubMed PMID: 16549750.

3. Koopmans G, Hasse B, Sinis N. Chapter 19: The role of collagen in peripheral nerve repair. Int Rev Neurobiol. 2009;87:363-79. Epub 2009/08/18. doi: 10.1016/S0074-7742(09)87019-0. PubMed PMID: 19682648.

Appendix C

IACUC (ANIMAL SUBJECTS) APPROVAL

University of Delaware
Institutional Animal Care and Use Committee
Annual Review

Title of Protocol: Non-viral gene delivery to excisionally-wounded mice

AUP Number: 1229-2022-1 ← **(4 digits only)**

Principal Investigator: Millicent Sullivan

Common Name: Mouse

Genus Species: Mus musculus

Pain Category: ***(please mark one)***

USDA PAIN CATEGORY: ***(Note change of categories from previous form)***

Category	Description
☐ **B**	Breeding or holding where NO research is conducted
☐ **C**	Procedure involving momentary or no pain or distress
☒ **D**	Procedure where pain or distress is alleviated by appropriate means (analgesics tranquilizers, euthanasia etc.)
☐ **E**	Procedure where pain or distress cannot be alleviated, as this would adversely affect the procedures, results or interpretation

Official Use Only

IACUC Approval Signature: [signature] DVM

Date of Approval: 3.1.2022

Appendix D

RIGHTS AND PERMISSIONS DOCUMENTATION

Keywords: targeted drug delivery, extracellular matrix, hydrogel, ECM ligand, ECM cell receptors

Citation: Hwang J, Sullivan MO and Kilick KL (2020) Targeted Drug Delivery via the Use of ECM-Mimetic Materials. *Front. Bioeng. Biotechnol.* 8:69. doi: 10.3389/fbioe.2020.00069

Received: 05 October 2019; **Accepted:** 27 January 2020;
Published: 18 February 2020.

Edited by:
Martin Ehrbar, University of Zurich, Switzerland

Reviewed by:
Mikaël M. Martino, Monash University, Australia
Silvia Minardi, Northwestern University, United States
Uwe Freudenberg, Leibniz Institute of Polymer Research (LG), Germany

***Correspondence:** Millicent O. Sullivan, msulliva@udel.edu; Kristi L. Kilick, klick@udel.edu

(Rights permission for Chapter 1)

License Number	5352711003200	Printable Details
License date	Jul 19, 2022	

Licensed Content

Licensed Content Publisher	Elsevier
Licensed Content Publication	Advanced Drug Delivery Reviews
Licensed Content Title	Extracellular matrix structure
Licensed Content Author	Achilleas D. Theocharis,Spyros S. Skandalis,Chrysostomi Gialeli,Nikos K. Karamanos
Licensed Content Date	Feb 1, 2016
Licensed Content Volume	97
Licensed Content Issue	n/a
Licensed Content Pages	24

Order Details

Type of Use	reuse in a thesis/dissertation
Portion	figures/tables/illustrations
Number of figures/tables/illustrations	1
Format	electronic
Are you the author of this Elsevier article?	No
Will you be translating?	No

About Your Work

Title	Extracellular matrix (ECM)-based biomaterial strategies to control delivery of gene and small molecule therapies in wound repair
Institution name	University of Delaware
Expected presentation date	Jan 2023

Additional Data

Portions	Figure 1

Requestor Location

Requestor Location	University of Delaware 150 Academy st. Colburn Lab NEWARK, DE 19716 United States Attn: Jeongmin Hwang

Tax Details

Publisher Tax ID	98-0397604

Price

Total	0.00 USD

Figure 1.1

ACS Publications
Most Trusted. Most Cited. Most Read.

Thermoresponsive Elastin-b-Collagen-Like Peptide Bioconjugate Nanovesicles for Targeted Drug Delivery to Collagen-Containing Matrices

Author: Tianzhi Luo, Michael A. David, Lucas C. Dunshee, et al
Publication: Biomacromolecules
Publisher: American Chemical Society
Date: Aug 1, 2017

PERMISSION/LICENSE IS GRANTED FOR YOUR ORDER AT NO CHARGE

This type of permission/license, instead of the standard Terms and Conditions, is sent to you because no fee is being charged for your order. Please note the following:

- Permission is granted for your request in both print and electronic formats, and translations.
- If figures and/or tables were requested, they may be adapted or used in part.
- Please print this page for your records and send a copy of it to your publisher/graduate school.
- Appropriate credit for the requested material should be given as follows: "Reprinted (adapted) with permission from {COMPLETE REFERENCE CITATION}. Copyright {YEAR} American Chemical Society." Insert appropriate information in place of the capitalized words.
- One-time permission is granted only for the use specified in your RightsLink request. No additional uses are granted (such as derivative works or other editions). For any uses, please submit a new request.

If credit is given to another source for the material you requested from RightsLink, permission must be obtained from that source.

Figure 1.2(A)

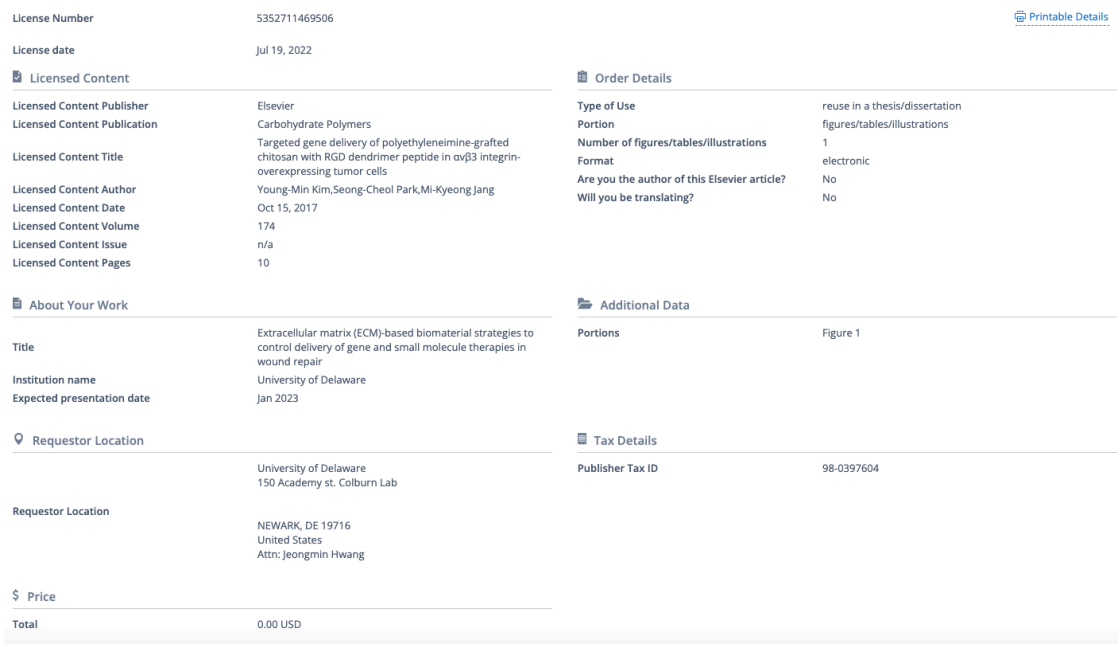

License Number	5352711469506
License date	Jul 19, 2022

Printable Details

Licensed Content

Licensed Content Publisher	Elsevier
Licensed Content Publication	Carbohydrate Polymers
Licensed Content Title	Targeted gene delivery of polyethyleneimine-grafted chitosan with RGD dendrimer peptide in αvβ3 integrin-overexpressing tumor cells
Licensed Content Author	Young-Min Kim,Seong-Cheol Park,Mi-Kyeong Jang
Licensed Content Date	Oct 15, 2017
Licensed Content Volume	174
Licensed Content Issue	n/a
Licensed Content Pages	10

Order Details

Type of Use	reuse in a thesis/dissertation
Portion	figures/tables/illustrations
Number of figures/tables/illustrations	1
Format	electronic
Are you the author of this Elsevier article?	No
Will you be translating?	No

About Your Work

Title	Extracellular matrix (ECM)-based biomaterial strategies to control delivery of gene and small molecule therapies in wound repair
Institution name	University of Delaware
Expected presentation date	Jan 2023

Additional Data

Portions	Figure 1

Requestor Location

Requestor Location	University of Delaware 150 Academy st. Colburn Lab NEWARK, DE 19716 United States Attn: Jeongmin Hwang

Tax Details

Publisher Tax ID	98-0397604

Price

Total	0.00 USD

Figure 1.2(B)

License Number	5352720238250
License date	Jul 19, 2022

Licensed Content

Licensed Content Publisher	John Wiley and Sons
Licensed Content Publication	ADVANCED THERAPEUTICS
Licensed Content Title	Peptide-Modified Dendrimer Nanoparticles for Targeted Therapy of Colorectal Cancer
Licensed Content Author	Joaquim M. Oliveira, Rui L. Reis, Subhas C. Kundu, et al
Licensed Content Date	Sep 9, 2019
Licensed Content Volume	2
Licensed Content Issue	11
Licensed Content Pages	11

Order Details

Type of use	Dissertation/Thesis
Requestor type	University/Academic
Format	Electronic
Portion	Figure/table
Number of figures/tables	1
Will you be translating?	No

About Your Work

Title	Extracellular matrix (ECM)-based biomaterial strategies to control delivery of gene and small molecule therapies in wound repair
Institution name	University of Delaware
Expected presentation date	Jan 2023

Additional Data

Portions	Figure 4(A)

Requestor Location

Requestor Location	University of Delaware 150 Academy st. Colburn Lab NEWARK, DE 19716 United States Attn: Jeongmin Hwang

Tax Details

Publisher Tax ID	EU826007151

Price

Total	0.00 USD

Figure 1.2(C)

License Number	5352720378139
License date	Jul 19, 2022

Licensed Content

Licensed Content Publisher	Springer Nature
Licensed Content Publication	International Orthopaedics
Licensed Content Title	A comprehensive clinical review of recombinant human bone morphogenetic protein-2 (INFUSE® Bone Graft)
Licensed Content Author	William F. McKay et al
Licensed Content Date	Jul 17, 2007

Order Details

Type of Use	Thesis/Dissertation
Requestor type	academic/university or research institute
Format	electronic
Portion	figures/tables/illustrations
Number of figures/tables/illustrations	1
Will you be translating?	no
Circulation/distribution	1 - 29
Author of this Springer Nature content	no

About Your Work

Title	Extracellular matrix (ECM)-based biomaterial strategies to control delivery of gene and small molecule therapies in wound repair
Institution name	University of Delaware
Expected presentation date	Jan 2023

Additional Data

Portions	Figure 2

Requestor Location

Requestor Location	University of Delaware 150 Academy st. Colburn Lab NEWARK, DE 19716 United States Attn: Jeongmin Hwang

Tax Details

Price

Total	0.00 USD

Figure. 1.3(A)

Figure. 1.3 (B) – Open access

SPRINGER NATURE

Laminin heparin-binding peptides bind to several growth factors and enhance diabetic wound healing

Author: Jun Ishihara et al
Publication: Nature Communications
Publisher: Springer Nature
Date: Jun 4, 2018

Figure 1.4(A)

License Number	5352720874066
License date	Jul 19, 2022

Licensed Content

Licensed Content Publisher	Elsevier
Licensed Content Publication	Acta Biomaterialia
Licensed Content Title	Collagen tethering of synthetic human antimicrobial peptides cathelicidin LL37 and its effects on antimicrobial activity and cytotoxicity
Licensed Content Author	Lindsay D. Lozeau,Jonian Grosha,Denis Kole,Fioleda Prifti,Tanja Dominko,Terri A. Camesano,Marsha W. Rolle
Licensed Content Date	Apr 1, 2017
Licensed Content Volume	52
Licensed Content Issue	n/a
Licensed Content Pages	12

Order Details

Type of Use	reuse in a thesis/dissertation
Portion	figures/tables/illustrations
Number of figures/tables/illustrations	2
Format	electronic
Are you the author of this Elsevier article?	No
Will you be translating?	No

About Your Work

Title	Extracellular matrix (ECM)-based biomaterial strategies to control delivery of gene and small molecule therapies in wound repair
Institution name	University of Delaware
Expected presentation date	Jan 2023

Additional Data

Portions	Figure 1 and Figure 6

Requestor Location

Requestor Location	University of Delaware 150 Academy st. Colburn Lab NEWARK, DE 19716 United States Attn: Jeongmin Hwang

Tax Details

Publisher Tax ID	98-0397604

Price

Total	0.00 USD

Figure 1.4(B)

License Number	5352720992194
License date	Jul 19, 2022

Licensed Content

Licensed Content Publisher	Elsevier
Licensed Content Publication	Biomaterials
Licensed Content Title	Cell recruitment and transfection in gene activated collagen matrix
Licensed Content Author	Silvia Orsi,Antonia De Capua,Daniela Guarnieri,Daniela Marasco,Paolo A. Netti
Licensed Content Date	Jan 1, 2010
Licensed Content Volume	31
Licensed Content Issue	3
Licensed Content Pages	7

Order Details

Type of Use	reuse in a thesis/dissertation
Portion	figures/tables/illustrations
Number of figures/tables/illustrations	1
Format	electronic
Are you the author of this Elsevier article?	No
Will you be translating?	No

About Your Work

Title	Extracellular matrix (ECM)-based biomaterial strategies to control delivery of gene and small molecule therapies in wound repair
Institution name	University of Delaware
Expected presentation date	Jan 2023

Additional Data

Portions	Figure 6

Requestor Location

Requestor Location	University of Delaware 150 Academy st. Colburn Lab NEWARK, DE 19716 United States Attn: Jeongmin Hwang

Tax Details

Publisher Tax ID	98-0397604

Price

Total	0.00 USD

Figure 1.5(A)

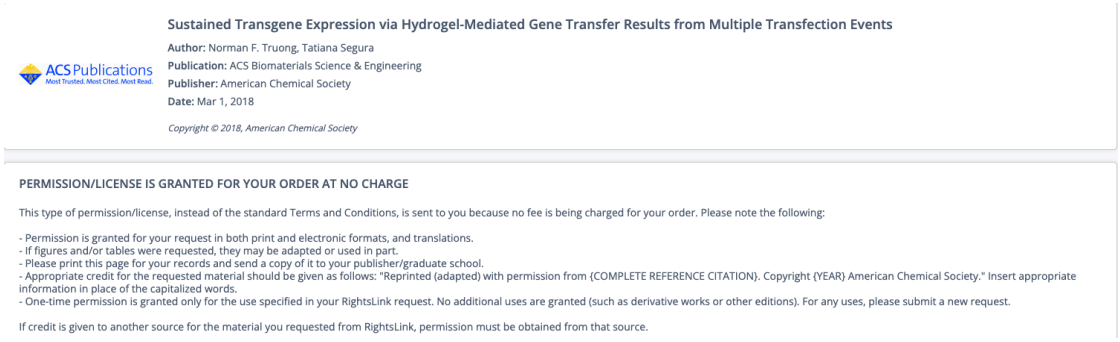

Sustained Transgene Expression via Hydrogel-Mediated Gene Transfer Results from Multiple Transfection Events

Author: Norman F. Truong, Tatiana Segura
Publication: ACS Biomaterials Science & Engineering
Publisher: American Chemical Society
Date: Mar 1, 2018

Copyright © 2018, American Chemical Society

PERMISSION/LICENSE IS GRANTED FOR YOUR ORDER AT NO CHARGE

This type of permission/license, instead of the standard Terms and Conditions, is sent to you because no fee is being charged for your order. Please note the following:

- Permission is granted for your request in both print and electronic formats, and translations.
- If figures and/or tables were requested, they may be adapted or used in part.
- Please print this page for your records and send a copy of it to your publisher/graduate school.
- Appropriate credit for the requested material should be given as follows: "Reprinted (adapted) with permission from {COMPLETE REFERENCE CITATION}. Copyright {YEAR} American Chemical Society." Insert appropriate information in place of the capitalized words.
- One-time permission is granted only for the use specified in your RightsLink request. No additional uses are granted (such as derivative works or other editions). For any uses, please submit a new request.

If credit is given to another source for the material you requested from RightsLink, permission must be obtained from that source.

Figure 1.5(B)

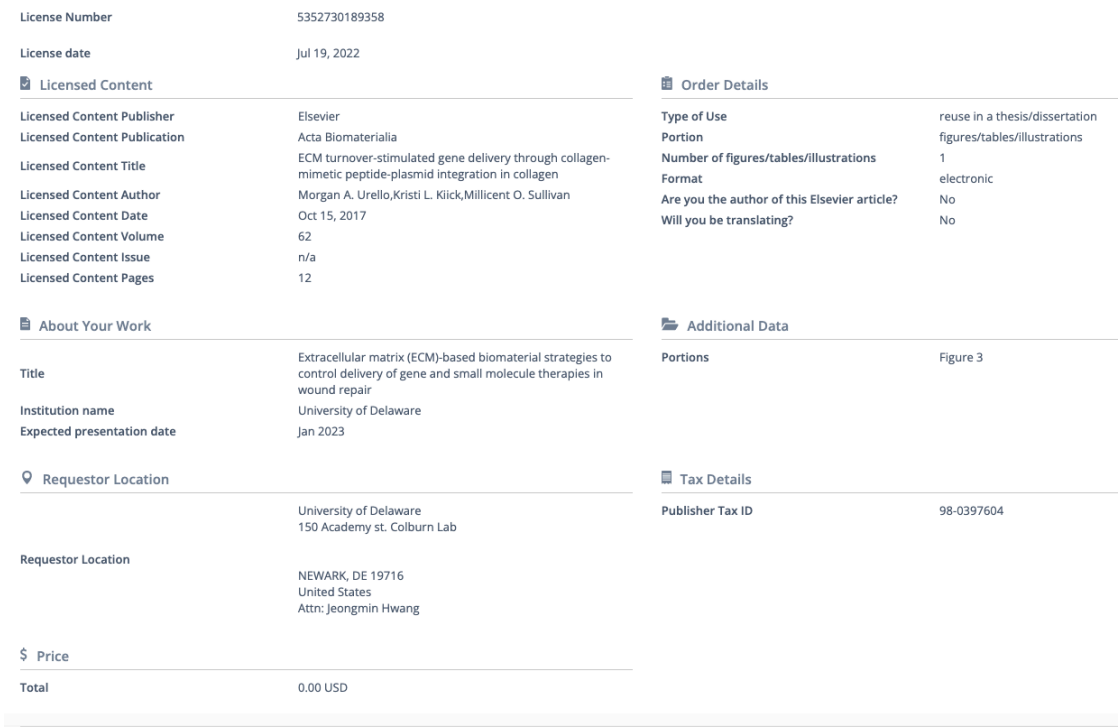

License Number	5352730189358
License date	Jul 19, 2022

Licensed Content

Licensed Content Publisher	Elsevier
Licensed Content Publication	Acta Biomaterialia
Licensed Content Title	ECM turnover-stimulated gene delivery through collagen-mimetic peptide-plasmid integration in collagen
Licensed Content Author	Morgan A. Urello,Kristi L. Kiick,Millicent O. Sullivan
Licensed Content Date	Oct 15, 2017
Licensed Content Volume	62
Licensed Content Issue	n/a
Licensed Content Pages	12

Order Details

Type of Use	reuse in a thesis/dissertation
Portion	figures/tables/illustrations
Number of figures/tables/illustrations	1
Format	electronic
Are you the author of this Elsevier article?	No
Will you be translating?	No

About Your Work

Title	Extracellular matrix (ECM)-based biomaterial strategies to control delivery of gene and small molecule therapies in wound repair
Institution name	University of Delaware
Expected presentation date	Jan 2023

Additional Data

Portions	Figure 3

Requestor Location

Requestor Location	University of Delaware 150 Academy st. Colburn Lab NEWARK, DE 19716 United States Attn: Jeongmin Hwang

Tax Details

Publisher Tax ID	98-0397604

Price

Total	0.00 USD

Figure 1.5(D)

1. Journal of materials chemistry. B, Materials for biology and medicine — 0.00 USD

Article: A CMP-based method for tunable, cell-mediated gene delivery from collagen scaffolds.

Order License ID	Pending	**Publisher**	Royal Society of Chemistry
ISSN	2050-750X	**Portion**	Image/photo/illustration
Type of Use	Republish in a thesis/dissertation		

Hide Details

LICENSED CONTENT

Publication Title	Journal of materials chemistry. B, Materials for biology and medicine	**Rightsholder**	Royal Society of Chemistry
Article Title	A CMP-based method for tunable, cell-mediated gene delivery from collagen scaffolds.	**Publication Type**	Journal
		Start Page	8174
		End Page	8185
Author/Editor	Royal Society of Chemistry (Great Britain)	**Issue**	46
		Volume	2
Date	01/01/2012		
Language	English		
Country	United Kingdom of Great Britain and Northern Ireland		

REQUEST DETAILS

Portion Type	Image/photo/illustration	**Distribution**	United States and Canada
Number of images / photos / illustrations	1	**Translation**	Original language of publication
		Copies for the disabled?	No
Format (select all that apply)	Electronic	**Minor editing privileges?**	No
Who will republish the content?	Academic institution	**Incidental promotional use?**	No
Duration of Use	Life of current edition	**Currency**	USD
Lifetime Unit Quantity	Up to 499		
Rights Requested	Main product		

NEW WORK DETAILS

Title	Extracellular matrix (ECM)-based biomaterial strategies to control delivery of gene and small molecule therapies in wound repair	**Institution name**	University of Delaware
		Expected presentation date	2023-01-02
Instructor name	NA		

ADDITIONAL DETAILS

Order reference number	N/A	**The requesting person / organization to appear on the license**	Jeongmin Hwang

REUSE CONTENT DETAILS

Title, description or numeric reference of the portion(s)	Figure 6	**Title of the article/chapter the portion is from**	A CMP-based method for tunable, cell-mediated gene delivery from collagen scaffolds.
Editor of portion(s)	Urello, M. A.; Kiick, K. L.; Sullivan, M. O.		
		Author of portion(s)	Urello, M. A.; Kiick, K. L.; Sullivan, M. O.
Volume of serial or monograph	2	**Issue, if republishing an article from a serial**	46
Page or page range of portion	8174-8185		
		Publication date of portion	2014-12-14

Print License

Total Items: 1 — **Total Due: 0.00 USD**

Figure 1.5(C)

Modified hyaluronic acid-collagen matrices trigger efficient gene transfer and prohealing behavior in fibroblasts for improved wound repair

Author: Jeongmin Hwang,Kristi L. Kiick,Millicent O. Sullivan

Publication: Acta Biomaterialia

Publisher: Elsevier

Date: 15 September 2022

Chapter 3